FRACTURES, LINEAMENTS AND SEISMIC REFLECTION DATA BEARING ON THE STRUCTURAL FABRIC in CHENANGO COUNTY, NEW YORK STATE: ELEMENTS OF EXPLORATION for NATURAL GAS FRACTURE PLAYS

REVISED FINAL

NYSERDA AGREEMENT NO.7545

July 22, 2008

Submitted by:

Dr. Robert Jacobi, Project Director
Nornew, Inc.
1412 Sweet Home Road
Suite 12
Amherst, New York 14228
(716) 568-2048
Email:Rjacobi@nornew.com

Submitted to:
Dr. John Martin, NYSERDA Project Manager
NYS Energy Research and Development Authority
17 Columbia Circle
Albany, NY 12203-6399

NOTICE

ABSTRACT

This research project focused on Chenango County, central New York State, and included outcrop fracture analyses, lineament analyses, and seismic reflection analyses. The primary goal was to identify the structural (fracture) fabric in Chenango County in order to better define potential structurally-controlled gas fairways as well as fracture patterns that may influence gas production. A second goal was to determine whether lineaments reflect structure observed both in outcrop and in seismic reflection data. The research demonstrated that the lineaments provide an indication of the structural fabric in the area of interest, but do not reflect a one-to-one complexity of the fracturing observed in, for example, adjacent outcrops. Integration of structure, lineament, and seismic data points to natural gas prospects that are structurally controlled, including prospects in the Theresa, Trenton/Black River, Oswego/Oneida, and Onondaga.

The University at Buffalo Rock Fracture Group (UBRFG) measured eight characteristics of more than 4000 fractures at 391 sites. The predominant fracture sets strike NNE and WNW. Fracture intensification domains (FIDs) are common, and many are collinear with nearby topographic features.

Lineaments were identified on digital elevation models (DEMs) and aeromagnetic data. These lineaments and EarthSat (1997) lineaments were tested statistically against the outcrop fracture data. The best correlation was found between lineaments and FIDs. Coincident aeromagnetic lineaments and surface lineaments suggest that these lineaments represent fracture systems that extend from the Precambrian to the (near) surface. Integrated lineament zones (ILZs) are defined by coincident lineaments recognized in more than one data set; the ILZs that are confirmed by FIDs probably represent fault systems.

About 80 km (50 miles) of 2-D seismic reflection profiles in central New York State display a significant number of fault systems that extend from the Precambrian basement to the (near)-surface. The fault systems have a long reactivation history, and controlled the preservation (and possibly deposition) of thinning units such as salt and the Oswego. Some of the fault systems exhibit flower structures, implying that these faults sustained strike-slip motion.

KEY WORDS

Appalachian Basin, faults, fractures, seismic reflection, lineaments

ACKNOWLEDGMENTS

This report included a strong field component; I am especially pleased to acknowledge the field personnel with whom I worked on this project; they are all fine geologists, even under sometimes trying field conditions. Field personnel included Nick Terech and Kelly McGuire, whose theses focused on Chenango County, and field assistants Paul Agle, Gareth Cross, Josh Stroup, Sean McGran, Dan Simpson, and Pat Wall. This report is an integration of all the personnel's contributions, and relies on the thesis work by Terech and McGuire. For assistance at Nornew, Inc, I thank Brian Gates and Al Leaver. It is a pleasure to work with Stu Loewenstein, and I thank him and Nornew for allowing this work to be made public. I also wish to acknowledge Dr. John Martin for his support and his viewpoints that added considerably to discussions concerning this research.

SUMMARY

The research conducted for this project included outcrop fracture analyses, lineament analyses, integration of lineaments with the potentially confirmatory fracture data, and seismic reflection analyses. The goal was to determine if the region was faulted and fractured, and if so, to determine the approximate extent and orientation of the faulting and fracturing. Knowledge concerning the structural fabric in the area of interest provides the foundation for determining natural gas prospects in structural plays.

The University at Buffalo Rock Fracture Group (UBRFG) measured eight characteristics of more than 4000 fractures at 391 sites in the area of interest in Chenango County, New York State. This extensive data set showed that the most common fractures strike NNE and WNW. Other facture sets are much less prominent except locally, and include ENE and N-striking fractures. Fracture intensification domains (FIDs), with fracture frequencies of >4 fractures/meter, are common in the area of interest, and many are collinear with nearby topographic features. FIDs elsewhere have been shown to be associated with faults. A plot of fracture frequency versus bed thickness of the versus interbedded sandstones/siltstones and gray shales showed no correlation between the two measures.

Lineaments were identified on digital elevation models (DEMs) and aeromagnetic anomalies in the areas of interest in Chenango County. These lineaments and EarthSat (1997) lineaments from Landsat images were integrated and then tested against the outcrop fracture data. The statistical comparison involved the use of weights of evidence. In the northern study area, NNE-trending lineaments from the 1:25,000 DEM, the 1:250,000 DEM, the topographic slope aspect map and EarthSat (1977) correlated positively with respect to outcrop fractures of all frequencies. For WNW-trending lineaments, EarthSat (1997) lineaments had the best correlation with outcrop data, whereas the lineaments from the 1:25,000 DEM had a negative Contrast Value. For other lineament and fracture orientation, the coincidence between groundtruth fractures and the lineaments was variable, depending on the orientation, lineament type, and fracture frequency. The best correlation was found between FIDs and lineaments, especially those identified on the 1:250,000 DEM. The worst correlation was between EW lineaments and outcrop fractures. NW- and N-trending EarthSat (1997) lineaments do not correlate well with outcrop data, a conclusion that was also reached for data in the Finger Lakes region (Jacobi, 2007).

The correlation among aeromagnetic lineaments, surface lineaments, and outcrop fractures suggests that these lineaments and fractures represent fracture systems that extend from the Precambrian (the source of the aeromagnetic anomalies) through the entire sequence to the surface (where the lineaments and fractures were identified). In the southern study area, these trends are NNW, ENE/NE, NW and N. Similar trends are inferred in the northern study area, with the addition of an EW trend. The integrated

lineament zones (which incorporate lineaments from DEMs, EarthSat (1997), and aeromagnetics) that are confirmed by FIDs probably represent fault systems (including those with aeromagnetic lineaments). These possible fault systems trend in the orientations listed above, plus NNE and rarely, EW. Although the intent was to use these integrated lineament zones with seismic reflection data to determine the trend and extent of fault systems observed on the seismic lines, the intense competition in the area of interest, and licensing agreements prevent such a presentation.

For this project about 80 km (50 miles) of 2-D seismic reflection profiles were analyzed. These lines display a significant number of fault systems that extend from the Precambrian basement to the (near)-surface, confirming the inference from the lineament analyses. Many of the fault systems correlate with surface FID and integrated lineament zones. The fault systems have a long reactivation history, based on growth fault geometries. Some faults are Iapetan-opening (rift) faults only, others were active through early Taconic Orogeny, whereas many ceased activity at end of the Taconic (immediately post-Trenton) time. Others extend into the Silurian and apparently were last active in the Salinic Orogeny, whereas other fault systems extend through the entire section. These fault systems controlled the preservation (and possibly deposition) of thinning units such as salt and the Oswego, since both pinch out at faults. Some of the fault systems have clear flower structures, implying that these faults sustained strike-slip motion, and the seismic lines crossed either a retraining bend or releasing bend (depending on the flower geometry). In terms of prospects, structural highs were recognized on the basement and Theresa, a few Trenton/Black River thin zones, the Oswego and lower units pinching out at the Silurian unconformity, and fault-bend folds over ramping thrusts in the Onondaga.

In summary, the lineaments were generally confirmed by outcrop fractures, especially outcrop FIDs. The fault systems inferred from the lineament and fracture analyses cross much of the area of interest, and seismic reflection profiles confirm that much of the area is faulted. The faults were active through most of the Paleozoic for which a rock record exists, and controlled the disposition of thin units. Flower structures indicate that some of the larger fault systems were strike slip for at least part of their motion history.

TABLE OF CONTENTS

LIST OF GRAPHICAL MATRIALS

LIST OF TABLES

INTRODUCTION

OBJECTIVES

The research discussed in this paper focused on Chenango County, New York State (Figure 1), where lineaments identified from digital elevation models (DEMs) and aeromagnetics were integrated with structural field work and interpretations of seismic data from central New York State (NYS). The primary objective was to define the structural (fracture) fabric in Chenango County in order to better define potential structurally-controlled gas fairways as well as fracture patterns that may influence gas production. A second goal was to determine whether lineaments reflect structure observed both in outcrop and in seismic reflection data. The research demonstrated that the lineaments record much of the structural fabric in the area of interest. Inferences from integrated lineament zones (e.g., aeromagnetic anomalies coincident with surface lineaments) and seismic reflection data indicate that fault reactivations have resulted in fracture systems that extend from Precambrian basement to high in the bedrock section, and in some cases, to the surface.

GEOLOGY OF THE STUDY AREA

Subsurface Stratigraphy of Potential Natural Gas-bearing Units

Cambrian Potsdam and Galway (formerly "Theresa"; Figure 2). The Cambrian sandstones of the Potsdam and Galway formations have not yet been tested or developed in eastern NYS. However, in western NYS the Cascade Brook, Bockhaln, and Northwoods fields tap the Galway ("Theresa"; e.g., Copley and Heim, 2006a, b). These fields are structure plays with small anticlinal structures over basement highs. Additionally, these fields are near the up-dip pinchout of the upper sands of the Galway ("Theresa") Formation. The Stahl well in western NYS penetrated about 15 m (50 feet) of high porosity sandstone (Loewenstein et al, 1998; Jacobi et al., 1999). The sandstone included well rounded quartz grains with quartz overgrowths. These rounded grains indicated that they had spent part of their history in aeolian dunes. The thickness of the Potsdam and Galway varies from about 152 m (500 ft) in northeast Chenango County to about 304 m (1000 ft) thick in southwestern Chenango County, based on wireline logs from one well in northeastern Chenango County and three wells in neighboring counties (Rickard, 1973). The depth of the base of the Potsdam varies from -1219 m (bsl) (-4000 ft [bsl]) in northeastern Chenango County to -2743 m (bsl) (-9000 ft [bsl]) in southwestern Chenango County, based on the same wells (Rickard, 1973).

Ordovician Trenton/Black River (Figure 2). The Trenton/Black River (T/BR) gas play in the Finger Lakes region of central NYS is the most prolific gas producer the northern Appalachian Basin. The reservoir is in the upper section of the Black River Formation, where it is fractured and hydrothermally dolomitized (e.g., Smith, 2006; Jacobi, 2007). The discovery field, the Glodes Corners Field, was developed by Columbia Natural Resources (CNR; the major T/BR fields are shown in Figure 1). More recent discoveries have led to a number of fields, including the nearby Muck Farm Field and the Wilson Hollow Field. Recoverable reserve estimates for Black River production in the Finger Lakes region range from about 1 bcf to 5 bcf per well.

Reservoir quality in the structurally controlled T/BR plays is dependent on secondary porosity in the carbonate section. In Ohio and Ontario this porosity results from 1) vugular porosity and intercrystalline porosity associated with secondary dolomitization, and 2) unmineralized open fracture/fault porosity, including fault rubble (e.g., Wickstrom, 1996; Smith, 2006). In the Glodes Corners Road Field, the Gray #1 well had gas shows at the top of the Black River in a low density zone that is dolomitized. CNR reported an open flow in this well of 3,290 mcfpd with no stimulation. This large natural flow is consistent with a highly fractured and/or vuggy reservoir. Production records from NYSDEC indicate that the Gray produced 665,104 mcf between 1996 and December, 1999, and produced 316,132 mcf in 1999.

Dissolution of carbonate and secondary mineralization is presumed to be related largely to fluid migration along active fault and fracture systems that extend to basement (e.g., Wickstrom, 1996; Smith, 2006; Jacobi, 2007). These faults generally display only modest Trenton offset; for example, the Harlem Field in Ohio has only ~10 m Trenton fault offset. Well logs from the Glodes Corners Road Field indicate a narrow fault zone that increases in stratigraphic offset upsection, increasing to 6 m offset in the Trenton. On seismic reflection profiles, the T/BR plays occur along fault zones that appear as narrow (~ 0.6 km, 2000') grabens with small regional offset (e.g., Jacobi et al., 2003, 2004a, b; Smith, 2006; Jacobi, 2007). These grabens are thought to be a result of a combination of 1) solution collapse, 2) reverse flower structures (along strike-slip faults), and 3) minor pull down from the lower velocities associated with dissolution and fault brecciation.

Vertical cores recovered from both sides of the bounding fault of the T/BR graben of the Quackenbush Field in the Finger Lakes region show that the limestone supratidal facies of the Black River are tight on the relatively high fault block, but the same facies have porosity and zebra fabrics in the dolomitized graben (Packard et al., 2008). Porosity determinations on the full diameter of an oriented horizontal core from the same field displays a range of porosities—from 2% to rare values as high as 8% (Jacobi, 2007; Agle et al., 2008; Packard, et al., 2008). Rare vuggy porosity was observed in the horizontal core. The main gas shows near the horizontal core appeared to be related to a rubble zone in the core that on an FMI log was judged to be a highly fractured fault zone (e.g., Jacobi, 2007). It appears that the fracture systems that link the matrix porosity are the gas delivery systems to the borehole. Vuggy porosity has been observed in other vertical cores from other fields and cores held by the NYS Museum (e.g., Smith, 2006).

The easterly and east-northeasterly trends of the Glodes Corners Road Field and fields to the south suggest that the these field are located along faults that are reactivated structures related to the older Iapetan opening/Cambrian Rome Trough development (e.g., Beardsley, 1999, 2001; Jacobi, 2007; Jacobi et al., 2002a,b; 2003, 2004a,b, 2005, 2006). Seismic reflection profiles show that many of the faults associated with the T/BR fields die out upsection at a reflector that represents the top of the Utica (Jacobi et al., 2003, 2008), based on Utica isopachs from wireline logs (Nyahay et al., 2008). The Taconic fluid migration is assumed to have ended when the fault ceased motion at about 450 Ma (Jacobi et al., 2008), but more recent veins in the horizontal core point to younger episodes of fluid migration, and in fact Jacobi et al. (2006a) suggested that several younger phases exist in the Mohawk Valley-Finger Lakes region (including the Salinic, NeoAcadian, and Alleghanian orogenic phases).

Most Trenton/Black River exploration continues to be concentrated in the Finger Lakes region.

Prior to this research, neither seismic nor deep wells were sufficiently dense to promote rigorous definition of T/BR plays in Chenango County. However, lineaments along the east-northeast trending faults in the Finger Lakes region (along which, for example, the Quackenbush Field is located) extend easterly into Chenango County (Jacobi, 2002), where T/BR grabens were observed on 2D seismic reflection data (Jacobi et al, 2003, 2004a,b). T/BR structures were also recognized farther east in Otsego County (e.g., Jacobi and Smith, 2000).

Ordovician Utica Formation (black shale; Figure 2). The black shales of the Utica Formation overlie the Trenton carbonates and are about 152 to 183 m (500 to 600 ft) thick, based on wireline analyses (for reviews of the black shale, see Martin, 2006; Nyahay et al, 2008). The top of the Utica slopes to the south from -610 m (bsl) (-2000 ft [bsl]) to -2134 m (bsl) (7000 ft [bsl]) (Nyahay et al, 2008). The lowest unit in the Utica Group, the Flat Creek, varies from about 30 m to 46 m (100 to 150 ft) thick. The Utica is thermally mature with Conodont Alteration Indices (CAI) of generally 4.5 with anomalous locales of 4 in the Chenango county region (Weary et al., 2000, 2001). North-northeasterly trending steep gradients in the CAI isograds west of Chenango County are coincident with fault systems proposed by Jacobi (2002), and suggest that fluid circulation along the faults influenced the thermal maturity (Jacobi, et al., 2007). The significantly smaller areal extent of particular Devonian CAI isograds (e.g., 4) compared to the Ordovician extent suggest that the Ordovician black shale reached their present values before Devonian times, i.e., the thermal event is a Taconic feature (Jacobi et al., 2006a). Since Tmax calculations are generally unreliable in the Utica Shale, vitrinite reflectance (%Ro) values are also undependable (Nyahay et al, 2008). The TOC of the Utica increases to the southeast from 2.5% to 3% (Nyahay et al, 2008). Nyahay et al. (2008) suggested that the Flat Creek Member should be productive in all of Chenango County, based on gas shows and hydrogen indices.

Oswego, Oneida and Other Sands (Figure 2). Post-Taconic Ordovician and Silurian sandstones include the Upper Ordovician Oswego and Queenston, the Lower Silurian Oneida, the Upper Silurian Herkimer, and the Lower/Middle Devonian Oriskany formations. To the east in Otsego County, Jacobi and Smith (2000) found that the Oneida sandstone has high porosity, and to the north in Madison County, Nornew, Inc. is currently producing from the Oneida and Oswego Formations in the Bradley Brook Field. Production records from the NYS DEC for the year 2000 show that the Nornew Lodor #1 produced over 50 MMCF of gas from the Oneida and Oswego. This ranked the Lodor 19th in total production for all producing wells in New York in 2000. In Bradley Brook Field some of the most productive Oneida wells are located on fault-related structure that is defined by proprietary seismic and well control. Other high productivity wells appear to be located on an erosional remnant associated with the Silurian unconformity that floors the Oneida. In Madison County, the Oneida sandstone has porosities as high as 15% over the erosional remnants (Ahmed, et al., 2006). Economic Oswego production is restricted to areas where high porosity sand units are within 15 m (50 ft) of the unconformity at the top of the Oswego. Because the erosional truncation (that resulted in the remnants) is thought to extend southward across NYS (Henderson and Timm, 1985; Ahmed, et al., 2006), a strong possibility exists that remnants similar to those in the Bradley Brook Field occur to the south in Chenango County.

The Upper Silurian Herkimer Formation of the Clinton Group was divided by Zenger (1966) into an eastern Jordanville Member of orthoquartzites and a western Joslin Member of carbonates, fine sandstones and interbedded shales, based on outcrop geology. Beinkafner (1981), using well cuttings and wireline logs, determined that the informal "lower interval" of the Herkimer consists largely of the Jordanville Member orthoquartzites (beach facies) in southern Chenango County, Joslin Member lagoonal carbonates (both limestones and dolostones) in northeastern Chenango County, and Joslin Member fine grained sandstones (offshore bars) in northwestern Chenango County. In the informal "upper interval", an eastward transgression resulted in the Joslin Member completely overstepping the Jordanville Member in Chenango County. The Herkimer Formation to the east in Otsego County has high porosities found in cuttings examined from wells (Jacobi and Smith, 2000). North of Chenango County in Madison County the Beers #1 produced 52,583 Mcf in 2001 from the Herkimer Formation. Beinkafner (1966) suggested that gas in the Herkimer may be trapped in zones of dolomitization, as well as stratigraphic pinchouts.

Devonian Marcellus Black Shale (Figure 2). The Marcellus Formation in Chenango County consists of the Union Springs dark grey to black shales overlain by the Cherry Valley limestone in turn overlain by black shales of the Chittenango that grade up into grey shales and silts of the Bridgewater and Cardiff members (all lumped together as the Oatka Creek Member in western NYS; for reviews, see Martin, 2006; Nyahay et al, 2008). The base of the Marcellus dips to the south from +229 m (asl) (+750 ft [asl]) in northeastern Chenango County to about -686 m (bsl) (-2250 ft [bsl]) in southern Chenango County. The Marcellus generally increases in thickness to the east from 152 m (500 ft) in the northwestern Chenango County to 244 m (800 ft) in southeastern Chenango County. Steep thickness gradients in the upper Marcellus and Cherry Valley along the western border of Chenango County suggest that a northerly trending syndepositional fault system was active along the western border of Chenango County in Union Springs and later Marcellus time. The TOC content of the Marcellus varies from about 4.05% in the southeast to about 7.55% in northwest Chenango County (Nyahay et al., 2008). The Marcellus is thermally mature in Chenango County and the vitrinite reflectance (%Ro) varies from about 3.5 in the northeast to 3.0 in the southwest, and Tmax is about 475 to 550^{o} C (Nyahay et al., 2008). The Marcellus appears to be an attractive target for black shale gas development (e.g., Nyahay et al., 2008)

Stratigraphy of Bedrock Units that Outcrop in the Study Area

The Upper Devonian Catskill Delta Complex crops out throughout Chenango County. The Catskill Delta Complex is a clastic wedge that consists of marine and non-marine sediments that washed off the uplifted highlands of the Acadian Orogeny to the east (e.g., Engelder and Oertel, 1985; and Isachsen et el., 2000, see The Catskill Delta, Woodrow and Sevon [eds., 1985] for a complete review). In western NYS the Catskill Delta Complex is a two-kilometer thick sequence of primarily marine sediment (except for the uppermost units), but the Catskill Delta Complex thickens eastward to seven kilometers of marine and non-marine sediments in eastern NYS (e.g., Engelder and Oertel, 1985; see The Catskill Delta, Woodrow and Sevon [eds., 1985] for a review). Outcrops in Chenango County consist of interbedded sandstone, siltstone, and shale of the Genesee and overlying Sonyea groups (e.g., Rickard et al, 1970; Fisher et al., 1970; Figure 2) that were deposited in a shallow-marine basin-margin (pro-delta) complex (e.g., Rickard, 1975; Dennison, 1985; Engelder and Oertel, 1985; Woodrow, 1985).

The Genesee Group is about 411 m (1350 ft) thick in Chenango County (Rickard, 1975), and consists of the following units in central/eastern NYS: the Otselic (Group) overlain by the Cincinnatus Group (Sevon and Woodrow, 1985). These units are time equivalents of the more well known, relatively deeper water facies to the west (arranged from base upsection): Geneseo Shale, Lodi Limestone, Penn Yan Shale/Renwick Shale, and the Ithaca Formation (e.g., Sevon and Woodrow, 1985; de Witt et al., 1993). The Sonyea Group is about 244 (800 ft) thick in Chenango County (Rickard, 1975), and in central/eastern NYS consists of (arranged from base upsection): Montour Shale, Triangle/Johns Creek, Sawmill Creek Shale, and Glen Aubrey. The western, better known time equivalents to these units are (from base to top): black shales of the Middlesex Shale and the gray shales of the Cashaqua Shale which grade eastward through the Rock Stream into the Glen Aubrey. Many of the shales and siltstones in central NYS such as the Rock Stream are regarded as turbidite facies of the Catskill Delta (e.g., de Witt et al., 1993).

Structure Bearing on Potential Natural Gas Reservoirs

Fractures. Only one structural study has been published that deals specifically with the area of interest. Pyron et al. (2003) conducted a detailed lineament, well log, and soil gas study in the fractured shale Genegantslet Field, an area of about 0.8 km^2 that is located in the present study area (Figure 1). Pyron et al. (2003) identified lineaments from air photos and analyzed 25 soil samples. Pyron et al. (2003) suggested that relatively high soil gas concentrations over the Genegantslet Field marked a zone where lineaments intersected. No faults were recognized the Pyron et al. (2003) study, but they suggested the Genegantslet wells are located along fracture trends and at fracture intersections.

To the west and south of Chenango County research has been conducted extensively on the joint patterns in the Appalachian Plateau for nearly 100 years (see reviews in Engelder and Geiser, 1980; Engelder, 1985; Younes and Engelder, 1999; and Jacobi, 2007). Although no bedrock fracture study specifically targeted Chenango County, Parker's (1942) fracture study of centrsal and eastern New York State included the Oxford 15' topographic quadrangle, which includes the southeastern corner of the present southern study area. Parker (1942) found three fracture sets in the Oxford quadrangle: Set I which strikes NNE and is quite planar; Set II which strikes WNW and is more curvilinear, and Set II, which strikes about N60^{o}E. The location and number of fractures measured in the Oxford quadrangle are not presented in Parker (1942), but he stated that the number of sites per quadrangle varies from 5 to 21, and the number of fractures measured in a quadrangle varied from 100 to 800. A review of the fracture research west of Chenango County is presented in Appendix 1 (Fracture Studies).

Fault-bend Fold Structural Traps. No study of surface folds has been published for Chenango County. However, Wedel (1932) mapped Alleghanian surface folds in the western and central parts of the Southern Tier of NYS (Figure 1), and traced fold axes as far east as the western border of Chenango County (Figure 1). Wedel (1932) used transit level lines on large outcrops and elevations of marker units to determine dips of stratigraphic units. He confirmed previously recognized folds (see Wedel, 1932, for references therein). Near the western Chenango border, the fold axes trend ENE to EW, and EarthSat's (1997) lineaments that are coincident with some of the fold axes trend EW across the southern part of Chenango County (Figure 1). The structural relief on these folds varies from about 46 m (150 ft) on the Firtree Anticline to about 12 m (40 ft) on the Watkins Anticline. These folds are related to Alleghanian ramping thrusts that have decollement in the Silurian salt section. Such thrusts and related folds are evident on seismic reflection lines in the Finger Lakes (e.g., Jacobi et al., 2003, 2004a, b, Jacobi, 2007). Seismic data show that the faults and folds affect the section as high as the Devonian Onondaga reflector and the overlying Marcellus Formation.

Faults. No published fault study is known that specifically targets Chenango County. However, Jacobi et al. (2004a, b) presented an interpretation of a seismic line in Chenango County that displayed a Trenton/Black River graben and a Taconic-aged thrust system. That seismic line also showed probable Iapetan-opening rift faults, based on growth fault geometries in the Precambrian-Theresa interval. Jacobi's (2002) fault map for the Appalachian Basin of NYS also proposed that several fault systems passed through Chenango County; additionally, these fault systems exhibit growth fault geometries, as inferred from well log interpretations, and as displayed on a cross section that included eastern Chenango County (Figure 2, Jacobi and Smith, 2000).

METHODOLOGY

FRACTURE DATA COLLECTION IN THE FIELD

Surface bedrock fracture data were collected by the University at Buffalo Rock Fracture Group (UBRFG). The primary geologists in the northern study area were Robert Jacobi and Nick Terech, and in the southern study area were Robert Jacobi and Kelly McGuire. Data were collected in the northern area during the summers of 2004 and 2005, and were collected in the southern map area during the summers of 2004 and 2005 and 2006.

At outcrops the UBRFG measured fracture characteristics, including strike, dip, spacing, apparent height, apparent length, fracture-abutting relationships, character of bedrock that contains the fracture (including bed thickness), and fracture geometry. In large outcrops, the UBRFG measured the fractures along a 100-meter scanline that was placed to intersect the facture sets. Measurement and data reduction techniques for the scanline followed Jacobi and Zhao (1996). On most outcrops, however, the "abbreviated method" was used, which is detailed in Jacobi (2007). In this method, the fracture sets are identified in the field, and the fracture characteristics are measured for 4 or more fractures (three spacings) in each set. If the fractures in a particular set displayed similar characteristics, then the maximum number measured was four; if there was a significant range in values, then more fractures of the set were measured. Several fracture sets have consistent master/abutting relationships with other fracture sets, and therefore master/abutting relationships can be used in some cases to decipher to which set a fracture belongs. However, other sets commonly display conflicting master/abutting relationships with certain other fracture sets. There was no maximum or minimum number of fracture sets necessary at each site, although at least two different fracture sets were needed to establish a master/abutting abutting relationship.

Although the UBRFG measured apparent height and apparent length of each fracture, the true fracture height and length was commonly obscured by glacial till, vegetation and debris. The UBRFG also recorded dipping beds and slumps found in outcrop.

FRACTURE DATA REDUCTION

Data reduction included establishing the average fracture frequency for each fracture set at each site. First, the orthogonal spacing between fractures of a given set was determined, and then the average spacing was calculated. This value was then used to calculate fracture frequency (fractures/meter, the inverse of fracture spacing) and standard deviation of the fracture spacing for each set present at the outcrop. The standard deviation provides a measure of dispersion among the data. If the fracture set at a particular site had a standard deviation larger than 0.5 fractures/meter and if a minimum of 5 fracture spacings had been measured within the set, then the fracture spacings were plotted on histograms in the manner of Witmer et al. (2002) and Witmer (2004). The histograms indicated whether the fracture spacing distributions were bimodal. If the histogram displayed outliers of unusually high and/or low fracture spacing values, these values were discarded from the data set and a new fracture frequency was calculated based on the remaining spacing data.

The orientation boundaries between various fracture sets were determined by plotting all the fracture orientations on a separate histogram (Figures 3 and 4) for the northern and the southern areas. The orientation boundaries between fracture sets are difficult to establish because the populations of individual fracture sets do not necessarily have normal distributions, and by definition, the boundaries occur in bins with small numbers of samples. The boundaries are therefore, to some degree, arbitrary, but were chosen based on distribution curve matching. Where possible, master/abutting relationships were used to better define the boundary by examining the master abutting relationship of all the sites in the orientation boundary region, and assigning the boundary to an orientation that divides sites with different master/abutting relationships. However, if the boundary in question is between fractures sets that have inconsistent relationships, of if the sample is sufficiently small that there are no master abutting relationships for sites in the boundary region, then the master/abutting relationship cannot assist in defining that particular boundary.

MODIFIED ROSE DIAGRAMS

Fracture data for the field sites are displayed on maps in a modified rose diagram developed by Jacobi and Fountain (1996) (Figure 5). Since most of the fractures have near-vertical dips (> 85^0), rose diagrams, rather than stereoplots, can be used. Rose diagrams have a distinct advantage (over poles to fracture surfaces in stereoplots) because 1) frequency of the fractures in a particular fracture set can be displayed in the rose diagram, unlike a stereogram, and 2) rose diagrams promote the ease of recognition of alignment of fractures with other elements (such as lineaments) since the petals of the rose diagram are parallel to the fracture strike, rather than the poles to fractures in a stereoplot that will form a cluster 90^0 away from the trend of the fractures and other elements. Unlike traditional rose diagrams that plot raw numbers of joint abundance, modified rose diagrams plot the fracture frequency for each fracture set in the upper semicircle, and the master/abutting relationships among the different sets in the lower semicircle. The fracture frequency eliminates the problems of sampling bias, and the different information displayed in the two semicircles eliminates the redundancy between the two semicircles inherent in usual rose (or propeller) diagrams.

The lower semi-circle on the modified rose diagram displays the master/abutting relationships for each fracture set at a particular site. Master and abutting relationships are indicated by the length of a petal for each set (Figure 5a). The master fracture set is the longest petal, whereas the shortest petal represents the youngest fracture set. The second longest petal in the represents the first abutting fracture set, and successively shorter petals represent more abutting fracture sets. Different color petals in the southern semicircle indicate different abutting relationships between the fracture sets (Figures 5a and 5b). Yellow petals represent orientations of regular fracture sets. Green petals of the same length indicate intersecting fracture sets. Purple petals of the same length show mutually abutting fracture sets and orange petals indicate that there is no observed relationship among the fracture sets with the orange petals.

MAPS

The transportation net and hydrography layer used as the base map were accessed at the Cornell University Geospatial Data Information Repository (CUGIR) website (http://cugir.mannlib.cornell.edu). The base maps with site locations were constructed in ArcMap; the base map was exported to Adobe Illustrator for maps that demanded layers of icons/data not easily manipulated in ArcMap.

Aeromagnetic lineaments were identified on an aeromagnetic map that was downloaded from the Ohio Geological Survey (http://www.ohiodnr.com/geosurvey/). Lineaments were drawn along the strike of steepest part of the aeromagnetic gradient, or along the strike of the inflection of the aeromagnetic gradient. Because the sedimentary section above Precambrian basement is largely transparent to aeromagnetic anomalies (if considering large anomalies on the order of 100 nT and larger, see Jacobi, 2007), it is assumed that these lineaments represent Precambrian structural and/or lithologic trends. Lineaments along these gradients may therefore represent structure in the basement. Aeromagnetic lineaments that coincide with FIDs (at the surface) may indicate that basement structure along these lineaments extend from Precambrian basement to the surface.

Topographic lineaments were identified in the northern study area on a Digital Elevation Model (DEM) downloaded from the Cornell University Geospatial Data Information Repository (CUGIR) website (http://cugir.mannlib.cornell.edu). For the southern study area, the topographic lineaments were identified on a Digital Elevation Model (DEM) downloaded from the USGS EROS website (www.seamless.usgs.gov). The image for the southern study area is a National Elevation Dataset Digital Elevation Model (NED DEM), which is a 1/3 arc second DEM, and is ten by ten meters/pixel. Horizontal datum is North American Datum 1983 (NAD 83), and the vertical datum is North American Vertical Datum of 1988 (NAVD88).

The DEM data were imported into the ArcMap program and a gray scale topographic map was constructed at 1:25,000 and 1:250,000 viewing scales in the northern amp area and 1:100,000 in the southern map area. Different viewing scales are used to identify lineaments with different characteristic lengths because more detailed topographic features are commonly not recognized on large scale images; for example, short linked creek segments with variable trends on a detailed DEM will appear as a single straight lineament on a regional DEM (e.g., 1:250,000). The grayscale DEM was transformed into a colored raster image because small-scale topographic features are less readily identified on the gray-scale DEM. Lineaments identified from the DEM are commonly streams and other waterways. Longer lineament trends are easier to identify on 1:250,000 scale image. The minimum length of a linear feature was defined as a lineament that is longer than 0.50 km. There is no maximum length criterion for lineament selection. Lineaments that have one or both endpoints in the boundaries of either the northern or southern study area are included in the analysis.

Lineament identification relies heavily on human visual senses, and tends to be, to different degrees, a subjective task. In order to measure the subjectivity of the operators picking lineaments in this study, a quality assurance program was used that tests the ability of different operators to reproduce the same lineaments. The ability of different operators to identify the same lineaments has been studied extensively (e.g., Wise, 1976; Wise, 1982; Wheeler and Wise, 1983), and the results are variable, but the maximum equivalency of lineaments picked by two operators is generally regarded to be only about 2/3s of the total lineament population.

For the quality assurance program in this study, two operators were assigned the same area on a DEM (1:30,000 scale in the northern map area and 1:100,000 in the southern study area), and given the same amount of time at the same time of day to independently determine the lineaments. In the northern map area the two operators were Dr. Robert Jacobi and Nick Terech, and in the southern map area the two operators were Dr. Robert Jacobi and Kelly McGuire. In the both the northern and southern areas lineament comparison between the two operators included the difference in orientation of nearby/overlapping lineaments, the difference in length of nearby/overlapping lineaments and percent of matching lineaments. These values determine the reproducibility of lineament selection by the assigned operators. After these operations, and after the reliability of the lineament identification process had been established, lineaments were identified in the remainder of the northern and southern map areas by Nick Terech and Kelly McGuire (respectively).

In the northern study area, Jacobi and Terech independently identified topographic lineaments on a 1:25,000 scale DEM polygon in the northeastern section of the northern study area (Figure 6a). Jacobi identified a total of 56 lineaments within the polygon and Terech identified a total of 48. Between Jacobi's and Terech's lineaments, forty-four lineaments were parallel or nearly parallel to each other. The percentage of topographic lineaments identified by Terech matching lineaments drawn by Jacobi is 78.6%, whereas the percentage of topographic lineaments identified by Jacobi that match lineaments selected by Terech was 91.3%.

In the southern study area, Jacobi and McGuire independently identified topographic lineaments on a 1:100,000 scale DEM polygon in the southern study area (Figure 6b). Lineaments picked by Jacobi that were coincident with those selected by McGuire were compared both in length and orientation; "coincident" here was defined as lineaments that touched somewhere along their length. Jacobi identified sixty-four lineaments within the test area on the DEM, whereas McGuire only picked twenty-six lineaments. The percentage of topographic lineaments identified by McGuire that match the lineaments drawn by Jacobi is 26% (of Jacobi's lineaments), and the percentage of topographic lineaments identified by Jacobi that match lineaments selected by McGuire was 73% (of McGuire's lineaments). Although McGuire selected significantly fewer lineaments, discussion after the selection process promoted a greater recognition of lineaments by McGuire. Furthermore, the lineaments defined as coincident had good agreement in orientation and length.

An alternative method for topographic lineament identification is to utilize a slope aspect map. A slope aspect map represents either the azimuth of the topographic slope or the gradient of the topographic slope; for this study the azimuth of the slope was used. A subroutine in ArcMap converts the DEM elevational data into a slope aspect map; the DEM data was again accessed at the CUGIR website (http://cugir.mannlib.cornell.edu). Criteria for selecting lineaments based on slope aspect depend on arbitrary slope length and width. Since Slope Aspect Lineament Zones (SALZs) often do not have parallel boundaries and the boundaries can exhibit small changes in orientation along their length, the strike of a SALZ is realized by drawing a best fit line through the SALZ. SALZs must demonstrate at least a 2:1 length to width ratio.

The first basin-wide lineament map in New York State that was derived exclusively from satellite imagery was generated in 1997 by Earth Satellite Corporation (Figure 1; EarthSat, 1997). The lineaments were identified on manipulated images from the Landsat Thematic Mapper (TM), which recorded solar radiation in seven spectral bands. The spatial resolution in six visible, near-infrared, and short wave infrared bands is 28.5 meters and the spatial resolution in the thermal infrared band is 120 meters. EarthSat (1997) sent the raw Landsat TM data (TM Band 2, TM Band 4, and TM Band 7) through a series of processing steps before lineament selection. First, EarthSat (1997) geocoded the Landsat TM data using ground control points and then resampled using a cubic convolution algorithm. Then they enhanced the data using a modified LaPlacian filter. Once enhanced, EarthSat (1997) colored balanced and mosaicked the scenes to form four 1^o x 2^o color composite map sheets at 1:250,000. EarthSat (1997) identified lineaments directly by "eye" on clearfilm (Mylar) overlays on the individual 1:250,000 scale images. In regions where EarthSat (1997) had overlapping images, stereoscopic inspection of those areas was possible. Out of ten total scenes, Chenango County was part of two overlapping adjacent scenes; the two scenes were collected on May 15, 1986 from path 15, Rows 30 and 31.

<u>Lineament Zones Detected From Multiple Data Sets (Integrated Lineament Zones)</u>

A lineament zone (LZs) is defined as a linear feature that is surrounded by an (arbitrary) 0.5 km buffer. Integrated LZs (ILZs) are defined as zones in which two or more LZs from different data sets have the same orientation and overlie one another. ILZs are identified based on the ordered criteria below:

1) Sites with FIDs
2) 1:25,000 scale DEM LZs
3) 1:250,000 scale DEM LZs
4) Slope Aspect Map LZs (SALZs)
5) EarthSat (1997) LZs
6) Aeromagnetic LZs

ILZs are first defined by FIDs overlying at least one other LZ (i.e. 1:25,000 scale DEM, SALZs, and or EarthSat (1997) LZs) trending in the same direction. If FIDs are not present, the second order of operations asks if any 1:25,000 scale DEM LZs intersect other parallel to nearly parallel LZs identified from the remaining four data sets, and so on. An arbitrary weight of “1” is assigned to each LZ type that comprises the ILZ (except for 0.5 allocated to FIDs with an orientation that falls close to, but outside of, the defined range for the trend of the ILZs in question). Adding the scores for each ILZ yields a value that gives some relative indication of the reality of the lineament as well as the probability that the ILZ represents a fault. In the northern study area the maximum score an ILZ can have is 6.5 and the minimum score is a 1.5. In the southern study area the maximum score an ILZ can have is 4 and the minimum score is a 1.5 (excluding aeromagnetic lineaments). Table Appendix 2-1 shows an example of the scores for N-trending ILZs in the northern study area (a complete set of such tables for each orientation can be found in Jacobi, 2008).

WEIGHTS OF EVIDENCE

Weights-of-evidence is a statistical method (e.g., Daneshfar and Benn, 2002) that can be used as a measure of the degree of spatial coincidence among lineaments. This technique was used to compare the degree of coincidence of lineaments from: 1) EarthSat (1997), 2) DEMs at various scales (1:25,000 and 1:250,000), and 3) orientations of fractures measured in the field. UBRFG personnel developed the specific methodology for use with these elements of comparison (Drechsel et al, 2004; Cruz et al., 2005; Cruz, 2005). Essentially the weights-of-evidence compares the area of overlap of the buffers around two elements being compared to the area without overlap (Details concerning the weights-of evidence methodology can be found in Cruz, 2005).

A buffer was first constructed around the lineaments; the size of the buffer can be arbitrary, but in this case was based on the observed width of FIDs. In Allegany County, soil gas anomalies and closely spaced outcrops across a fault system indicated that FIDs are usually narrow, less than 0.5 km wide (Jacobi and Fountain, 1996). A buffer of 0.5 km on each side of the lineament was therefore chosen. A value of "L" was assigned to areas that are within the buffer zone of a lineament, whereas areas outside the buffer zone are assigned a value of –L. Field sites also have a buffer area, "F"; and areas with no sites have an area of " –F" (Cruz, 2005). Field sites were given an area of 10 meters^2, and the area of the Region of Interest (ROI) has a buffer of 500 meters around the center of every field site.

The following formulae were used to calculate positive and negative weights-of-evidence values:

Positive: $W_i + = \ln \{P(L_i|F) / (L_i|-F)\}$

Negative: $W_i - = \ln \{P(-L_i|F) / (-L_i|-F)\}$

$P(L_i|F) = N(L \cap F) / N(F)$

$P(L_i|-F) = N(L \cap -F) / N(-F)$

$P(-L_i|F) = N(-L \cap F) / N(F)$

$P(-L_i|-F) = N(-L \cap -F) / N(-F)$

$C_i = W_i+ - W_i-$

where P = probability, N = number of instances, ∩ = intersection of two sets, Wi+ = the positive correlation component, Wi- = the negative correlation component, and C = contrast. Contrast (C) measures the strength of correlation between the spatial distribution of field data points and lineaments. As (C) increases, the stronger the correlation between lineaments and fractures. A (C) value of zero indicates that there is no correlation between the field points and lineaments. A negative (C) value indicates that a negative correlation between the field points and lineaments exists.

Additionally,

P(Li|F) : number of sites with appropriate fracture trend within the lineament buffer / total number of sites with appropriate fracture trend.

P(Li|-F): (area of lineament buffer – area of sites with appropriate fracture trend) / (Area of Region of Interest – area of sites with appropriate fracture trend).

P(-Li|F): number of sites with appropriate fracture trend outside the lineament buffer / total number of sites with appropriate fracture trend.

P(Li|F) : {area of Region of Interest – (area of lineament buffer + area of sites with appropriate fracture trend)} / (are of Region of Interest – area of sites with appropriate fracture trend).

Weights-of-evidence were calculated for comparisons between various orientations of lineaments and similarly-oriented fracture sets at sites. For the northern study area the lineaments included the EarthSat (1997) Landsat lineaments and the lineaments identified on the 1:25,000 and 1:250,000 DEMs. The sites with appropriately oriented fracture sets were tested for fracture frequencies greater than 0.0 fractures/meter, greater than 2.0 fractures/meter, and greater than 4.0 fractures/meter. For the southern study area the lineament included those from the EarthSat (1997) Landsat lineaments and lineaments identified on the 1:100,000 DEMs. The sites in the southern study area with appropriately-oriented fracture sets were tested for fracture frequencies between 2 and 4 fractures per meter and greater than 4.0 fractures per meter. A maximum contrast value was calculated for each orientation in the southern study area.

Each lineament orientation for the three datasets has a calculated contrast derived from sites with fractures of the same orientation. Comparison of the calculated Contrast Values for each dataset reveals which particular sets of lineaments (orientations and base—Landsat or DEM) best reflect the fracture data observed in the field (i.e., the lineaments are statistically "groundtruthed").

The Contrast Value is quite sensitive to slight adjustments in the input values in the weights-of-evidence method (e.g., Cruz, 2005). For example, the Contrast Value increases dramatically as the number of sites with appropriate fractures within the lineament buffer increases from just 1% to 10%. In contrast, increasing the total site area, while maintaining all other input values, only slightly increases the Contrast Value. Finally, as the buffer area of a lineament increases, the Contrast Values decrease.

SEISMIC REFLECTION 2-D DATA

As part of this research program, Nornew Inc. licensed about 82 km of 2-D seismic reflection lines in central New York State and then sent the data to Sterling to be re-processed. After re-processing, Stuart Lowenstein (Nornew, Inc.) and Robert Jacobi (University at Buffalo) traced prominent reflectors and identified faults within the sub-surface. The early interpretations, completed in 2003, were presented at several conferences (Jacobi et al., 2003, 2004a,b, 2005). However, the present intense competition in oil and gas exploration in the Chenango County region precludes presentation of the specific location and details of these seismic lines; rather, selected lines from central New York State are presented herein.

The identification of shallow reflectors (Silurian Oneida and above) in these early interpretations was based on:

1) reflector characteristics similar to those of known reflectors elsewhere in NYS,
2) the distinctive geometry of the reflectors (e.g., the unconformity below the Oneida Formation), and
3) one synthetic seismogram for the upper reflectors from a sonic log in Chenango County.

The deeper reflector identifications in these interpretations were not based on synthetic seismograms. Reflector identification below the Trenton/Black River was difficult because the number and character of reflectors above Precambrian was different than to the west and north. Further, the top-of-Precambrian was also difficult to ascertain in some areas. Recently, seismic lines using three synthetic seismograms were reinterpreted, as well as multiple cross ties from proprietary data not included in this report. Based on one deep well with a sonic log, the synthetic seismogram indicates that the top-of-Precambrian is marked by a polarity shift of 180^o, which means that at that particular site the Precambrian contact is a reflector trough, not peak. Such a situation is possible if the top of Precambrian is severely weathered, for example.

RESULTS

FRACTURE ANALYSES

Fracture Distribution

The University at Buffalo Rock Fracture Group (UBRFG) measured more than 2600 fractures at 201 sites in the northern study area and more than 1400 fractures at more than 190 sites in the southern study area (locations of study areas shown in Figure 1). All the fracture orientations for the northern and southern areas are plotted on histograms (Figures 3, 4), from which the orientation boundaries between various fracture sets were determined (Tables 1 and 2).

The NNE- and WNW-striking fractures are the most abundant fractures measured in the northern and southern study areas (Figures 3, 4). The NNE- and WNW-striking fractures are parallel to fractures in the immediate counties to the west that Engelder and Geiser (1980) believed were strike-perpendicular (Set I) and strike-parallel (Set II) fractures (respectively). In the northern study area the 10^o orientation bin (represented by one petal on a rose diagram) with the most fracture orientations are in the ranges of 20°-29° (NNE) and 290°-299° (WNW) (Figure 3). In the southern study area the orientation bin with the maximum number of fractures is rotated counterclockwise from the northern area for both NNE and WNW-striking fracture sets: 5^o for NNE-striking fractures and 10^o for WNW-striking fractures. That both sets display a consistent counterclockwise rotation between the northern and southern study areas suggests that the proposed rotation may reflect reality, rather than simply a sampling problem. The observed rotations could result from a regional, far-field curving stress field, similar to that suggested by

Zhao and Jacobi (1996) and Younes and Engelder (1999), or the rotation could reflect a local stress deviation caused by an open fault system.

The rarest fracture sets in the northern study area are EW- and NW-striking fractures, with the least common fractures in the 10^{o} orientation bins of 80°-89° (EW) and 330°-339° (NW). A significant difference in the distribution of fractures between the two study areas is the number of N-striking fractures. In the northern study area, the number of N-striking fractures is distinctly negligible, whereas in the southern study area N-striking fractures are the third most prevalent, significantly more common (twice as many) than the next most common fracture sets (NW- and ENE-striking fractures). This high number of N-striking fractures the southern study area may indicate the proximity to major northerly-striking faults; such a fault may occur along the northerly-trending valley in which Smithville Flats is located (location of Smithville Flats shown in Figure 1) .

For the northern study area the fracture frequencies for each fracture set at each site, and the abutting relationships among the fracture sets are displayed on the modified rose diagrams (Figure 7a-q). Fracture intensification domains (FIDs) observed at sites (and fracture sets with near-FID fracture spacing) are shown for the northern area in Figure 8. For the southern study area, the fracture frequencies for each fracture set at each site, and the abutting relationships among the fracture sets, are displayed on the modified rose diagrams (Figure 9a to 9n). Fracture intensification domains (FIDs) observed at sites (and fracture sets with near-FID fracture spacing) are shown for the southern area in Figure 10.

Fracture Master/Abutting Relationships

In order to determine the age relationships of the fracture sets from master/abutting relationships (the master fracture is older), a scatter plot of all fracture intersections in the study area was generated that displays the orientation of the master fracture versus its first abutting fracture at each fracture intersection for which data exists for both the northern study area (Figure 11a) and the southern study area (Figure 11b). Determining the sequence of fracture sets from abutting relationships is equivocal because 1) several intersecting fracture sets are apparently mutually abutting, and 2) for several fracture sets, the sample population of intersections is extremely small (on the order of 1-4 intersections), so conclusions drawn from such a small number of intersections are not definitive (e.g., Figure 11c). Mutually abutting fracture sets may indicate switching of local stress axes during a single phase of fracture development (Bai et al., 2002), or may indicate that one (or both) sets recorded multiple stress reactivation phases. In either case, the mutually abutting relationship indicates an overlap in timing of development. The stick figure (Figure 11d) is a cartoon that displays the primary intersection relationships for fractures sets in the southern study area.

NNE- and WNW-Striking Fracture Intersections. The dominant fracture sets, NNE- and WNW-striking fractures, are also the dominant master fractures in both study areas. These two fracture sets appear to be mutually abutting (Figure 11a). However, in the northern study area twice as many NNE-striking fractures are master to WNW-striking fractures (220 intersections) as WNW-striking fractures are master to NNE-striking fractures (113 intersections). A similar relationship occurs in the southern study area (59 NNE-striking fractures are master to WNW striking fractures whereas 19 WNW fractures are master to NNE-striking fractures). The appreciably greater number of NNE-striking fractures as master suggests that the NNE-striking fractures appeared first before the WNW-striking fractures (Figure 11d), but that the development of both sets with infilling fractures overlapped in time.

The relationship of NNE-striking fractures master to WNW-striking fractures is consistent with the fracture trends to the west where Engelder and Geiser (1980) proposed that strike-perpendicular (Set I) fractures predate the strike-parallel (Set II) fractures. However, as documented by Jacobi and Fountain (1996) and by many later UBRFG research projects (e.g., Jacobi 2007), strike-parallel fractures are also observed to be master to the strike-perpendicular fractures, especially if the strike-parallel fractures occur in a Fracture Intensification Domain (FID). The strike-parallel fractures that are master to strike-perpendicular fractures indicate that the abutting strike-perpendicular fractures developed relatively late in the Alleghanian (or later), and/or indicate that the master strike-parallel fractures (WNW-striking) developed relatively early in the fracture history. From the seismic reflection profiles in Chenango County and regions to the east, and from well log analyses (Jacobi and Smith, 2000), it is clear that fault reactivation throughout the rock record is common. Further, the Alleghanian Orogeny was a protracted orogeny. It is therefore very possible that the NNE-striking fractures that abut WNW-striking fractures reflect relatively late orogenesis. These fractures would be “filling in” unfractured rock between the earlier NNE-striking fractures until fracture saturation occurred.

ENE- and E-Striking Fracture Intersections. In the northern study area the third most common fracture intersection is the intersection between ENE- and WNW-striking fractures. Generally, ENE(a)-striking fractures are master to WNW-striking fractures (16 intersections), although three intersection record the opposite master/abutting relationship. Thus, ENE(a)-striking fractures generally predate WNW strike-parallel fractures.

For ENE(a)-striking fracture intersections with NNE-striking fractures, the number of fracture intersections is small; in the northern study area, the master fracture set is equally distributed between ENE(a) and NNE-striking fractures, but in the southern study area, ENE-striking fractures are master to the NNE-striking fractures (5 master intersections vs. 1 abutting intersection). Thus, it is possible that ENE(a) fractures formed first, before WNW and NNE-striking fractures, but that their time of generation overlapped.

Farther west in Allegany County and in the Finger Lakes region, many ENE-striking fractures developed before the strike-perpendicular fractures, and may be Acadian or early Alleghanian in age (Jacobi and Fountain, 1996; Engelder et al., 2001; Lash et al., 2004; Engelder and Whitaker, 2006). Jacobi et al., (2002a, b, 2003, 2004b) suggested that the ENE-strike reflects deep faulting along ENE-striking trends that predated generation of the strike-perpendicular fractures (Set I). Consistent with this interpretation are the ENE-striking fractures that are master to the WNW and NNE-striking fractures area in the present study area (northern). The younger ENE-striking fractures could be later Alleghanian, reflecting later movements on ENE-tending faults, or could be even younger, as suggested for similar striking fracture to the northwest (e.g., Gross and Engelder, 1991).

E-striking fractures are never master to ENE-striking fractures, although the sample is low (3 intersections). One ENE-striking fracture is master to a NNE-striking fracture in the northern study area, and E-striking fractures are master to N-striking fractures more commonly that the opposite relationship (5 intersections vs. 3 for the opposite relationship). Thus, it appears that the rare E-striking fractures postdate the ENE-striking fractures, but are contemporaneous with the NNE-striking fractures, and in a few cases, predate NNE- and N-striking fractures.

NW- and N-Striking Fracture Intersections. NW-striking fractures are never master to E-striking fractures, although the sample is very small. Consistent with the inferred relatively young age of the NW-striking fractures are the observations that NW-striking fractures abut ENE-striking fractures (eight intersections vs. 1 for the opposite relationship in the northern study area) and abut NNE-striking fractures (twice vs. once for the opposite relationship in the southern study area). In the southern study area NW-striking fractures also abut N-striking fractures (12 intersections vs. 1 for the opposite relationship).

In the southern study area N-striking fractures abut NNE-striking fractures (5 intersections vs. 2 for the opposite relationship), and abut WNW-striking fractures (7 intersections vs. 0 for the opposite relationship). This abutting consistency indicates that the N-striking fractures in general developed after both the cross-strike and strike parallel fractures. Furthermore, in the northern study area N-striking fractures abut E-striking fractures (although the sample is small).

N-striking fractures and ENE-striking fractures are mutually abutting (with a very small sample of two intersections. Because of the abutting relationships with WNW- and E-striking fractures, most of the N-striking fractures are relatively young (consistent with the abutting relationship with the ENE-striking fractures), and that the master relationship of one ENE-striking fracture may indicate that the ENE-striking fractures were generated both early in the history, and late (e.g., Acadian and neotectonic). No intersections between NW- and N-striking fractures were observed, so the relationship between these two relatively young fracture sets is unknown.

The northern study area includes four sites with fracture relationships that may imply stress rotations. Sites 199a (Inset A, Figure 7b); 260b (Inset G, Figure 7h), and 164 (Inset J, Figure 7k) indicate a clockwise rotation in stress fields that generated WNW-, N-, and NE- striking fractures, whereas site 33 (Inset D, Figure 7e) suggests a counter-clockwise rotation in the stress field that generated NNE-tending fractures. A model developed by Zhao and Jacobi (1997) shows that a clockwise stress rotations should be expected near the study area (central-eastern New York), and counter-clockwise stress rotations should be expected in western New York. However, studies in western NYS (Jacobi et al., 2002c; Witmer et al., 2002; Witmer, 2004) show both clockwise and counter-clockwise stress rotations are present. The conflicting stress rotations may be the result of changes in localized stresses due to stress release across open faults (Jacobi et al., 2002c).

NNW-Striking Fractures. In the southern map area NNW-striking fractures always abut NNE-striking fractures (4 intersections; Cluster Q in Figure 11b). NNW-striking fractures and ENE-striking fractures are mutually abutting, but intersections with ENE-striking fractures as the master are more common (5 intersections vs. 3 for the opposite relationship). It appears that NNW-fractures developed after cross-strike fractures, but the relationship with other fractures is obscure since the sample populations are extremely small—usually 1 or 0. NNW-striking fractures are always master to NE, WNW and NS, whereas NNW striking fractures also mutually abutted other fracture sets (Table 3).

Effect of Bed Thickness on Fracture Frequency

In order to determine whether fracture frequency is dependent on sedimentary bed thickness 332 values of fracture frequency were compared with thickness of the fractured bed in the northern study area. Figure 12 does not reveal a significant relationship between bedding thickness and fracture frequency. Bed thicknesses range from 1 cm to 64 cm for the 332 fracture frequencies. Fracture frequencies measured in 1 cm thick beds range from 1.85-4.63 fractures/meter. The mean range of fracture frequency is relatively consistent across all bed thicknesses. For example, fracture frequencies measured in the 2 cm thick beds range from 0.48-8.16 fractures/meter, whereas the range of fracture frequencies for beds greater than or equal to 15 cm thick is 0.33-11.76 fractures/meter.

Lineament Zones (LZs) in the Northern Study Area From the 1:25,000 Scale DEM

The 1:25,000 scale DEM image of the northern study area yielded a total of 229 LZs (Figure 13). The most common lineament orientation is NNE (Table 4), consistent with the most common fracture trend (NNE). Eighteen of the 80 NNE-trending LZs have outcrops, and nine of those LZs have at least one site that displays a NNE-striking FID (Figure 14). The least common LZ orientation trends EW (Table 4), consistent with the least abundant fracture orientation in the study area (EW). Fifteen outcrops occur in two of these LZs, but none of these outcrops includes an E-trending FID (Figure 15).

Thirty-three WNW-trending LZs were identified (Figure 16, Table 4). Two thirds of these LZs do not include field sites (Table 4), but seven of the ten LZs with field sites are confirmed by at least one WNW-trending FID. Of the 27 ENE-trending LZs, seven incorporate outcrops, and outcrops in two of these LZs include at least one field site with an ENE-striking FID (Figure 17, Table 4). Thirty-six NW-striking LZs were identified (Figure 18). Only one quarter of the NW-trending LZs pass across field sites, and of these LZs with field sites, only one LZ was confirmed by sites with NW-striking FIDs. Each of the NW-striking LZs terminate against NNE-striking LZs, consistent with the general master/abutting relationship found between NW- and NNE-striking fractures sets (see earlier section). The number of N-trending LZs (48) is large (Figure 19) compared to the distribution of fracture orientations. One third of the N-trending LZs incorporate field sites (Table 4), and a N-trending FID occurs in one of these LZs.

In both western and central NYS, lineaments associated with FIDs commonly mark fault zones (e.g., Jacobi and Fountain, 1993, 1996, Jacobi et al., 2002a, Jacobi, 2007). Thus, all of the lineaments confirmed with FIDs may represent faults (NNE, WNW, ENE, NS, and NW-trending lineaments), and only the EW-trending lineaments have no confirmatory FIDs. Additionally, Jacobi et al. (2002d) found that lineaments longer than 0.5 km (such as the lineaments identified in this study) more likely trace faults compared to shorter lineaments.

Lineament Zones (LZs) in the Northern Study Area from the 1:250,000 Scale DEM

The 1:250,000 scale DEM image of the northern study area yielded 159 LZs (Figure 20). Like the shorter lineaments identified on the 1:25,000 DEM, the most abundant LZs found in the study area on the 1:250,000 scale DEM trend NNE, the second most abundant trend is NS, and the least abundant trend is EW (see Table 5 for details).

Thirteen of the NNE-trending LZs have a total of 63 sites within them; fourteen of these field sites confirm seven of the NNE-trending LZs with NNE-striking FIDs (Table 5).   Most (28) of the N-trending LZs do not cross field sites; however the remaining six LZs have a total of twenty-nine field sites, and two of these LZs include sites with N-striking FIDs (Table 5). Thus, the sparse N-striking fractures do confirm two of the N-trending LZs. Table 5 summarizes the other lineament trends.

<u>Lineament Zones in the Northern Study Area from the Slope Aspect Map (SALZs, Figure 21)</u>

Unlike the LZs identified on the DEMs, the slope aspect map yielded more N-trending SALZs than any other orientation (Table 6). One third of the N-striking SALZs contain field sites; however, none has N-striking FIDs. The second most-common SALZ trend is NNE, as might be expected from the DEM lineaments and the fracture distribution. About half of the NNE-trending SALZs (3 of 7) include field sites (Table 6). One NNE-trending SALZ contains multiple sites with NNE-striking FIDs, whereas the other two NNE-trending SALZs have NNE-striking FIDs nearby. Five WNW-trending SALZs were identified, including the longest SALZ which passes through the center of the northern study area. Two of these SALZs contain field sites, and both of these SALZs are confirmed by FIDs at the sites (see Table 6 for details for these and other lineament trends).

<u>Lineament Zones in the Northern Study Area from EarthSat (1997)</u>

EarthSat (1997) identified 70 lineaments in the study area from their Landsat Thematic Mapper (TM) images (Table 7, Figure 22). Consistent with SALZs, the most common orientation of EarthSat's (1997) lineaments in the northern study area is N-trending. Eight of the N-trending LZs contain field sites, but none has N-striking FIDs. Again like the SALZs, the second most common LZ trend is NNE. Of the seven LZs with field sites, three are confirmed by sites with NNE-striking FIDs. Furthermore, many of the NNE-striking LZs are close to other sites that exhibit NNE-striking FIDs.

Fourteen WNW-trending LZs were defined by EarthSat (1997) within the study area (Figure 16). Eight of the WNW-striking LZs contain at least one field site, and 75% of these LZs are confirmed by WNW-striking FIDs. Two nearly overlapping WNW-striking LZs, including the longest LZ that passes through the center of the field area, account for ten of the thirteen field sites with WNW-striking FIDs.

Fourteen ENE(a and b)-trending LZs were identified in the study area by EarthSat (1997; Table 7, Figure 17). A single site with an ENE-striking FID is located in two long ENEa-trending LZs. Field sites with ENE-striking FIDs are located near several ENE-trending LZs. Four NW-trending LZs are located in the study area (Figure 18). Although three of the LZs have field sites, none has NW-striking FIDs (Table 7). EarthSat (1997) did not identify any EW-striking LZs in the study area.

<u>Lineament Zones in the Northern Study Area from Aeromagnetic Data (Figure 23)</u>

The most common aeromagnetic lineament orientation in the study area is N-trending, like the SALZ and EarthSat (1997) lineaments (Table 8). Of the four NS-trending LZs, only one contains sites in the northern study area (Figure 19) and none of the sites has NS-striking FIDs. The two NW-striking LZs in the study area are the two longest aeromagnetic LZs (Figure 18). Both NW-striking LZs contain sites but only one LZ is confirmed by a NW-striking FID (Table 8). The other NW-striking LZ has two sites with NW-striking FIDs immediately south of the LZ.

One of the two WNW-striking aeromagnetic LZs includes nineteen field sites (Figure 16). Eight of these sites have WNW-striking FIDs (Table 8). The stream in which the sites are located is coincident with the aeromagnetic LZ, suggesting the stream is eroding along a structural fabric that extends from the Precambrian basement (Figure 16). In the study area, the minimally represented NNE-, ENE- and E-trending aeromagnetic LZs have no appropriately oriented FIDs (Table 8).

Lineament Zones in the Northern Study Area from Multiple Data Sets (Integrated Lineament Zones)

Integrated LZs (ILZs) are defined as zones in which two or more LZs from different data sets have the same orientation and are coincident. The most common ILZ trend in the northern study area is NNE, consistent with the LZs and the distribution of fracture orientations (for detailed tables concerning the ILZs, see Jacobi, 2008). The maximum score among NNE-striking ILZs is 4, which is attained by five different NNE-striking ILZs (#4, 31, 34, 35, 45; Figure 14a). The spatial distribution of high-valued NNE-trending ILZs forms two zones, one in the northwestern part of the study area, and one toward the southeastern part of the map area (Figure 14a). It is probable that NNE-trending faults occur along these two zones.

North-trending ILZs are the second most common (a total of 45) in the northern study area. The maximum score among N-striking ILZs is 6.5, but the highest score is only 4.5 (ILZ 13, Figure 19). Other ILZs with relatively high scores of 4 include ILZs #6, 22, 25, 33, 34, and 36; those with moderate scores of 3.5 include #11, 14, and 23. NS-striking FIDs are the rarest FID orientation found within NS-striking LZs. The spatial distribution of high valued N-trending ILZs form three zones (or clusters) across the study area: one in the western part, one in the central part that includes a large number of ILZs and a smaller zone immediately to the west, and one in the eastern part of the study area (Figure 19). A less well defined zone also occurs between the central and western zones. It is probable that N-trending faults occur along these zones.

Thirty-one WNW-striking ILZs were identified in the study area. WNW-striking ILZs # 12 and 21 (Figure 16) have a score of 5, which is the highest among all ILZs. Nearly half (14 out of 31) of the WNW-striking ILZs are confirmed by at least one site with WNW-striking FIDs. Other ILZs with high scores (4.0) include ILZs #1, 3, 10, 11, 13, 14, 15, and 26. These high scoring ILZs form three zones in the study area, including the longest lineament in the study area, the “Beaver Meadow” ILZ (Figure 16).

Twenty-nine ENE-trending ILZs were compiled in the study area. Out of a maximum score of 6.5, the highest scores for ENE-trending ILZs are only 3.5: ILZs #10, 15, and 17 (Figure 17). These ILZs, coupled with nearby ILZs with a score of 3, suggest three possible fault zones in the study area: one in the northwestern part of the study area and two that straddle the center of the study area (Figure 17).

Twenty-three NW-trending ILZs were recognized in the study area. Two NW-trending ILZs have relatively high scores of 4.5: ILZs # 15 and 23 (Figure 18); one has a score of 4 (ILZ # 20), and two with scores of 3.5 (ILZs #7 and 16). The high scoring ILZs form three zones in the study area; all are either on, or straddle, the Beaver Meadow lineament (identified on Figure 16), and extend from Norwich to the northwest part of the northern study area (Figure 18). Five E-trending ILZs are found within the study area. No sites with EW-striking fracture intensifications occur in any of the ILZs; the highest scores are very low at 2.5 for ILZs # 2 and 3 (Figure 15).

Weights of Evidence for Lineaments in the Northern Study Area

The Contrast (C) Values for each dataset in the northern study area are shown in Figure 24. Inspection of Figure 24 reveals that if comparing lineaments to sites with appropriately oriented fractures that have unrestricted fracture frequencies (> 0.0 fractures/meter), then the lineaments identified on the 1:250,000 DEM generally have better C values compared to the lineaments chosen from the 1:25,000 DEM. NNE-, ENE-, WNW-, NW-, and NS-trending lineaments all have positive C values for the 1:250,000 DEM lineaments, whereas only NNE-, ENE-, and NW-trending 1;25,000 DEM lineaments have positive C values (Figure 24). The low C values indicate that most of the 1:25,000 DEM LZ trends are not strongly confirmed (or "groundtruthed") by appropriately oriented fractures. The C values for EarthSat (1997) lineaments also are generally worse than the 1:250,000 DEM lineaments for sites with appropriately oriented fractures that have unrestricted fracture frequencies. The exception is WNW-trending EarthSat (1997) lineaments that have a significantly higher C values than either set of DEM lineaments. Note that none of the E-trending lineaments (identified from any image) has a positive C value.

For field sites with fracture frequencies >2.0 fractures/meter (for fractures with appropriate orientation), the LZs with the best C values generally are also those identified on the 1:250,000 DEM. NNE-, ENE-, WNW-, NW-, and NS-trending LZs all have positive C values, although WNW- and NW-trending LZs have low positive C values, and are therefore only poorly confirmed by field sites with >2.0 fractures/meter. As with the unrestricted fracture frequency sites, WNW-trending LZs identified by EarthSat (1997) have the best C values.

For field sites with FIDs (fracture frequencies >4.0 fractures/meter) of appropriate orientation, the LZs with the best C values generally are those identified on the 1:250,000 DEM. NNE-, ENE-, WNW-, NW-, and NS-trending LZs all have positive C values. NNE-, ENE-, and N-trending 1:250,000 LZs have significantly positive C values, and are therefore strongly confirmed by sites with appropriately oriented FIDs. Since FIDs may represent faults (e.g., Jacobi and Fountain, 1996, 2002), these 1:250,000 DEM LZ probably represent faults.

East-trending 1:25,000 DEM LZs failed to yield a C value for any of the fracture frequencies (>0.0, >2.0, and >4.0) because no field sites fell within any 1:25,000 DEM LZ. The negative C values for 1:250,000 E-trending LZs also indicate that E-trending lineaments are not confirmed by field sites, and probably do not represent major fault systems. EarthSat (1997) lineaments had strongly negative C values for NW and NS trending lineaments for all fracture frequencies, a conclusion that was also reached for data in the Finger Lakes region (Jacobi, 2007).

Lineament Zones in the Southern Study Area from a 1:100,000 Scale DEM and from EarthSat (1997)

Within the southern study area 196 LZs were identified by McGuire on a 1:100,000 DEM (Figure 25) and EarthSat (1997) identified sixty-two lineaments from a Landsat TM mosaic (Figure 25). The most common lineament trend from the 1:100,000 DEM and from EarthSat (1997) is NNE, like the northern field area (Figure 26). Seventeen of the NNE- trending 1:100,000 DEM LZs contain field sites, of which four exhibit FIDs with a NNE orientation (Figure 26).

The second most common 1:100,000 DEM LZ trend in the southern field area is oriented NE (Figure 27). Eleven of these LZs contain 29 field sites, but none of the sites exhibits an FID with a NE strike. The third most-common 1:100,000 DEM LZ trend in the southern field area is ENE (Figure 28). Three of the eighteen LZs contain six field sites, of which two exhibit ENE-striking FIDs (Figure 28). Interestingly, the least common trend of EarthSat (1997) LZs is ENE.

Seventeen 1:100,000 DEM LZs and thirteen EarthSat (1997) LZs trend EW within the southern field area (Figure 29), but none of the buffered LZs contains a field site with an EW-trending FID. Ten 1:100,000 DEM LZs and seven EarthSat (1997) lineaments trend N within the southern field area (Figure 30). Three of the 1:100,000 DEM LZs and two of the EarthSat (1997) LZs contain field sites with FIDs that strike N (Figure 30). This number of lineaments and confirming sites is significantly greater than in the northern study area.

Nine 1:100,000 DEM LZs and four EarthSat (1997) LZs trend WNW within the southern field area (Figure 31). Two of the nine 1:100,000 DEM LZs, but no EarthSat (1997) LZs, contain FIDs that strike WNW (Figure 31). Four 1:100,000 DEM LZs and three 1:100,000 DEM LZs trend NW within the southern field area, but none contain field sites. No NNW-trending DEM lineaments were identified in the detailed DEM inspection, but several valleys in the central and western parts of the study area have a NNW general trend.

Lineament Zones in the Southern Study Area from Aeromagnetic Gradients

The majority of prominent aeromagnetic lineaments in Chenango County are located outside the southern study area (Figure 32), but eight aeromagnetic lineaments fall within the southern study area. The two NNW-trending aeromagnetic lineaments, located in the central and western parts of the southern study area, are each coincident with an EarthSat (1997) LZ that trends NNW (Figure 32). Another more northerly-trending aeromagnetic lineament in the center of Smithville Flats (located between the two NNW- trending LZs) is also coincident with two EarthSat (1997) LZs (Figure 33). This coincidence suggests that the EarthSat (1997) lineaments represent fracture systems that extend from Precambrian basement to the surface.

The only aeromagnetic lineament that trends NNE is located in the southwestern portion of the southern study area where it is coincident with one 1:100,000 DEM LZ. The single NE-trending aeromagnetic lineament, located in the northeastern part of the southern study area, is coincident with four similarly-trending 1:100,000 DEM LZs. Two NW-trending aeromagnetic lineaments were identified in the northern and northeastern parts of the southern study area (Figure 32). Although neither of these is coincident with lineaments from other data sets (Figure 33), both are on-trend with NW-trending valley segments. Another NW-trending aeromagnetic lineament occurs in the western part of the southern study area. This lineament also is not coincident with any identified lineament from other data sets; however, a long NW-trending valley extends SE from near the lineament (Figure 33).

Each aeromagnetic lineament is either coincident with another lineament from another data set, or is on-trend with a nearby valley segment. Thus, each of these aeromagnetic lineaments and associated surface lineaments suggests that these lineaments represent fracture systems that extend from the Precambrian basement to the surface or near-surface. It would appear that each fault system in the Precambrian basement represented in the aeromagnetic data has been reactivated sufficiently to result in fractured surface bedrock.

Lineament Zones in the Southern Study Area from Multiple Data Sets (Integrated Lineament Zones, ILZs)

Integrated Lineament Zones (ILZs) are defined as zones in which two or more LZs from different data sets have the same orientation and are coincident. Like the northern study area, in the southern study area the most common ILZ trend is NNE (Figure 26). The highest score for the NNE- trending ILZs is 3 (ILZs #13 and #24). In the ILZs several FIDs occur that have a clockwise orientation compared to the ILZ trend (Figure 26). The general zone of ILZs in the northwestern to north central part of the southern study area with sites that exhibit NNE-striking FIDs probably represents a fault system. Other ILZs with NNE-striking FIDs in the eastern part of the study area, and EarthSat/DEM ILZs in the southern part of the study area may also represent fault zones.

Unlike the northern study area, in the southern study area the second-most common ILZ trend is NS (Figure 30). The highest score for N-trending ILZ is a relatively low 2. FIDs and 1:100,000 DEM LZs contribute to the majority of high scores (ILZ # 1, 4 and 10-15). ILZs along the N-trending valley in the western part of the study area, and the ILZs in the northeastern part of the map area probably represent fault systems. The western ILZs are located in the region of the northerly trending aeromagnetic gradient, and therefore fractures probably extend from the surface to Precambrian basement.

Both E- and NE-trending ILZs are third most-common within the southern study area. For E- and ENE-trending ILZs the highest score is 2.5 (ILZs #1 and #3 for E, and #7 for ENE) (Figures 29, 27, respectively). The total lack of confirmatory E- and ENE-striking FIDs makes it difficult to predict whether the ILZs actually represent faults. However, the NE trend of the aeromagnetic lineament in the central western and north-central part of the study area suggests that the NE-trending valley segment and related ILZs (#2, #3, #4, Figure 27) are related to a fault system that extends to basement.

In the southern study area only one NNW-trending ILZ, # 1, has an associated NNW-striking FID (Figure 34). This ILZ (#1) is located between two valleys with generally NNW trends.

These valleys and ILZ #1 are located in the region of a NNW trending aeromagnetic lineament, and therefore may represent a fracture system that extends to Precambrian basement.

Two ILZs were identified for each of the following trends: WNW, NW and ENE. Both WNW-trending ILZs include a WNW-striking FID (Figure 31). Both ILZs probably represent faults, and are on-trend with an aeromagnetic lineament with similar trend. Thus, ILZs #1 and #2 likely are associated with faults that extend to basement. The high number of additional WNW-striking FIDs suggests that more WNW-striking faults exist in the study area. For example, the WNW-trending EarthSat (1997) lineament #A (Figure 29) is on strike with a WNW-trending valley and a WNW trending FID. NW-trending EarthSat LZ (#1) includes a NW-striking FID (Figure 35), and thus may indicate a NW-tending fault. Valleys with NW- to NNW-trends and NW- to NNW-striking FIDs on-strike with the valleys suggest that the additional NW to NNW-trending valleys may indicate faults. Both ENE-trending ILZs include confirmatory ENE-striking FIDs (Figure 28), and therefore most likely indicate faults in these areas. The major ENE-trending valley in the southeastern part of the study area (essentially a northeastern extension of ILZ #1) is on-trend with an aeromagnetic gradient to the NE, and therefore may be indicative of structure that extends to basement.

Weights of Evidence for Lineaments in the Southern Study Area

Weights of evidence for sites with two to four fractures per meter established strong positive contrast values for NNE- and EW-trending 1:100,000 DEM LZs (Figure 36) and for NNE-, EW-, WNW-, NS- and NE-trending EarthSat (1997) LZs (Figure 36). Weights of evidence in all other 1:100,000 DEM LZ orientations could not be established because no sites with 2 to 4 fractures/m occur within the LZs. NNW-, ENE- and NW- trending lineaments have a zero contrast value for two to four fractures per meter.

Weights of evidence for FIDs (> 4.0 fractures/meter) determined strong positive C values for NNE-, NS-, and WNW-trending 1:100,000 DEM LZs (Figure 37) and for NNE-, NS-, NNW- and NW-trending EarthSat (1997) LZs (Figure 37). Negative C values were not calculated for any of the 1:100,000 DEM LZs and EarthSat (1997) LZs, but NNW-, NW-, EW-, and NE-trending 1:100,000 DEM LZs have zero or near-zero C values. Similarly, zero and near-zero C values were calculated for NE-, E-, and WNW-trending EarthSat (1997) LZs. These zero and near-zero C values indicate that NNW-, NW-, E-, and NE-trending 1:100,000 DEM LZs and NE-, E-, and WNW-trending EarthSat (1997) LZs are not confirmed by FIDs striking in the appropriate direction.

Lineaments and the Genegantslet Field

NNE- and NE- trending lineaments are prominent in the Pyron et al. (2003) data (Figure 37). A NNE-trending EarthSat (1997) lineament is quite distant from the Pyron et al. (2003) study area, but the trend is collinear with Pyron et al. (2003) lineaments (Figure 37). The false color image in this report contains several NNE- and NE-trending lineaments (Figure 38). These lineaments that are in the Pyron et al. (2003) study area are coincident with, or on trend with, the Pyron et al. (2003) lineaments (although the density of the Pyron et al., 2003, lineaments is so high that almost any false color image lineament would intersect the Pyron et al., 2003 lineaments).

NNW-trending lineaments are also common in the Pyron et al. (2003) data (Figure 37). The NNW-trending EarthSat (1997) lineament at the southwestern corner of the Pyron et al. (2003) study area is nearly collinear with NNW-trending swarm of lineaments that is about 0.25-0.5 km northeast of the EarthSat lineament (Figure 37). One outlier of this Pyron et al. (2003) lineament swarm is almost coincident with the EarthSat (1997) lineament. In the false-color image NNW-trending lineaments are rare, but they are on-trend with Pyron et al. (2003) lineaments (Fig. 38). NW- to WNW-trending lineaments are more common, but do not have a counterpart in the Pyron et al., (2003) data. A field site about 1.0 km southwest of the southwest corner of the Pyron et al. (2003) study area exhibits two fracture sets, including one with a NNW strike (Figure 37). These fractures indicate that the NNW-trending lineaments in the Pyron et al (2003) and EarthSat (1997) studies most likely do reflect bedrock structure.

N-trending lineaments are rare in the Pyron et al. (2003) data (Figure 37). However, a N-striking FID and coincident N-trending EarthSat (1997) lineament are located in the center of the Genegantslet field (Figure 38). Although Pyron et al. (2003) did not recognize any N-trending lineaments along this EarthSat (1997) lineament in their air photo, they did identify a series of N-trending lineaments about 0.5 km east of the EarthSat (1997) N-trending lineament (Figure 37). Similarly, Pyron et al. (2003) N-trending lineaments are nearly on trend with the EarthSat (1997) lineament about 0.15 km to the south of the EarthSat (1997) lineament. In summary, N-trending lineaments that are observed in Pyron et al.'s (2003) air photo data are also observed in the EarthSat (1997) Landsat data and confirmed in the outcrop fracture data.

ENE-trending lineaments are also relatively rare in the Pyron et al. (2003) data, and are non-existent in the EarthSat (1997) data and false color image for the area. However, a field site with ENE-striking fractures is located about 1.0 km southwest of the southwest corner of the Pyron et al. (2003) study area where ENE-tending lineaments were observed by Pyron et al. (2003, Figure 37).

WNW-trending lineaments were not observed by Pyron et al. (2003), but the false color image does exhibit a few WNW-trending lineaments (Figure 38). This trend is also rare in fracture data, but the field site in the center of the Pyron et al. (2003) study area does exhibit W to WNW-striking fractures. This site is about 0.05 km away from a WNW-trending lineament observed on the false color image.

In summary, all of the Pyron et al. (2003) lineament trends were observed in at least one other data set including EarthSat (1997) lineaments, false color image from this study, or fracture sets observed in outcrop. Additionally, the false color image and fractures indicate that a relatively rare WNW-trending fracture and lineament set also is in the area, but not recognized in the Pyron et al. (2003) data.

Pencil Cleavage

Pencil cleavage was observed at several sites in the southern study area (Figure 39). Stereonets show all but one of the measured cleavage surfaces strike north; dips are disposed in three clusters: steeply east (essentially vertical), and moderately east and west (Figure 40). Pencil cleavage with opposite dips, even in the same outcrop, has been observed in regions to the west in Allegany County (e.g., Jacobi and Fountain, 1996). Most of the sites with pencil cleavage in the present study occur along the walls of N-striking valleys, and could be related to faulting in the proximity of the N-trending valleys. The outcrops in the southern study area are generally so poor that it was not possible in most cases to determine if the pencil cleavage is bedding-restricted. However, in a few sites, the pencil cleavage appeared to be so. The northerly strike and bedding restricted nature are consistent with NeoAcadian west-directed slip zones that resulted from a west-directed S_H, as proposed for units to the east (e.g., Engelder and Geiser, 1979). However, even bedding restricted pencil cleavage could result from NeoAcadian or Alleghanian motion on splays off the possible N-striking faults.

4.2 SEISMIC REFLECTION (2-D) ANALYSES

Because of the nature of the licensing agreements, only reflectors and interpreted faults are displayed. Further, the intense competition in the area of interest among gas exploration companies forces this report to not reveal the location of these seismic lines in central New York State, or the exact depth of the reflectors (the top of each seismic display is not ground surface), or the orientation of the seismic reflection profile, or the orientation of structures observed on the seismic lines as inferred from coincident surface lineaments and FIDs.

Seismic Line A

Seismic Line A is about 29.8 km (18.5 miles) long, and displays a significant number of fault systems (Figures 41 to 45). Reflectors were identified based on "industry practice" and synthetic seismograms from two wells nearby another seismic line that was then correlated to this line. The Silurian Unconformity is well displayed, with the underlying Oswego Formation pinching out below the unconformity; the overlying Oneida Formation maintains a fairly constant thickness across the seismic line (Figure 44. The Trenton section (between the Trenton and Black River reflectors) is relatively thin here, and probably thins to near-zero in the left half of the seismic section (up-dip from fault #8, Figure 41). Note that the dashed purple reflector may be a sub-Black River-top reflector, or less likely, may be the Black River top. If the first scenario is valid for the equivocal dashed reflector below the "Trenton", then the Trenton exhibits dramatic thinning across fault #8. Such significant thinning is consistent with the Mohawk Valley section where Trenton equivalent units can be very thin (e.g., Agle et al., 2006). Locally continuous reflectors immediately below the top-of-Precambrian are observed in the down-dip part of the seismic line. On other seismic lines these reflectors appear to onlap zones that do not have continuous, recognizable reflectors. The onlap, plus their flat-lying nature, suggests that these reflectors represent are post-Grenvillian sedimentary sequences that onlap possible Precambrian (Grenvillian) topographic highs.

As observed on seismic lines to the west in the Finger Lakes region (Jacobi et al. 2002a, b; 2003; Jacobi et al., 2004a, b; Jacobi, 2007), different faults affect different parts of the section. Several faults affect only the Trenton and/or deeper parts of the section. For example, faults #7 and #8 (Figure 41) extend from basement up to the Trenton, whereas faults #5 and #6 appear restricted to units of probable Knox time and older. Only a few faults on this seismic line offset Precambrian basement but do not extend high into the Theresa (e.g., fault #9); these faults were probably restricted to Iapetan opening tectonics. Similarly, a few faults are restricted to the post-Grenvillian Precambrian sedimentary section (fault #10). The lack of significant Iapetan opening fault-controlled sedimentation on this line is particularly evident when the seismic line is flattened on the Theresa (Figure 42). On this figure the Theresa-top-of-Precambrian contact interval generally increases thickness gradually and monotonously down-dip with only a few minor offsets on the Precambrian contact.

Fault system #4 and fault #8 have a significant effect on the Black River reflector and the Trenton seismic reflector interval (Figures 41 and 43). The Trenton interval is generally thicker down dip from fault system #4/4a (see especially Figure 43), and the Trenton interval may thin in the region of fault system 4 (arrow at fault systems #4/4a on Figure 43), although reflector identification is difficult in this local region. Similarly, the Trenton interval up-dip from fault #8 may thin to sub-seismic thickness (arrow at fault #8 in Figure 43). Thus, the thickness of the Trenton-Black River interval appears structurally controlled, as is the case in the Mohawk Valley. The possible thinning in the region of fault system #4 may indicate a T/BR target. The faults that affect the T/BR (and Knox), but that do not extend above these reflectors, are related to Taconic tectonics.

Some faults and fault systems extend from basement to the Silurian Unconformity. Fault system #1 controlled the pinch out of the Oswego at the unconformity (Figures 41 and 43). Faults in fault systems #4b and #4c terminate at the Silurian Unconformity (Figure 41). Like the Finger Lakes region, other faults appear to extend from Precambrian up into the post-Lockport Silurian section (Figure 41). These faults thus probably are a result of tectonics during the Salinic Orogeny.

A few faults and fault systems extend through much, or all, of the section (Figure 41). Fault system #4 extends from Precambrian basement through all identified reflectors, including the Tully. Fault system #3 extends from Precambrian basement to perhaps the Onondaga and higher. This fault system was active during the Silurian Unconformity time, since a small remnant of Oswego occurs in the fault system (Figure 44). The fault system was reactivated later, since the fault system offsets the Lockport reflector. This fault system has a positive flower structure appearance (Figure 41). Coupled with the observed local thrusts extending away from the main trend (e.g. offsetting the Lockport), it is suggested that this fault system represents a strike slip (or oblique slip) restraining-bend geometry. Fault system #2 is less well developed; whether it extends through the salt section to the Onondaga and above is equivocal (Figure 41). If the local faults at Lockport and higher horizons are a part of this fault system, then the fault pattern is similar to very poorly developed negative flower structure that reflects part of releasing bend geometry. The most recent age of these fault systems is probably NeoAcadian or younger (Alleghanian).

Several thrust faults affect the Onondaga and are floored in the Silurian salt section (Figure 41). Particularly classic faults are indicated by three arrows on the down-dip part of the seismic line (Figure 41), but others occur up dip as well, including two that are associated with fault systems #2 and #3. All of the local thrusts occur either above fault systems (e.g., #4b and #4c), or as noted above, are associated directly with fault systems (#2 and #3). This linkage is consistent with the suggestion that units heavily fractured from faulting below or within the unit are susceptible to the development of thrust ramps. This theory was developed for southwestern Pennsylvania by Scanlin and Engelder (2003) and for northwestern Pennsylvania and western and central NYS by Jacobi et al. (2003, 2004a, 2005, 2006)

A large number of faults affect the Tully Formation (Figure 41). Some, such as fault systems #2 and #3, extend from Precambrian basement, but others (e.g., systems #11 and #12) have a suprastructural nature, and appear to be localized to units above the Onondaga. The tectonic thickening of the Tully fold associated with fault system #12 (Figures 41, 43 and 45) is obvious. Unlike Onondaga folds with a core of salt and interbedded shales, the core of the Tully fold must lack salt. The number of faults in the Devonian shale (and interbedded sand) section above the Onondaga is impressive, and indicates that simple 'pancake" geology for the Devonian shale section is not the norm here. This relatively complicated structural view is consistent with field work as far west as the Clarenden-Linden Fault System in western NYS, where Jacobi and Fountain (1996) found highly disturbed zones of Devonian interbedded sands and shales. For example, in one creek they found 5 stacked bedding-restricted thrust zones, including a recumbent fold. Many of these structurally high fault systems occur over deeper fault systems, implying that the same hypothesis for the location of the Onondaga thrusts may be applied to many of these Tully and higher faults.

Seismic Line B

Seismic Line B is about 37.5 km (23.3 miles) long, and, like seismic line A, displays a significant number of fault systems (Figures 46 to 50). Reflectors were identified based on "industry practice" and synthetic seismograms from two wells nearby another seismic line that was then correlated to this line.

On this line relief on the top of the Precambrian is quite evident. Structural relief between faults #2 and #3 extends to the Theresa top, but does not affect the Trenton. In contrast, although the Precambrian high at arrow #e and fault system #8 has a significant sediment onlap in the lowest Paleozoic sections (sub-Theresa-top, see Figure 47), this Precambrian topographic high was also the locus of episodic faulting higher in the section, as high as the Silurian salt section. Intervals above the Trenton and below the Top-of-salt thin over the region of the Precambrian high (Figures 47, 48). However, the local faults of system #8 were not active from the sub-Theresa-top reflector time until after Trenton, since these intervals do not thin or thicken across the structure (Figure 47). Similarly, this fault system does not display a growth-fault geometry from the Silurian salt through the Tully (these intervals do not thin across the high (Figure 50). Fault #9a and fault systems #9, #10, and #11 all show growth fault geometries in the Theresa-Precambrian interval (Figure 47). It is suggested these faults all developed initially during Iapetan opening tectonics.

A significant number of fault systems penetrate from the Precambrian to the Silurian section, and some to the highest horizons of the seismic line; these fault systems include #1, #6, #8, #9, #10, and #11. As discussed for fault system #8 above, these systems show evidence of fault reactivations in the form of growth fault geometries across the faults for certain reflector intervals. For example, fault system #6 and #7 controlled the pinch out of the Oswego Formation (Figure 49). However, little fault activity occurred between Oneida and Lockport time, since the interval gradually thickens with no sharp increases across fault systems. In contrast, the Lockport to Top-of-salt interval increases across fault system #6, #10, and #11 (as well as across #8 discussed earlier). If the Tully horizon is picked correctly, then fault systems #1 and #10 were active during the Onondaga to Tully interval, since significant down-dip thinning (relative to the

Onondaga) occurs across these faults (Figure 50). The splays on fault system #9 define a modified positive flower structure, suggestive of a strike-slip fault with a restraining bend geometry (note the down-dip-directed thrust of the Lockport). This geometry (petals down-dip) is the same as the positive flower structure (fault system #3 on Line A, Figure 41). Fault system #10 is a much narrower system than #9, but it too has a few splays, with thrusts directed down-dip in the Lockport (arrow #h in Figure 46)

A number of thrusts of the Onondaga are also observed on this seismic line. A few are isolated (arrow #a on Figure 46), but most lie above deeper fault systems (arrow #b, #f, #i and those associated with fault system #11; Figure 46). As discussed for seismic line A, this association is probably not fortuitous—the relatively highly fractured Onondaga in these fault systems probably provided a weakened structural member that was conducive to developing thrust ramps. One relatively large salt and thrust-cored anticlinal system is evident at arrow #c on Figure 46.

The Devonian section above the Tully displays a dramatic thinning between fault system #10 on the up-dip side and fault system #6/7 on the down-dip side (Figure 46). The lower reflectors are truncated (purple reflectors on Figure 46), and the continuous upper reflector intervals thin over the structure. The U-shape geometry is similar to the cross section of a slump scar. That the fault systems appear to have localized the edges of the structure suggest that fault activity destabilized the sedimentary section above the Tully Formation, causing a slump (sediment slide). The slump scar (slide scar) would be the surface that truncates the purple reflectors in Figure 46. Fault system #10 was active in Tully time, as determined from the growth fault geometry of the Tully reflector across fault system #10 (Figure 50). A sediment slide (or slump) of this magnitude is not surprising in this section, since a 33+m (100+ ft) section of multiple debrites/seismites was found near Smithville Flats.

Seismic Line C

Seismic Line C is about 14.9 km (9.25 miles) long, and, like seismic lines A and B, displays a number of fault systems (Figures 51 to 55). Reflectors were identified based on "industry practice" and synthetic seismograms from two wells nearby another seismic line that was then correlated to this line.

On this seismic line relief on the top of the Precambrian, relative to the Theresa, is evident across several faults: #1, #2, #3, #4, #8/8a, #10, #11, #12, and #12a (Figures 51 and 52). These faults were thus active during Iapetan-opening and Rome-Trough-time tectonics. Some of these faults ceased activity soon after deposition over the Precambrian commenced (e.g., #7, Figures 51 and 52), whereas a majority were active through Theresa and into Trenton/Black River time; many ceased activity at the end of Trenton time (Figures 51, 52, and 53). For example, on the left side of the seismic line, none of the first eight faults extends much above the Trenton (including #1, #2, #3, #5), although fault #5 and perhaps #4 have counterparts higher in the section. A similar situation exists on the right side of the seismic line, where faults #8, #11 and #12 do not extend far above the Trenton or Black River reflectors (Figures 51, 52, and 53). Several of these faults appear to have ceased activity at the end of Black River time (e.g., #8, #9) or during Trenton time (# 11a). For most of the line, the Trenton interval remains a fairly constant thickness (Figure 53), but at fault #11a, the Trenton interval thins to the right (Figure 53), and thins in the region between faults #4 and about #5. Finally, some of the faults clearly offset the post-orogenic

(Grenvillian) Precambrian reflectors, such as fault #8 (Figure 51). Based on the timing of fault development, the faults discussed above developed initially as Iapetan-opening (rift) faults, and were reactivated in the Taconic.

A significant reduction in the number of faults occurs above the Trenton; only a few faults and fault systems extend into the Silurian. For example, fault #12a offsets the Silurian unconformity and apparently controlled the pinch out of the Oswego (which pinched out at the fault; Figures 51, 52, and 53). This fault (as a system which includes the nearby fault on the right), may extend to near the top-of-Lockport, but the Lockport itself shows no significant offset. However, because thrusts of the Onondaga and Tully are localized above this fault, fractures of the fault system may have may extended higher in the section to provide a local weakened zone for development of the relatively high angle thrusts.

The only other significant fault system that occurs above the Silurian Unconformity is fault system 4a, which has a positive flower structure geometry. The Onondaga is disposed in an anticline across the fault system. This is a probable strike-slip fault system, which the seismic line crosses at a restraining bend. Unlike the restraining bends on the other two seismic lines, this bend has its petals radiating in an up-dip direction.

CONCLUSIONS

In the interbedded sandstones/siltstones and gray shales of Chenango County, the UBRFG measured eight characteristics of more than 2600 fractures at 201 sites within the northern study area and over 1400 fractures at more than 190 sites southern study area. This extensive data set showed that the most common fractures in both the northern and southern study areas strike NNE (thought to be “cross-strike”, or Set I, fractures in this region) and WNW (“strike-parallel”, or Set II, in this region). Other sets are much less prominent except locally, and include ENE- and N-striking fractures. Fracture intensification domains (FIDs) with fracture frequencies of >4 fractures/meter are common in the area of interest, and many are collinear with nearby topographic features. Elsewhere, FIDs have been shown to be associated with fault systems in these types of rocks. A plot of bed thickness versus fracture frequency showed no correlation between the two measures. Master/abutting relationships showed that the majority of ENE-striking fractures are the oldest, and predate the accepted dominant Alleghanian NNE- and WNW-striking fractures. N-striking fractures generally came relatively late in the history of fracture development.

Lineaments were identified on digital elevation models (DEMs) and aeromagnetic anomalies in the areas of interest in Chenango County. These lineaments and EarthSat (1997) lineaments from Landsat images were integrated and then tested against the outcrop fracture data. The statistical comparison involved the use of weights of evidence. In the northern area, NNE-trending lineaments from the 1:25,000 DEM, the 1:250,000 DEM, topographic slope aspect map and EarthSat (1977) all had positive Contrast Values (a positive number indicates a coincidence between data sets) with respect to outcrop fractures of all frequencies. For WNW-trending lineaments, EarthSat (1997) lineaments had the best correlation. For other lineament and fracture orientation, the coincidence between groundtruth fractures and the lineaments was variable, depending on the orientation, lineament type, and fracture frequency. In general the best correlation was found between FIDs and lineaments, especially those identified on the 1:250,000 DEM. The worst correlations involved EW-trending lineaments, none of which had a positive C value. EarthSat (1997) lineaments had strongly negative C values for NW and NS trending lineaments in the northern study area, a conclusion that was also reached for data in the Finger Lakes region (Jacobi, 2007). For the southern study area, C values for lineaments tested against outcrop fractures had positive values (for those sets that could be calculated).

The correlation between aeromagnetic lineaments and surface lineaments, as well as fractures, suggests that these lineaments and fractures represent fracture systems that extend from the Precambrian through the entire sequence to the surface. In the southern study area, these trends are NNW, ENE/NE, NW and N. Similar trends are inferred in the northern study area, with the addition of an EW trend. The integrated lineament zones that are confirmed by FIDs probably represent fault systems (including those with aeromagnetic lineaments). These possible fault systems trend in the directions listed above, plus NNE and rarely (if ever), EW. Although the intent was to combine these integrated lineament zones with seismic reflection data to determine the trend and extent of fault systems observed on the seismic lines, the intense competition in the area of interest and licensing agreements prevent such a presentation.

For this project about 80 km (50 miles) of 2-D seismic reflection profiles were analyzed. These lines display a significant number of fault systems that extend from the Precambrian basement to the (near)-surface, as inferred from the lineament analyses. Many of the fault systems correlate with surface FID and integrated lineament zones. The fault systems have a long reactivation history, based on growth fault geometries. Some faults are Iapetan opening (rift) faults only; others were active through early Taconic, whereas many were active through Trenton time. Many ceased activity soon after the Trenton (the faults extend only a short distance above the Trenton). Others extend into the Silurian and apparently were last active in the Salinic, whereas other fault systems extend through the entire section. These fault systems controlled the preservation (and possibly deposition) of units such as salt and the Oswego, since both pinch out at faults. Some of the fault systems have clear flower structures, implying that these faults sustained strike-slip motion, and the seismic lines crossed either a retraining bend or releasing bend (depending on the flower geometry).

In terms of prospects, structural highs were recognized on the basement and Potsdam/Theresa, a few Trenton/Black River anomalies, the Oswego and lower units pinching out at the Silurian unconformity, and fault-bend folds over ramping thrusts in the Onondaga, as well as fracture porosity along the fault systems.

In summary, the lineaments were generally confirmed by outcrop fractures, especially the FIDs. The inferred fault systems cross much of the area of interest, and seismic reflection profiles confirm the faulted nature of central NYS. The faults were active through most of the Paleozoic for which a rock record exists, and controlled the disposition of thin units. Flower structures indicate that some of the larger fault systems were strike slip for at least part of their motion history.

REFERENCES

Ahmed, Khurrum, Loewenstein, Stuart, and Jacobi, Robert, 2006, Characteristics of the Bradley Brook Field; The Eastern-Most Economically Productive Gas Field in the Appalachian Basin in New York State: Geological Society of America, Abstracts with Programs, v. 41, n. 2, p. 66

Bahat, D., and Engelder, T., 1984, Surface morphology on cross-fold joints of the Appalachian Plateau, New York and Pennsylvania: Tectonophysics, v. 104, p. 299-313.

Bai, Taixu, Maerten, Laurent, Gross, Michael, and Aydin, Atilla, 2002, Orthogonal cross joints: do they imply a regional stress rotation?: Journal of Structural Geology, v. 24, p. 77-88.

Baudo, Andrew I, and Jacobi, Robert D., 1999, Fracture patterns along a 2.3 km scanline in the Appalachian Plateau, Cattaraugus County, western NY: statistical analysis and implications for fault activity: Geol. Soc. Am., Abstract w/ Programs, v. 31, n. 2, p. A-3.

Baudo, A., and Jacobi, R. D., 2000, Fractal and geostatistical analyses of fractures along a 4 km scanline in the Appalachian Plateau, SW New York State: Geol. Soc. Am., Abstracts w/ Programs, v. 32, n.1, p. A4

Beardsley, R.W., 1999, Field report, Exhibit C(G) to report: Characterization of Glodes Corners Road reservoir. NYSDEC. http://www.dec.state.ny.us/website/dmn/BlackRiver/images/cnrrptcg.gif, accessed November 29, 2006.

Beardsley, R.W., 2001, Trenton/Black River. Presentation at “The Role of Appalachian Supply in a 30 TCF Market” (NYSERDA, IOGA & GTI, Ellicottville, NY).

Beinkafner, Kathie J., 1981, Quantitative analysis of the Herkimer Formation (Upper Silurian) in the subsurface of central New York State: New York State Bulletin (Albany NY) no. 437, 31 pp.

Copley, David L., and Heim, L. Robert, 2006a, Preliminary Subsurface Correlations of the Theresa (Galway) Sandstone Formation in New York State: Implications for Exploration: AAPG Eastern Section Meeting Abstracts, http://www.searchanddiscovery.com/documents/2006/06091eastern/abstracts/copley.htm, Accessed August 25, 2007.

Copley, David L., and Heim, L. Robert, 2006b, Preliminary Subsurface Correlations of the Theresa (Galway) Sandstone Formation in New York State: Implications for Exploration: Ontario-New York Oil and Gas Conference, Forty-Fifth Annual

Conference (Ontario Petroleum Institute, London, Ontario), Session No, 4, No. 10 p. 1-24.

Cruz, C.A., 2005. Satellite Image Enhancements, Lineament Identification and Quantitative Comparison with Fracture Data, Central New York State. State University of New York at Buffalo (Buffalo, NY), Unpub. Master's Thesis, 127 pp.

Cruz, Cheri, Jacobi, Robert D., Everett, John R., and Staskowski, Ronald J., 2005, ASTER and Landsat lineaments in central NYS: Image processing and groundtruthing for fractures: Geological Society of America, Abstracts with Programs, Geological Society of America, Abstracts with Programs, v. 37, n. 1, p. 58.

Daneshfar, B., and Benn, K., 2002. Spatial relationships between natural seismicity and faults, southwestern Ontario and north-central New York State, *in* Neotectonics and Seismicity in Eastern Great Lakes Basin, R. Fakundiny, R. Jacobi and M. Lewis (eds.): Tectonophysics, 353 (1-4), p 31-44.

Dennison, John M., 1985, Catskill Delta shallow marine strata, *in:* The Catskill Delta Donald L. Woodrow and William D. Sevon (Eds.): Geological Society of America, Sp. Paper 201, p. 91-106.

de Witt , W., Roen, J.B., and Wallace, L.G., 1993, Stratigraphy of Devonian Black Shales and Associated Rocks in the Appalachian Basin: Petroleum Geology of the Devonian and Mississippian Black Shale of Eastern North America, USGS Bulletin 1909, pages B1-B57.

Drechsel, Cheri A., Jacobi, Robert D., Everett, John R., and Staskowski, Ronald J., 2004, ASTER lineaments, faults, and reservoirs in the Appalachian Basin of New York State: Geological Society of America, Abstracts with Programs, v. 36, n. 2, p. 146.

EarthSat (Earth Satellite Corporation), 2003, Assessing the contribution of satellite hyperspectral data to petroleum exploration. New York State Energy Research and Development Authority (NYSERDA) (Albany, New York), 35 pp.

Engelder, T., 1985, Loading paths to joint propagation during a tectonic cycle: an example from the Appalachian Plateau, U.S.A.: Journal of Structural Geology, 7, p. 459-476.

Engelder, T. and Geiser, P., 1979, The relationship between pencil cleavage and lateral shortening within the Devonian section of the Appalachian Plateau, New York, Geology, v. 7, p. 460-464.

Engelder, T., and Geiser, P., 1980, On the use of regional joint sets as trajectories of paleostress fields during the development of the Appalachian Plateau, New York: Journal of Geophysical Research, 85, 6319-6341.

Engelder, T., 1982, Is there a genetic relationship between selected regional joints and contemporary stress within the lithosphere of North America?: Tectonics, v. 1, p. 161-177.

Engelder, Terry, and Oertel, G., 1985, Correlation between abnormal pore pressure and tectonic jointing in the Devonian Catskill Delta: Geology, v. 13, p. 863-866.

Engelder T., and Whitaker, A., 2006, Early jointing in coal and black shale: Evidence for an Appalachian-wide stress field as a prelude to the Alleghanian orogeny: Geology, v 34, p. 581-584.

Engelder, T., Haith, B.F., and Younes, A., 2001, Horizontal slip along Alleghanian joints of the Appalachian plateau: evidence showing that mild penetrative strain does little to change the pristine appearance of early joints: Tectonophysics, v. 336, p.31-41.

Fisher, D.W., Isachsen, Y.W., Rickard, L.V., Broughton, J.G., and Offield, T.W., 1961, Geologic map of New York, Finger Lakes Sheet: New York State Museum and Science Service (Albany, NY).

Davies, Graham R., and Smith, Langhorne B., Jr. 2006, Origin and reservoir characteristics of Upper Ordovician Trenton-Black River hydrothermal dolomite reservoirs in New York: American Association Petroleum Geologists Bull., v 90, p.1691-1718.

Gross, M., and Engelder, T., 1991, A case for neotectonic joints along the Niagara Escarpment: Tectonics, v. 10, p. 631-641.

Henderson, G. J., and Timm, C. M., 1985, Ordovician stratigraphic hydrocarbon entrapment potential of Appalachia: Oil and Gas Journal, p. 118-125.

Isachsen, Y.W., Landing, E., Lauber, J.M., Rickard, L.V., Rogers, W.B., 2000, Geology of New York: A Simplified Account, 2nd ed.: New York State Museum (Albany, NY), 294 pp.

Jacobi, R.D., 2002, Basement faults and seismicity in the Appalachian Basin of New York State: Tectonophysics, 353, 75-113.

Jacobi, Robert D., 2007, Final Technical Report (May 31, 2000-May 15, 2007): Innovative Methodology for Detection of Fracture-Controlled Sweet Spots in the Northern Appalachian Basin: Department of Energy/NETL, Morgantown, WV, 143 pp. and 258 figures.

Jacobi, R.D. and Fountain, J.C., 1996, Determination of the seismic potential of the Clarendon-Linden Fault System in Allegany County, Final Report: NYSERDA (Albany, NY), 2106 pp. and 31 oversized maps.

Jacobi, Robert and Zhao, Meng, 1996, Rapid and rigorous outcrop fracture trace mapping and analyses, In Contaminant Hydrogeology in Fractured Bedrock (J. Fountain, Ed.): Geol. Soc. Am. (Northeast Section, Buffalo meeting) short course notes, p. 1-19.

Jacobi, Robert, and Smith, Gerald, 2000, Part I, Core and cutting analyses, surface structure, faults and lineaments, and stratigraphic cross-sections based on previous investigations, *in*: Geologic Investigation of the Gas Potential in the Otsego County Region, Eastern New York State, Final Phase One Report to Millennium Natural Resources Development, L.L.C., (Robert Jacobi, Ed.): Final Report: presented to NYSERDA (Albany NY) on 9/8/00, 85 p.

Jacobi, Robert, Loewenstein, Stuart, and Romans, Brian, 1999, The Basal Sandstone in the Stahl #1 well, Wyoming County, New York; Is It a Correlative of the Rose Run Sandstone? Final Report: Presented 5/6/99 to NYSERDA, 16 pp.

Jacobi, Robert D., Fountain, John C., Lugert, Courtney M., Wehn, Karen S., Nelson, Travis, Budney, Lucas, and Zybala, Jon G., 2002a, Fracture Intensification Domains, fracture flow, and Trenton-Black River faults in the Finger Lakes region, NYS: Geol. Soc. Am., Northeastern Section Annual Meeting (Springfield, MA) Abstracts, v. 34, n. 1, p. A-11.

Jacobi, Robert D., Fountain, John C., Nelson, Travis, and Lugert, Courtney M., 2002b, Reactivated Precambrian faults in the Appalachian Basin of NYS: Geol. Soc. Am., Abstracts with programs, v. 34, n. 6, p. 79.

Jacobi, R. D., Fountain, J., and Loewenstein, S., 2002c, Demonstration of an exploration technique integrating Earthsat's Landsat lineaments, soil gas anomalies, and fracture intensification domains for the determination of subsurface structure in the Bass Island Trend, New York State, Final Report: presented to NYSERDA (Albany NY) on 7/22/02, 188 p.

Jacobi, Robert D., Eastler, Thomas E., and Xu, Jiandong, 2002d, Methodology for remote characterization of fracture systems in enemy bedrock underground facilities, *in* The Environmental Legacy of Military Operations, Russell Harmon and J. Ehlen (eds.): Geol. Soc. Am. Engineering Geology Division, v. 14, p. 27-60.

Robert D. Jacobi, John Fountain, Courtney Lugert, Travis Nelson, Gerald Smith, Thomas Mroz, and John Martin, 2003, Identifying Trenton/Black River targets in the northern Appalachian Basin (NYS): Demonstration of integrated exploration tools: American Assoc. Petrol. Geol. Annual Meeting program, v. 12, p. A44

Jacobi, Robert D., Smith, Gerald, Fountain, John, Fagan, JP, and Industrial Associates, 2004a, Fault systems in New York State and carbonate reservoirs: Trenton/Black River and younger plays: American Assoc. Petrol. Geol. Annual Meeting Program, v. 13, p. A70.

Jacobi, Robert D., Loewenstein, Stuart, Smith, Gerald, Fountain, John, Lugert, Courtney, and Martin, John, 2004b, Iapetan Opening/Rome Trough-Related Faults and Their Reactivation History in New York State: AAPG Eastern Section Meeting Abstracts, http://www.searchanddiscovery.com/documents/abstracts/2004eastern/jacobi02.htm, Accessed January 3, 2005.

Jacobi, R. D., Loewenstein, S., and Smith, G. 2005: Seismic Data Bearing on Iapetan Opening/Rome Trough-Related Faults, Their Reactivation History and Effect on Deposition in the Appalachian basin of New York State: AAPG National Meeting Abstracts, http://www.searchanddiscovery.com/documents/abstracts/2005annual_calgary/abstracts/jacobi.htm , Accessed May 4, 2006

Jacobi, R. D., Loewenstein, S., and Smith, G. 2005b: Seismic Data Bearing on Iapetan Opening/Rome Trough-Related Faults, Their Reactivation History and Effect on Deposition in the Appalachian basin of New York State: AAPG National Meeting Abstracts,

Jacobi, R.D., Loewenstein, S., Smith, G., and Martin, J., 2005c, Ordovician fault systems in the Appalachian Basin of New York State: Geological Society of America, Abstracts with Programs, v. 37, n. 1, p. 5.

Jacobi, Robert D., Kim, Jon, Agle, Paul A., Gale, Marjorie, Becker, Laurence, Mitchell, Charles and Smith, Gerald, 2006a, Generation of Lower Paleozoic carbonate reservoirs in the Appalachian Basin of New York State: faults, timing, and the plate tectonic connection: Ontario-New York Oil and Gas Conference, Forty-Fifth Annual Conference (Ontario Petroleum Institute, London, Ontario), Session No, 6, No. 21 p. 1-36.

Jacobi, R.D. Loewenstein, S., and Smith, G., 2006b, Seismic Evidence for Iapetan Fault Control of the Arcuate Map Pattern of the Pennsylvania Salient: Geological Society of America, Abstracts with Programs, v. 41, n. 2, p. 84.

Jacobi, Robert D., Kim, Jon, Agle, Paul A., Gale, Marjorie, Becker, Laurence, Mitchell, Charles, and Smith, Gerald, 2007, Generation of Lower Paleozoic Carbonate Reservoirs in the Appalachian Basin of NYS: The Plate Tectonic Connection: IOGA Annual Meeting (Buffalo, NY, November 6, 2007)

Lash, G.G., Loewy, S., and Engelder, T., 2004, Preferential jointing of Upper Devonian black shale, Appalachian Plateau, USA: Evidence supporting hydrocarbon generation as a joint-driving mechanism: in Cosgrove, J. W., and Engelder, T., eds., The initiation, propagation, and arrest of joints and other fractures: Geological Society of London Special Publications, v. 231, p. 129-151

Loewenstein, Stuart, Jacobi, Robert, and Martin, John, 1998, Geologic assessment of core data from the Stahl #1 and correlation with the Rose Run of Ohio: Am. Assoc. Petrol. Geol., v. 82, p. 1770.

Lugert, Courtney M., Jacobi, Robert D., When, Karen, S., and Fountain, John, 2001, Tracing deep structure: Fractures analysis in the Finger Lakes region of the Appalachian Plateau, NYS: Geol. Soc. Am., Annual Meeting Program, v. 33, n. 6, A-394.

Lugert, Courtney M., Jacobi, Robert D., Wehn, Karen S., Fountain, John C., and Zybala, Jon G., 2002, Coincidence of fracture intensification domains with Trenton-Black River faulting in the Finger Lakes region, New York State: Part 1, Seneca Lake: Geol. Soc. Am., Northeastern Section Annual Meeting (Springfield, MA) Abstracts, v. 34, n. 1, p. A-3.

Martin, John, 2006, The status of shale gas in New York: Ontario-New York Oil and Gas Conference, Forty-Fifth Annual Conference (Ontario Petroleum Institute, London, Ontario), Session No, 4, No. 12 p. 1-38.

McGuire, Kelly, 2007, Fracture, Lineament, and Seismic Data: Indication of Fault Patterns in the Appalachian Basin in East-central New York State: unpub MS thesis, University at Buffalo (Buffalo, NY), 324 pp.

McGuire, Kelly M., Jacobi, Robert D., Terech, Nicholas, and Agle, Paul, 2006a, Integration Of Fracture Patterns And Lineaments For Fault Mapping In The Appalachian Basin Of Central New York State: Geological Society of America, Abstracts with Programs, v. 41, n. 2, p. 69.

McGuire, Kelly M., Jacobi, Robert D., Terech, Nicholas, and Agle, Paul, 2006b, Integration of Fracture Patterns and Lineaments for Fault Mapping in Southwestern Chenango County, New York: AAPG Eastern Section Meeting Abstracts (Buffalo, NY), http://www.searchanddiscovery.com/documents/2006/06091eastern/abstracts/mcguire.htmAccessed January 29, 2007

Nickelsen, R. P., and Hough, V. D., 1967, Jointing in the Appalachian Plateau of Pennsylvania: Geological Society of America Bulletin, v. 78, p.609-630.

Nyahay, Richard, Leone, James, Smith, Langhorne, Martin, John, and Jarvie, Daniel, 2008, Update on the regional assessment of gas potential in the Devonian Marcellus and Ordovician Utica shales in New York: Geological Society of America, Abstracts with Programs, 43rd Annual Meeting, paper No. 28-6. http://gsa.confex.com/gsa/2008NE/finalprogram/abstract_135310.htm Accessed May 29, 2008

Parker, J. M., 1942, Regional systematic jointing in slightly deformed sedimentary rocks: Geological Society of America Bulletin, v. 53, p.381-408.

Pyron, Arthur, Viellenave, Jim, Fontana, John, 2003. New York Devonian black shale: A Barnett-like play in waiting. Oil and Gas Journal, January 13 issue, 8 pp.

Rawnsley, K. D., Peacock, D. C. P., Rives, T, and Petit, J-P, 1998, Joints in the Mesozoic sediments around the Bristol Channel Basin: Journal of Structural Geology, v. 20, p. 1641-1661.

Rickard, Lawrence V., Fisher, Donald W., 1970, Geologic Map of New York. Finger Lakes Sheet: New York State Museum (Albany, NY), 1 sheet

Rickard, Lawrence V., 1973, Stratigraphy and structure of subsurface Cambrian and Ordovician carbonates of new York: New York State Museum and Science Service (Albany, NY), Map and Chart series n. 18, 26 pp and 19 plates

Rickard, L., V., 1975, Correlation of the Devonian rocks in New York State: New York State Museum and Science Service (Albany, NY), Map and Chart Series, n.24.

Rogers, William B. Isachsen, Yngvar W., Mock Timothy D., and Nyahay Richard E., 1990, New York State geological highway map: New York State Museum (Albany, NY), Educational Leaflet 33.

Scanlin, M.A., and Engelder, T., 2003, The basement versus the no-basement hypothesis for folding within the Appalachian Plateau detachment sheet: Am. Journal of Science, v. 303, p. 519-563.

Sevon, William D., and Woodrow, Donald L., 1985, Middle and Upper Devonian stratigraphy, *in:* The Catskill Delta Donald L. Woodrow and William D. Sevon (Eds.): Geological Society of America, Sp. Paper 201, p. 1-7.

Terech, Nicholas, 2006, Fracture Patterns, Lineaments and Seismic Reflection Data: Integration for Fault Mapping in the Appalachian Basin of East-Central New York State: Unpub MS thesis, University at Buffalo (Buffalo, NY), 257 pp.

Terech, Nicholas, Jacobi, Robert D., McGuire Kelly, and Agle, Paul, 2005, Fracture patterns, lineaments, and seismic reflection data: integration for fault mapping in the Appalachian basin of east-central New York State: Geological Society of America, Abstracts with Programs, v. 37, n. 1, p. 83.

Tober, B. K., and Jacobi, R. D., 2000, Fracture trends and spacing in the Appalachian Plateau of western New York: implications for the Bass Island trend and north-striking lineaments: Geol. Soc. Am., Abstracts w/ Programs, v. 32, n.1, p. A79

Weary, David J., Ryder, Robert T., and Nyahay, Richard, 2000, Thermal maturity patterns (CAI and %Ro) in the Ordovician and Devonian rocks of the Appalachian basin in New York State: U.S. Geological Survey, Open File Report 00-496, 34 pp.

Weary, D. J., Ryder, R. T., and Nyahay, R., Thermal maturity patterns in New York State using CAI and %Ro: Northeastern Geology and Environmental Sciences, Vol. 23, No. 4, 2001, 20 pp.

Wedel, A. A., 1932, Geologic Structure of the Devonian Strata of South-Central New York: New York State Museum Bulletin, v. 294, 73 p.

Wickstrom, L. H., 1996, Play MOF: Middle Ordovician fractures carbonates, *in:* J. B. Roen and B. J. Walker (eds.), The Atlas of Major Appalachian gas Plays: W. Virginia Geol. Surv., v. 25, p. 172-176.

Witmer, T.C., 2004, The Relationship among Fracture, Lineaments and Faults: Structural Geology of the Collins Center 7.5' Quadrangle, New York State: Unpub Master's Thesis, State University of New York at Buffalo.

Witmer, Todd C., Jacobi, Robert D., and Zybala, Jon G., 2002, Fractures in the Collins Center 7.5' quadrangle, western New York State: Implications for faulting: Geol. Soc. Am., Northeastern Section Annual Meeting (Springfield, MA) Abstracts, v. 34, n. 1, p. A-3.

Wheeler, R.I., and Wise, D.U., 1983, Linesmanship and the practice of linear geo-art; discussion and reply: Geological Society of America Bulletin, 94 (11), p. 1377- 1379.

Wise, D.U., 1976, Linesmanship; guidelines for a thriving geologic artform, Utah Geological Association Publication, (5), p. 635-636.

Wise, D.U., 1982, Linesmanship and the practice of linear geo-art, Geological Society of America Bulletin, 93 (9), p. 886-888.

Woodrow, Donald L., 1985, Paleogeography, paleoclimate, and sedimentary processes of the Late Devonian Catskill Delta, *in:* The Catskill Delta Donald L. Woodrow and William D. Sevon (Eds.): Geological Society of America, Sp. Paper 201, p. 51-63.

Woodrow, Donald L., and Sevon, William D., 1985, The Catskill Delta (Woodrow and Sevon, eds.): Geological Society of America, Sp. Paper 201, 246 pp.

Younes, A., and Engelder, T., 1999, Fringe cracks: key structures for the interpretation of progressive Alleghanian deformation of the Appalachian Plateau: Geological Society of America Bulletin, v. 111, p. 219-239.

Zhao, M., and Jacobi, R.D., 1997, Formation of regional cross-fold joints in the northern Appalachian Plateau: Journal of Structural Geology, 19, 817-834.

Zenger, Donald H. 1966, Redefinition of the Herkimer Sandstone (Middle Silurian), New York: Geological Society of America Bulletin, v. 77, p. 1159-1166.

APPENDIX 1
REVIEW OF FRACTURE RESEARCH WEST OF THE PRESENT STUDY AREA

The closest fracture field research to Chenango County in the Appalachian Basin includes data from near Binghamton, New York (Engelder and Geiser, 1980). Engelder and Geiser (1980), following earlier studies (e.g., Parker, 1942; Nickelsen and Hough, 1967) established three joint sets in NYS. Set I fractures are approximately orthogonal to the arc of Alleghanian fold and thrust belt, and hence are called “cross-strike” or “cross-fold” fractures. In the farthest eastern outcrops that Engelder and Geiser (1980) analyzed (but still southwest from the present study area), Set I fractures strike NNE.

Set I fractures were divided into Ia and Ib, with orientations less than 30^{o} apart. Set Ib fractures fan across NYS, generally orthogonal to the arc of Alleghanian fold traces (e.g., Engelder and Geiser, 1980). Although Engelder and Geiser (1980) believed that Set 1a fractures “show no evidence of...rotation [and] the strike of the joints maintains parallelism for 100 km before abruptly rotating about 20^{o} to the east” (p. 6334), Engelder and Geiser (1980) also stated that “in general, the mean orientations of... Ia rotate counterclockwise from east to west...” (p. 6323).

Set II fractures are oriented parallel to the Alleghanian fold and thrust belt, and are therefore called “strike-parallel” or “fold-parallel” fractures. In the outcrops closest to the present study area, Engelder and Geiser’s (1980) Set II fractures strike WNW. Engelder and Geiser (1980) believed that a third set of fractures, Set III, have a constant orientation of about N60^{o}E across NYS.

The proposed relationships among these fracture sets have often appeared to be contradictory. Parker (1942) proposed that sets 1a and 1b were a conjugate shear pair, but Nickelsen and Hough (1967) suggested that sets Ia and Ib were *not* a conjugate shear pair because of a lack of evidence for shear and inconsistency in the fracture sets that form the conjugate pair. Based on tenuous relationships among fractures (with essentially no abutting relationships), Engelder and Geiser (1980) proposed that Ia fractures formed prior to sets II and III, during the Alleghanian Orogeny, during the Main Phase of the Alleghanian Orogeny (in which σ_1 was oriented in a generally northerly direction. They thought that Set Ib developed during later uplift, but that “residual strain” remaining from a deformation event that predated the development of Set Ia guided the later growth of Set Ib fractures; i.e., although Set Ib fractures propagated after Set Ia fractures, the Set Ib fractures developed in response to a residual strain from a deformational event that predated the development of Ia fractures. Engelder and Geiser (1980) suggested that Set Ib fractures reflected strain developed during the “Lackawanna Phase” of the Alleghanian Orogeny (in which σ_1 was in a generally NNW direction).

In 1985 Engelder reversed the proposed fracture history of Set I. In the deeper portions of the Devonian Catskill Delta Complex (such as in the present study area), Engelder (1985) now believed that Set Ib fractures developed first and Set Ia fractures and coeval cleavage surfaces developed later. In contrast, in the stratigraphically higher portions of the Catskill Delta Complex (including central and western NYS), Engelder (1985) offered a different story. At one outcrop in Taughannock Falls State Park (which is located on the southwest shore of Cayuga Lake), Set Ia fractures are master to Set Ib fractures, from which Engelder (1985) inferred that Set Ia fractures developed first, during the Main Phase of the Alleghanian Orogeny, and that the Set Ib fractures therefore developed during post-Alleghanian uplift. However, in the same park, Bahat and Engelder (1984) also found Set Ib fractures in siltstones and Set Ia fractures in shales, indicating to Engelder (1985) that Set Ib fractures in the siltstone beds developed first during the Lackawanna Phase, and the Ia joints within the shale beds during the Main Phase. Engelder (1985) concluded that there must have been several times of Set Ib fracture generation (partly because he assumed that Set Ia fractures had a consistent age across the basin). Engelder (1985) maintained that these differences in fracture generation history could be expected, given the different stress histories that resulted from deep burial vs. shallow burial of the Devonian section.

The complexities of the model described above for the generation of Set I fractures were simplified in 1997, when Zhao and Jacobi suggested that the two cross-strike fractures sets resulted from an arcuate stress field (in map view) migrating through the region during the Alleghanian Orogeny. In their model, as the stress field penetrated the Appalachian Basin, stress rotations with the opposite sense-of-rotation would occur at the opposite ends of the arc: counterclockwise in western NYS and clockwise in eastern NYS. In the Finger Lakes region, Younes and Engelder (1999) affirmed that both sets developed during a rotation of the Alleghanian stress field (Engelder et al., 2001), as predicted by the Zhao and Jacobi (1997) model.

Continued detailed fracture studies across western and central NYS since the time of the Zhao and Jacobi (1997) model (e.g., Baudo and Jacobi, 2000; Tober and Jacobi, 2000; Jacobi, 2007) revealed relationships between Set Ia and Ib fractures that conflict with the general Zhao and Jacobi (1997) model. The sense of rotation between Set Ia and Ib can be opposite to the general model, and is commonly inconsistent among local areas. Based on these ubiquitous inconsistencies, Jacobi et al. (2002) suggested that many of the observed cross-strike fracture rotations are not the result of far field regional Alleghanian stress rotations; rather, they are the result of local stress rotations that developed in response to major fault systems. Such local stress rotations could have resulted from faults that were “open” after a stress release or, as suggested by Rawnsley et al. (1998), from perturbations resulting from points of convergence along the fault.

Set II, “strike-parallel”, fractures also have different explanations and proposed timings of development. Engelder and Geiser (1980) suggested that “the most likely time is during the development of folds while the upper beds are above a neutral fiber” (p. 6334). Engelder and Geiser (1980) placed the timing of the folding and fracturing after the generation of Set Ia fractures, but still during the Alleghanian Orogeny. Engelder (1985) suggested that the Set II fractures are release joints that developed during post-Alleghanian uplift, based on their shallow distribution in cored sections (generally < 500m), and that “they are not cut by Alleghanian structures” (p. 468). Because the, Younes and Engelder (1999) questioned whether the ENE-striking fractures resulted from the same stress field, because the rotation inferred from twist hackles on an ENE-striking fracture set remains constant across the Finger Lakes region, whereas the rotation inferred from twist hackles on an cross-strike fracture set does not remain constant. Younes and Engelder (1999) suggest that the fractures developed during tectonic relaxation after the Alleghanian Orogeny.

The maximum horizontal compressive stress of the present stress field is oriented approximately collinearly with the strike of Set III fracture. Engelder (1982, 1985) and Gross and Engelder

(1991) therefore believed that these fractures were neotectonic in origin. However, the offset of Set III fractures along Set I fractures suggested to Engelder et al. (2001) that the Set III fractures are actually Acadian in age, and were caused by "high fluid pressure developed during the burial of the Catskill Delta before the onset of the Alleghanian Orogeny" (p. 40). Lash et al. (2004) concurred with an Acadian age, based on abutting relationships that suggested that the ENE-striking fractures were the oldest, and predated the Alleghanian cross strike fractures. More recently, Engelder and Whitaker (2006) suggested that Set III fractures first began to develop in Late Pennsylvanian time in coal, and Late Pennsylvanian to Permian time in Devonian black shale and other clastics in the Finger Lakes region. To the west in Allegany County, Jacobi and Fountain (1996) found that ENE-striking FIDs (oriented parallel to either Set II or Set III fractures) generally predate the Alleghanian cross-strike Set I fractures.

FIGURE CAPTIONS

Figure 1. Location of Chenango County and field areas, New York State. Chenango County shown in light gray. The northern study area in Chenango County for lineaments and outcrop fractures is shown in dark gray. The southern study area in Chenango County for lineaments and outcrop fractures is shown in blue. The location of the Pyron et al. (2003) study is small yellow STAR in the southern study area. Smithville Flats is located immediately west of the star. Thin red lines are lineaments from EarthSat (1997). Green thick lines are Alleghanian fold axes from Wedel (1932). Short elongate purple blobs in central NYS are selected Trenton/Black River fields. The thick blue line is the approximate limit of Silurian salt. After Jacobi (2002).

Figure 2. Stratigraphic columns and geologic cross section for the Appalachian Basin in central/eastern New York State. A) Cambrian through Middle Devonian (west is on the left; from Smith, unpub., after Rogers et al. 1990). B) Middle and Upper Devonian detailed stratigraphic column for central New York State (after Sevon and Woodrow, 1985). C) Geological cross section for Otsego and eastern Chenango County. The upper panels show the location of the cross section (the E-W red line in the upper right panel), and the lower panel shows the geological cross section based on formation “tops” from wells (well locations shown in the upper right panel). Gray bands in the upper right panel indicate possible fault systems based on Jacobi’s (2002) integration of EarthSat (1997) lineaments with other data sets. (after Jacobi and Smith, 2000).

Figure 3. Fracture distribution in the northern study area and orientation boundaries of the fracture sets. After Terech et al. (2005) and Terech (2006).

Figure 4. Fracture distribution in the southern study area and orientation boundaries of the fracture sets. After McGuire et al. (2006a and b), McGuire (2007)

Figure 5a**.** Explanation of a modified rose diagram. After Jacobi (2007).

Figure 5b. Examples of fracture intersections and their portrayal on the modified rose diagram.

Figure 6a. Comparison of lineament selections on a 1:25,000 DEM by two operators in the northern study area. DEM data from the Cornell University Geospatial Data Information Repository (CUGIR) website (http://cugir.mannlib.cornell.edu). After Terech et al. (2005) and Terech (2006).

Figure 6b.	Comparison of lineament selections by two operators in the southern study area. DEM data from the USGS EROS website (www.seamless.usgs.gov). After McGuire et al. (2006a and b), McGuire (2007).
Figure 7a	Index map displaying locations of field sites and inset maps (Figures 7b to 7q) in the northern study area. For location of the northern study area, see Figure 1. After Terech et al. (2005) and Terech (2006).
Figure 7b	Enlarged Inset Map A of sites with modified rose diagrams. Figure 7a shows the location of the Inset; see Figure 5 for an explanation of modified rose diagrams. After Terech et al. (2005) and Terech (2006).
Figure 7c	Enlarged Inset Map B of sites with modified rose diagrams. Figure 7a shows the location of the Inset; see Figure 5 for an explanation of modified rose diagrams. After Terech et al. (2005) and Terech (2006).
Figure 7d	Enlarged Inset Map C of sites with modified rose diagrams. Figure 7a shows the location of the Inset; see Figure 5 for an explanation of modified rose diagrams. After Terech et al. (2005) and Terech (2006).
Figure 7e.	Enlarged Inset Map D of sites with modified rose diagrams. Figure 7a shows the location of the Inset; see 5 for an explanation of modified rose diagrams. After Terech et al. (2005) and Terech (2006).
Figure 7f.	Enlarged Inset Map E of sites with modified rose diagrams. Figure 7a shows the location of the Inset; see Figure 5 for an explanation of modified rose diagrams. After Terech et al. (2005) and Terech (2006).
Figure 7g.	Enlarged Inset Map F of sites with modified rose diagrams. Figure 7a shows the location of the Inset; see Figure 5 for an explanation of modified rose diagrams. After Terech et al. (2005) and Terech (2006).
Figure 7h.	Enlarged Inset Map G of sites with modified rose diagrams. Figure 7a shows the location of the Inset; see Figure 5 for an explanation of modified rose diagrams. After Terech et al. (2005) and Terech (2006).
Figure 7i.	Enlarged Inset Map H of sites with modified rose diagrams. Figure 7a shows the location of the Inset; see Figure 5 for an explanation of modified rose diagrams. After Terech et al. (2005) and Terech (2006).
Figure 7j.	Enlarged Inset Map I of sites with modified rose diagrams. Figure 7a shows the location of the Inset; see Figure 5 for an explanation of modified rose diagrams. After Terech et al. (2005) and Terech (2006).

Figure 9c.	Enlarged Inset Map 2 of sites with modified rose diagrams. Figure 9a shows the location of the Inset; see Figure 5 for an explanation of modified rose diagrams. After McGuire et al. (2006a and b), McGuire (2007).
Figure 9d.	Enlarged Inset Map 3 of sites with modified rose diagrams. Figure 9a shows the location of the Inset; see Figure 5 for an explanation of modified rose diagrams. After McGuire et al. (2006a and b), McGuire (2007).
Figure 9e.	Enlarged Inset Map 4 of sites with modified rose diagrams. Figure 9a shows the location of the Inset; see Figure 5 for an explanation of modified rose diagrams. After McGuire et al. (2006a and b), McGuire (2007).
Figure 9f.	Enlarged Inset Map 5 of sites with modified rose diagrams. Figure 9a shows the location of the Inset; see Figure 5 for an explanation of modified rose diagrams. After McGuire et al. (2006a and b), McGuire (2007).
Figure 9g.	Enlarged Inset Map 6 of sites with modified rose diagrams. Figure 9a shows the location of the Inset; see Figure 5 for an explanation of modified rose diagrams. After McGuire et al. (2006a and b), McGuire (2007).
Figure 9h.	Enlarged Inset Map 7 of sites with modified rose diagrams. Figure 9a shows the location of the Inset; see Figure 5 for an explanation of modified rose diagrams. After McGuire et al. (2006a and b), McGuire (2007).
Figure 9i.	Enlarged Inset Map 8 of sites with modified rose diagrams. Figure 9a shows the location of the Inset; see Figure 5 for an explanation of modified rose diagrams. After McGuire et al. (2006a and b), McGuire (2007).
Figure 9j.	Enlarged Inset Map 9 of sites with modified rose diagrams. Figure 9a shows the location of the Inset; see Figure 5 for an explanation of modified rose diagrams. After McGuire et al. (2006a and b), McGuire (2007).
Figure 9k.	Enlarged Inset Map 10 of sites with modified rose diagrams. Figure 9a shows the location of the Inset; see Figure 5 for an explanation of modified rose diagrams. After McGuire et al. (2006a and b), McGuire (2007).
Figure 9l.	Enlarged Inset Map 11 of sites with modified rose diagrams. Figure 9a shows the location of the Inset; see Figure 5 for an explanation of modified rose diagrams. After McGuire et al. (2006a and b), McGuire (2007).
Figure 9m.	Enlarged Inset Map 12 of sites with modified rose diagrams. Figure 9a shows the location of the Inset; see Figure 5 for an explanation of modified rose diagrams. After McGuire et al. (2006a and b), McGuire (2007).

Figure 9n. Enlarged Inset Map 13 of sites with modified rose diagrams. Figure 9a shows the location of the Inset; see Figure 5 for an explanation of modified rose diagrams. After McGuire et al. (2006a and b), McGuire (2007).

Figure 10a. Fracture intensification domains (FIDs) observed at sites in the southern study area. Fracture sets with near-FID fracture spacing also shown. Note correspondence between FID trends and trends of valleys.

Figure 10b. Spatial correspondence between fracture intensification domains (FIDs) and nearby topographic features in the southern study area. Ellipses indicate a coincidence between the location and trend of a topographic feature (generally valley) and an FID. Note that all the major valleys have sites nearby with FIDs that trend collinearly with the valley.

Figure 11a. Master/abutting orientations for fracture intersections in the northern study area. Circled relationships indicate that at least three such relationships occur within the study area. After Terech et al. (2005) and Terech (2006).

Figure 11b. Master/abutting orientations for fracture intersections in the southern study area. Circled clusters discussed in text. After McGuire et al. (2006a and b), McGuire (2007).

Figure 11c. Sequence of fracture generation in the northern study area, based on master-abutting relationships. Arrows indicate that mutually abutting relationships are common between the specified fracture sets. After Terech et al. (2005) and Terech (2006).

Figure 11d. General fracture history for the southern study area portrayed in a schematic "stick" diagram. Small numbers in a ratio at intersection indicate the number of intersections observed as portrayed (numerator) vs. the number of intersections observed with the opposite relationship. Large numbers in parentheses indicate the relative order of first appearance of the fracture sets, based on abutting relationships. A "+" symbol indicates that the fracture set is younger than the associated number, but no intersections allow determination of how much younger relative to other younger sets

Figure 12. Scatter plot of bed thickness versus fracture frequency. The dotted red line represents a 1:1 relationship. Note that the fracture spacings display little relationship to bedding thickness, except that most fracture spacings are greater than the bedding thickness (lie to the right of the 1:1 relationship curve). After Terech et al. (2005) and Terech (2006).

Figure 13. Lineaments identified on a 1:25,000 scale DEM of the northern study area. DEM data from the Cornell University Geospatial Data Information Repository (CUGIR) website (http://cugir.mannlib.cornell.edu). After Terech et al. (2005) and Terech (2006).

TABLE CAPTIONS

Table 1. Simplified Probabilistic Analysis of NS-striking ILZs for the northern study area. For each numbered ILZ, each lineament from a different source (e.g. aeromagnetics) and FID of appropriate trend that fall in the ILZ buffer is assigned a value of 1.0, except for FIDs with a strike that is near to, but outside, the range for N-trending lineaments. The maximum value that a N-trending ILZ can receive is 6.5. High scores confirm the presence of the ILZ and suggest that the lineament reflects structure. Table from Terech et al. (2005) and Terech (2006)

Table 2. Fracture set orientations in the northern study area. After Terech et al. (2005) and Terech (2006).

Table 3. Fracture sets in the southern study area: orientation boundaries, number of fractures in each set, average strike and standard deviation from average strike. After McGuire et al. (2006a and b), McGuire (2007).

Table 4. Master Abutting relationship scores for fractures in the southern study area. Each orientation set is given a score of 1 for each intersection where a fracture of that set is master. The rows across establish the number of master fractures for a particular set. The columns down establish the number of abutting fractures within a particular set. After McGuire et al. (2006a and b), McGuire (2007).

Table 5. Comparison among Lineament Zone orientation sets in the northern study area identified from a 1:25,000 DEM, sites in the Lineament Zones, and the number of sites with appropriately oriented FIDs. After Terech et al. (2005) and Terech (2006).

Table 6. Comparison among Lineament Zone orientation sets in the northern study area identified from a 1:250,000 DEM, sites in the Lineament Zones, and the number of sites with appropriately oriented FIDs. After Terech et al. (2005) and Terech (2006).

Table 7. Comparison among Lineament Zone orientation sets in the northern study area identified from a Slope Aspect Map, sites in the Lineament Zones, and appropriately oriented FIDs. After Terech et al. (2005) and Terech (2006).

Table 8. Comparison among Lineament Zone orientation sets in the northern study area identified by EarthSat (1997), sites in the Lineament Zones, and appropriately oriented FIDs. After Terech et al. (2005) and Terech (2006).

Table 9. Comparison among Lineament Zone orientation sets in the northern study area identified from aeromagnetic gradients, sites in the Lineament Zones, and appropriately oriented FIDs. After Terech et al. (2005) and Terech (2006).

Table 10. Simplified Probabilistic Analysis of NNE-striking ILZs for the northern study area. For each numbered ILZ, each lineament from a different source (e.g. aeromagnetics) and FID of appropriate trend that fall in the ILZ buffer is assigned a value of 1.0, except for FIDs with a strike that is near to, but outside, the range for NNE-trending lineaments. The maximum value that a N-trending ILZ can receive is 6.5. High scores confirm the presence of the ILZ and suggest that the lineament reflects structure. Table from Terech et al. (2005) and Terech (2006)

Table 11. Simplified Probabilistic Analysis of WNW-striking ILZs for the northern study area. For each numbered ILZ, each lineament from a different source (e.g. aeromagnetics) and FID of appropriate trend that fall in the ILZ buffer is assigned a value of 1.0, except for FIDs with a strike that is near to, but outside, the range for WNW-trending lineaments. The maximum value that a N-trending ILZ can receive is 6.5. High scores confirm the presence of the ILZ and suggest that the lineament reflects structure. Table from Terech et al. (2005) and Terech (2006)

Table 12. Simplified Probabilistic Analysis of ENE-striking ILZs for the northern study area. For each numbered ILZ, each lineament from a different source (e.g. aeromagnetics) and FID of appropriate trend that fall in the ILZ buffer is assigned a value of 1.0, except for FIDs with a strike that is near to, but outside, the range for ENE-trending lineaments. The maximum value that a N-trending ILZ can receive is 6.5. High scores confirm the presence of the ILZ and suggest that the lineament reflects structure. Table from Terech et al. (2005) and Terech (2006)

Table 13. Simplified Probabilistic Analysis of NW-striking ILZs for the northern study area. For each numbered ILZ, each lineament from a different source (e.g. aeromagnetics) and FID of appropriate trend that fall in the ILZ buffer is assigned a value of 1.0, except for FIDs with a strike that is near to, but outside, the range for NW-trending lineaments. The maximum value that a N-trending ILZ can receive is 6.5. High scores confirm the presence of the ILZ and suggest that the lineament reflects structure. Table from Terech et al. (2005) and Terech (2006)

Table 14. Simplified Probabilistic Analysis of EW-striking ILZs for the northern study area. For each numbered ILZ, each lineament from a different source (e.g. aeromagnetics) and FID of appropriate trend that fall in the ILZ buffer is assigned a value of 1.0, except for FIDs with a strike that is near to, but outside, the range for EW-trending lineaments. The maximum value that a N-trending ILZ can receive is 6.5. High scores confirm the presence of the ILZ and suggest that the lineament reflects structure. Table from Terech et al. (2005) and Terech (2006)

Table 15a Contrast Values for 1:25,000 Scale DEM lineaments (northern study area) and appropriately-oriented fractures with frequencies greater than 0.0 fractures/meter. From Terech et al. (2005) and Terech (2006).

Table 15b. Contrast Values for 1:25,000 Scale DEM lineaments (northern study area) and appropriately-oriented fractures with frequencies greater than 2.0 fractures/meter. From Terech et al. (2005) and Terech (2006).

Table 15c. Contrast Values for 1:25,000 Scale DEM lineaments (northern study area) and appropriately-oriented fractures with frequencies greater than 4.0 fractures/meter (FIDs). From Terech et al. (2005) and Terech (2006).

Table 16. Simplified Probabilistic Analysis of NNE-trending ILZs for the southern study area. For each numbered ILZ, each lineament from a different source (e.g. aeromagnetics) and FID of appropriate trend that fall in the ILZ buffer is assigned a value of 1.0, except for FIDs with a strike that is near to, but outside, the range for NNE-trending lineaments. The maximum value that a N-trending ILZ can receive is 4.0. High scores confirm the presence of the ILZ and suggest that the lineament reflects structure. From McGuire et al. (2006a and b), McGuire (2007).

Table 17. Simplified Probabilistic Analysis of N-trending ILZs for the southern study area. For each numbered ILZ, each lineament from a different source (e.g. aeromagnetics) and FID of appropriate trend that fall in the ILZ buffer is assigned a value of 1.0, except for FIDs with a strike that is near to, but outside, the range for N-trending lineaments. The maximum value that a N-trending ILZ can receive is 4.0. High scores confirm the presence of the ILZ and suggest that the lineament reflects structure. From McGuire et al. (2006a and b), McGuire (2007).

Table 18. Simplified Probabilistic Analysis of E-trending ILZs for the southern study area. For each numbered ILZ, each lineament from a different source (e.g. aeromagnetics) and FID of appropriate trend that fall in the ILZ buffer is assigned a value of 1.0, except for FIDs with a strike that is near to, but outside, the range for E-trending lineaments. The maximum value that a N-trending ILZ can receive is 4.0. High scores confirm the presence of the ILZ and suggest that the lineament reflects structure. From McGuire et al. (2006a and b), McGuire (2007).

Table 19. Simplified Probabilistic Analysis of NE-trending ILZs for the southern study area. For each numbered ILZ, each lineament from a different source (e.g. aeromagnetics) and FID of appropriate trend that fall in the ILZ buffer is assigned a value of 1.0, except for FIDs with a strike that is near to, but outside, the range for NE-trending lineaments. The maximum value that a N-trending ILZ can receive is 4.0. High scores confirm the presence of the ILZ and suggest that the lineament reflects structure. From McGuire et al. (2006a and b), McGuire (2007).

Table 20. Simplified Probabilistic Analysis of NNW trending Integrated Lineament Zones for the southern study area. For each numbered ILZ, each lineament from a different source (e.g. aeromagnetics) and FID of appropriate trend that fall in the ILZ buffer is assigned a value of 1.0, except for FIDs with a strike that is near to, but outside, the range for NNW-trending lineaments. The maximum value that a N-trending ILZ can receive is 4.0. High scores confirm the presence of the ILZ

and suggest that the lineament reflects structure. From McGuire et al. (2006a and b), McGuire (2007).

Table 21. Simplified Probabilistic Analysis of WNW trending Integrated Lineament Zones for the southern study area. For each numbered ILZ, each lineament from a different source (e.g. aeromagnetics) and FID of appropriate trend that fall in the ILZ buffer is assigned a value of 1.0, except for FIDs with a strike that is near to, but outside, the range for WNW-trending lineaments. The maximum value that a N-trending ILZ can receive is 4.0. High scores confirm the presence of the ILZ and suggest that the lineament reflects structure. From McGuire et al. (2006a and b), McGuire (2007).

Table 22. Simplified Probabilistic Analysis of NW trending Integrated Lineament Zones for the southern study area. For each numbered ILZ, each lineament from a different source (e.g. aeromagnetics) and FID of appropriate trend that fall in the ILZ buffer is assigned a value of 1.0, except for FIDs with a strike that is near to, but outside, the range for WNW-trending lineaments. The maximum value that a NW-trending ILZ can receive is 4.0. High scores confirm the presence of the ILZ and suggest that the lineament reflects structure. From McGuire et al. (2006a and b), McGuire (2007).

Table 23. Simplified Probabilistic Analysis of ENE-trending Integrated Lineament Zones for the southern study area. For each numbered ILZ, each lineament from a different source (e.g. aeromagnetics) and FID of appropriate trend that fall in the ILZ buffer is assigned a value of 1.0, except for FIDs with a strike that is near to, but outside, the range for WNW-trending lineaments. The maximum value that a ENE-trending ILZ can receive is 4.0. High scores confirm the presence of the ILZ and suggest that the lineament reflects structure. From McGuire et al. (2006a and b), McGuire (2007).

Table 24. Weights of evidence calculated for DEM lineaments and sites that have appropriately-oriented fractures with a fracture frequency of 2-4 fractures/meter in the southern study area. From McGuire et al. (2006a and b), McGuire (2007).

Table 25. Weights of evidence calculated for DEM lineaments and sites that have appropriately-oriented fractures with a fracture frequency of 4 or more fractures/meter in the southern study area. From McGuire et al. (2006a and b), McGuire (2007).

Table 26. Weights of evidence calculated for EarthSat (1997) lineaments and sites that have appropriately-oriented fractures with a fracture frequency of 2-4 fractures/meter in the southern study area. From McGuire et al. (2006a and b), McGuire (2007).

Table 27. Weights of evidence calculated from EarthSat (1997) lineaments and sites that have appropriately-oriented FIDs (fractures with a fracture frequency of 4 or more

fractures/meter) in the southern study area. From McGuire et al. (2006a and b), McGuire (2007).

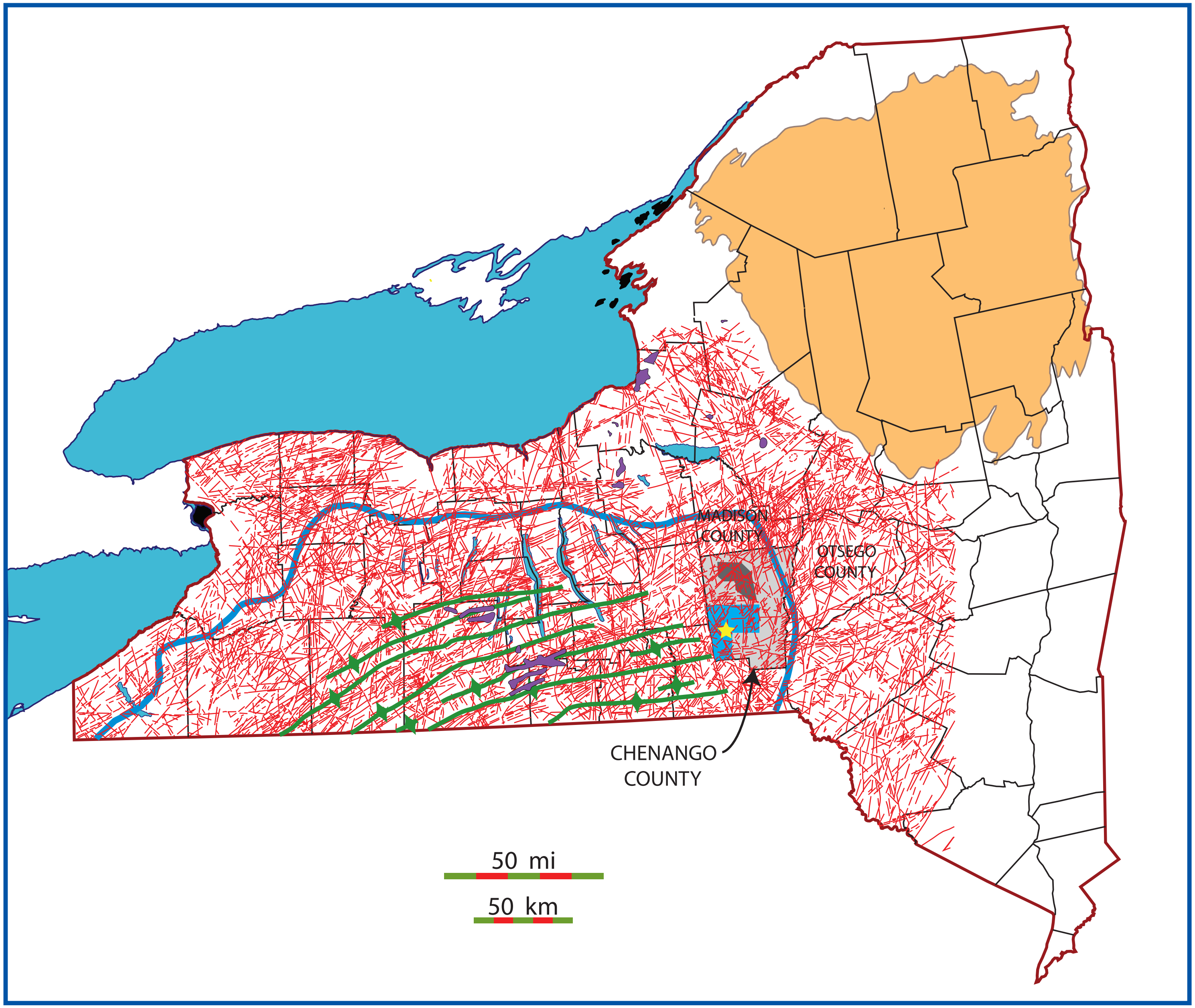

Figure 1

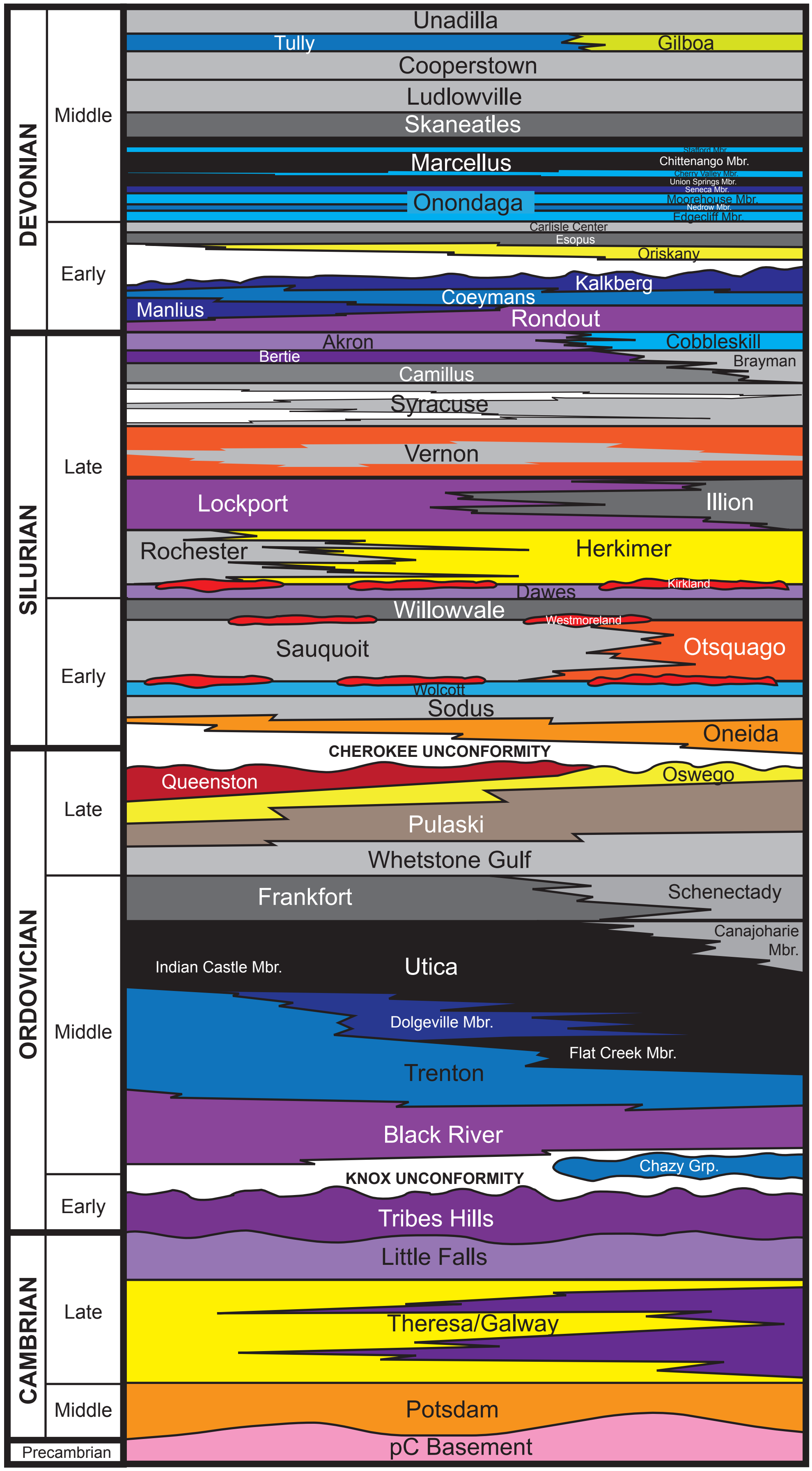
DEVONIAN
Middle
Early
SILURIAN
Late
Early
ORDOVICIAN
Late
Middle
Early
CAMBRIAN
Late
Middle
Precambrian
Unadilla
Tully
Gilboa
Cooperstown
Ludlowville
Skaneatles
Stafford Mbr.
Marcellus
Chittenango Mbr.
Cherry Valley Mbr.
Union Springs Mbr.
Seneca Mbr.
Onondaga
Moorehouse Mbr.
Nedrow Mbr.
Edgecliff Mbr.
Carlisle Center
Esopus
Oriskany
Kalkberg
Coeymans
Manlius
Rondout
Akron
Cobbleskill
Bertie
Brayman
Camillus
Syracuse
Vernon
Lockport
Illion
Rochester
Herkimer
Kirkland
Dawes
Willowvale
Westmoreland
Sauquoit
Otsquago
Wolcott
Sodus
Oneida
CHEROKEE UNCONFORMITY
Queenston
Oswego
Pulaski
Whetstone Gulf
Frankfort
Schenectady
Canajoharie Mbr.
Indian Castle Mbr.
Utica
Dolgeville Mbr.
Flat Creek Mbr.
Trenton
Black River
Chazy Grp.
KNOX UNCONFORMITY
Tribes Hills
Little Falls
Theresa/Galway
Potsdam
pC Basement

Figure 2a

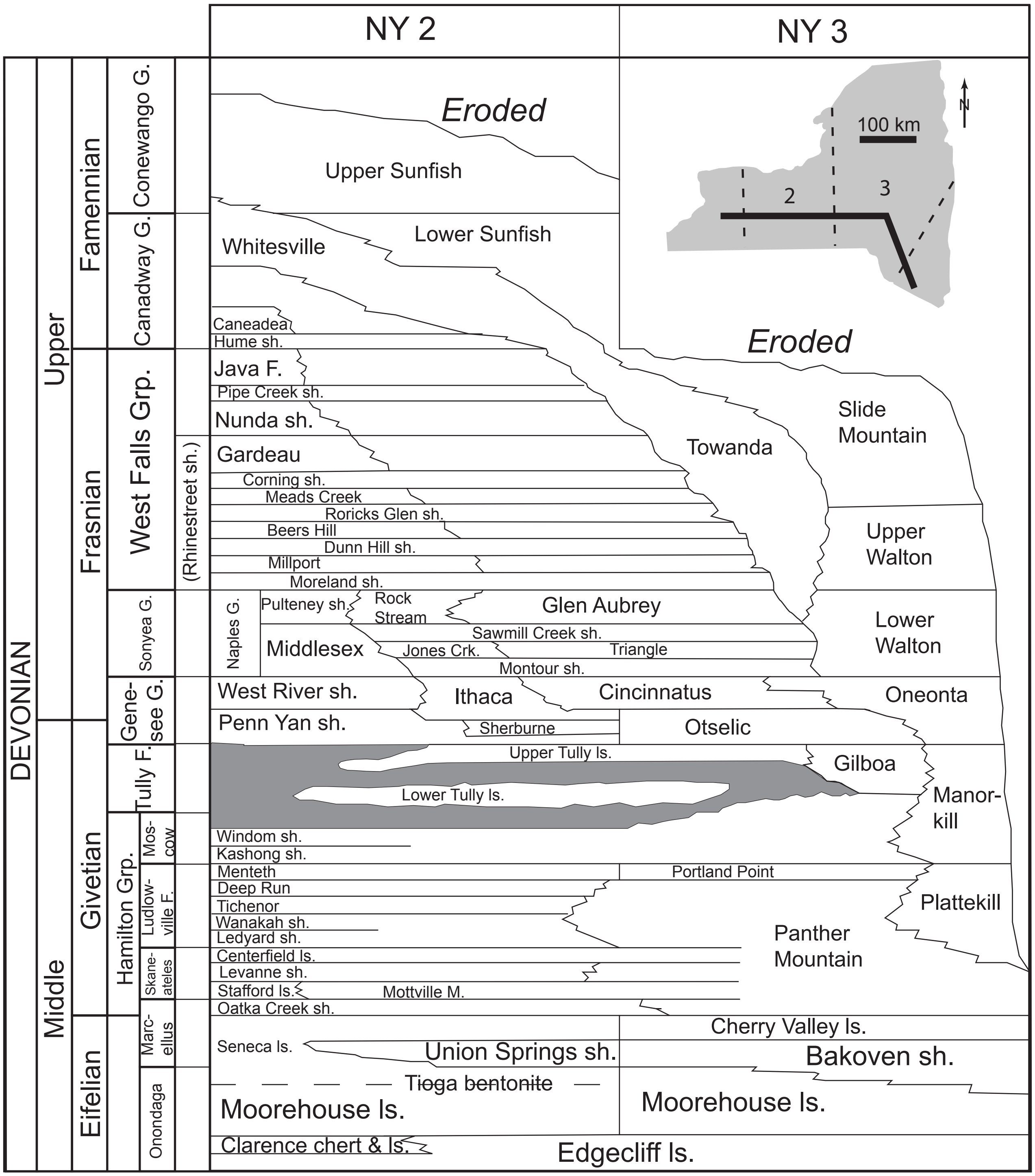
NY 2
NY 3
DEVONIAN
Upper
Middle
Famennian
Frasnian
Givetian
Eifelian
Conewango G.
Canadway G.
West Falls Grp.
Sonyea G.
Gene-see G.
Tully F.
Hamilton Grp.
Mos-cow
Ludlow-ville F.
Skane-ateles
Marc-ellus
Onondaga
(Rhinestreet sh.)
Naples G.
Eroded
Upper Sunfish
Lower Sunfish
Whitesville
Caneadea
Hume sh.
Java F.
Pipe Creek sh.
Nunda sh.
Gardeau
Corning sh.
Meads Creek
Roricks Glen sh.
Beers Hill
Dunn Hill sh.
Millport
Moreland sh.
Pulteney sh.
Rock Stream
Glen Aubrey
Middlesex
Sawmill Creek sh.
Jones Crk.
Triangle
Montour sh.
West River sh.
Ithaca
Cincinnatus
Oneonta
Penn Yan sh.
Sherburne
Otselic
Upper Tully ls.
Gilboa
Lower Tully ls.
Manor-kill
Windom sh.
Kashong sh.
Menteth
Portland Point
Deep Run
Tichenor
Wanakah sh.
Ledyard sh.
Plattekill
Panther Mountain
Centerfield ls.
Levanne sh.
Stafford ls.
Mottville M.
Oatka Creek sh.
Cherry Valley ls.
Seneca ls.
Union Springs sh.
Bakoven sh.
Tioga bentonite
Moorehouse ls.
Moorehouse ls.
Clarence chert & ls.
Edgecliff ls.
Eroded
Towanda
Slide Mountain
Upper Walton
Lower Walton
100 km
N
2
3

Figure 2b

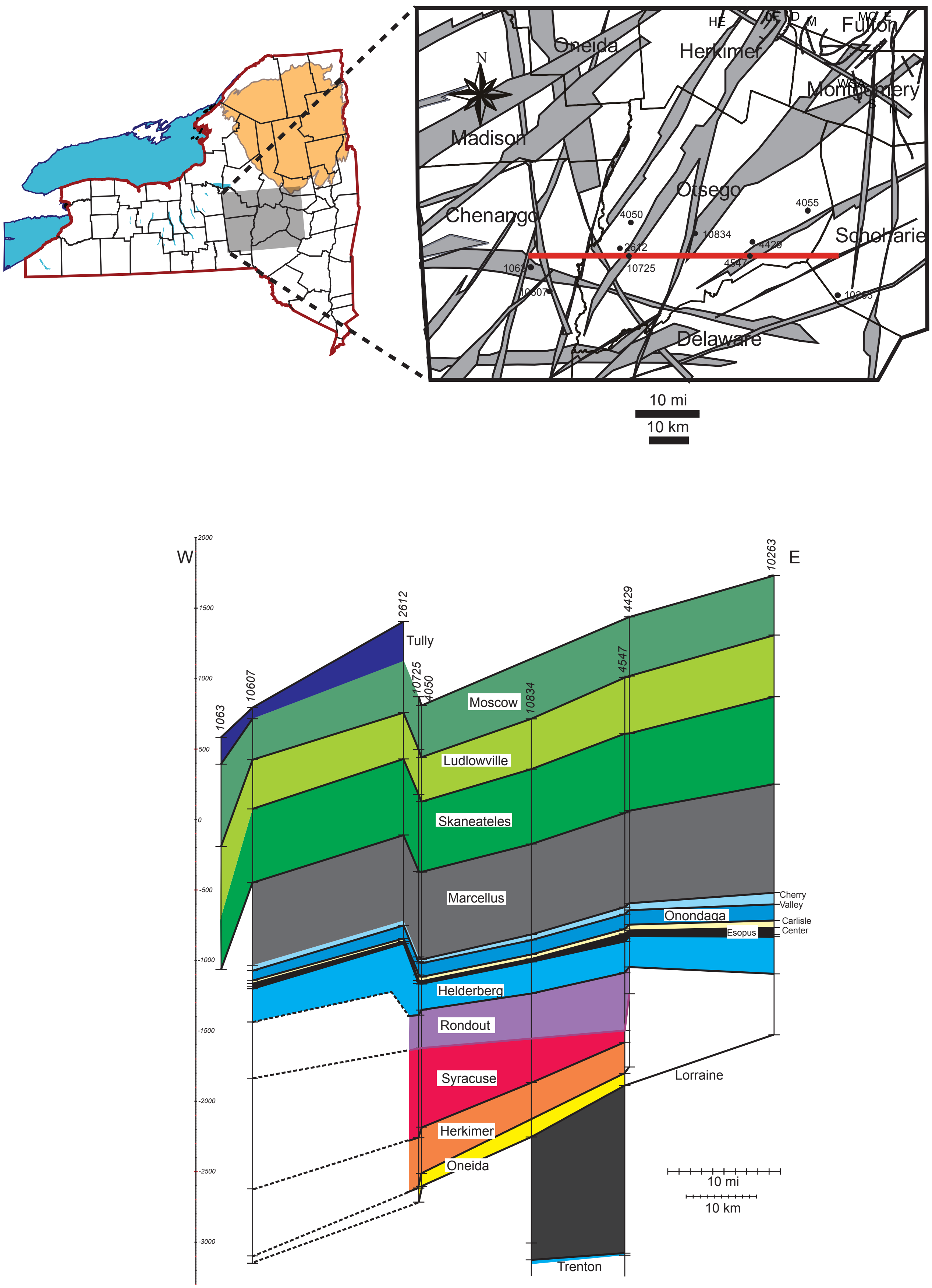
Oneida
Herkimer
Fulton
Montgomery
Madison
Otsego
Chenango
Schoharie
Delaware
N
10 mi
10 km
W
E
Tully
Moscow
Ludlowville
Skaneateles
Marcellus
Cherry Valley
Onondaga
Carlisle Center
Esopus
Helderberg
Rondout
Syracuse
Herkimer
Oneida
Lorraine
Trenton
1063
10607
2612
10725
4050
10834
4547
4429
10263

FIGURE 2C

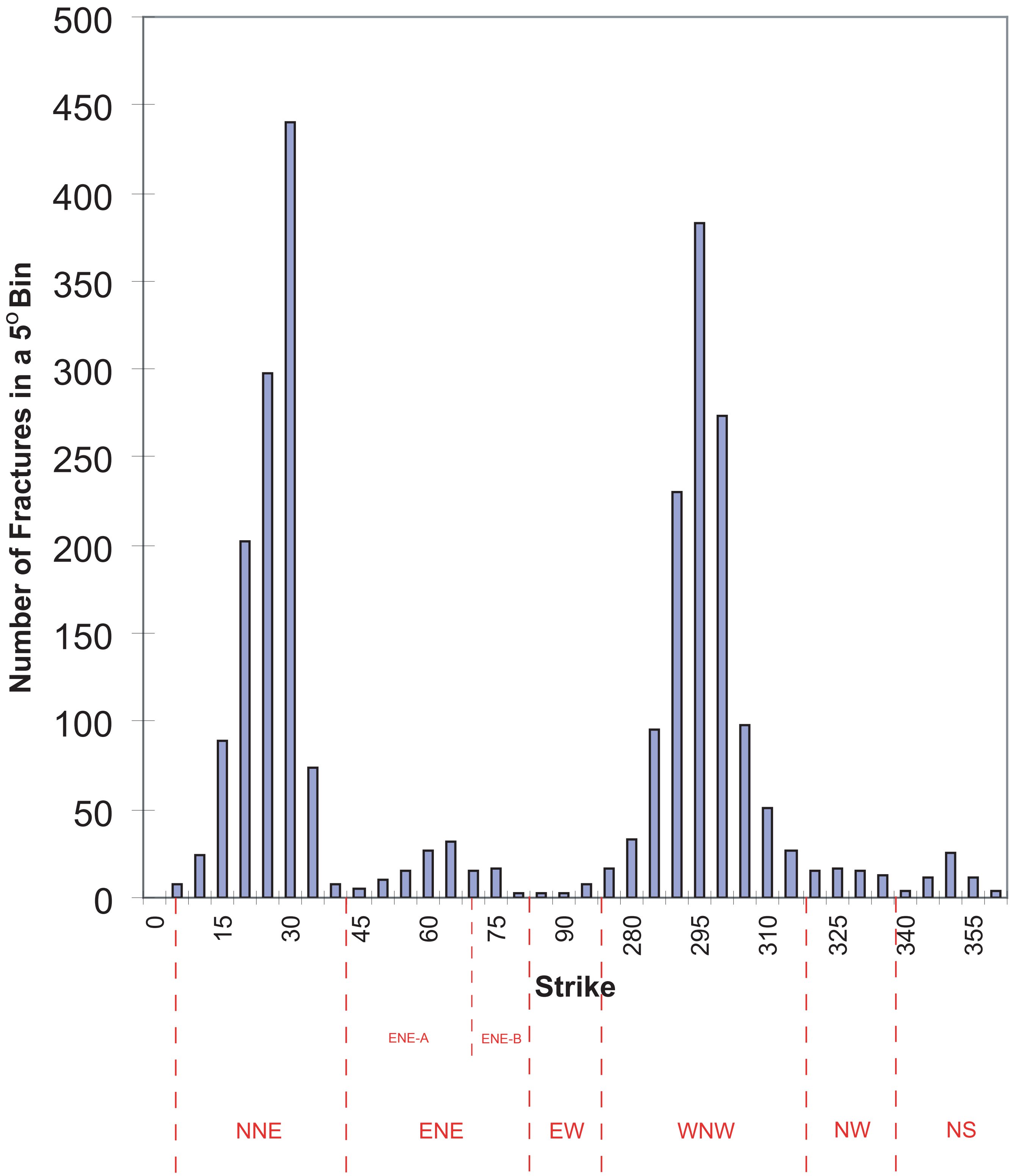
Number of Fractures in a 5° Bin
500
450
400
350
300
250
200
150
100
50
0
0
15
30
45
60
75
90
280
295
310
325
340
355
Strike
ENE-A
ENE-B
NNE
ENE
EW
WNW
NW
NS

Figure 3

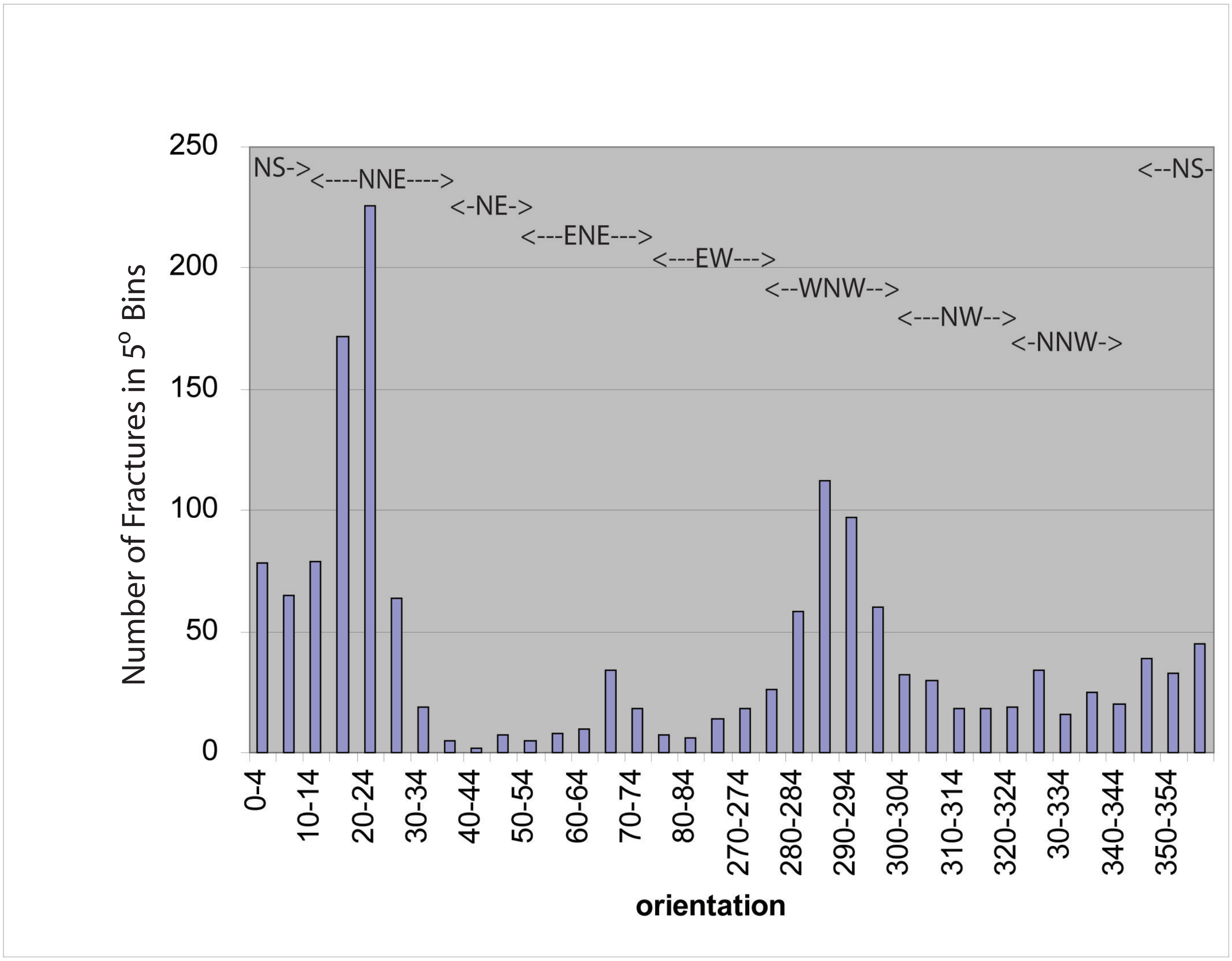

250
200
150
100
50
0
Number of Fractures in 5° Bins
NS->
<----NNE---->
<-NE->
<---ENE--->
<---EW--->
<--WNW-->
<---NW-->
<-NNW->
<--NS-
0-4
10-14
20-24
30-34
40-44
50-54
60-64
70-74
80-84
270-274
280-284
290-294
300-304
310-314
320-324
30-334
340-344
350-354
orientation

Figure 4

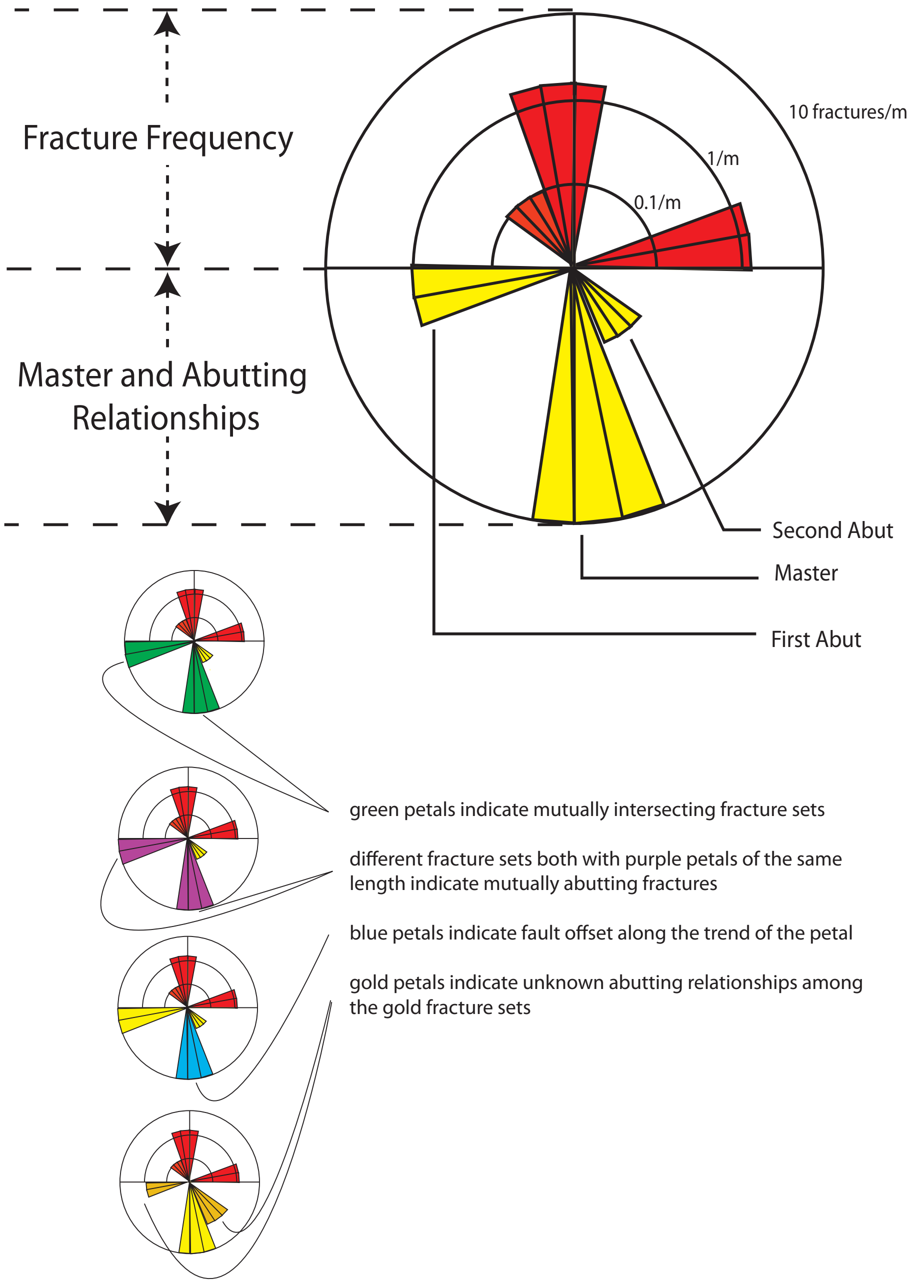
Fracture Frequency
Master and Abutting Relationships
10 fractures/m
1/m
0.1/m
Second Abut
Master
First Abut
green petals indicate mutually intersecting fracture sets
different fracture sets both with purple petals of the same length indicate mutually abutting fractures
blue petals indicate fault offset along the trend of the petal
gold petals indicate unknown abutting relationships among the gold fracture sets

Figure 5a

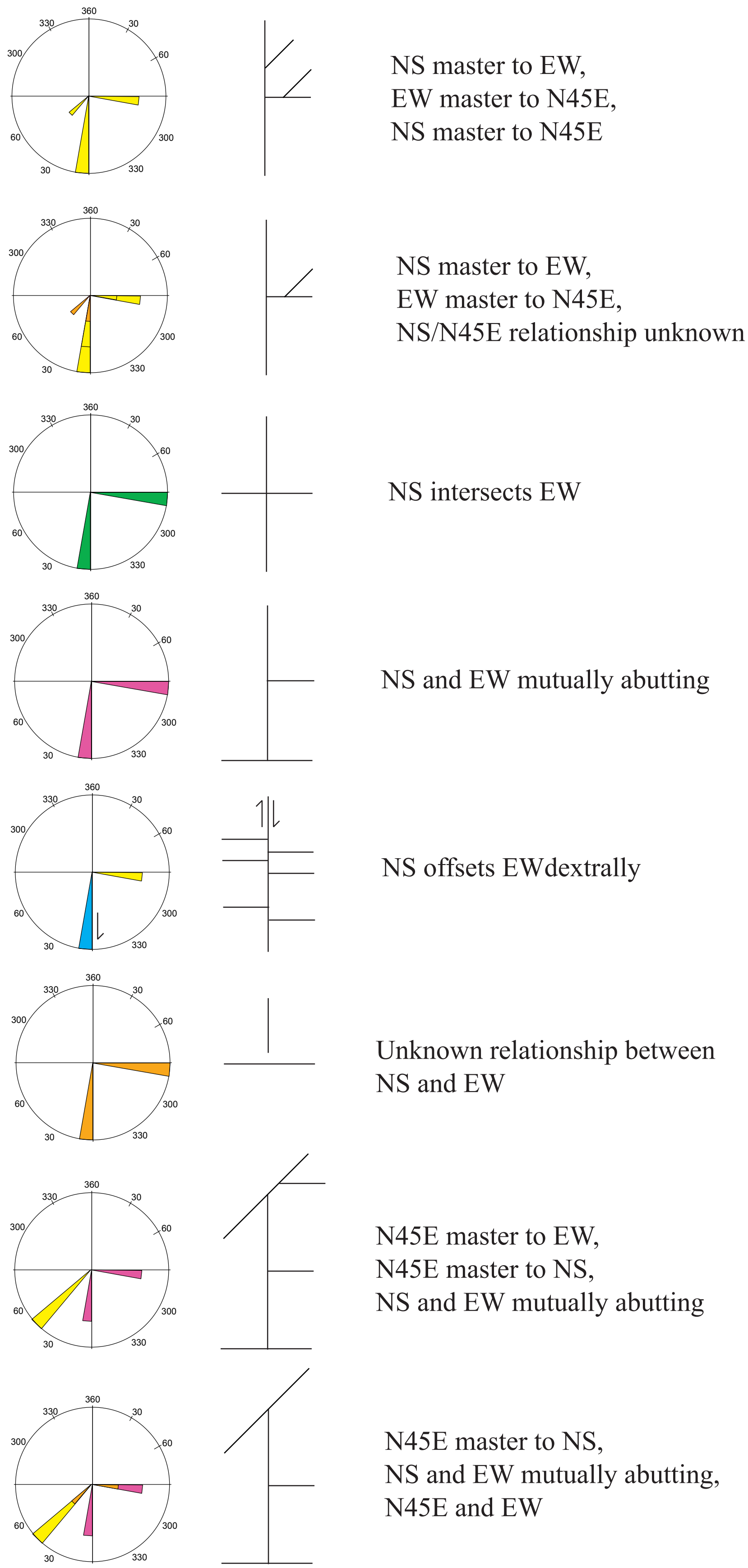
NS master to EW,
EW master to N45E,
NS master to N45E
NS master to EW,
EW master to N45E,
NS/N45E relationship unknown
NS intersects EW
NS and EW mutually abutting
NS offsets EWdextrally
Unknown relationship between
NS and EW
N45E master to EW,
N45E master to NS,
NS and EW mutually abutting
N45E master to NS,
NS and EW mutually abutting,
N45E and EW

Figure 5b

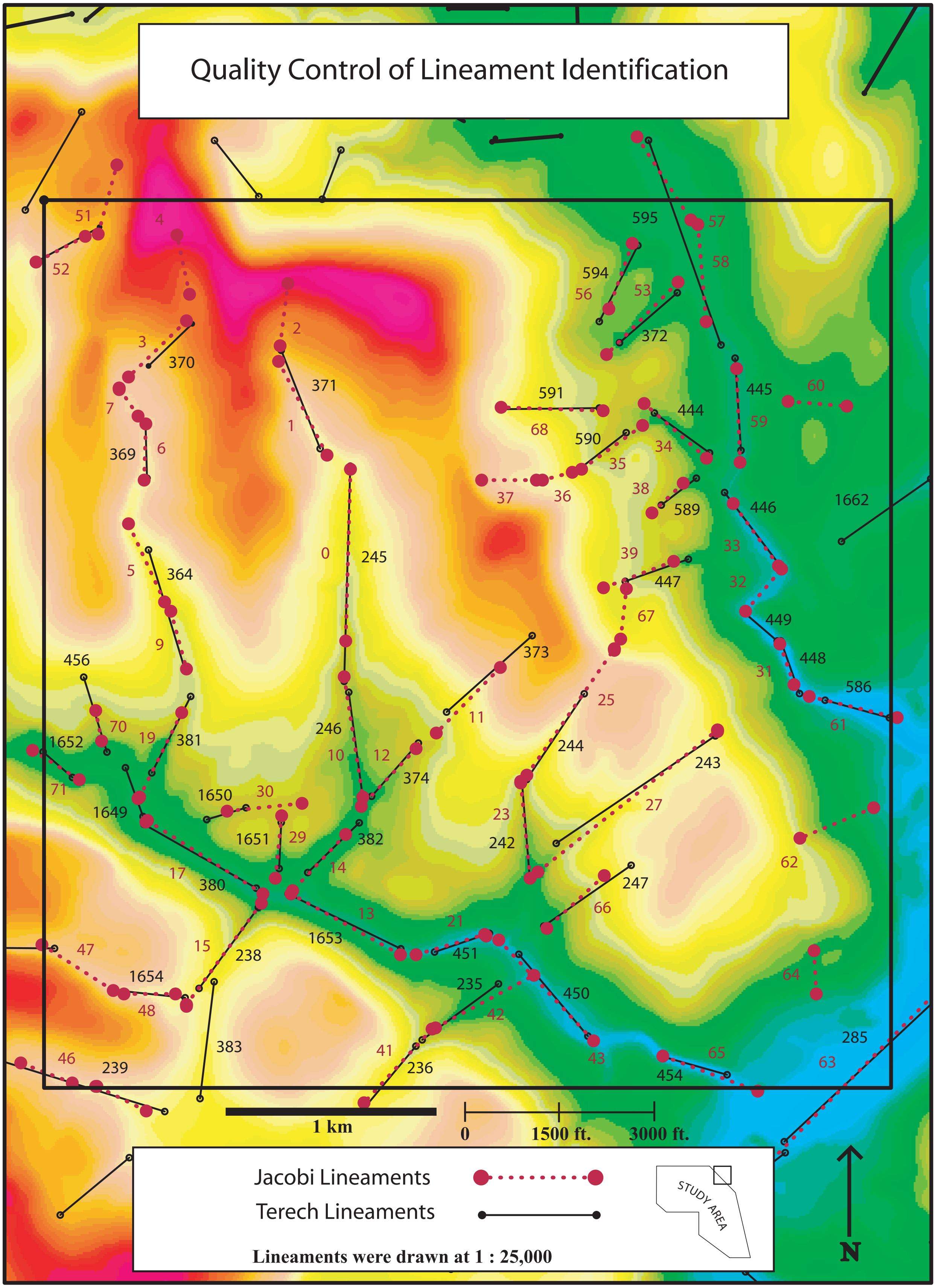

Quality Control of Lineament Identification
1 km
0
1500 ft.
3000 ft.
Jacobi Lineaments
Terech Lineaments
Lineaments were drawn at 1 : 25,000
STUDY AREA
N

Figure 6a


J1
J2
J3
J4
J5
K3
J6
J7
K4
J11
J12
J13
K5
K2
J9
K1
J10
J17
J16
J21
J8
K6
J14
K9
K7
K8
J21
J19
J20
J15
K14
K10
K13
K12
J29
J30
K11
J31
K18
J23
J28
J22
J26
J26
J27
K17
K16
K15
J24
J38
K19
J36
J32
J33
K20
J37
J35
J34
J44
J39
J42
K21
J41
J45
J43
J54
K22
J50
J47
J40
J49
J51
J48
K24
J46
J52
K25
J56
K23
J53
J55
K26
J59
J57
J58
J60
J64
J61
J62
J63
0
2KM

Figure 6b

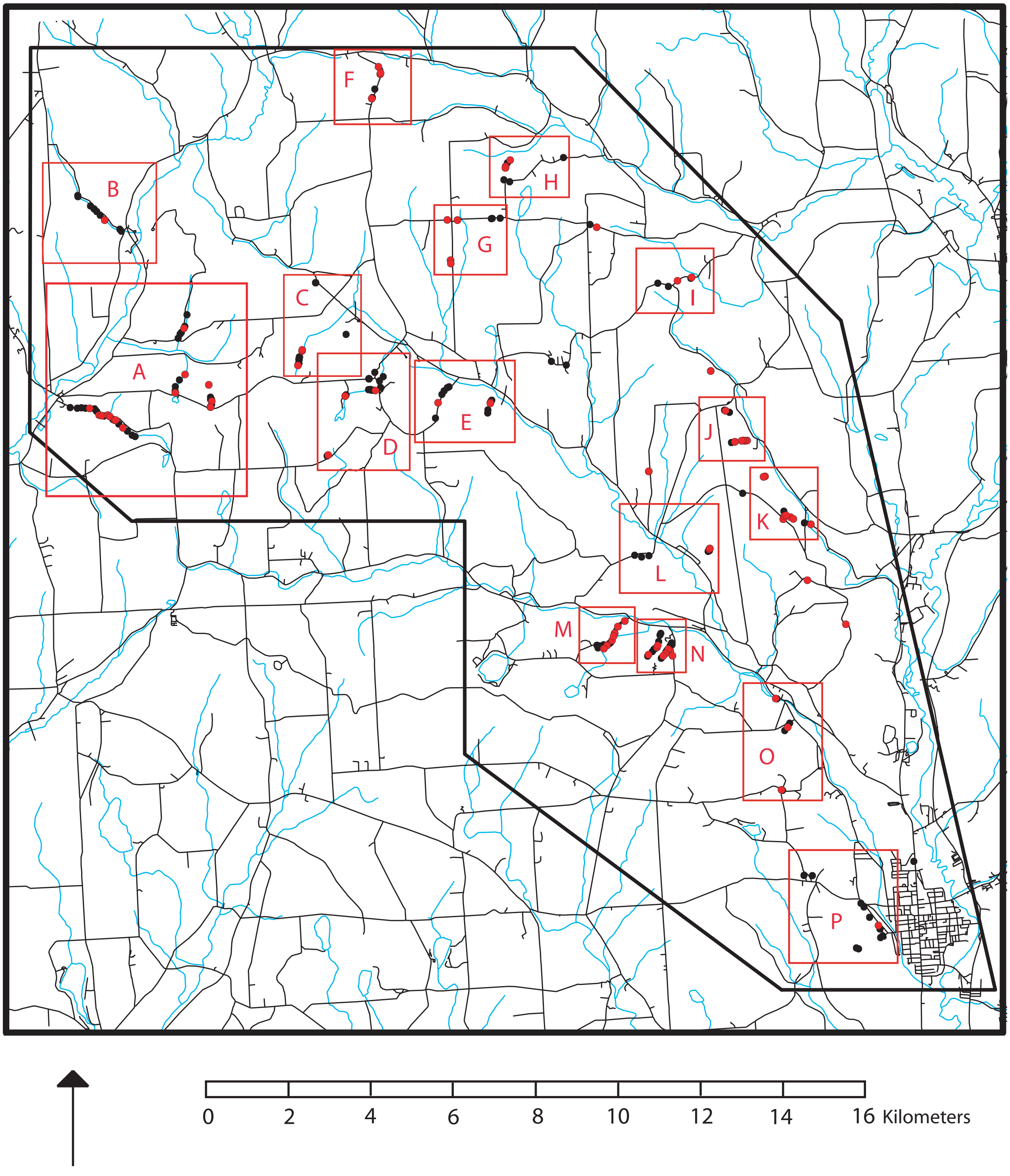

Figure 7a

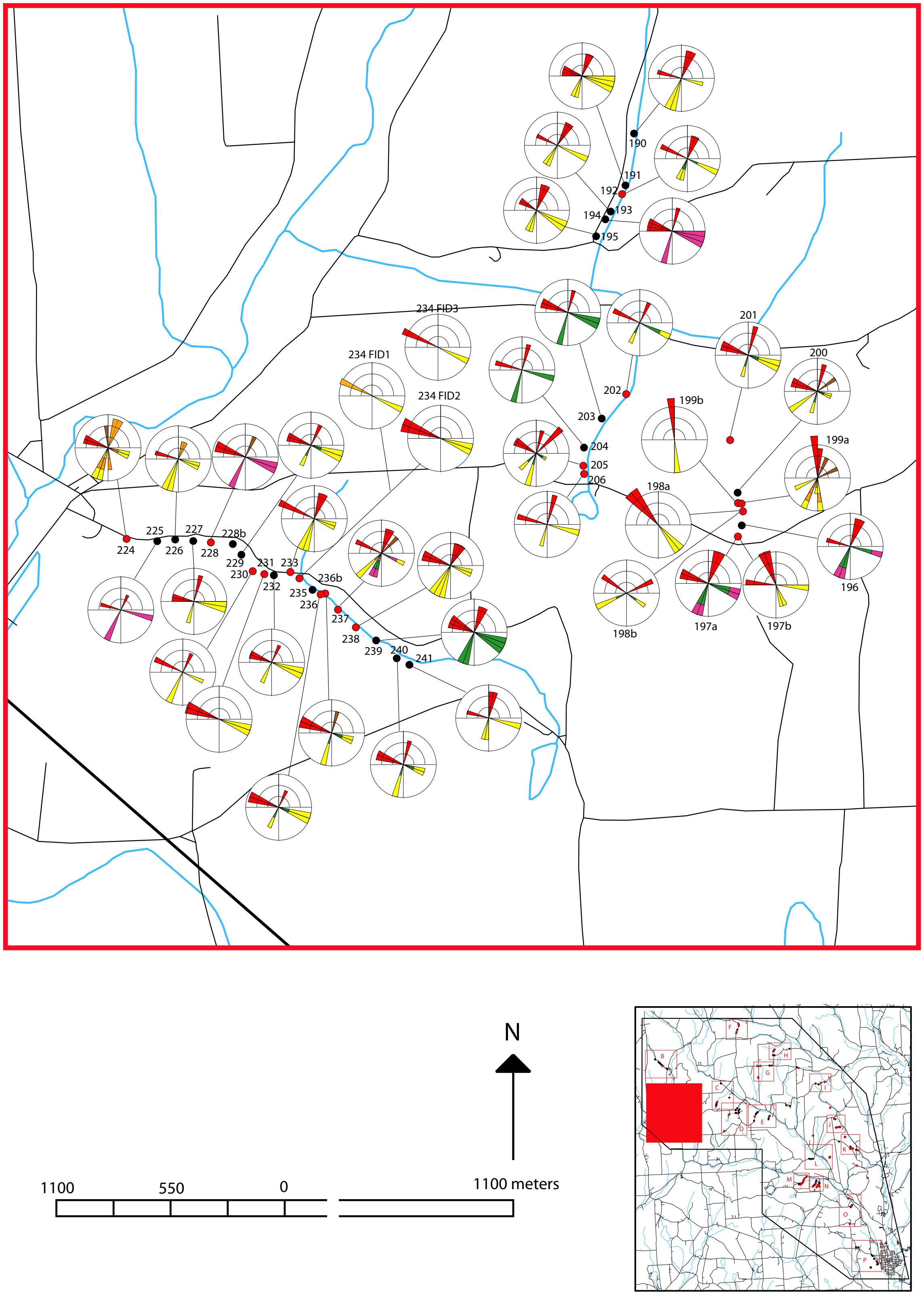

190
191
192
193
194
195
196
197a
197b
198a
198b
199a
199b
200
201
202
203
204
205
206
224
225
226
227
228
228b
229
230
231
232
233
235
236
236b
237
238
239
240
241
234 FID1
234 FID2
234 FID3
N
1100
550
0
1100 meters

Figure 7b

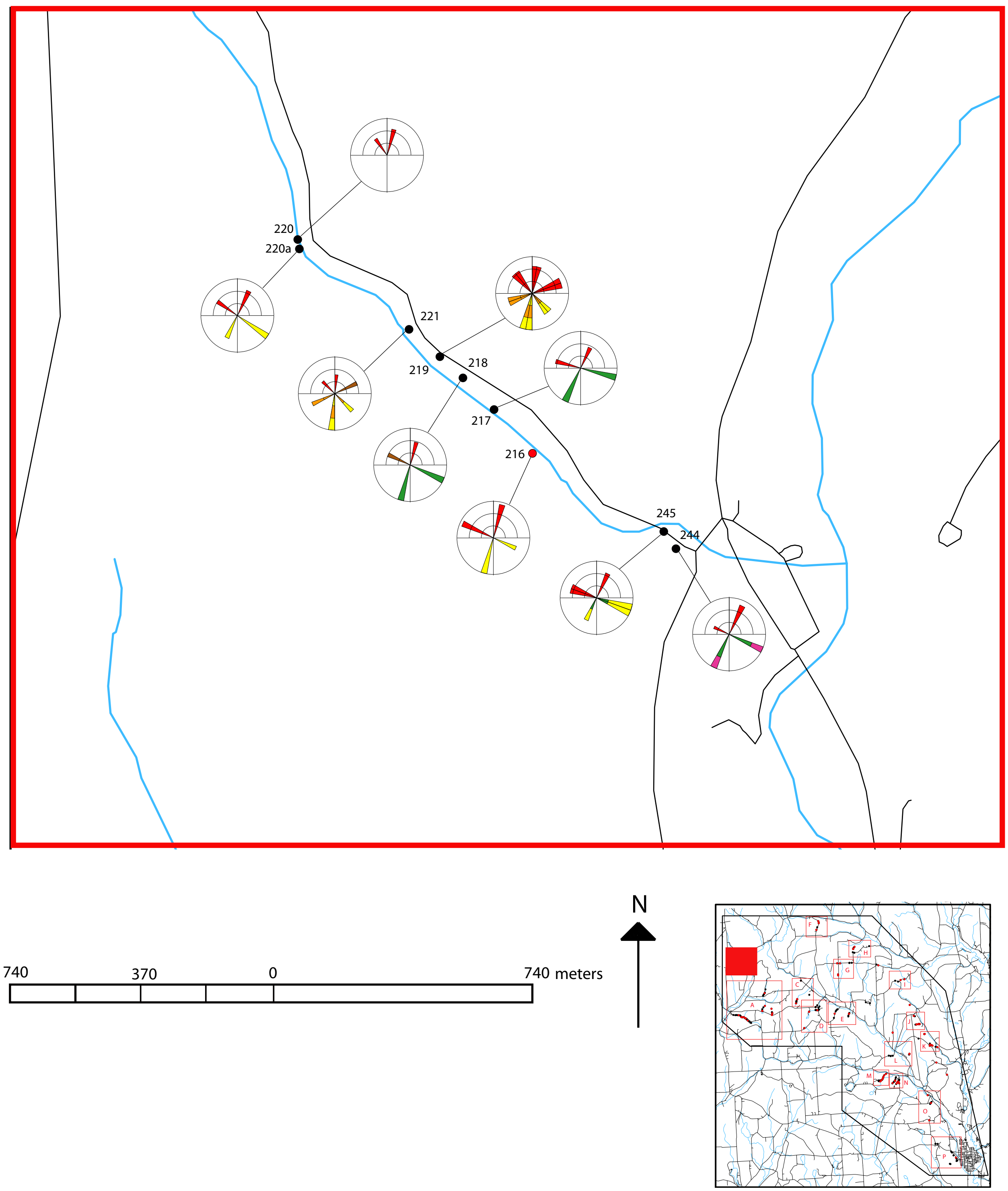

Figure 7c

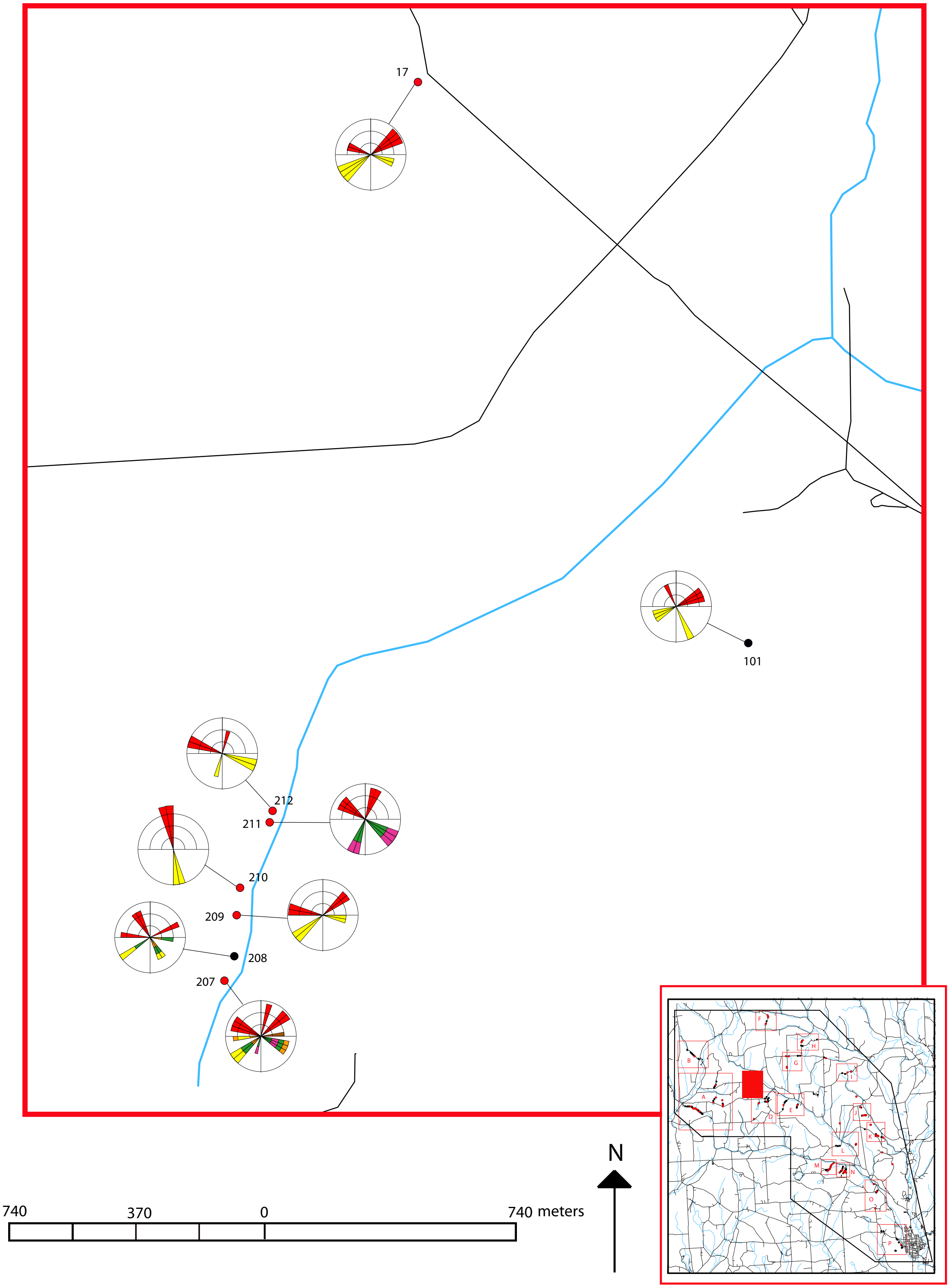

Figure 7d

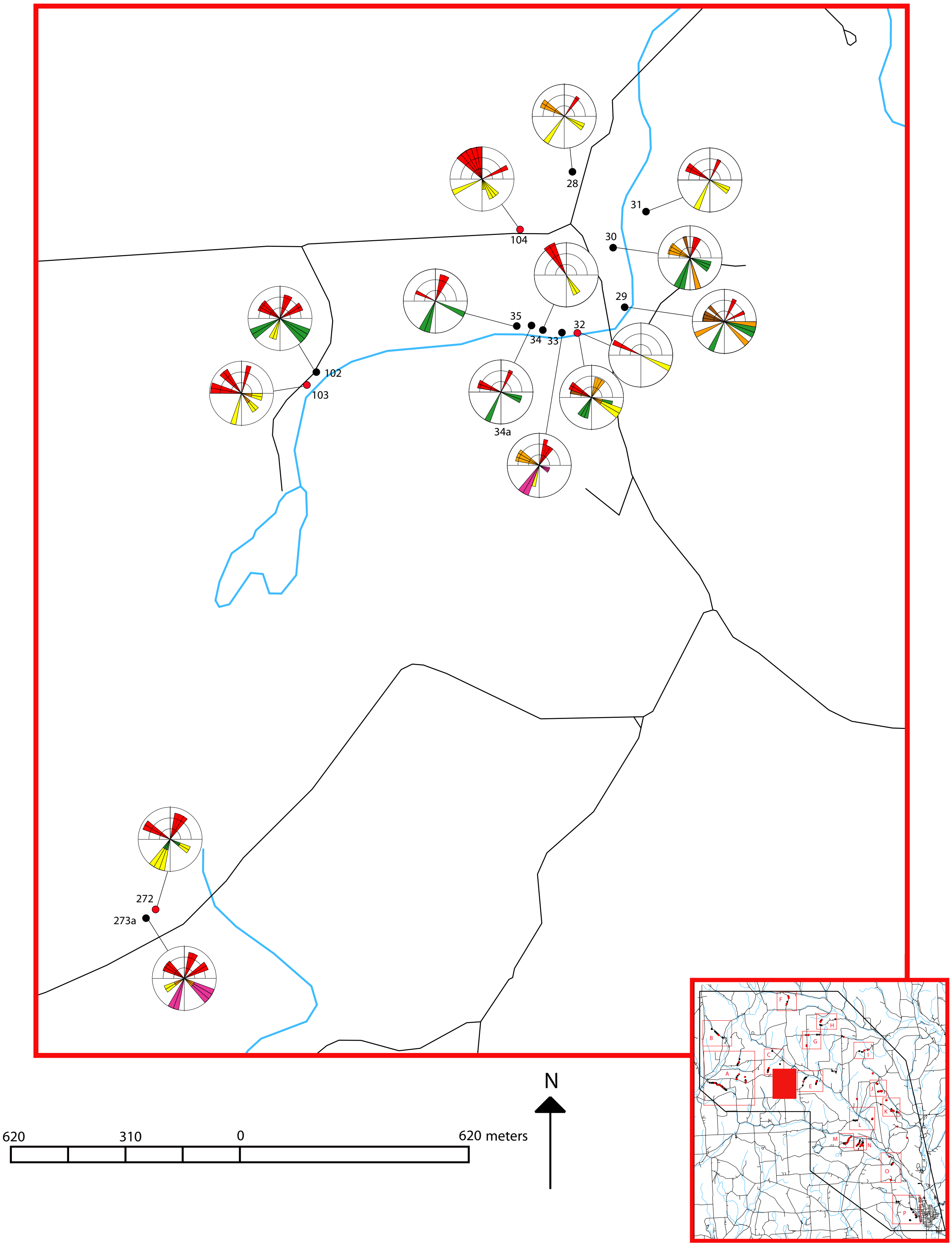
28
104
31
30
29
35
34
33
32
102
103
34a
272
273a
620
310
0
620 meters
N

Figure 7e

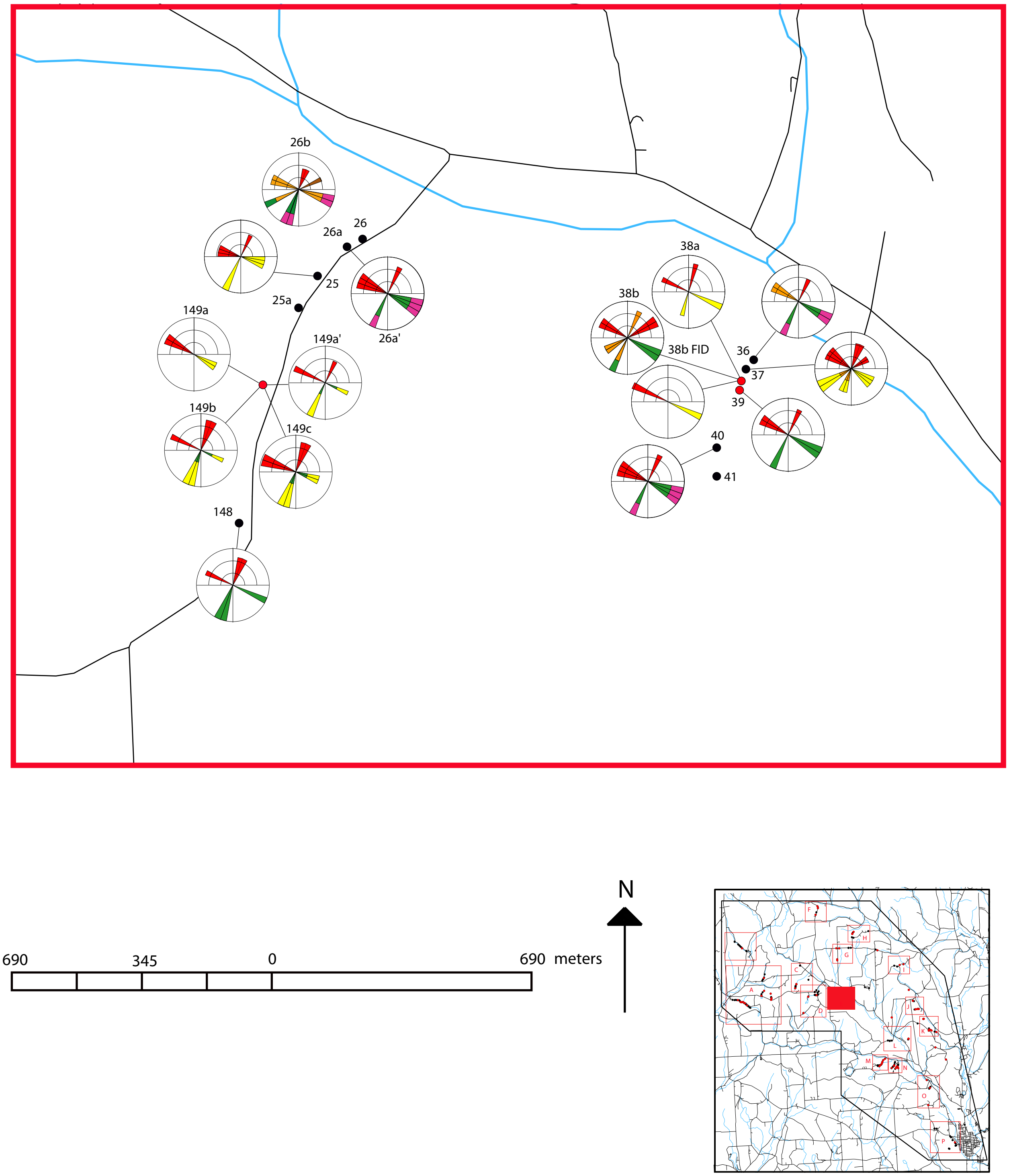

26b
26
26a
25
25a
26a'
149a
149a'
149b
149c
148
38a
38b
38b FID
36
37
39
40
41
690
345
0
690 meters
N

Figure 7f

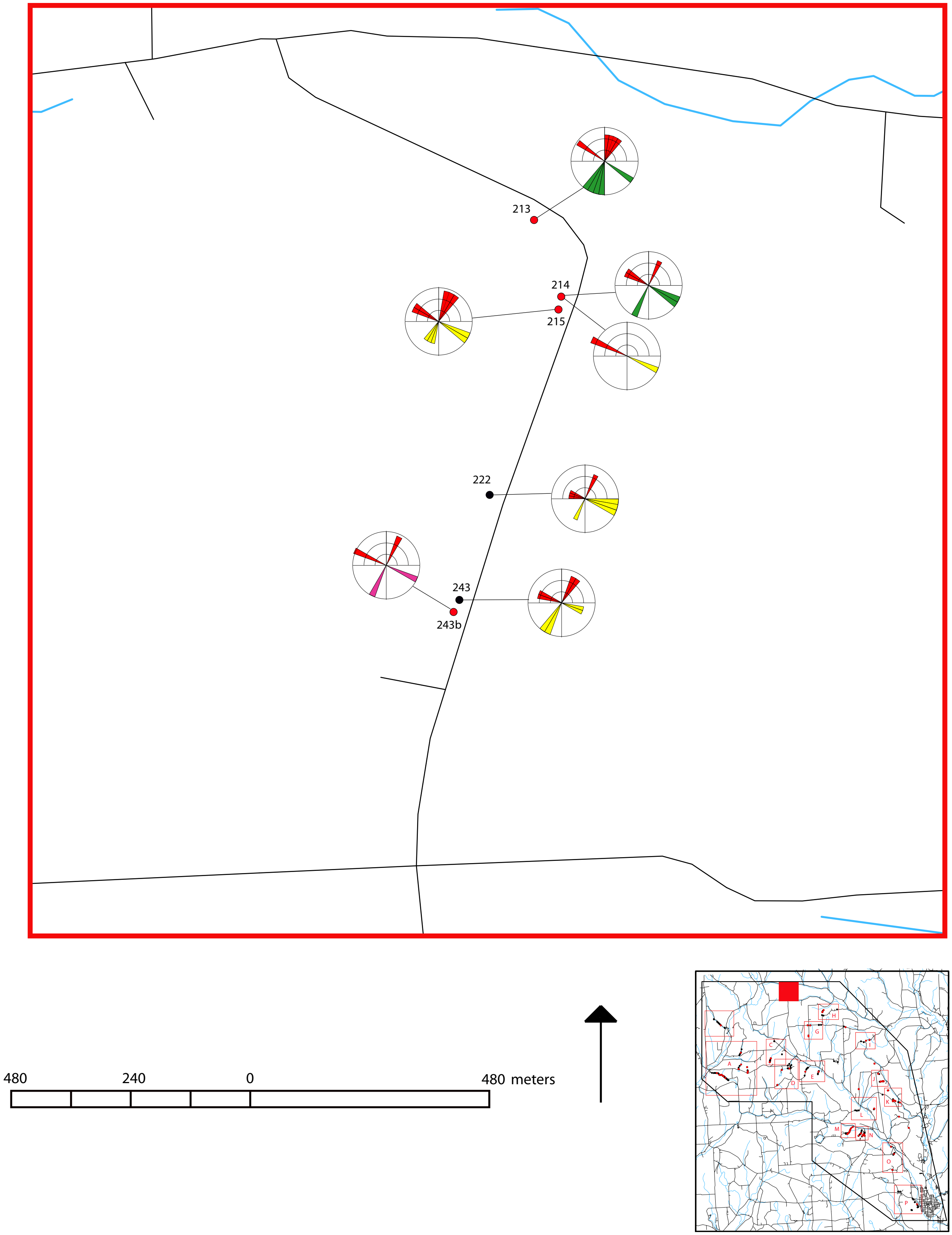

Figure 7g

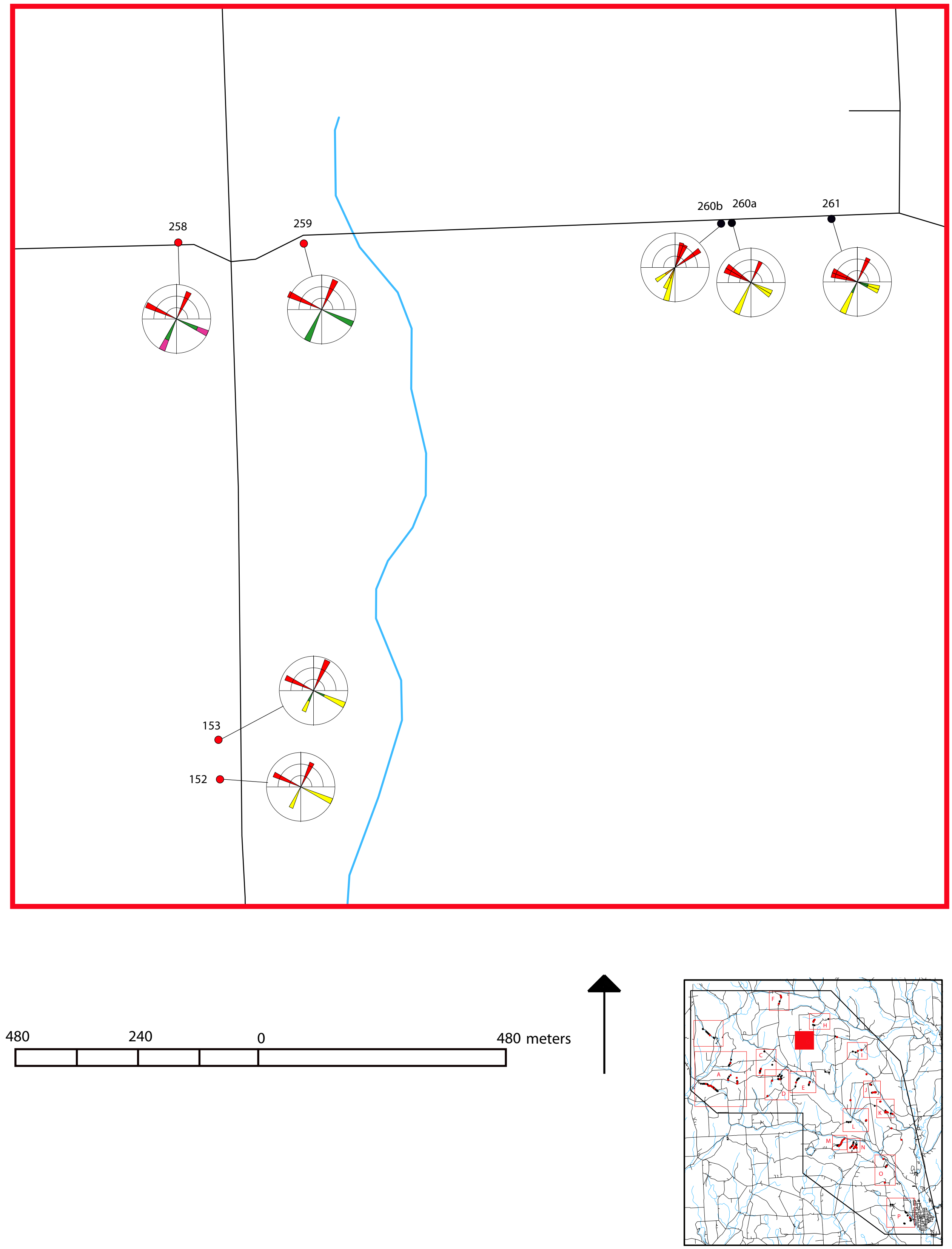

Figure 7h

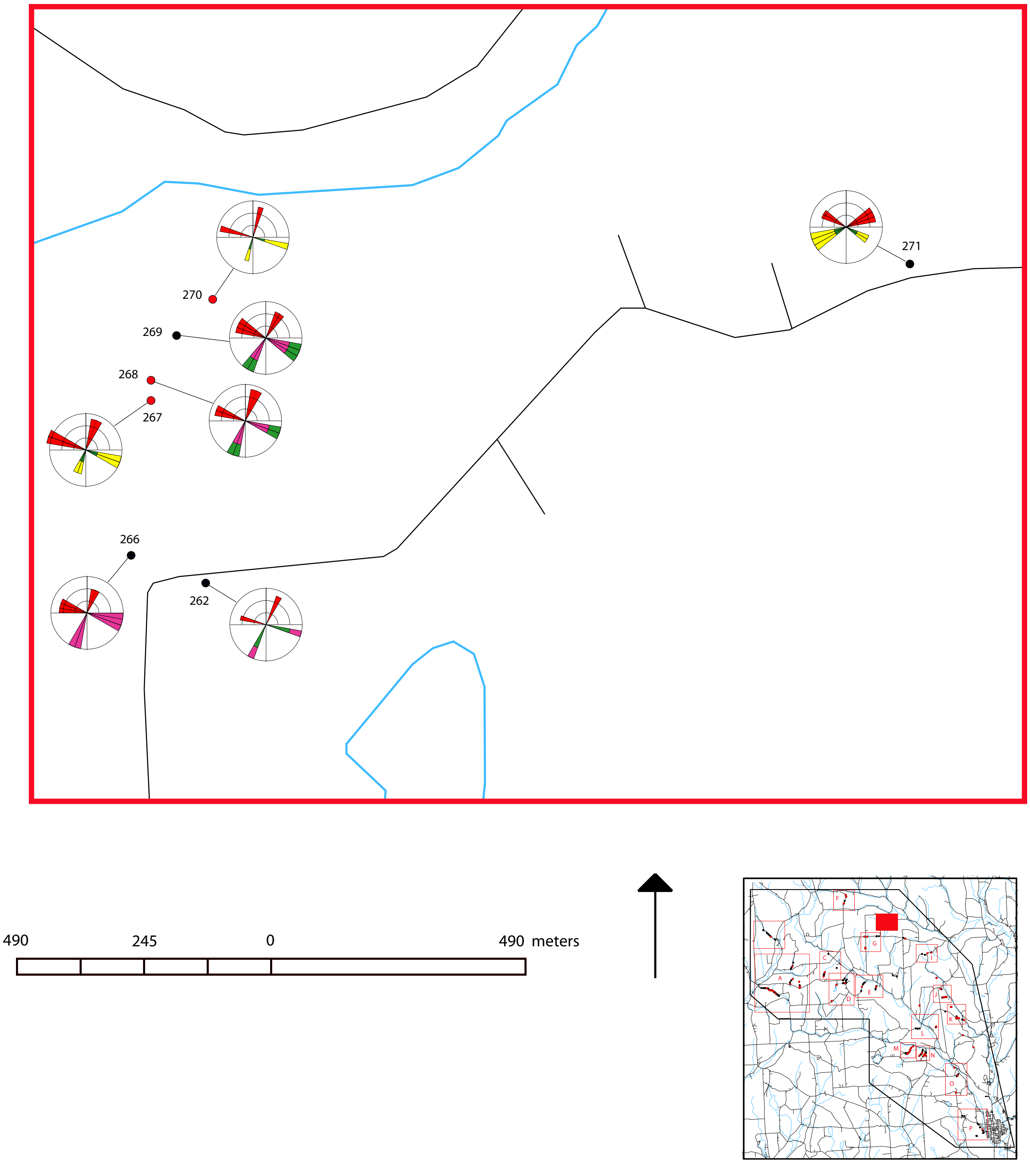

Figure 7i

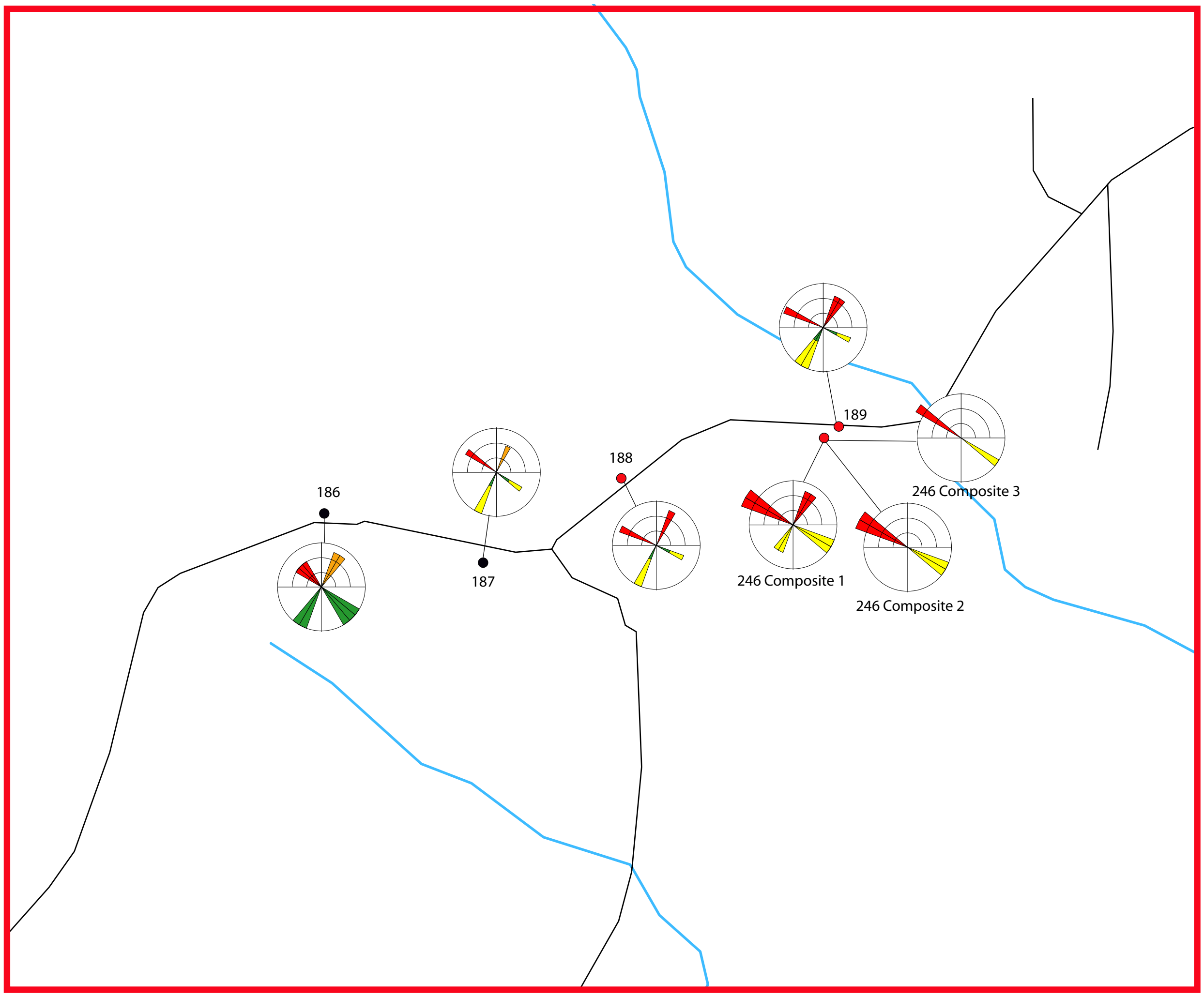
186
187
188
189
246 Composite 1
246 Composite 2
246 Composite 3

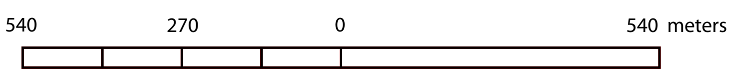
540
270
0
540 meters

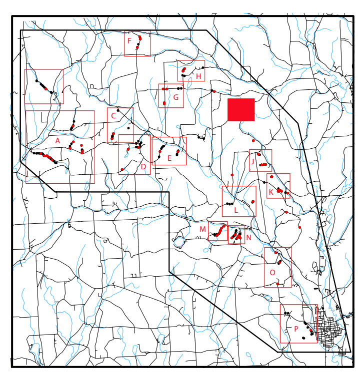

Figure 7j

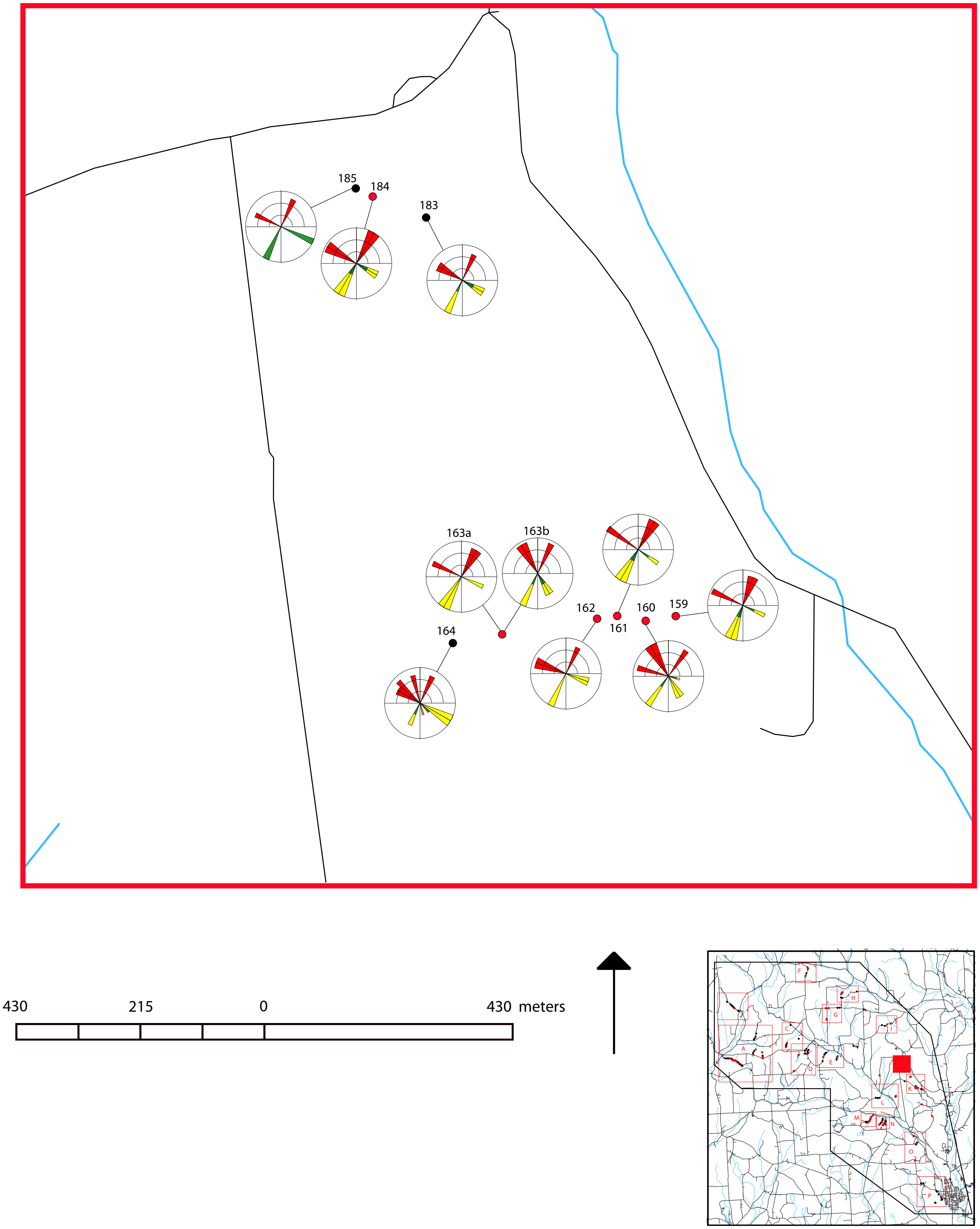

Figure 7k

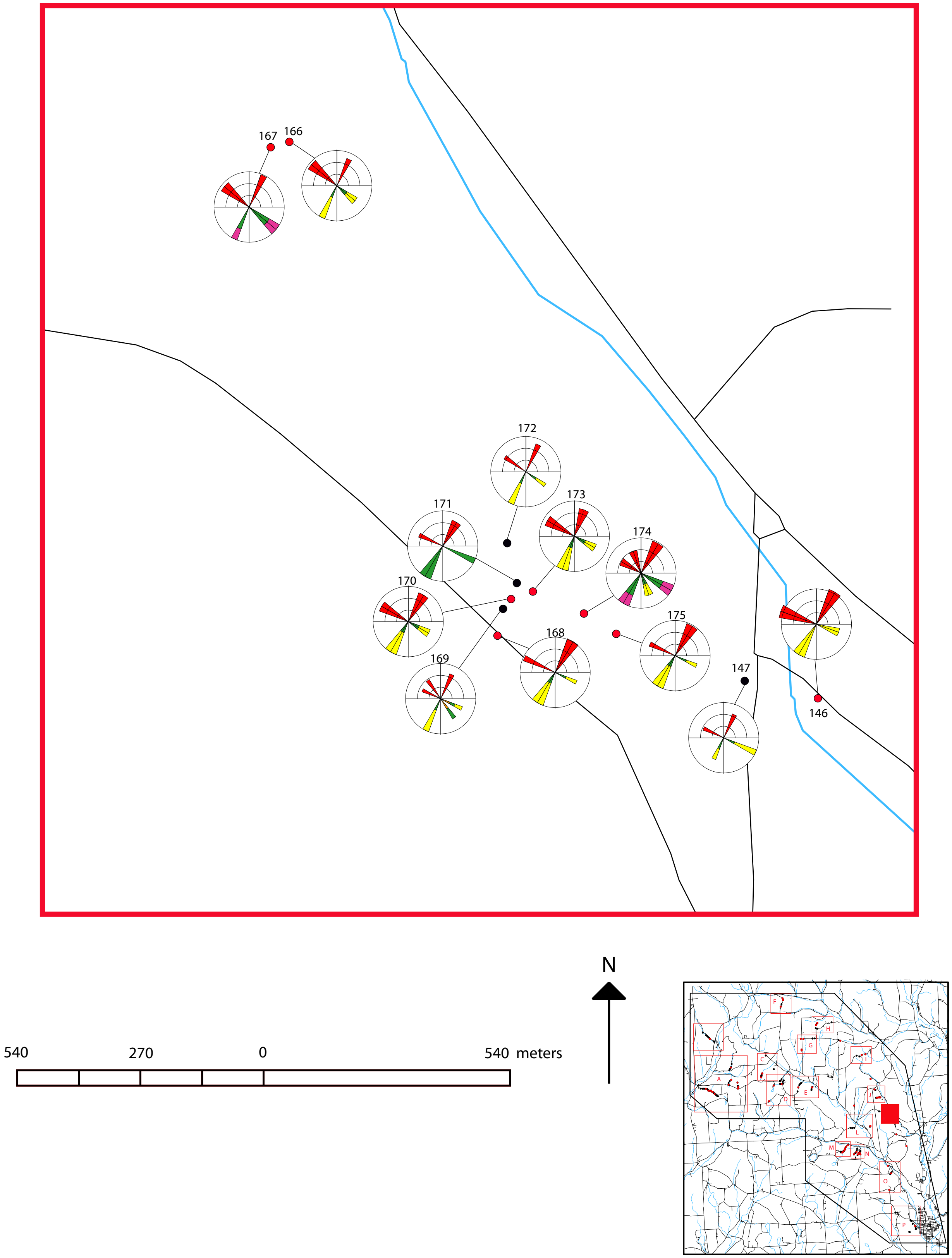

167
166
172
171
173
174
170
175
168
169
147
146
540
270
0
540 meters
N

Figure 7l

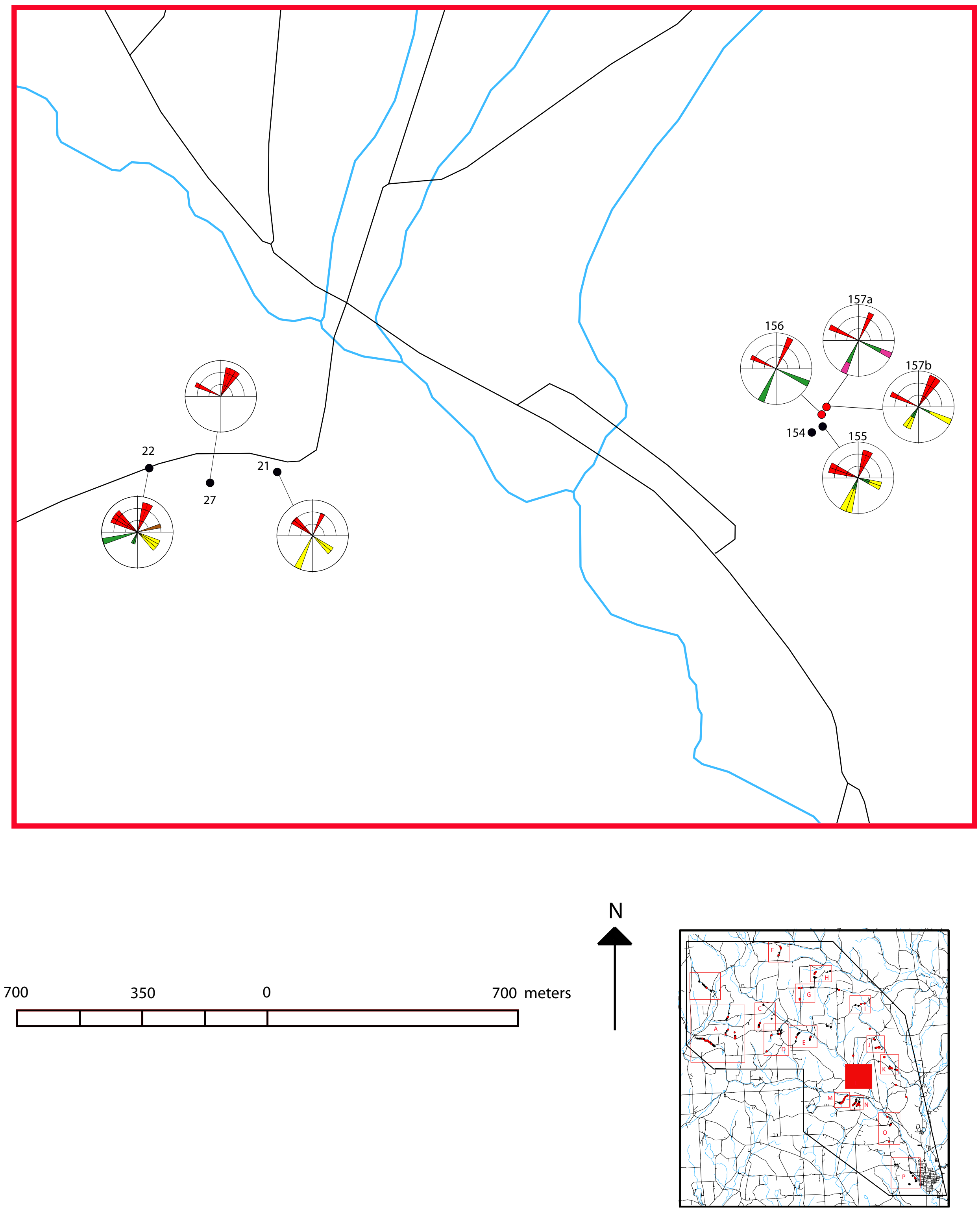

Figure 7m

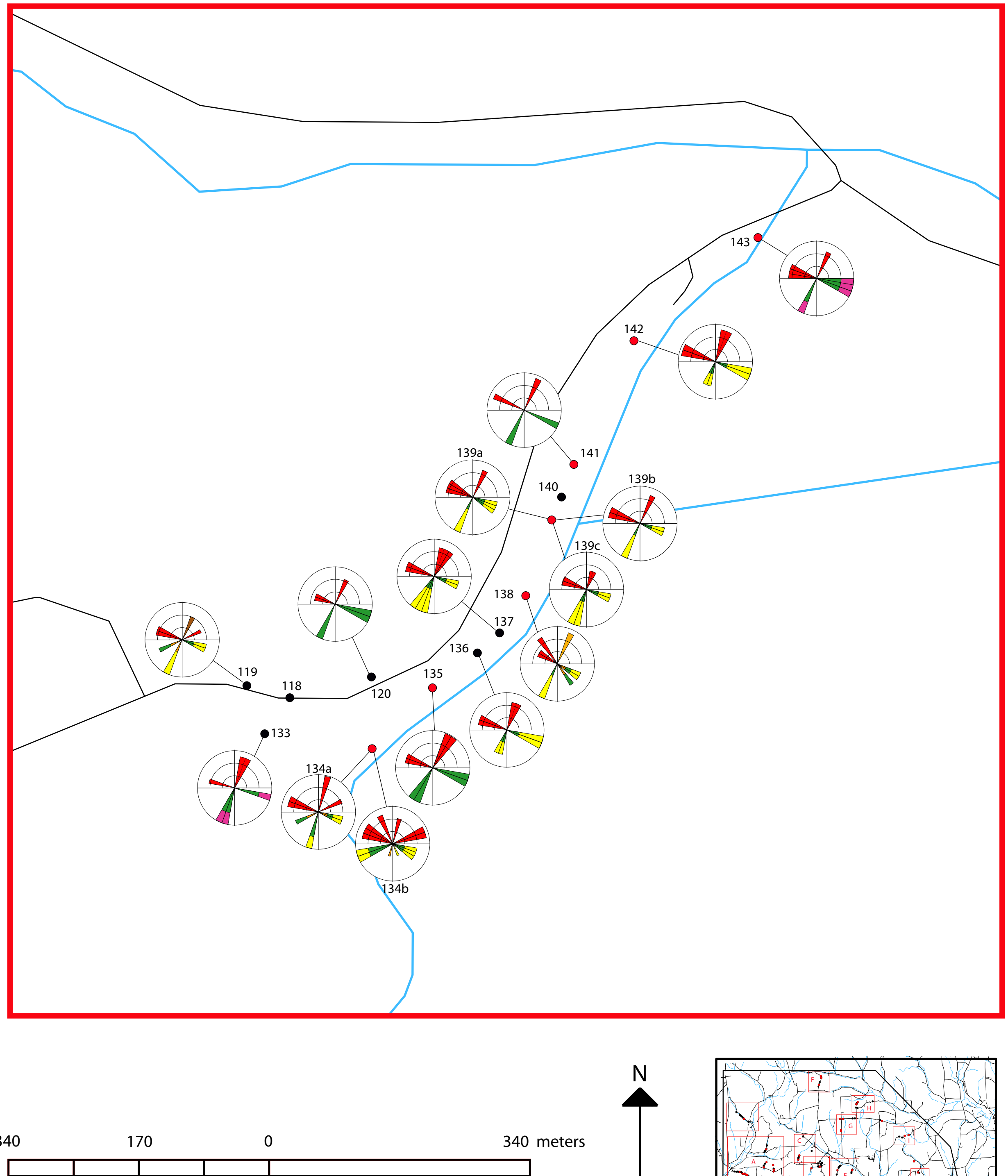
143
142
141
140
139a
139b
139c
138
137
136
135
134a
134b
133
120
119
118
340
170
0
340 meters
N

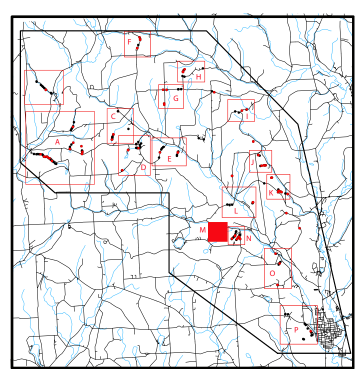

Figure 7n

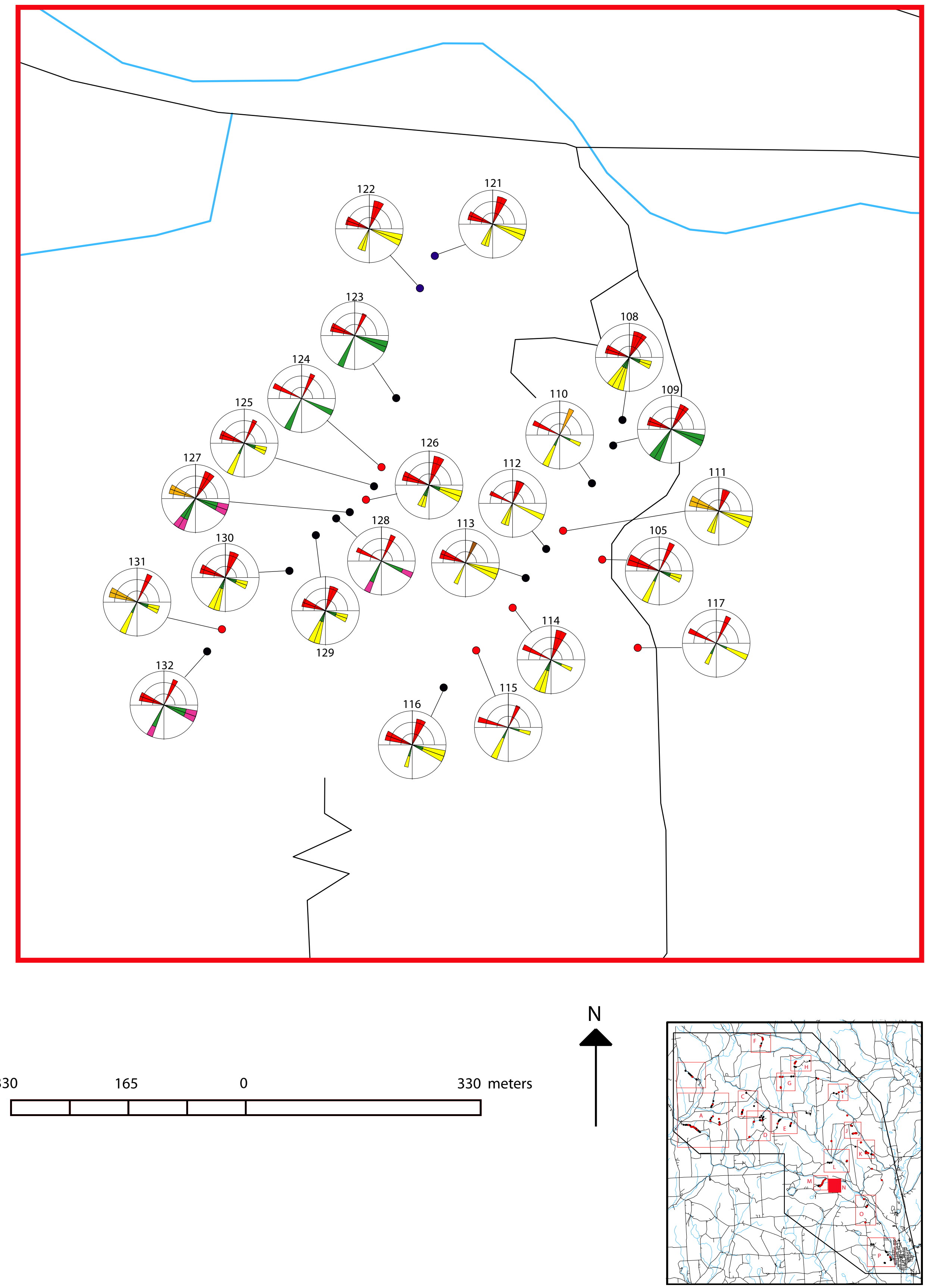

122
121
123
108
124
110
109
125
126
127
112
111
128
113
105
130
131
129
114
117
132
115
116
330
165
0
330 meters
N

Figure 7o

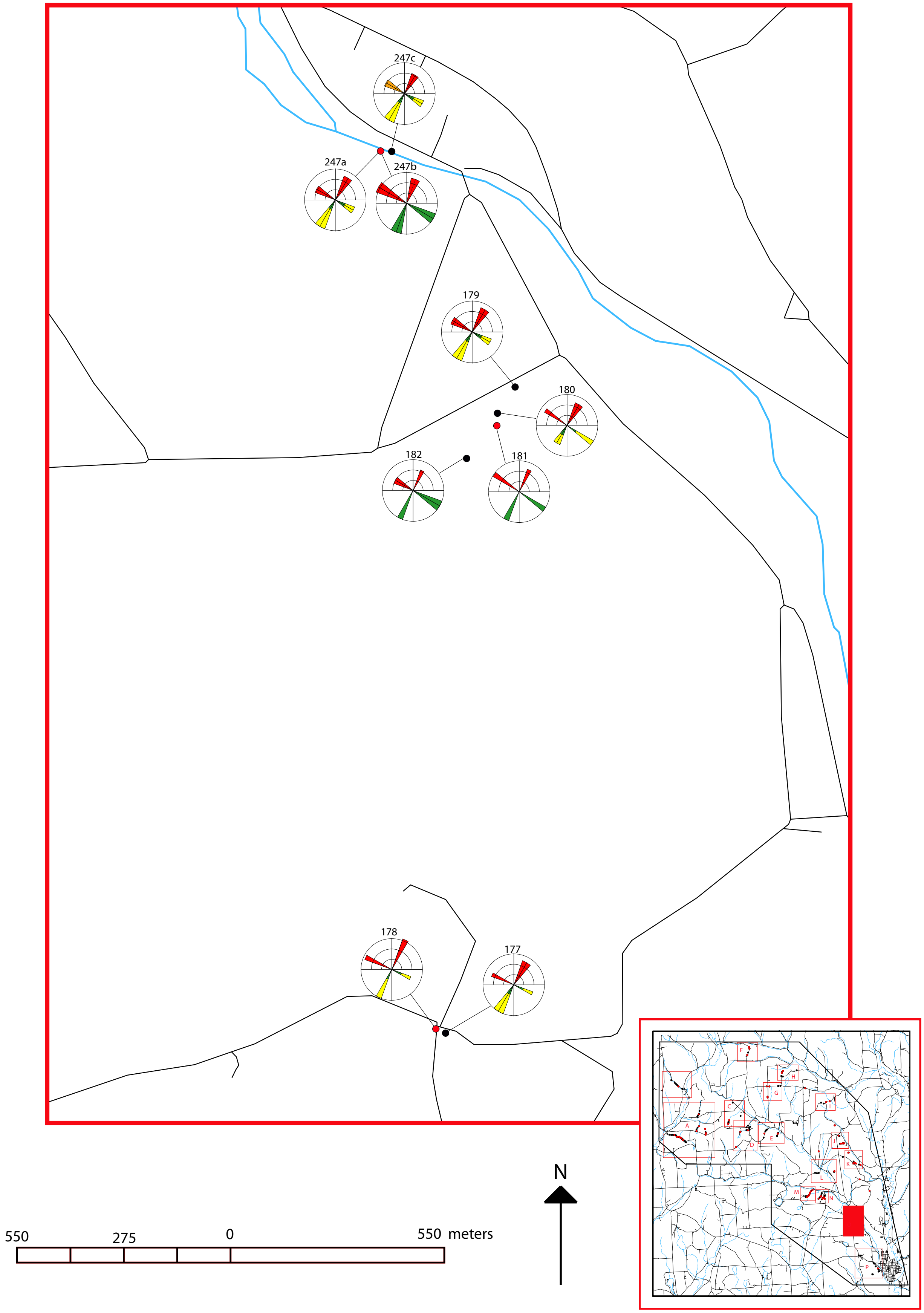

Figure 7p

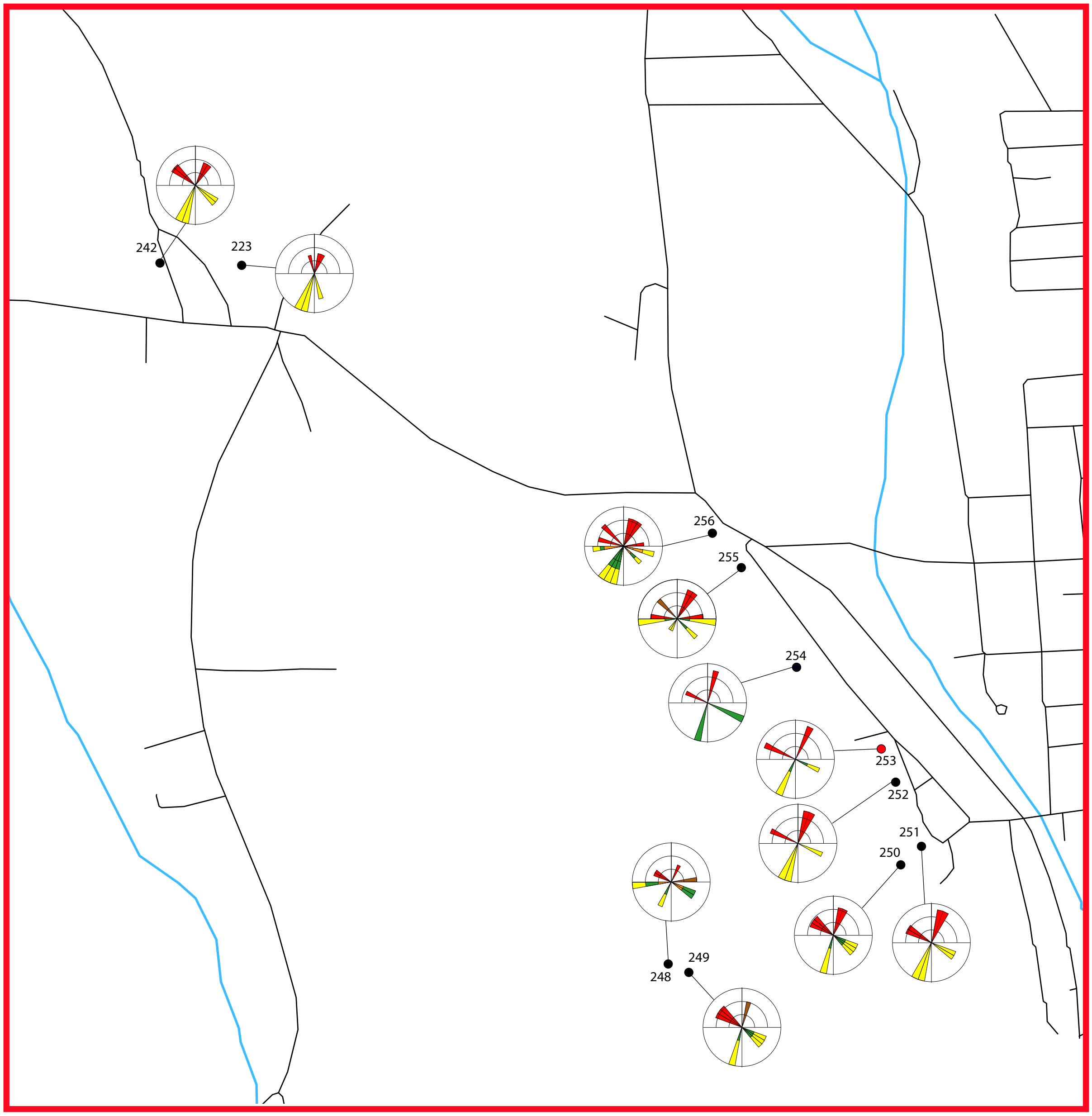
242
223
256
255
254
253
252
251
250
248
249

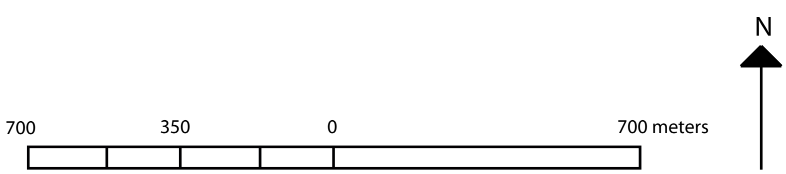
700
350
0
700 meters
N

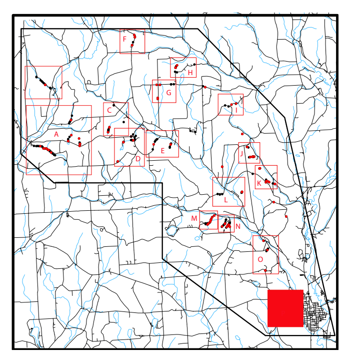

Figure 7q

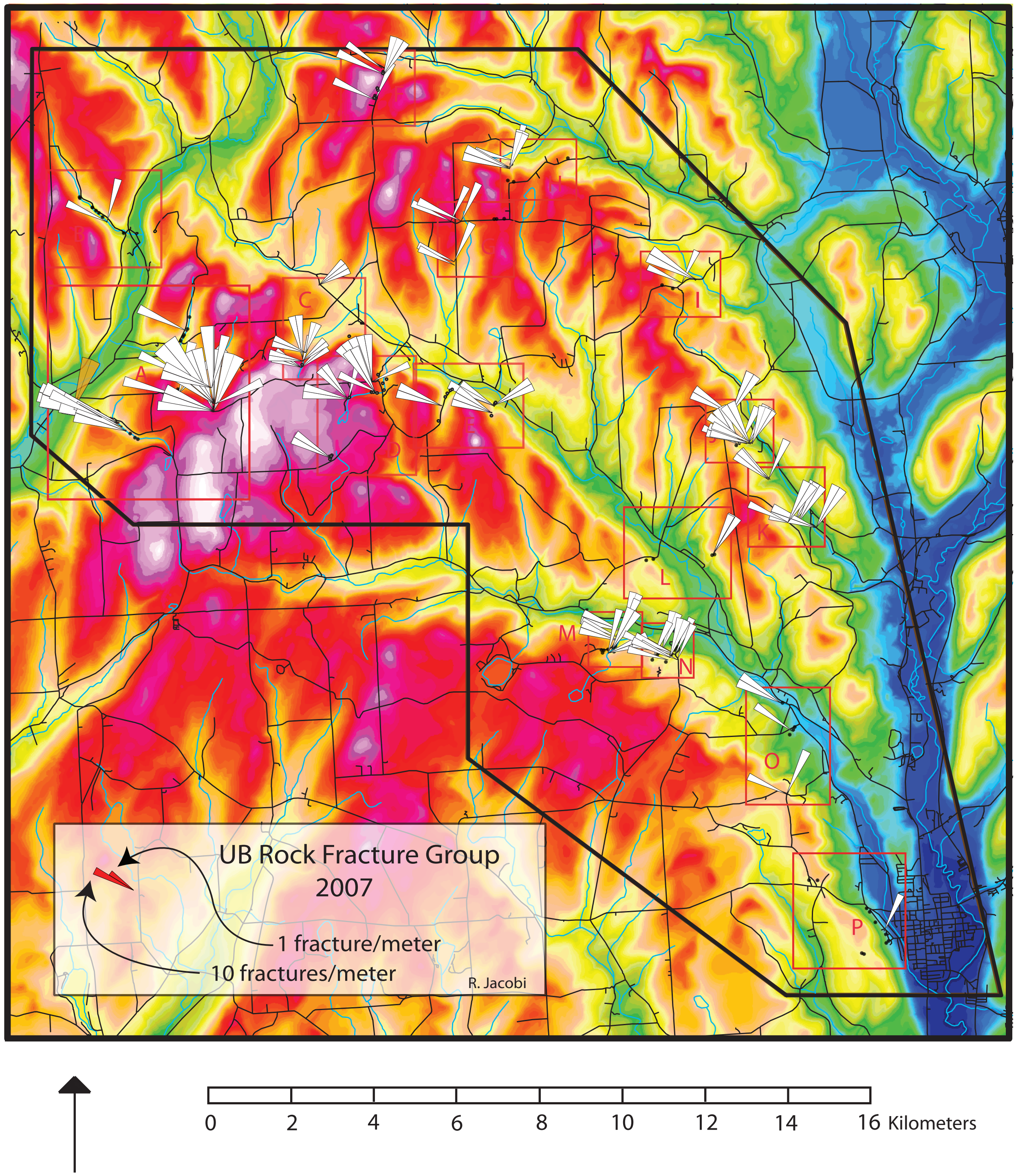

A
B
C
D
I
J
K
L
M
N
O
P
UB Rock Fracture Group
2007
1 fracture/meter
10 fractures/meter
R. Jacobi
0
2
4
6
8
10
12
14
16 Kilometers

Figure 8a

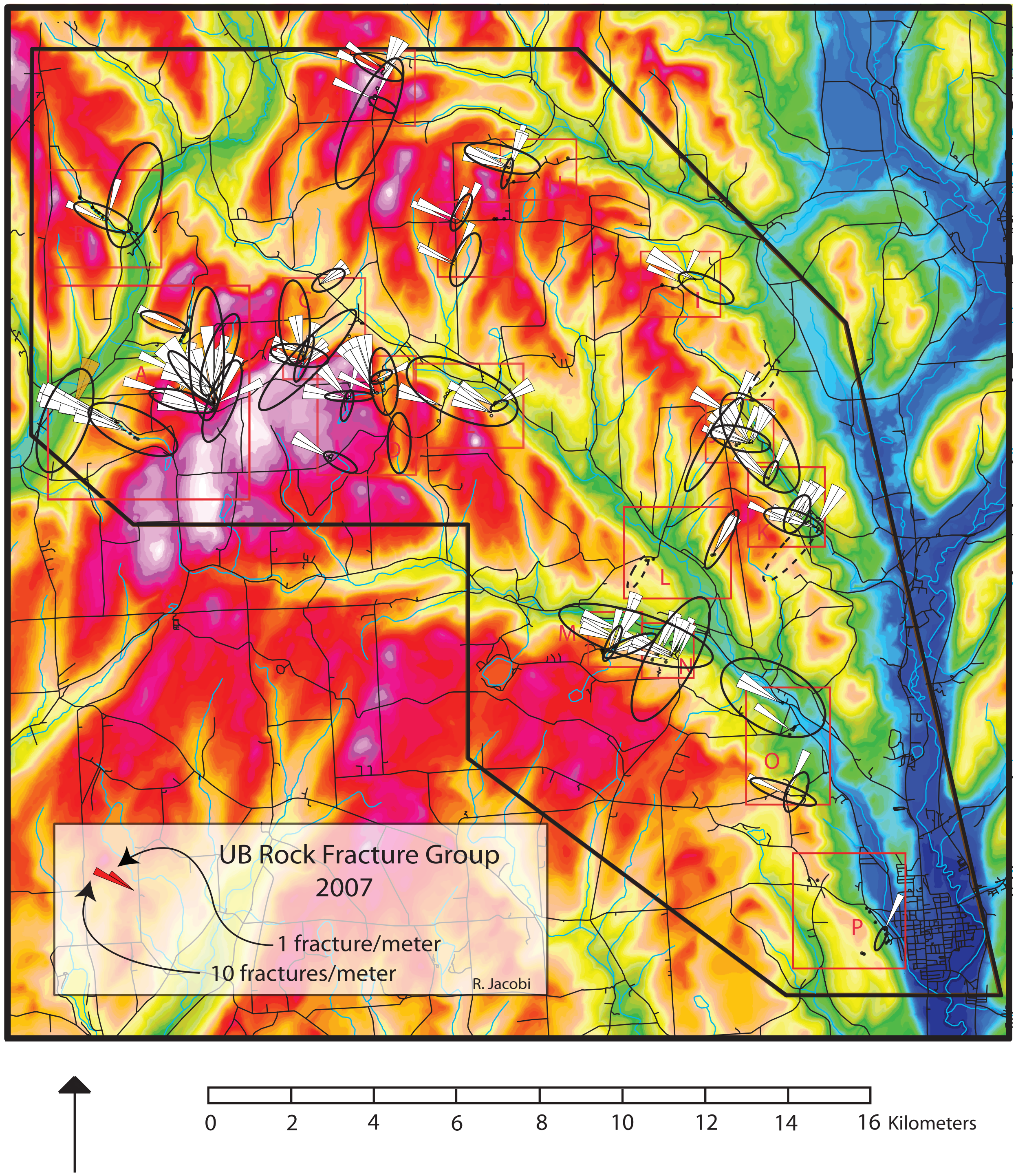
UB Rock Fracture Group
2007
1 fracture/meter
10 fractures/meter
R. Jacobi
A
B
C
K
L
M
N
O
P
0
2
4
6
8
10
12
14
16 Kilometers

Figure 8b

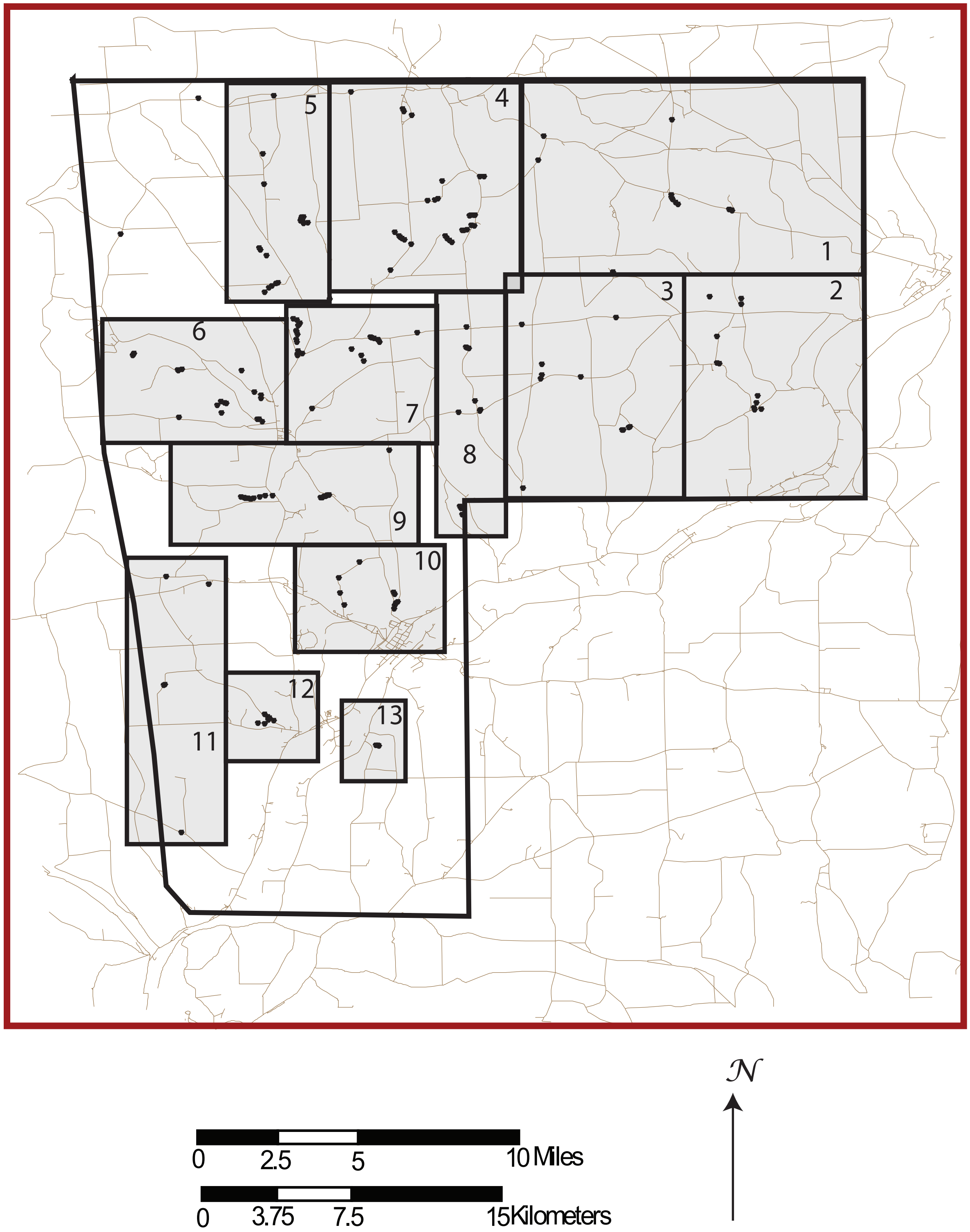

Figure 9a

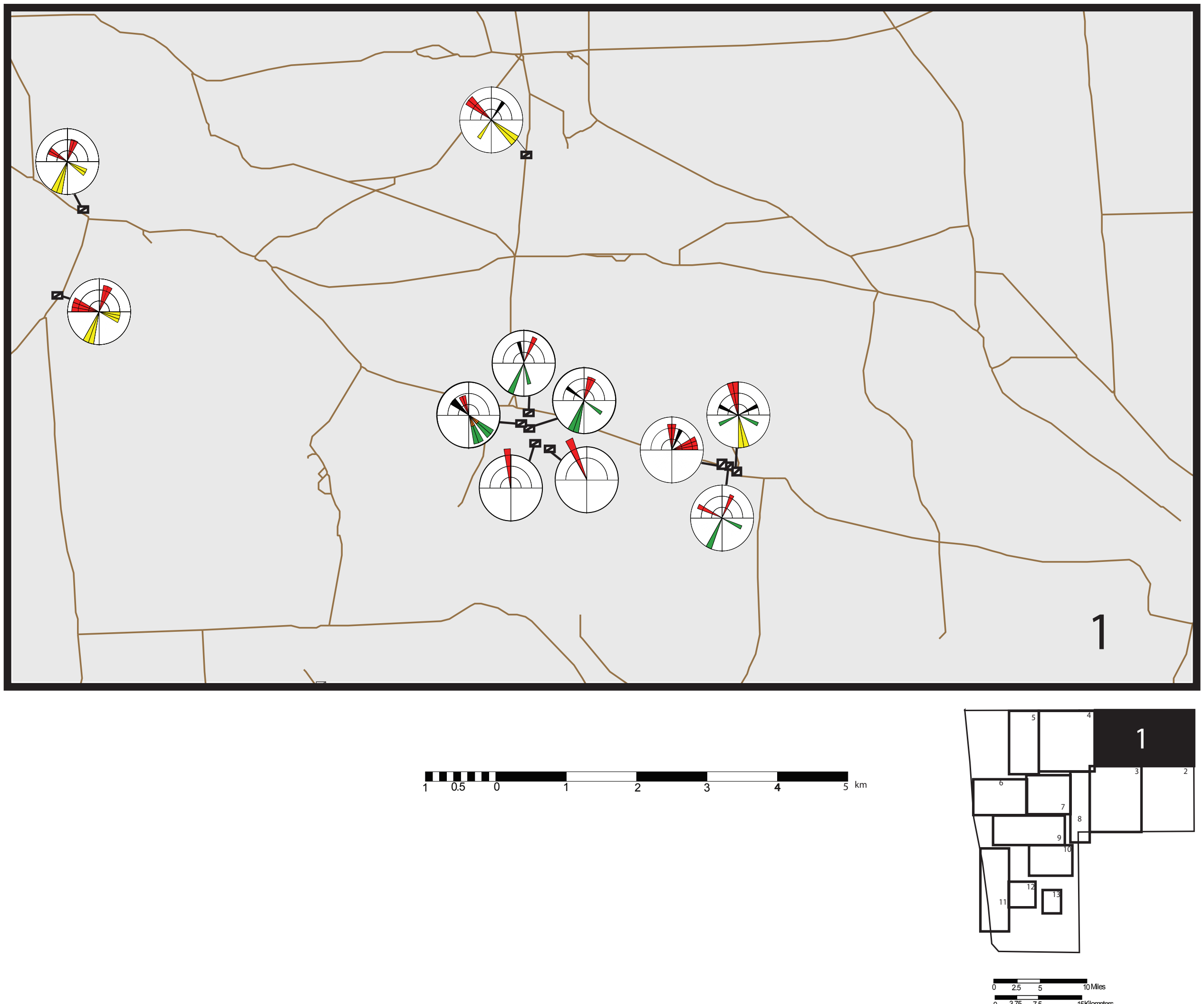
1
1 0.5 0 1 2 3 4 5 km
1
5
4
3
2
6
7
8
9
10
11
12
13
0 2.5 5 10 Miles
0 3.75 7.5 15 Kilometers

Figure 9b

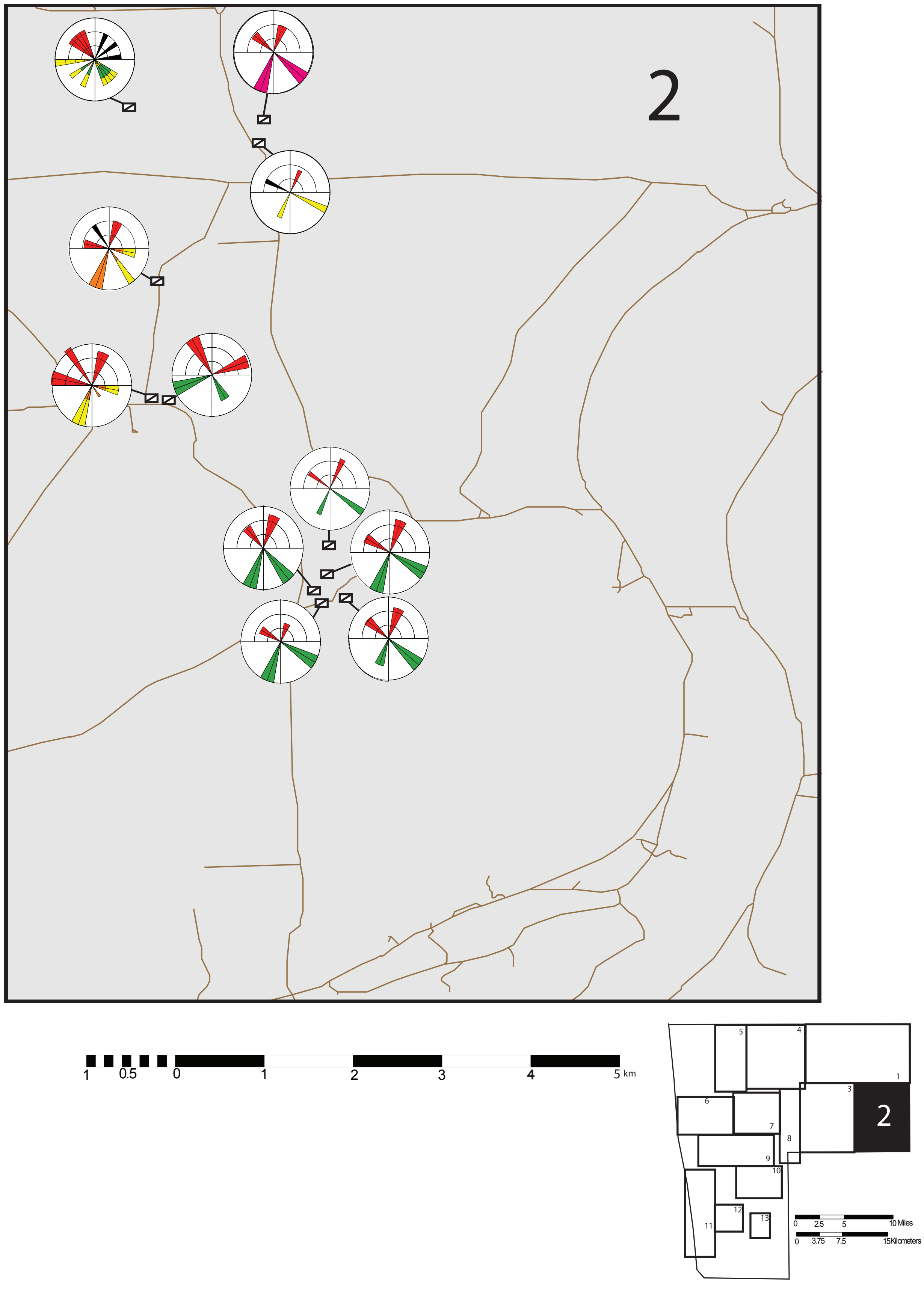

Figure 9c

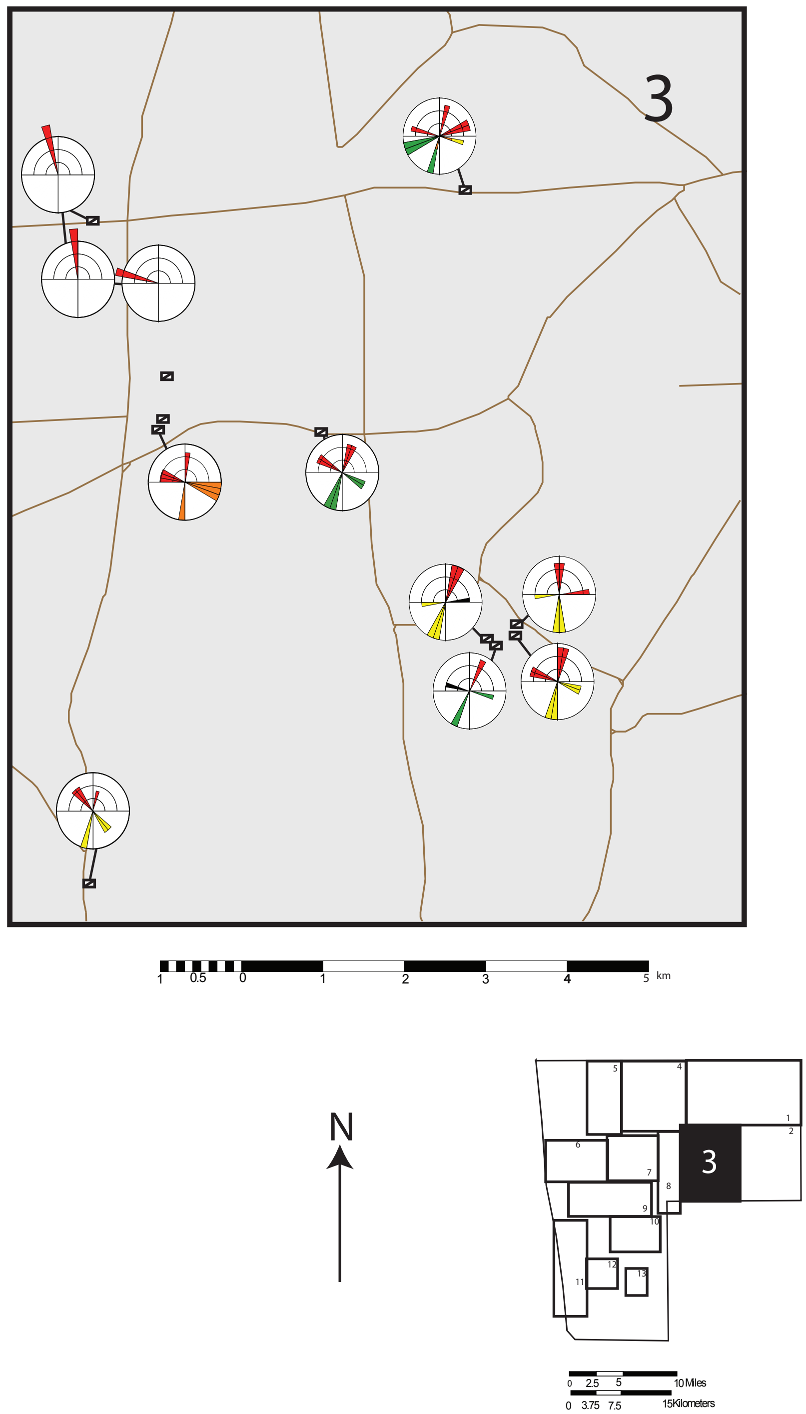
3
1
0.5
0
1
2
3
4
5
km
N
5
4
1
2
6
7
3
8
9
10
11
12
13
0
2.5
5
10 Miles
0
3.75
7.5
15 Kilometers

Figure 9d

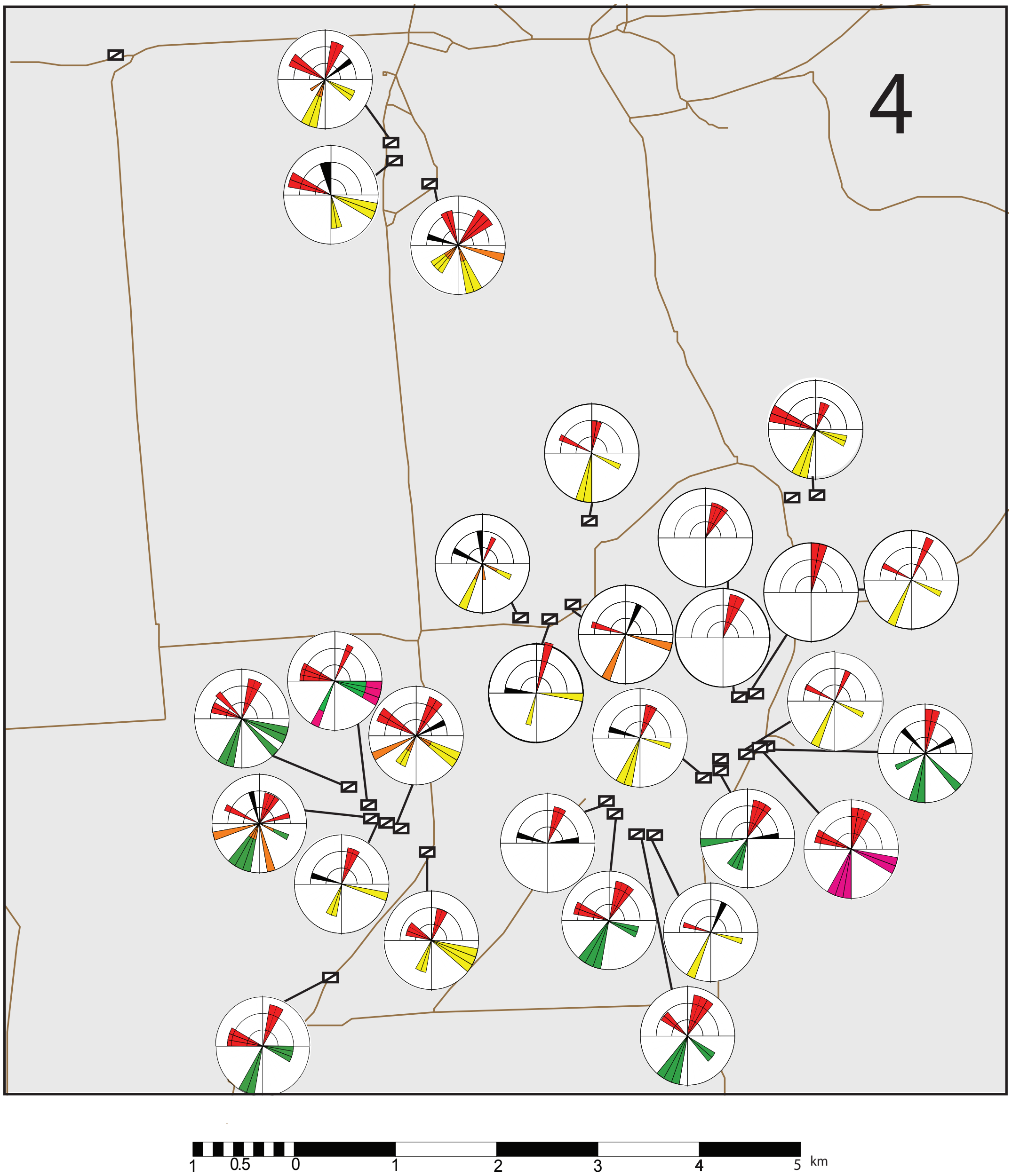

N

Figure 9e

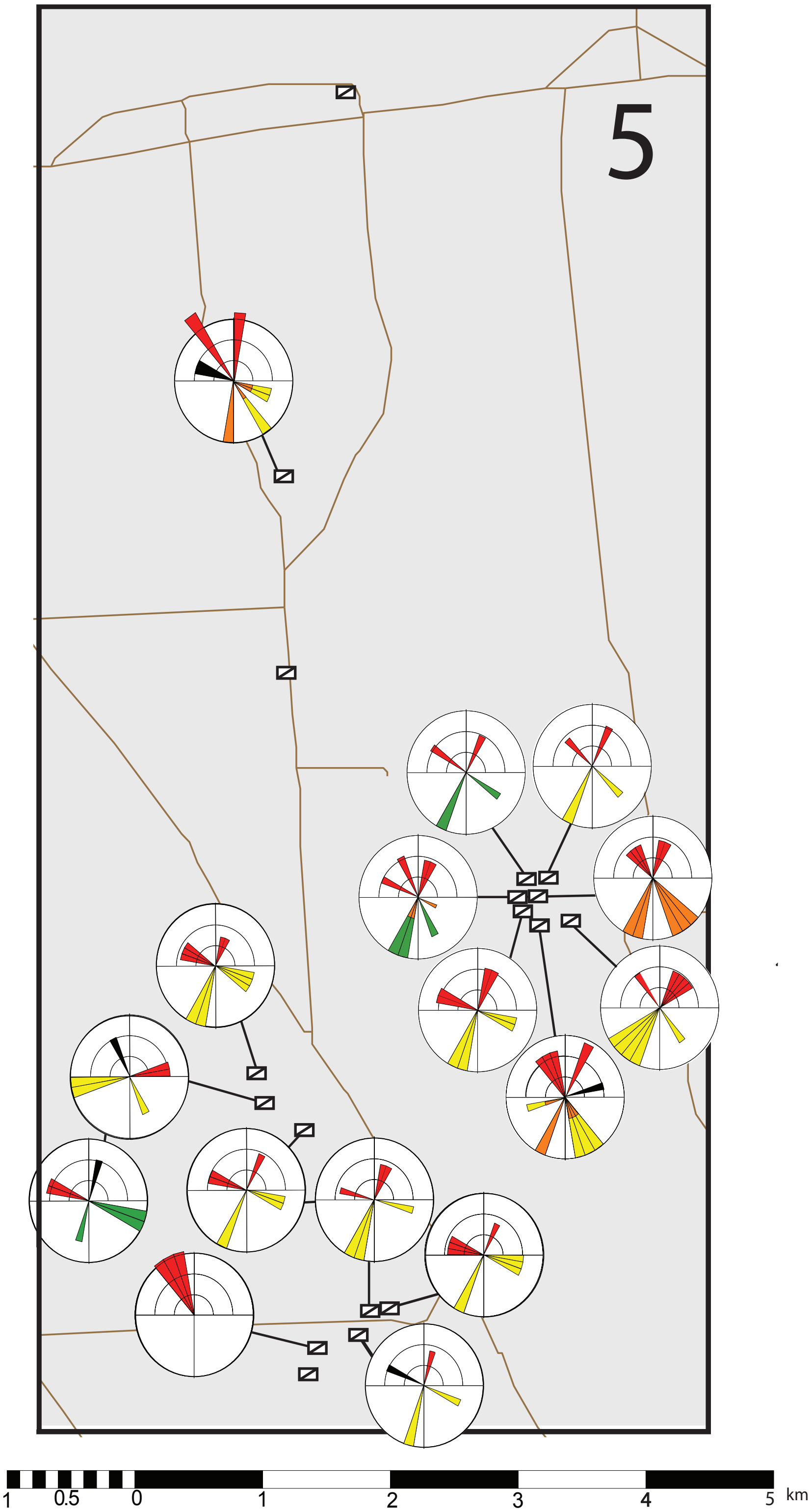

5
1
0.5
0
1
2
3
4
5
km

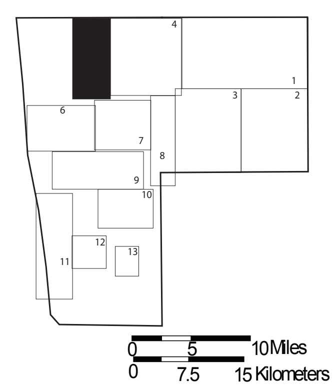

4
1
2
3
6
7
8
9
10
11
12
13
0
5
10 Miles
0
7.5
15 Kilometers

Figure 9f

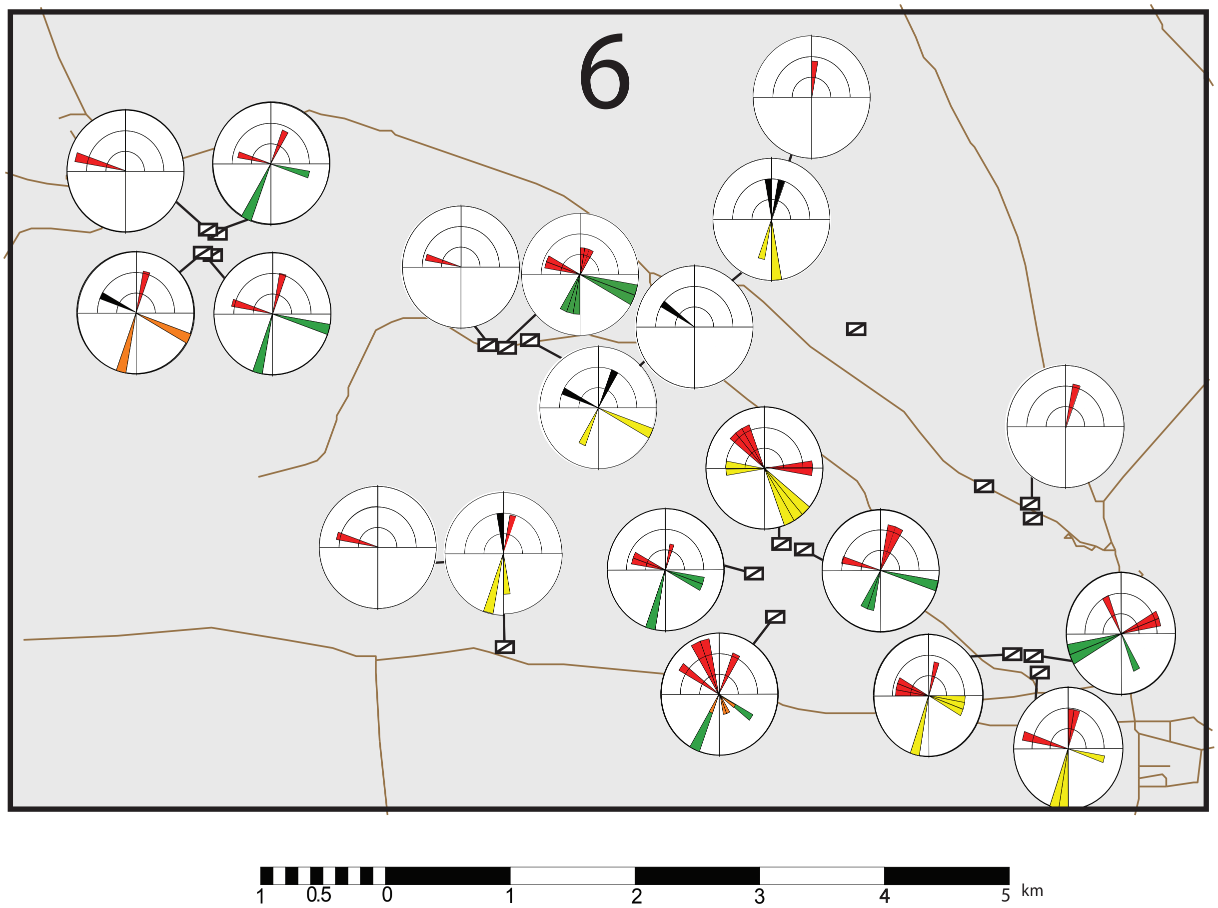

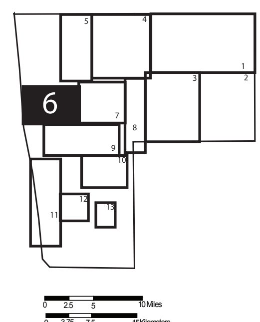

Figure 9g

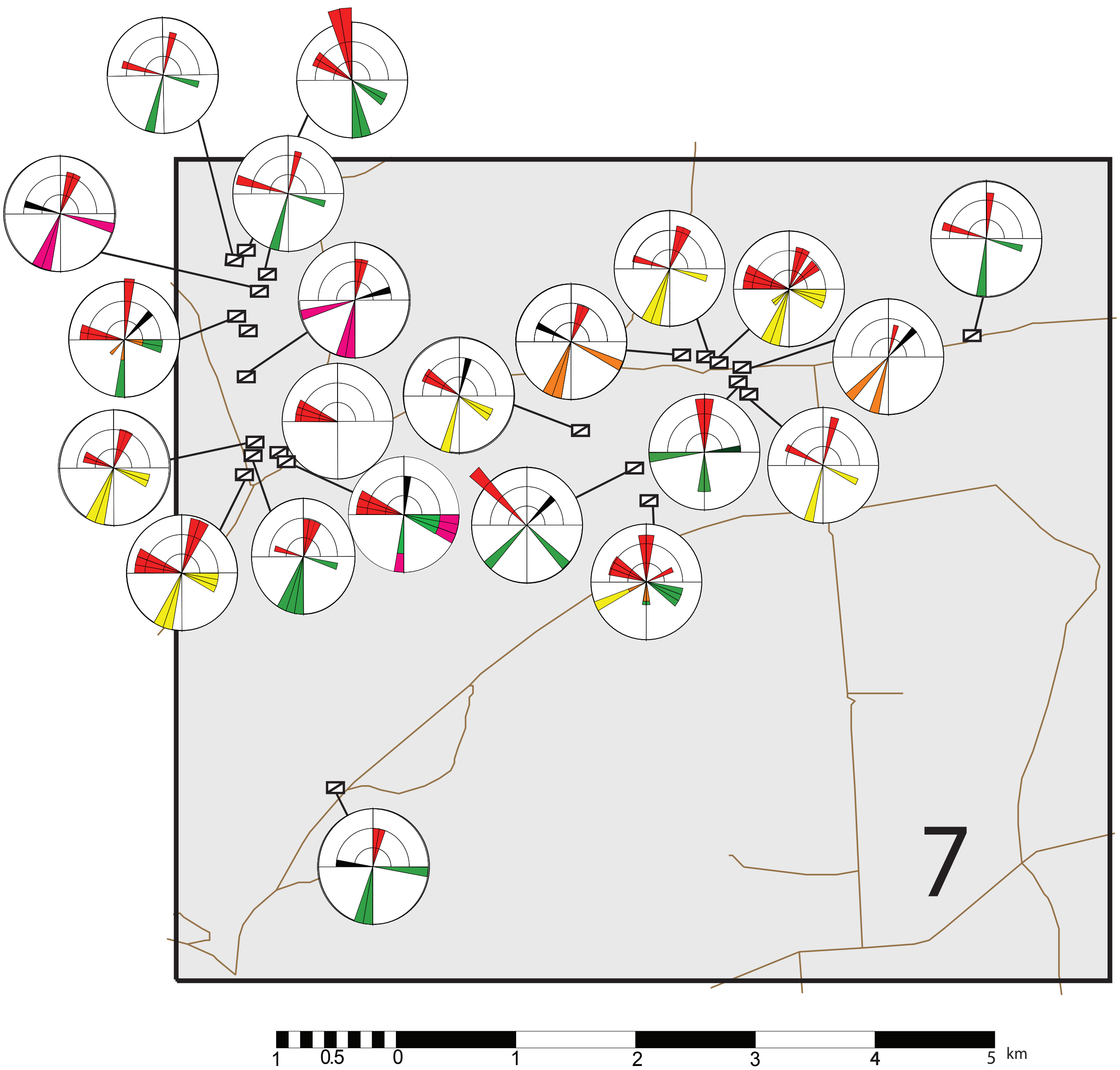

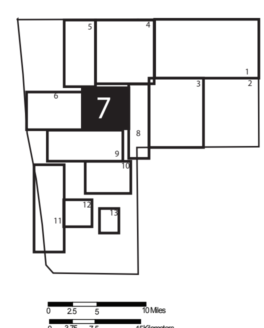

Figure 9h

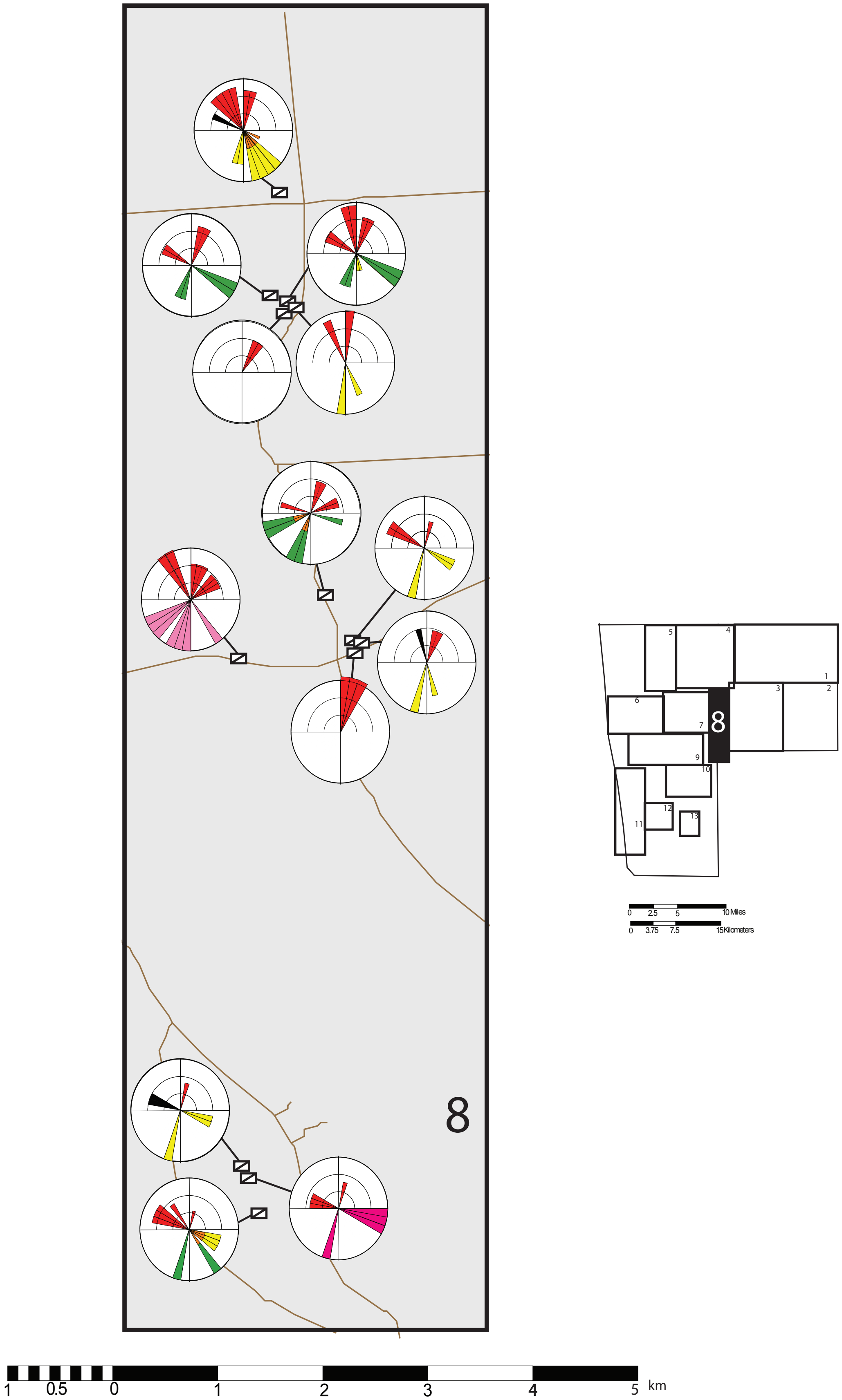
8
1 0.5 0 1 2 3 4 5 km
1
2
3
4
5
6
7
9
10
11
12
13
0 2.5 5 10 Miles
0 3.75 7.5 15 Kilometers

Figure 9i

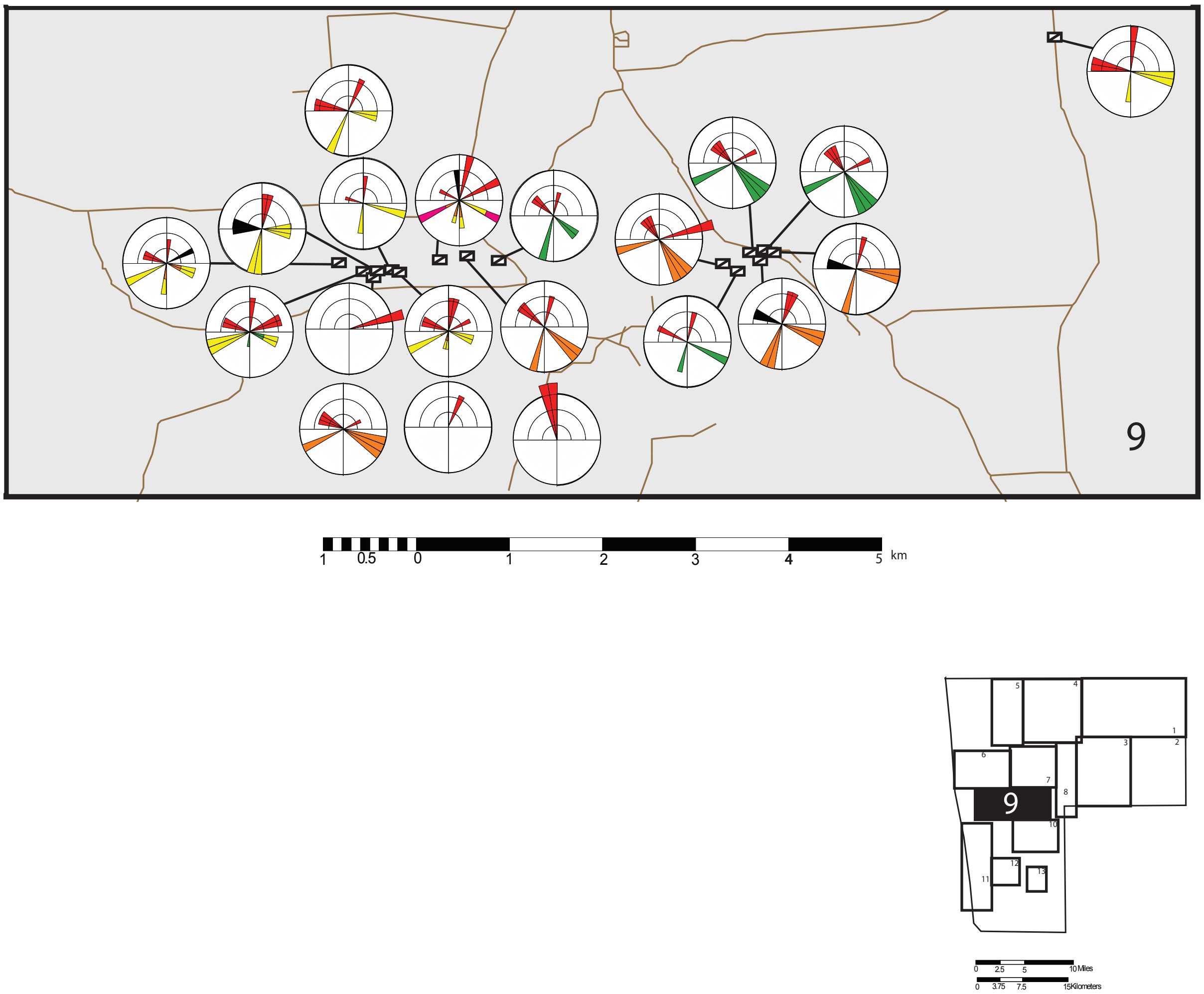

Figure 9j

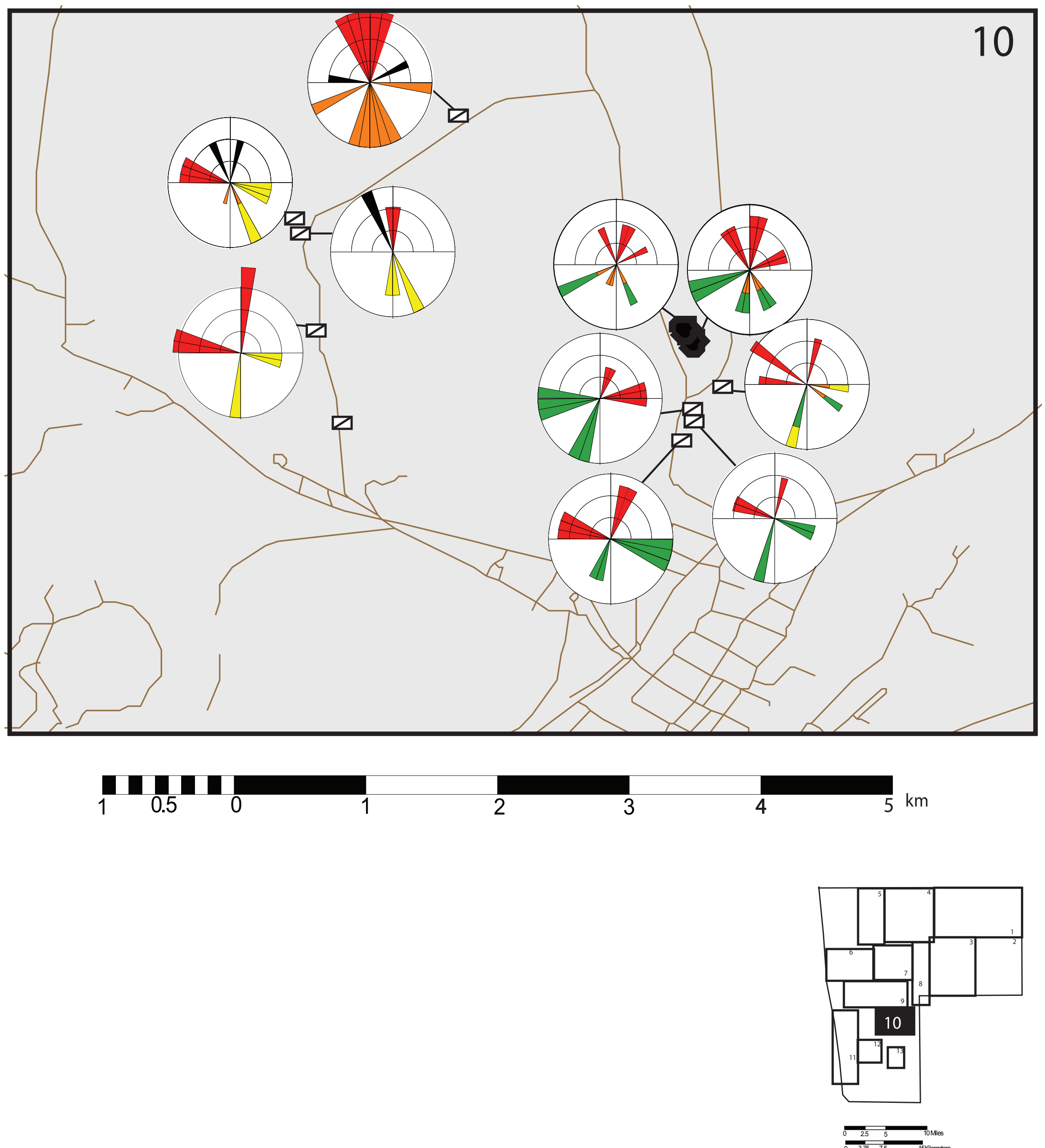
10
1 0.5 0 1 2 3 4 5 km
5
4
1
3
2
6
7
8
9
10
12
13
11
0 2.5 5 10 Miles
0 3.75 7.5 15 Kilometers

Figure 9k

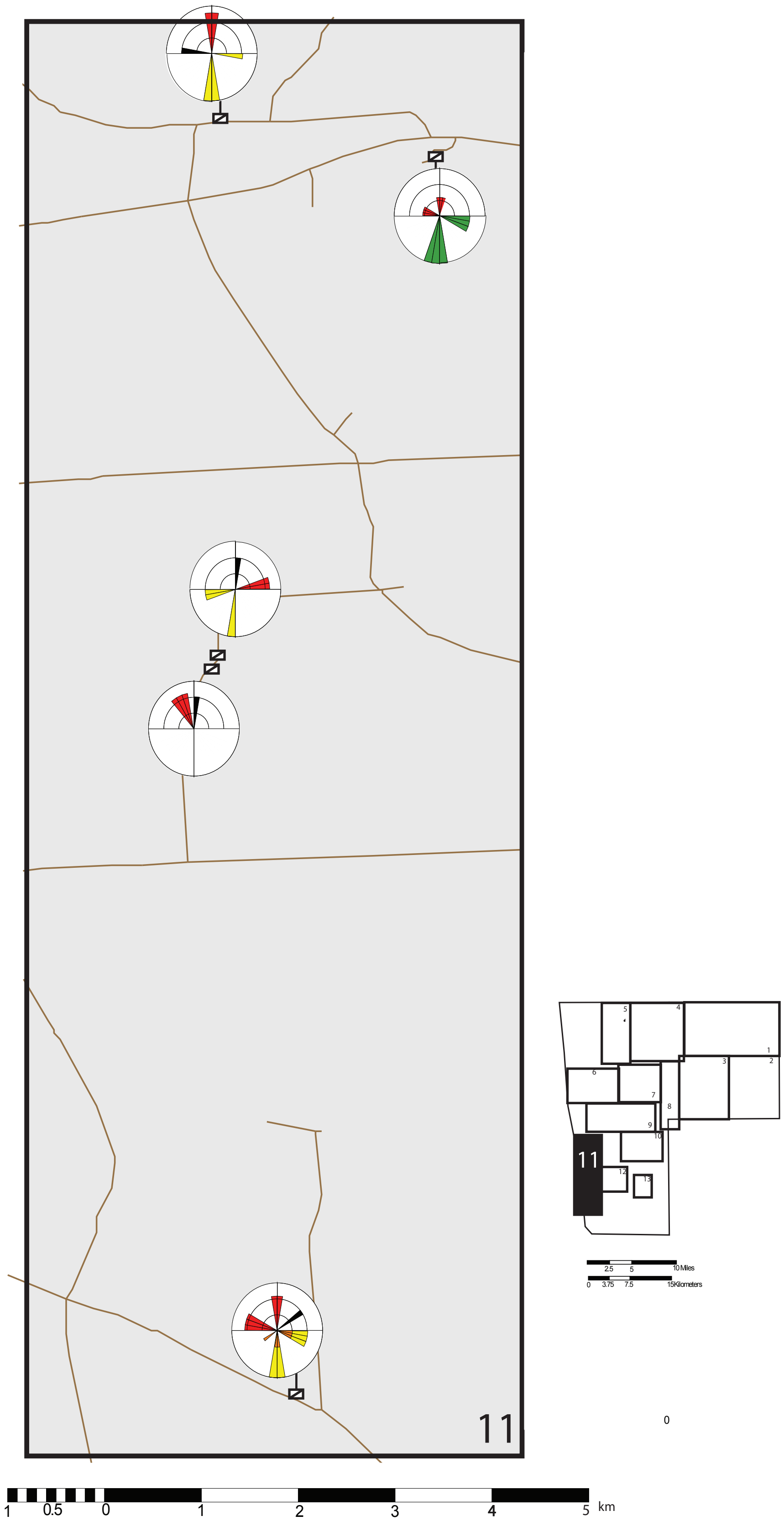

Figure 91

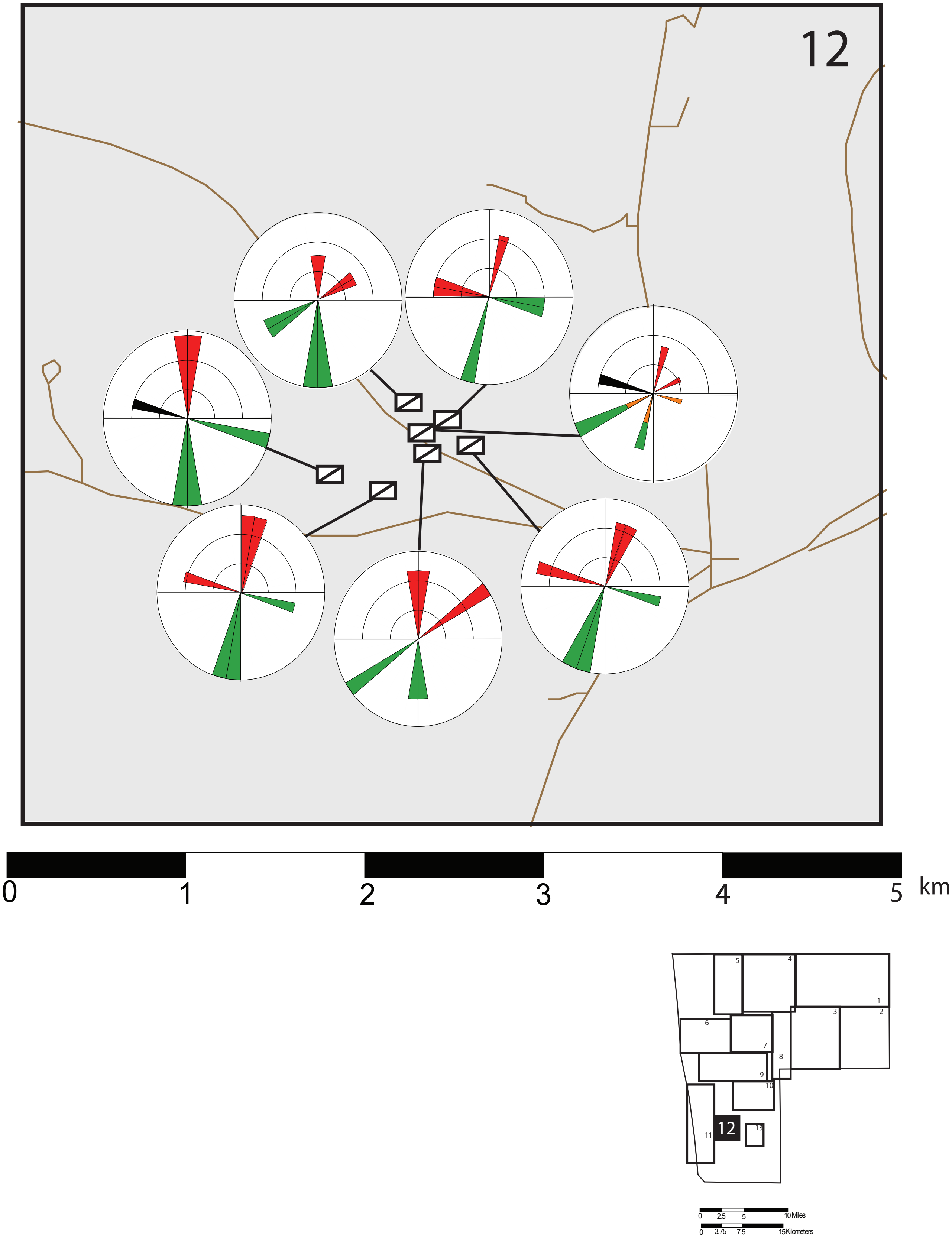
12
0
1
2
3
4
5
km
5
4
1
2
3
6
7
8
9
10
12
13
11
0 2.5 5 10 Miles
0 3.75 7.5 15 Kilometers

Figure 9m

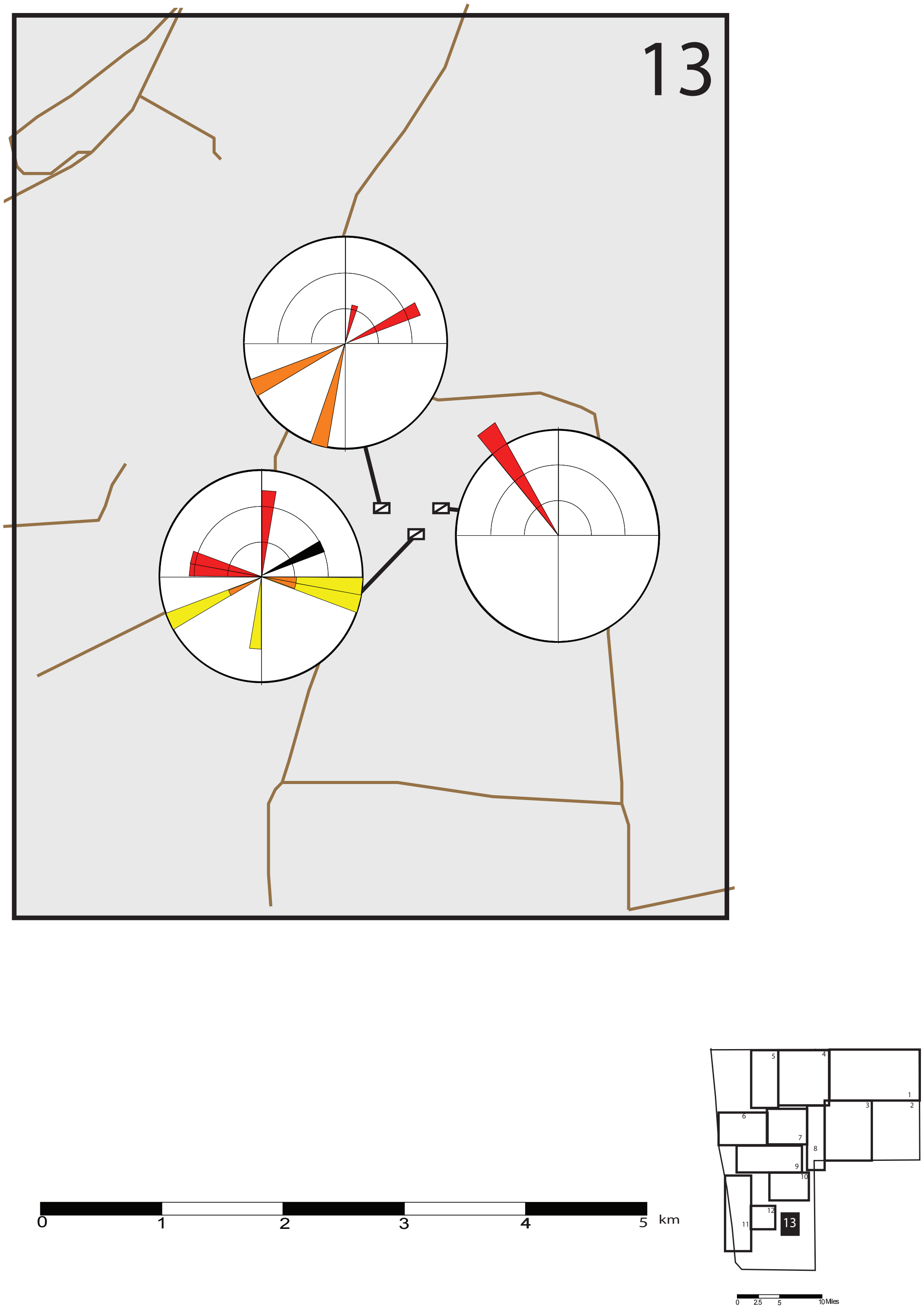

Figure 9n

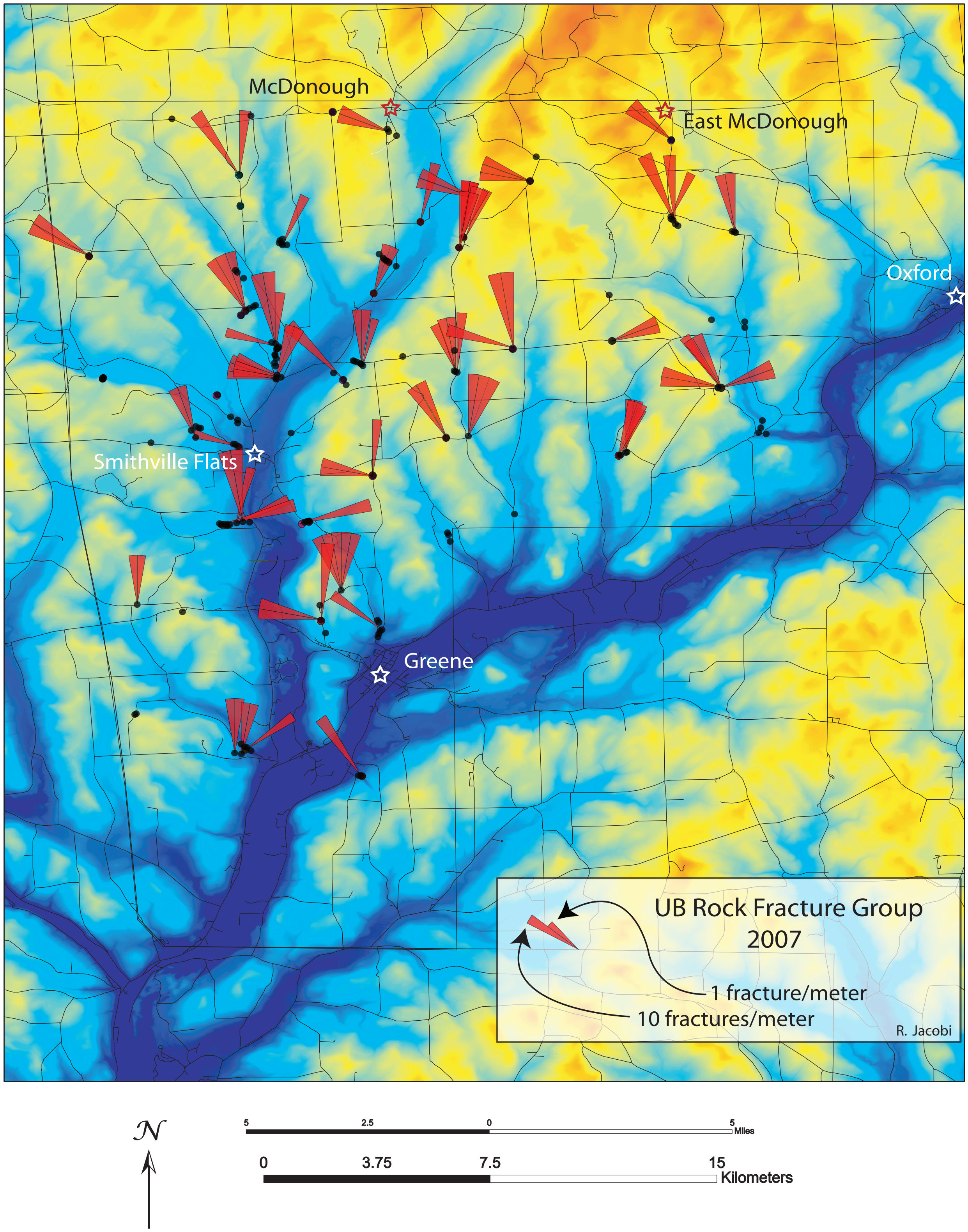

McDonough
East McDonough
Oxford
Smithville Flats
Greene
UB Rock Fracture Group
2007
1 fracture/meter
10 fractures/meter
R. Jacobi
N
5
2.5
0
5
Miles
0
3.75
7.5
15
Kilometers

Figure 10a

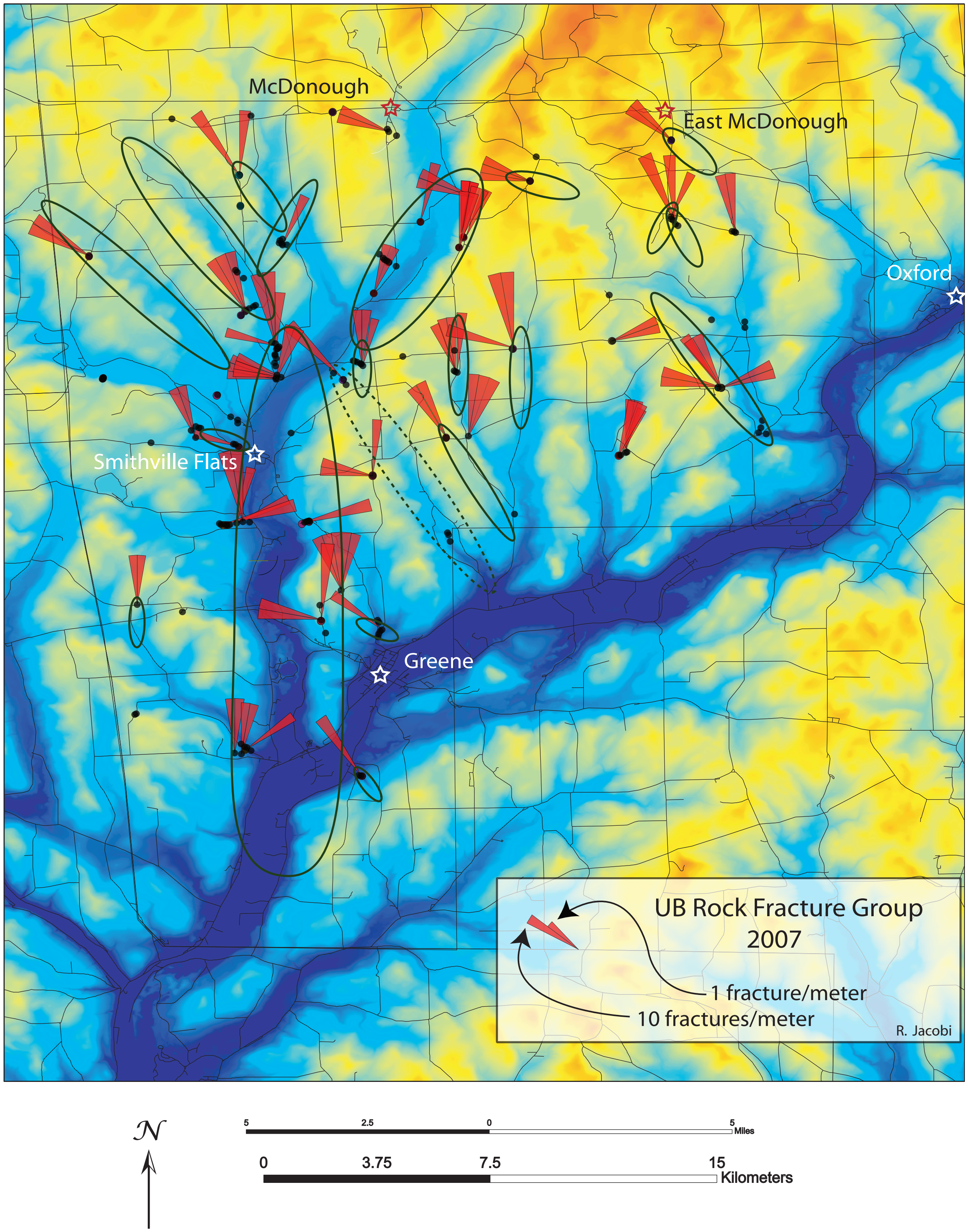
McDonough
East McDonough
Oxford
Smithville Flats
Greene
UB Rock Fracture Group
2007
1 fracture/meter
10 fractures/meter
R. Jacobi
N
5
2.5
0
5
Miles
0
3.75
7.5
15
Kilometers

Figure 10b

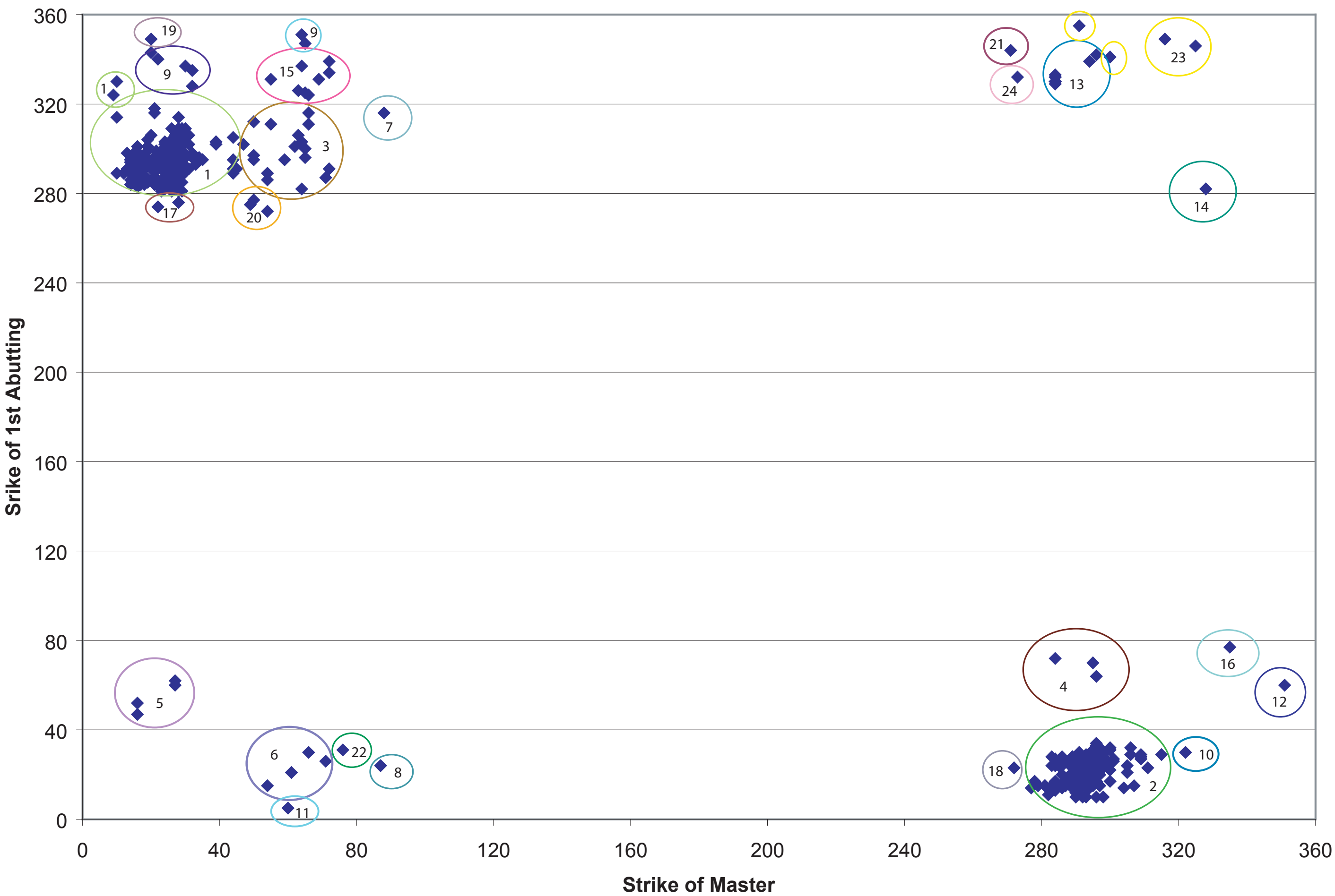

Master Set	Abutting Set		Master Set	Abutting Set		Master Set	Abutting Set	
NNE	WNW	1	NNE	NW	9	NNE	EW	17
WNW	NNE	2	NW	NNE	10	EW	NNE	18
ENE "a"	WNW	3	ENE "a"	NS	11	NNE	NS	19
WNW	ENE "a"	4	NS	ENE "a"	12	ENE "a"	EW	20
NNE	ENE "a"	5	WNW	NW	13	EW	NS	21
ENE "a"	NNE	6	NW	WNW	14	ENE "b"	NNE	22
NNE	EW	7	ENE "a"	NW	15	WNW	NS	23
EW	NNE	8	NW	ENE "b"	16	EW	NW	24

Figure 11a

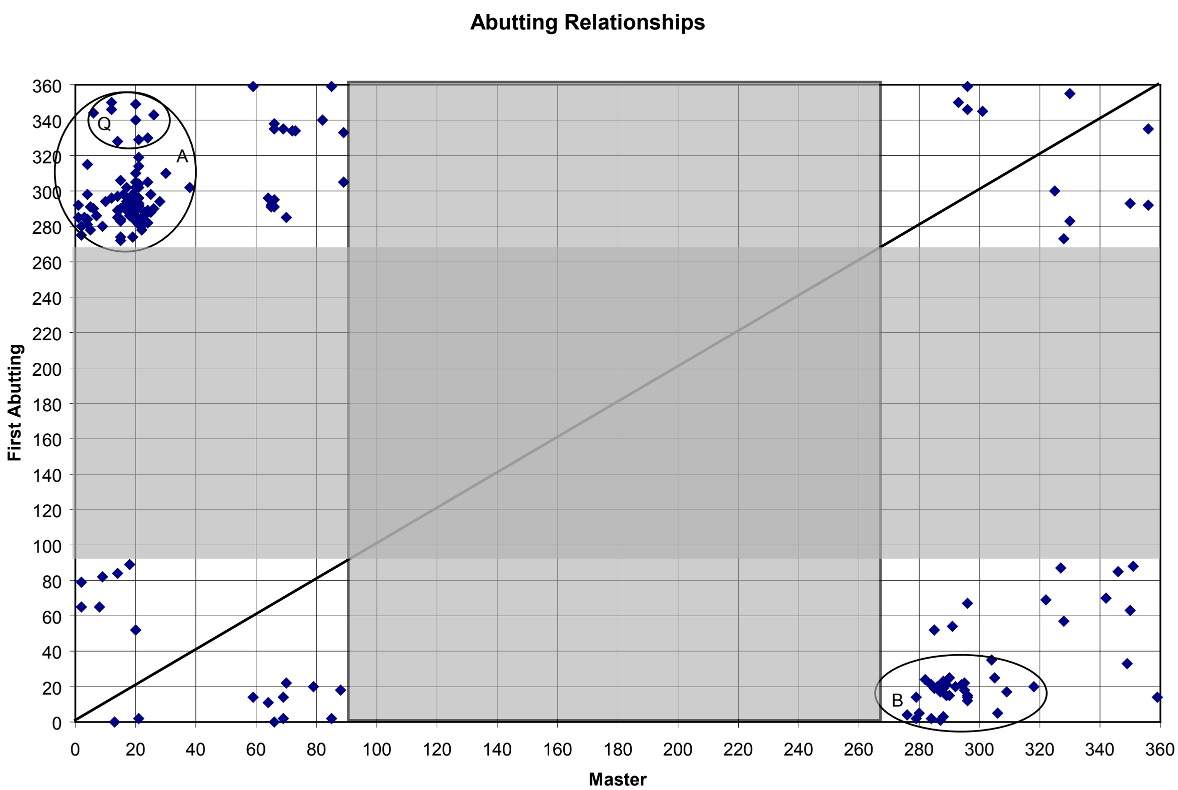

Abutting Relationships
First Abutting
Master
Q
A
B
0
20
40
60
80
100
120
140
160
180
200
220
240
260
280
300
320
340
360

Figure 11b

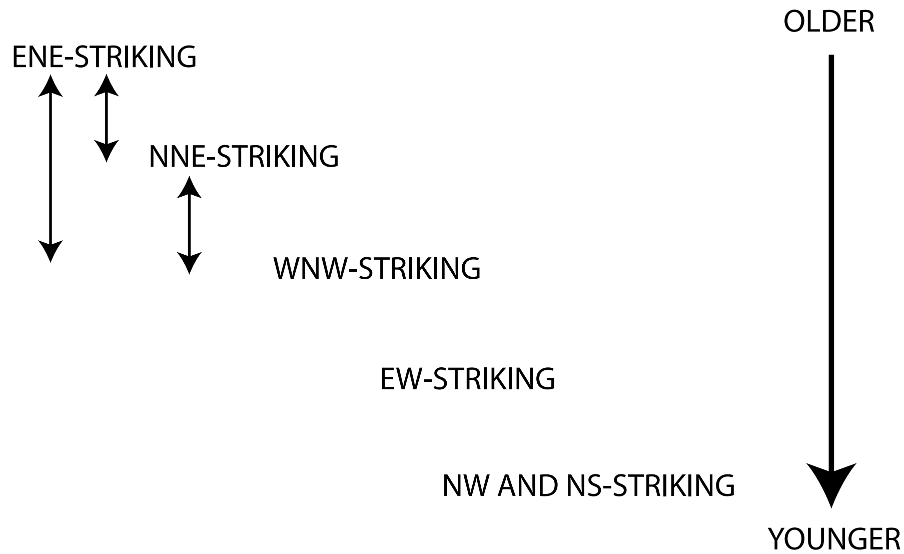
OLDER
ENE-STRIKING
NNE-STRIKING
WNW-STRIKING
EW-STRIKING
NW AND NS-STRIKING
YOUNGER

Figure 11c

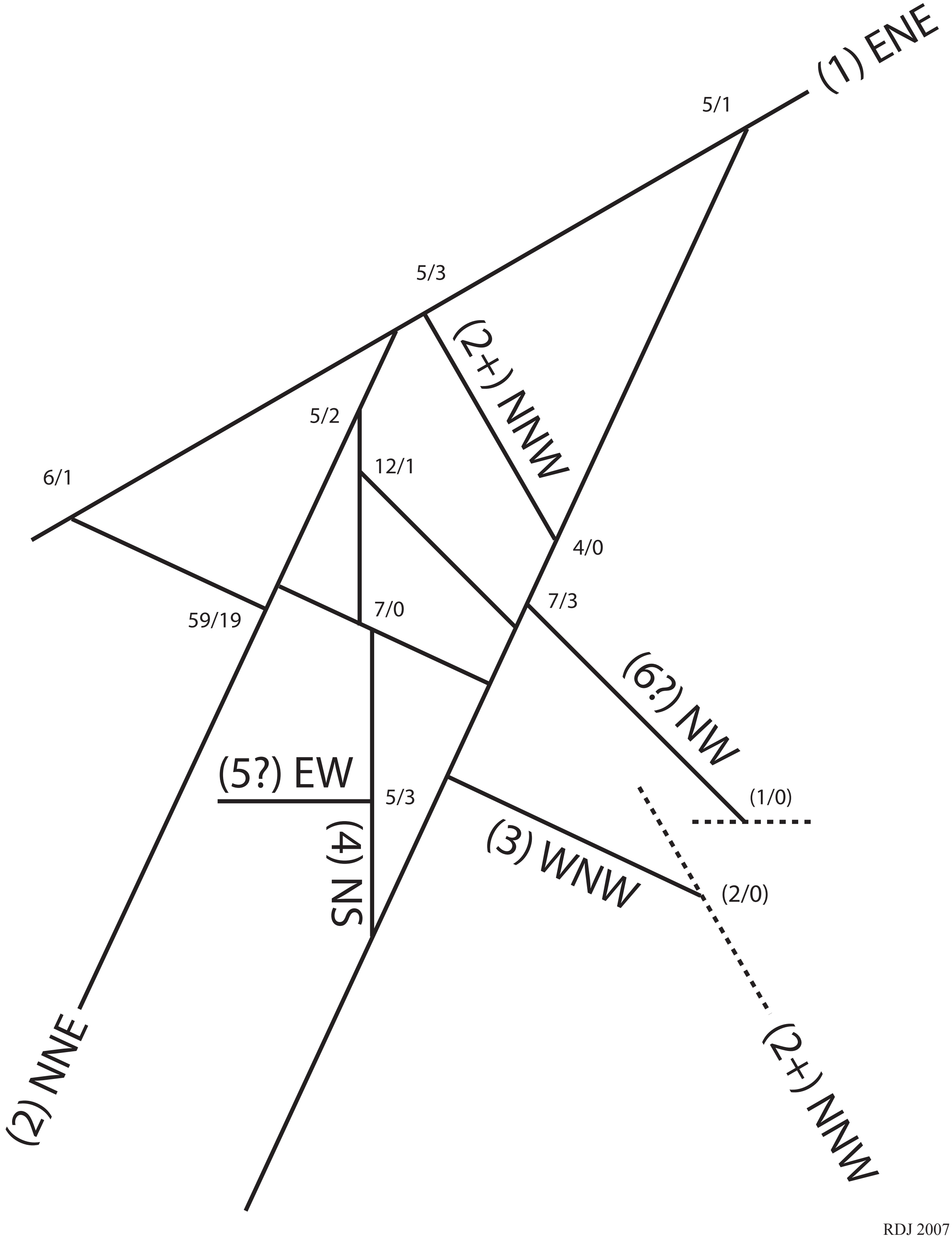
(1) ENE
5/1
5/3
(2+) NNW
5/2
12/1
6/1
4/0
7/3
7/0
59/19
(6?) NW
(5?) EW
5/3
(1/0)
(4) NS
(3) WNW
(2/0)
(2) NNE
(2+) NNW
RDJ 2007

Figure 11d

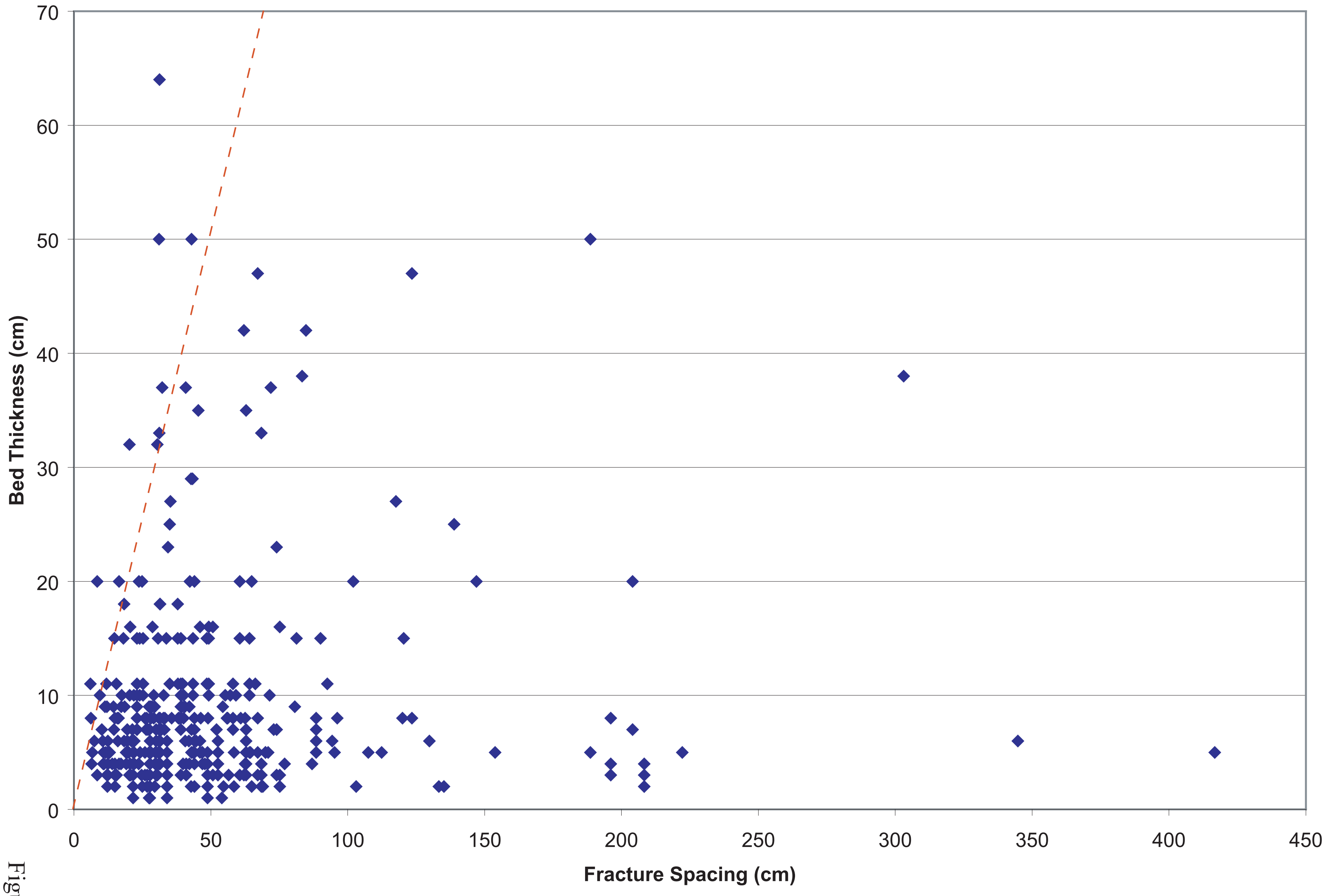

Bed Thickness (cm)
0
10
20
30
40
50
60
70
0
50
100
150
200
250
300
350
400
450
Fracture Spacing (cm)

Figure 12

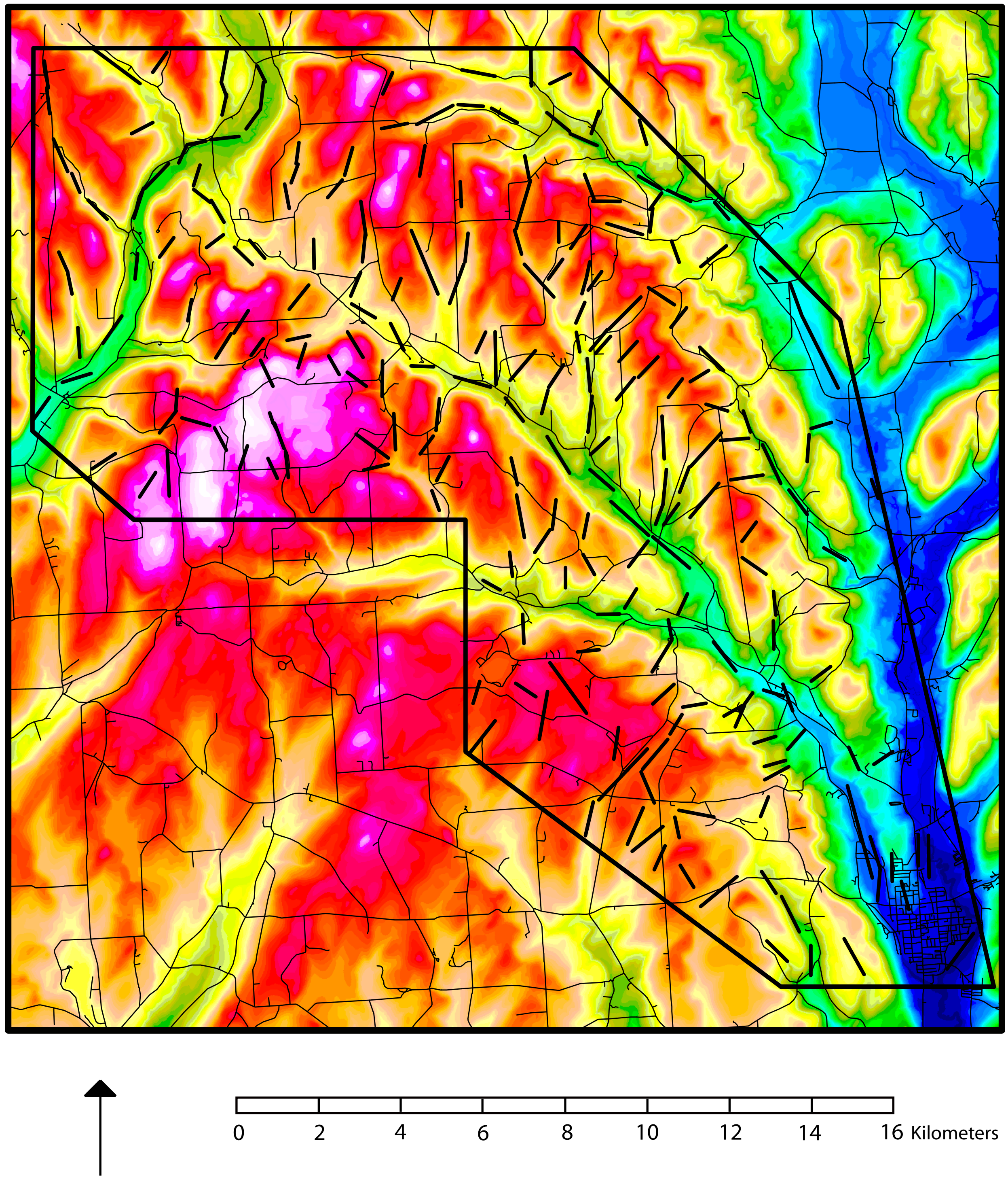

Figure 13

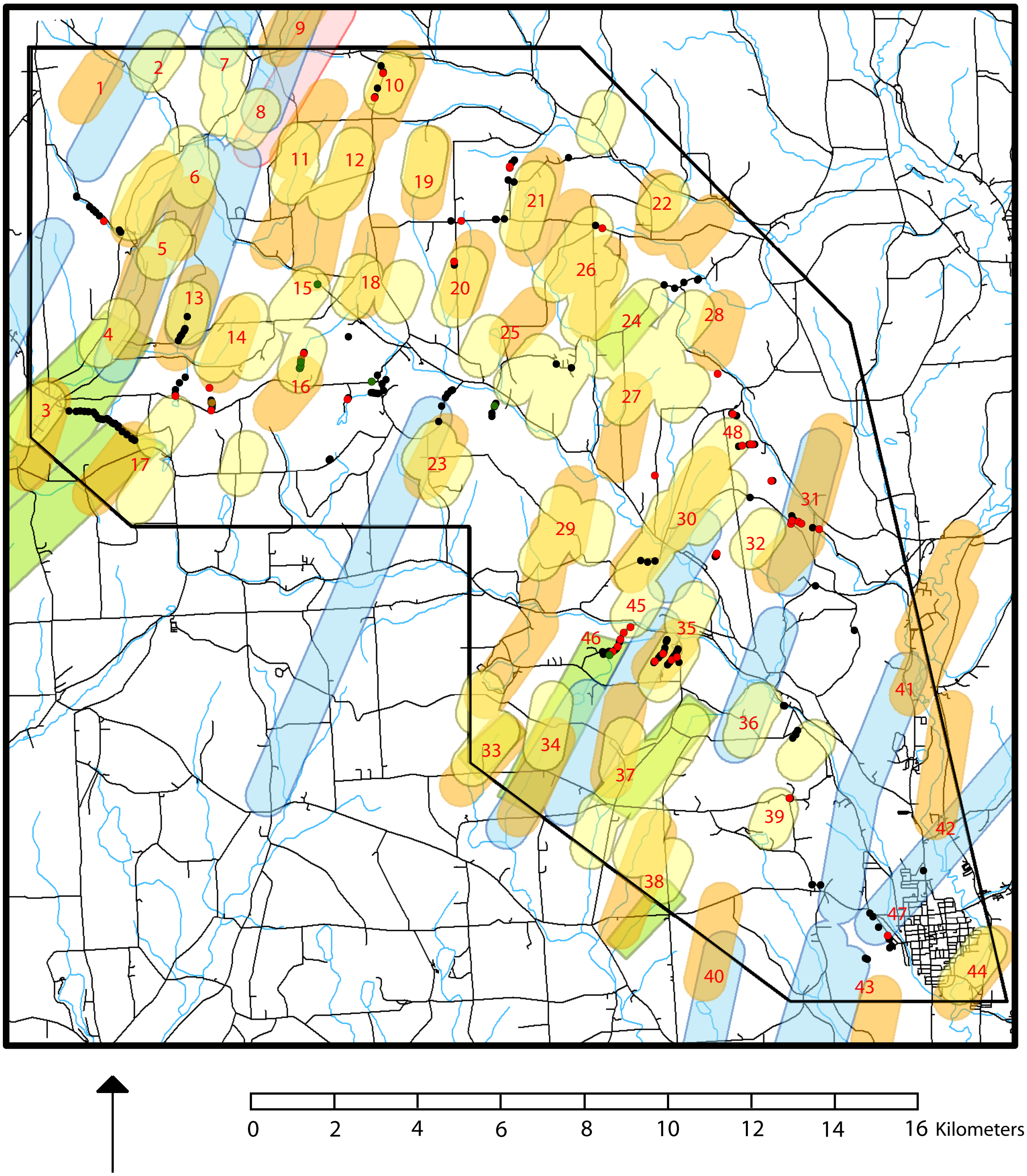

1
2
3
4
5
6
7
8
9
10
11
12
13
14
15
16
17
18
19
20
21
22
23
24
25
26
27
28
29
30
31
32
33
34
35
36
37
38
39
40
41
42
43
44
45
46
47
48
0
2
4
6
8
10
12
14
16 Kilometers

Figure 14a

LEGEND FOR LINEAMENT ZONE AND INSET MAPS

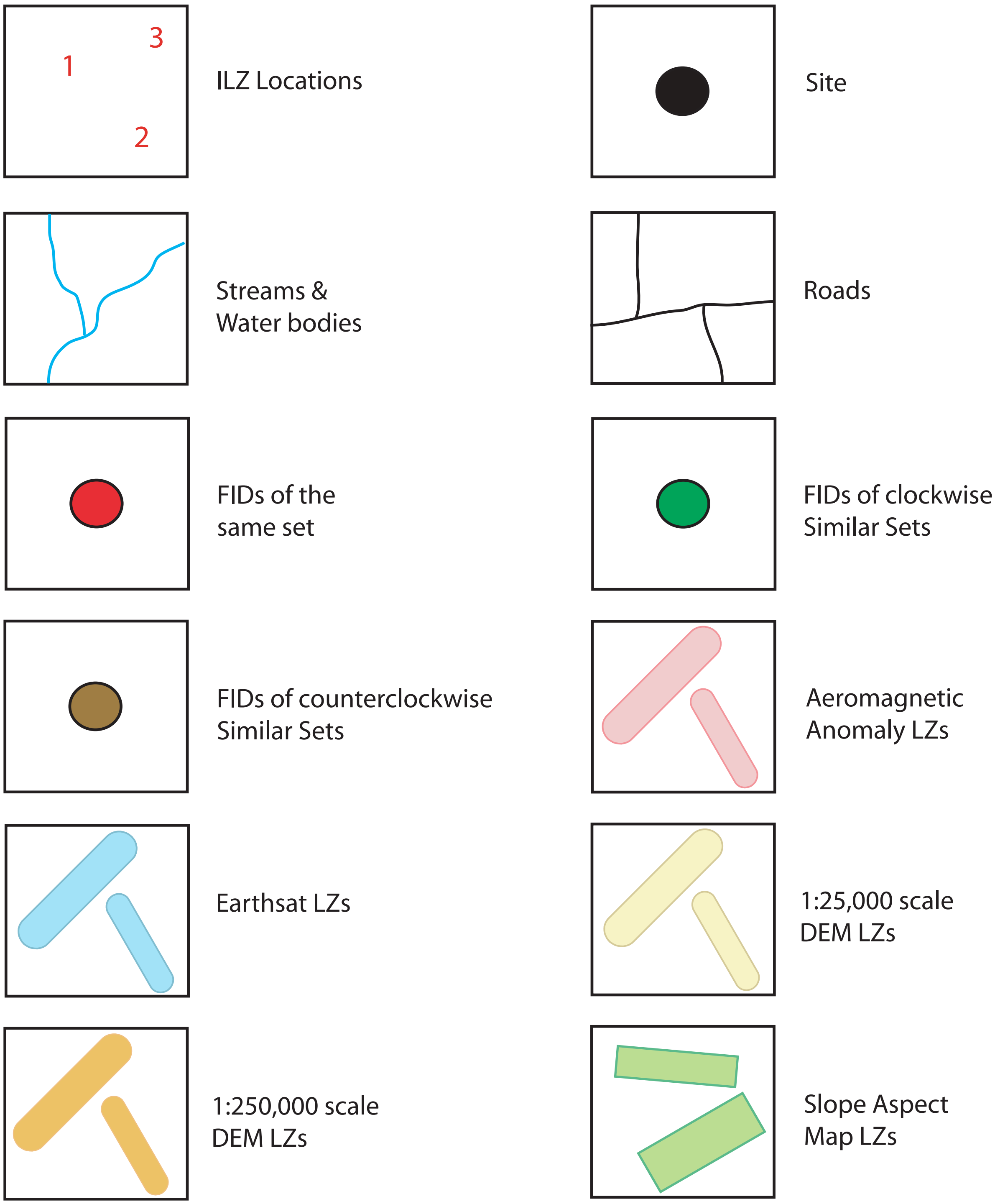

Figure 14b

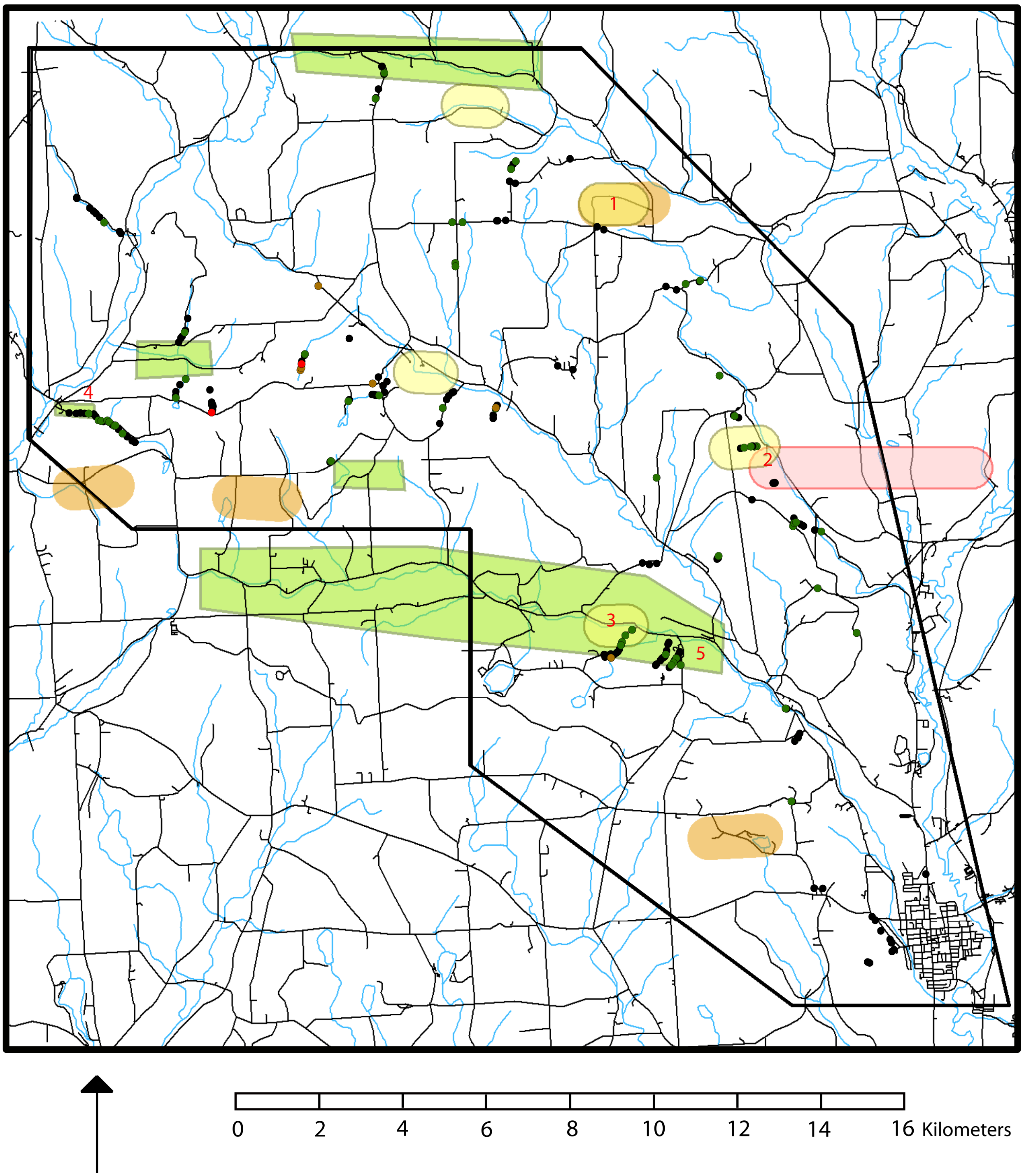

Figure 15

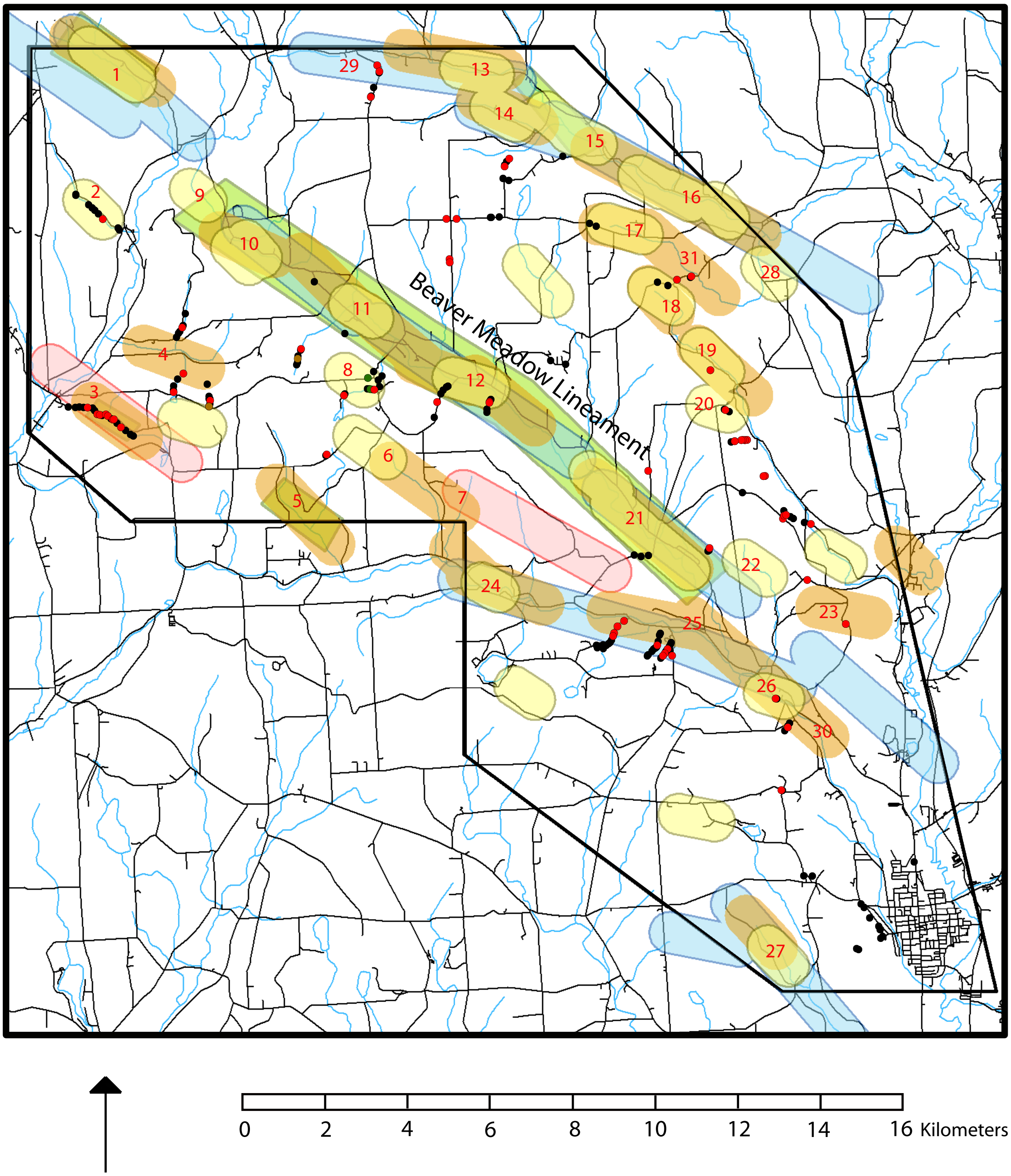
Beaver Meadow Lineament
1
2
3
4
5
6
7
8
9
10
11
12
13
14
15
16
17
18
19
20
21
22
23
24
25
26
27
28
29
30
31
0
2
4
6
8
10
12
14
16 Kilometers

Figure 16

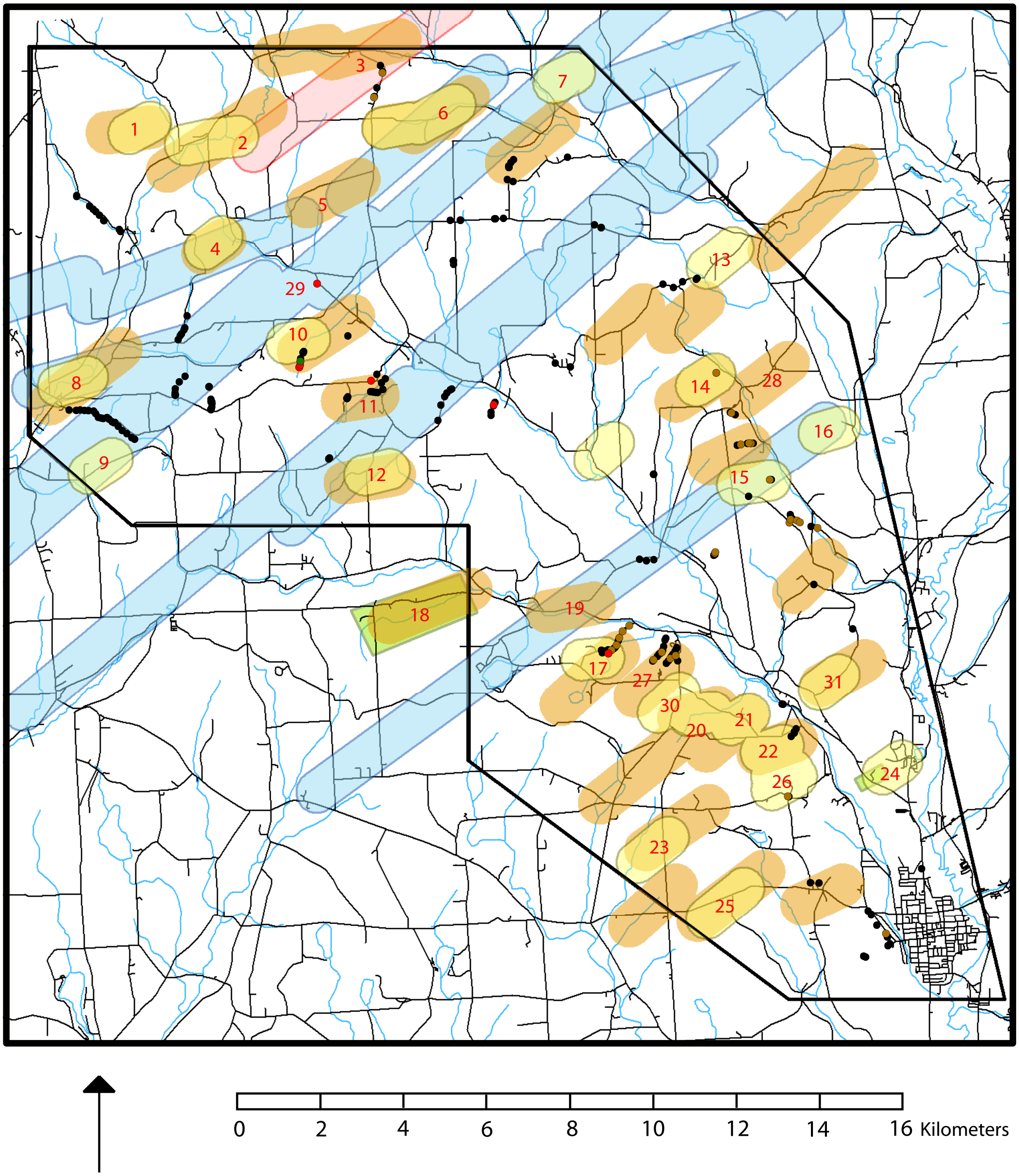
1
2
3
4
5
6
7
8
9
10
11
12
13
14
15
16
17
18
19
20
21
22
23
24
25
26
27
28
29
30
31
0
2
4
6
8
10
12
14
16 Kilometers

Figure 17

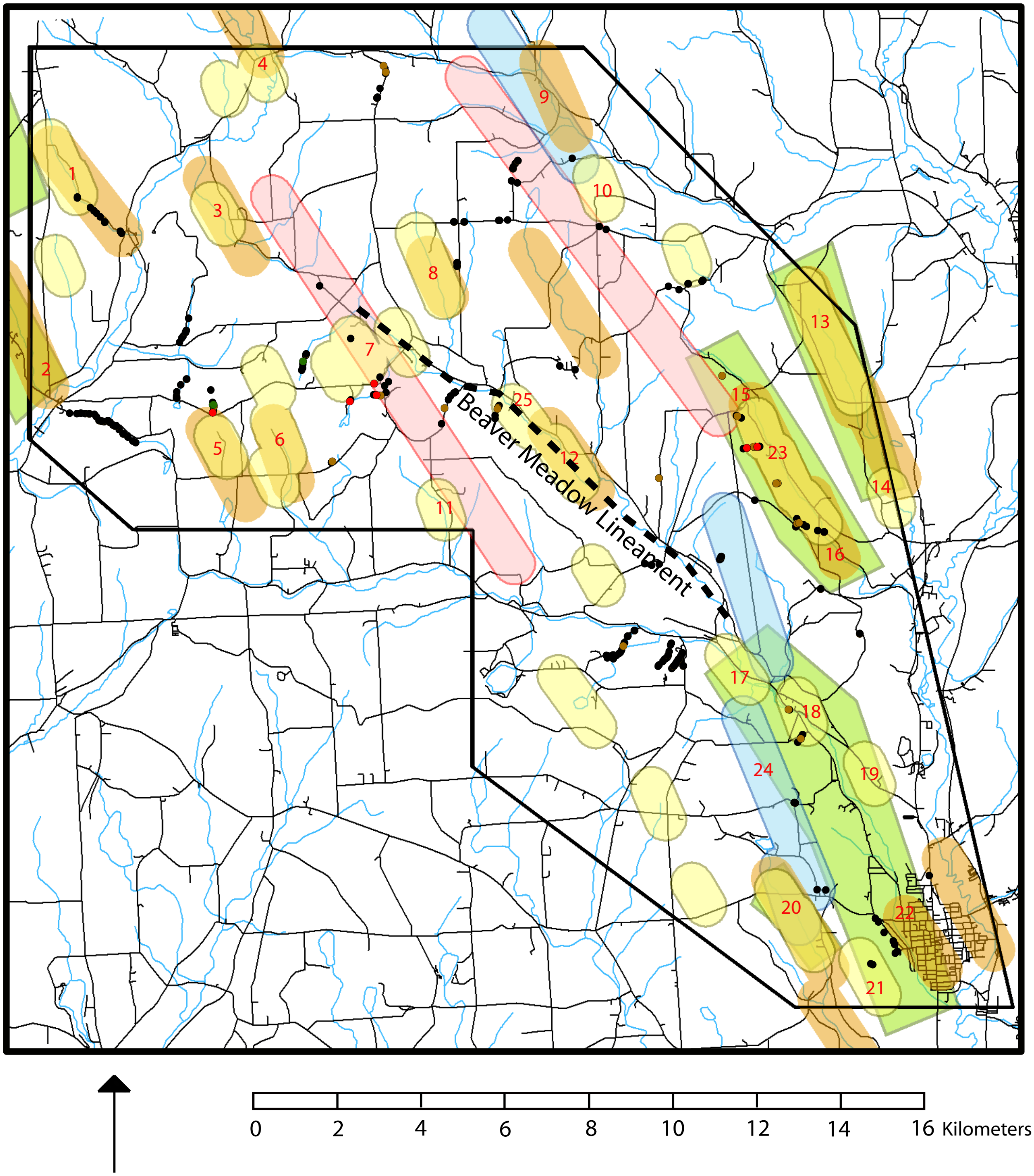

1
2
3
4
5
6
7
8
9
10
11
12
13
14
15
16
17
18
19
20
21
22
23
24
25
Beaver Meadow Lineament
0
2
4
6
8
10
12
14
16 Kilometers

Figure 18

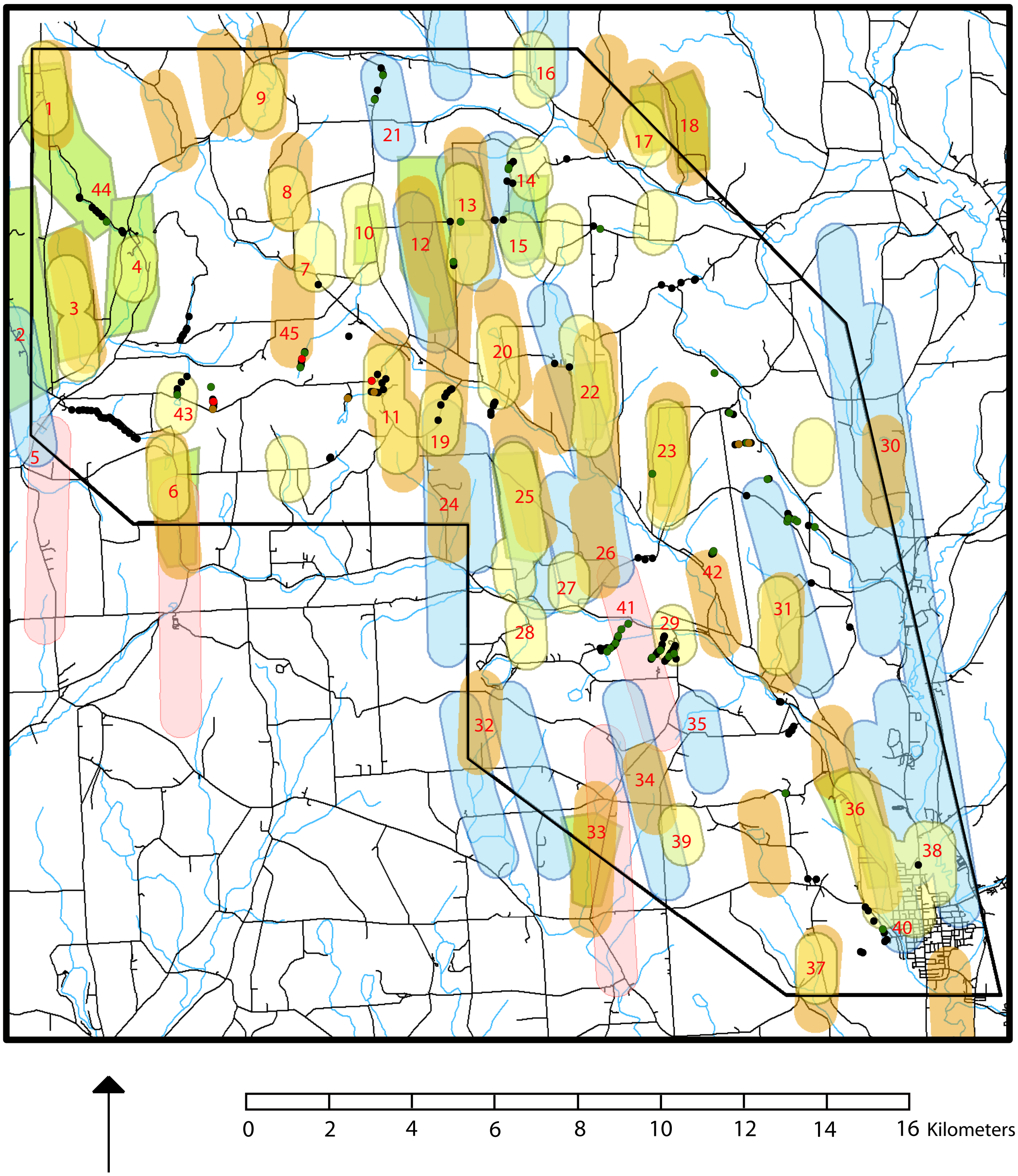
1
2
3
4
5
6
7
8
9
10
11
12
13
14
15
16
17
18
19
20
21
22
23
24
25
26
27
28
29
30
31
32
33
34
35
36
37
38
39
40
41
42
43
44
45
0
2
4
6
8
10
12
14
16 Kilometers

Figure 19

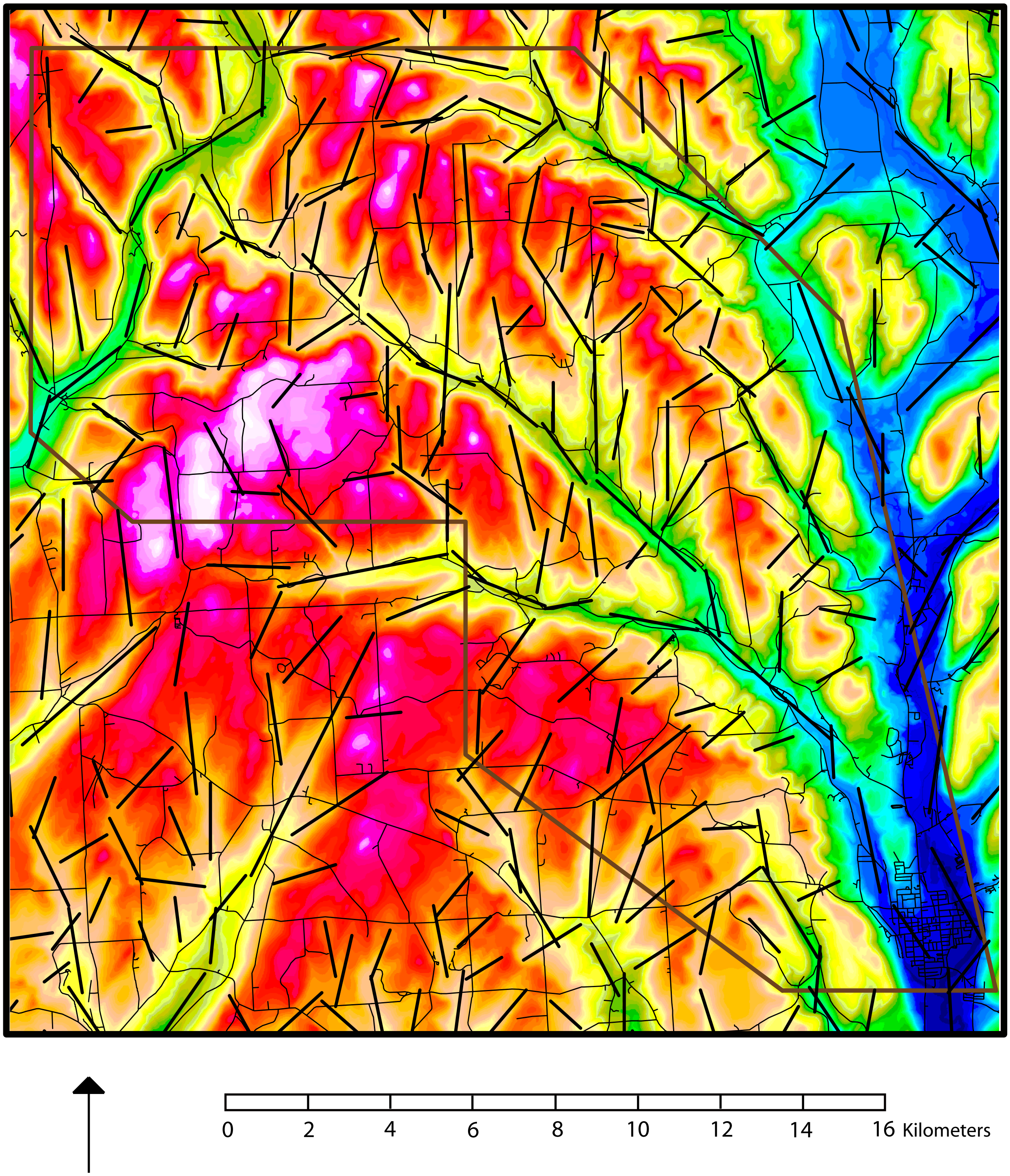

Figure 20

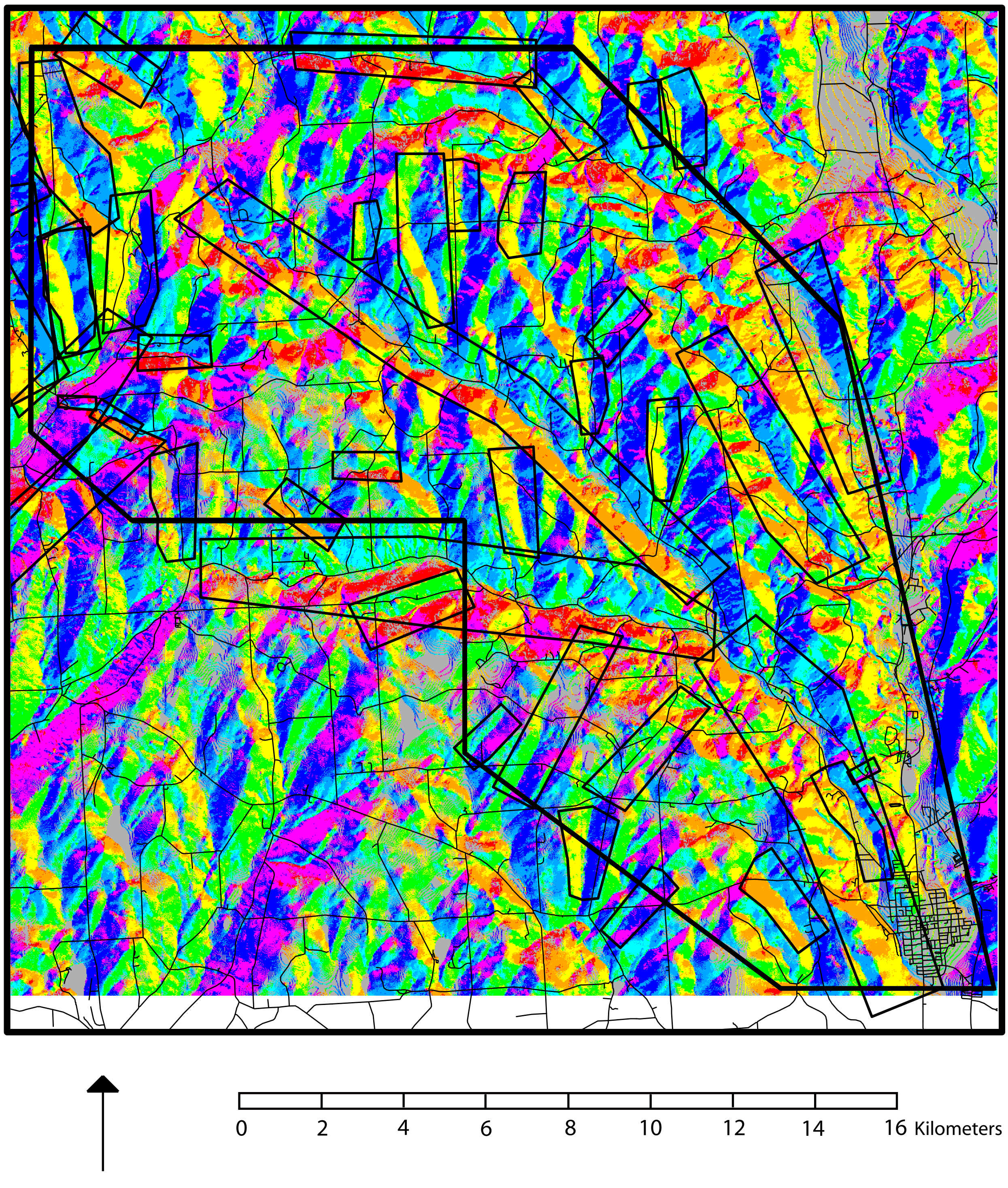

Figure 21a

LEGEND FOR SLOPE ASPECT MAP

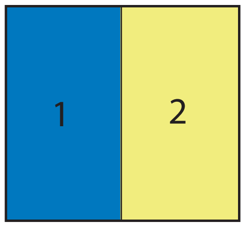

NS-trending Lineament
(East-dipping [2] & West-dipping [1] slope)

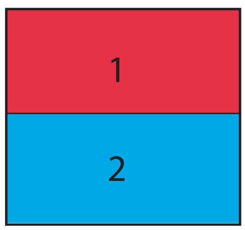

EW-trending Lineament
(North-dipping [1] and South-dipping [2] slope)

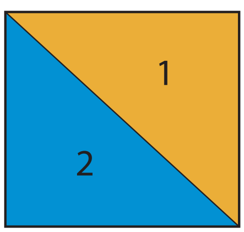

NW-trending Lineament
(SE-dipping [1] & NW-dipping [2] slope)

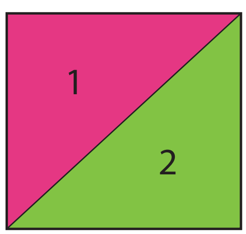

NE-trending Lineament
(NW-dipping [1] & SE-dipping [2] Slope)

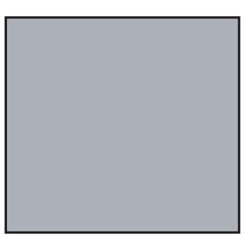

Flat Surface

Figure 21b

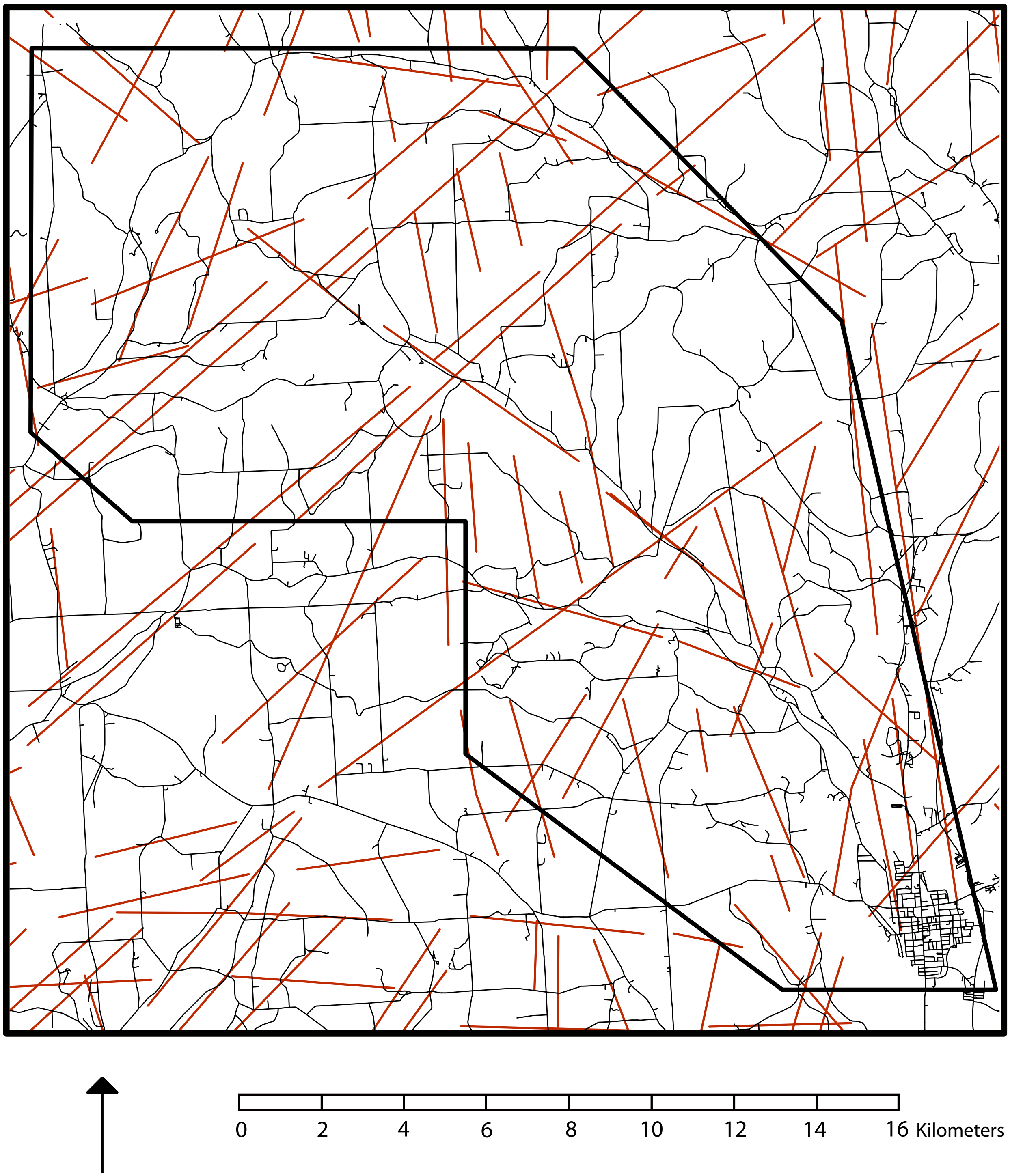

Figure 22

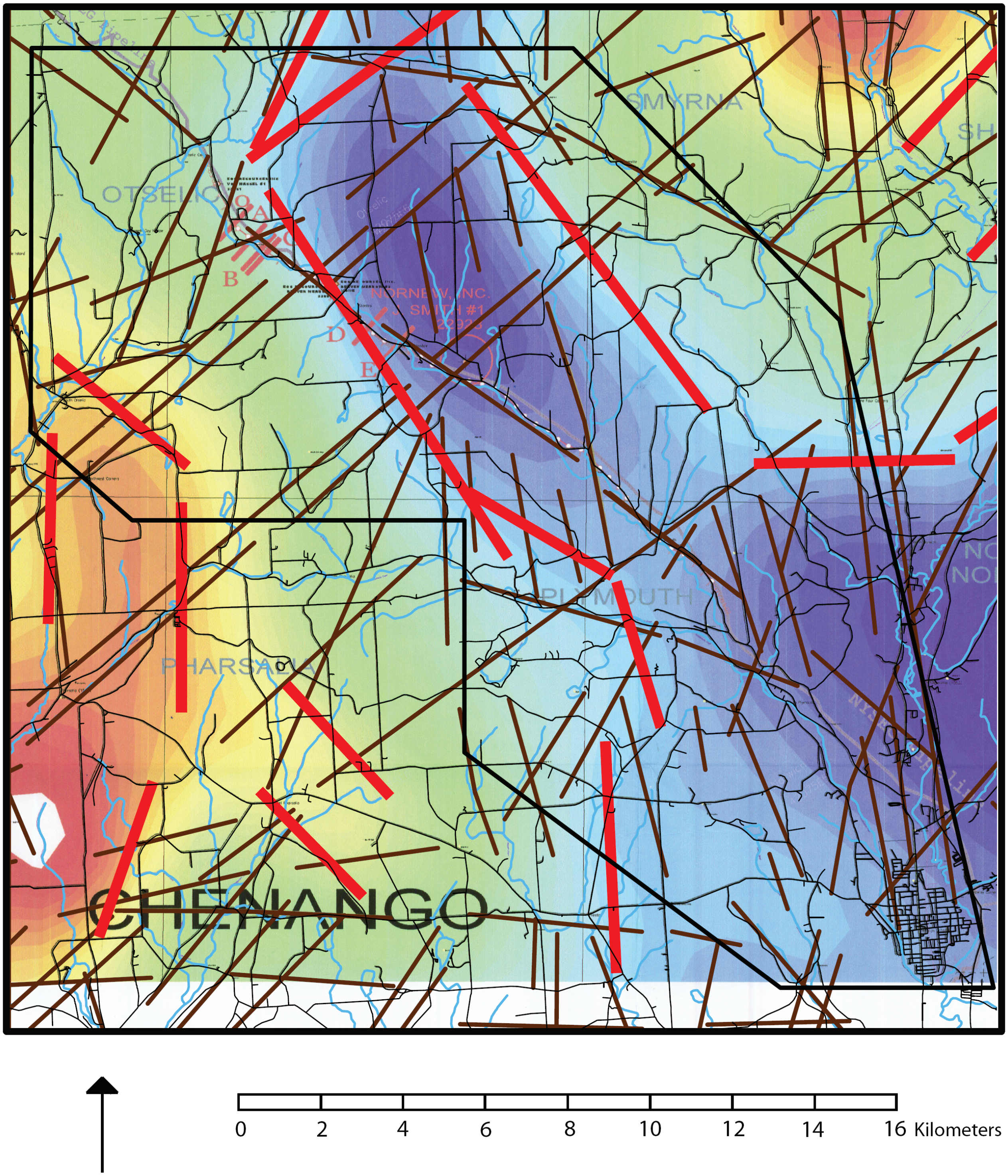

OTSELIC
SMYRNA
PLYMOUTH
PHARSALIA
CHENANGO
NORNEW, INC.
A
B
D
E
0
2
4
6
8
10
12
14
16 Kilometers

Figure 23

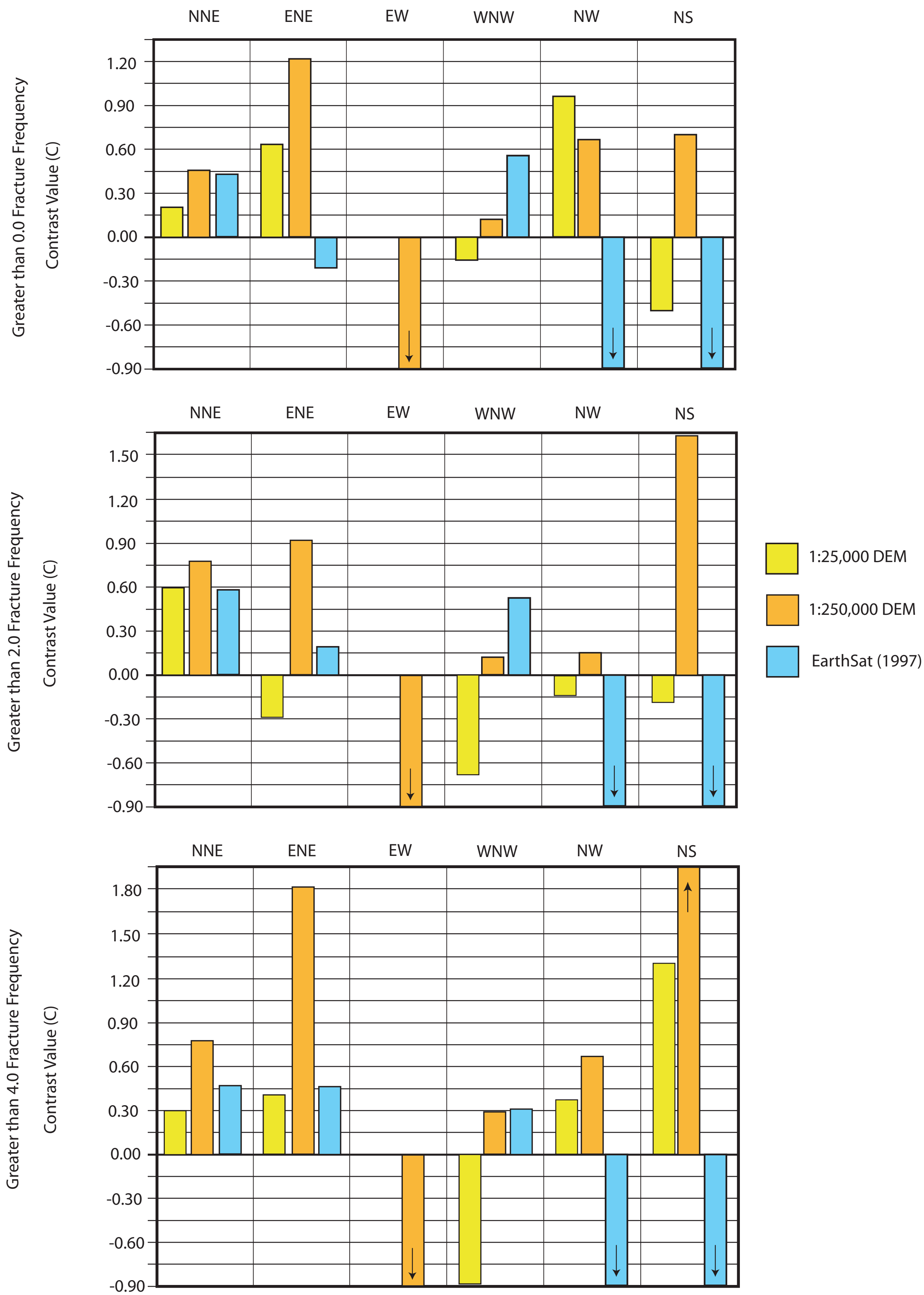
NNE
ENE
EW
WNW
NW
NS
Greater than 0.0 Fracture Frequency
Contrast Value (C)
1.20
0.90
0.60
0.30
0.00
-0.30
-0.60
-0.90
Greater than 2.0 Fracture Frequency
1.50
Greater than 4.0 Fracture Frequency
1.80
1:25,000 DEM
1:250,000 DEM
EarthSat (1997)

Figure 24

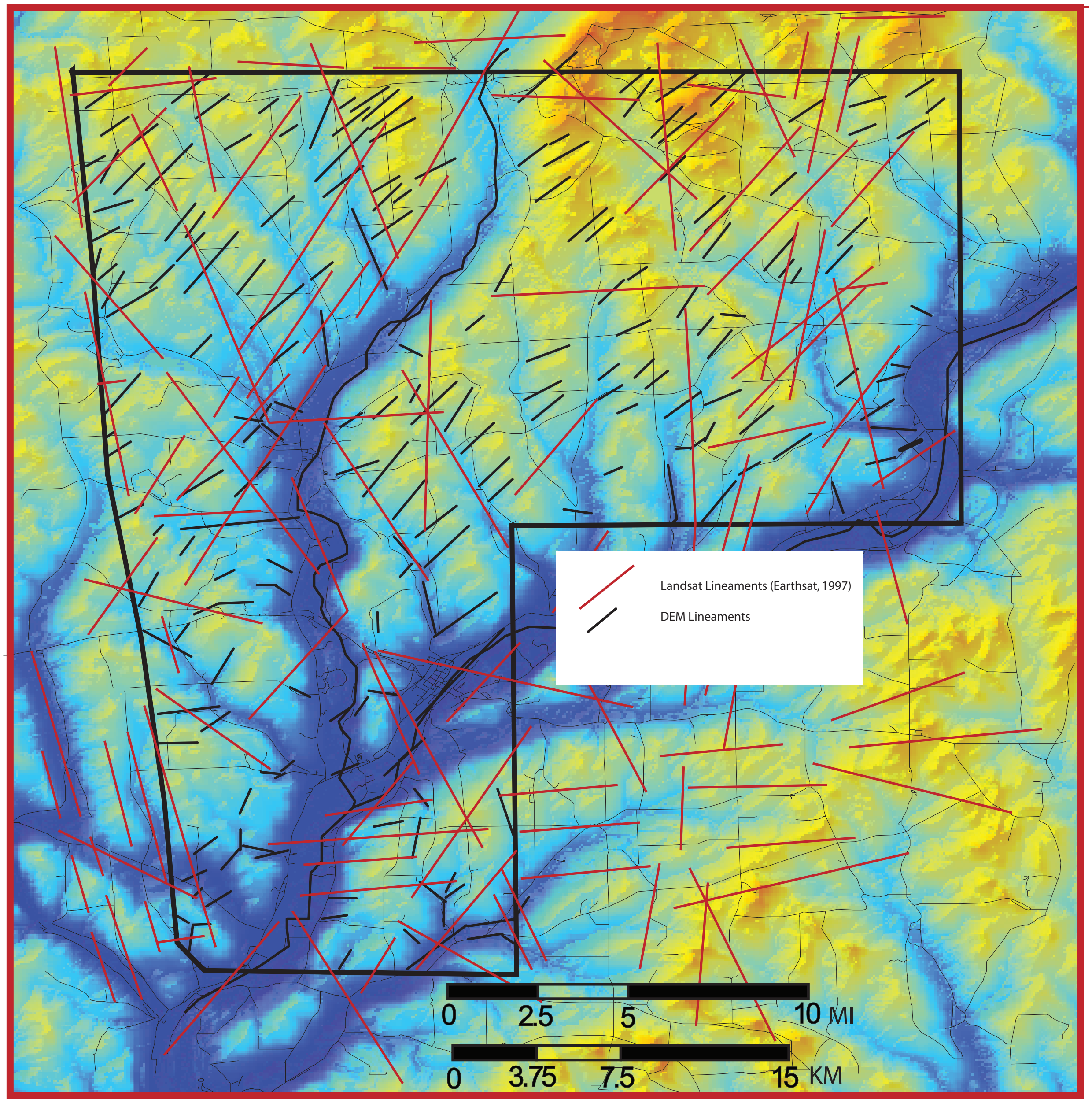
Landsat Lineaments (Earthsat, 1997)
DEM Lineaments
0
2.5
5
10 MI
0
3.75
7.5
15 KM

Figure 25

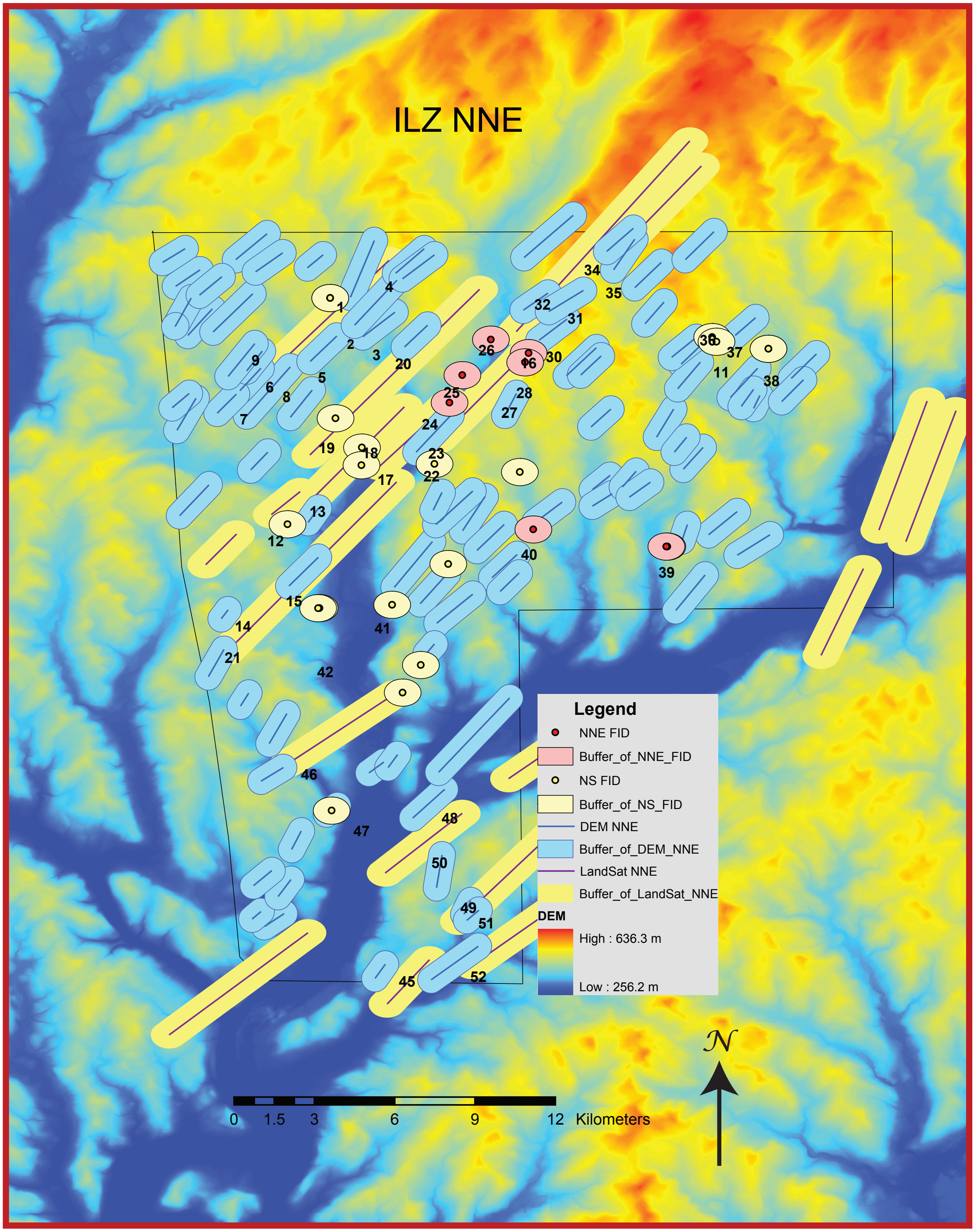
ILZ NNE
Legend
NNE FID
Buffer_of_NNE_FID
NS FID
Buffer_of_NS_FID
DEM NNE
Buffer_of_DEM_NNE
LandSat NNE
Buffer_of_LandSat_NNE
DEM
High : 636.3 m
Low : 256.2 m
0 1.5 3 6 9 12 Kilometers
N

Figure 26

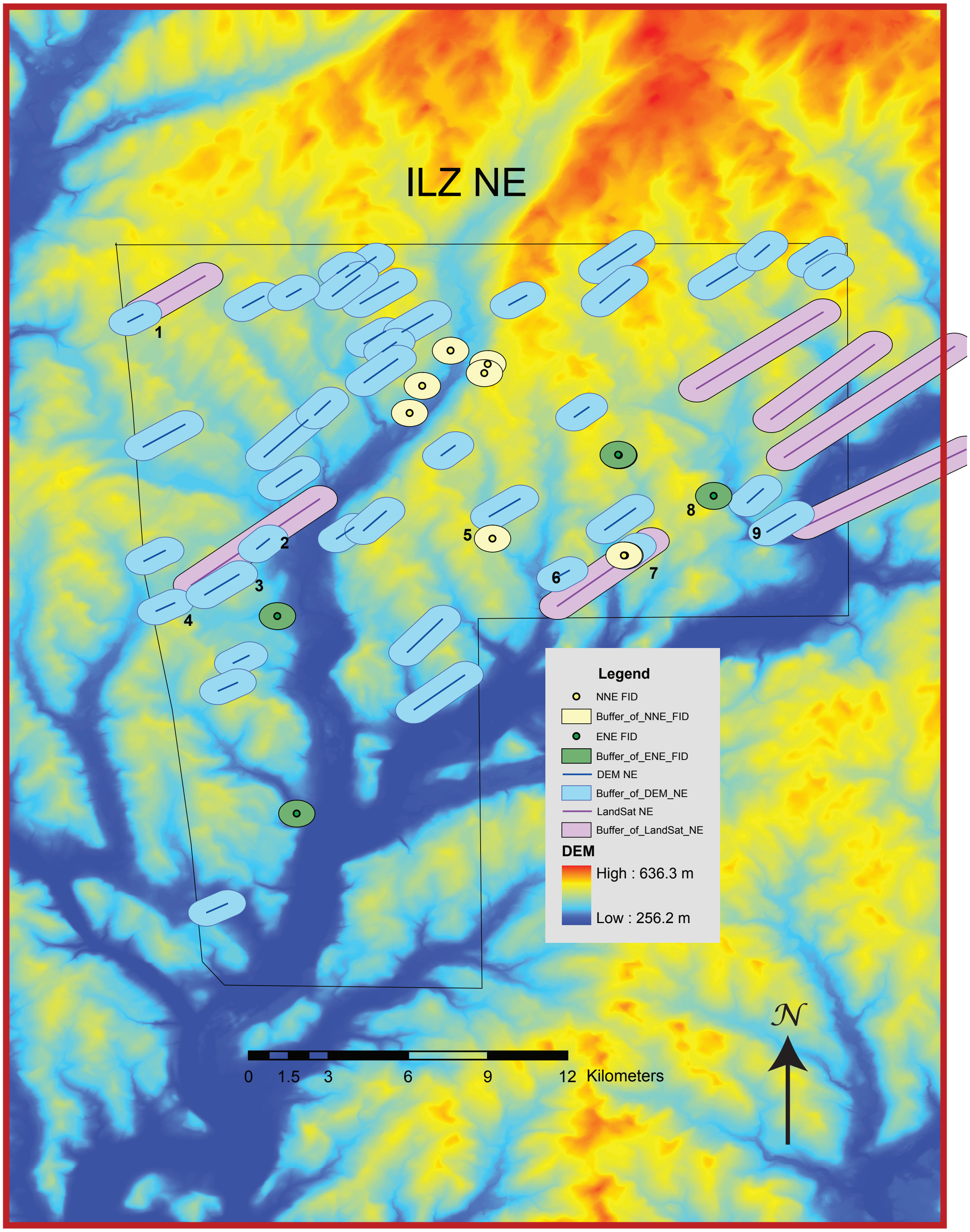

ILZ NE
1
2
3
4
5
6
7
8
9
Legend
NNE FID
Buffer_of_NNE_FID
ENE FID
Buffer_of_ENE_FID
DEM NE
Buffer_of_DEM_NE
LandSat NE
Buffer_of_LandSat_NE
DEM
High : 636.3 m
Low : 256.2 m
0 1.5 3 6 9 12 Kilometers
N

Figure 27

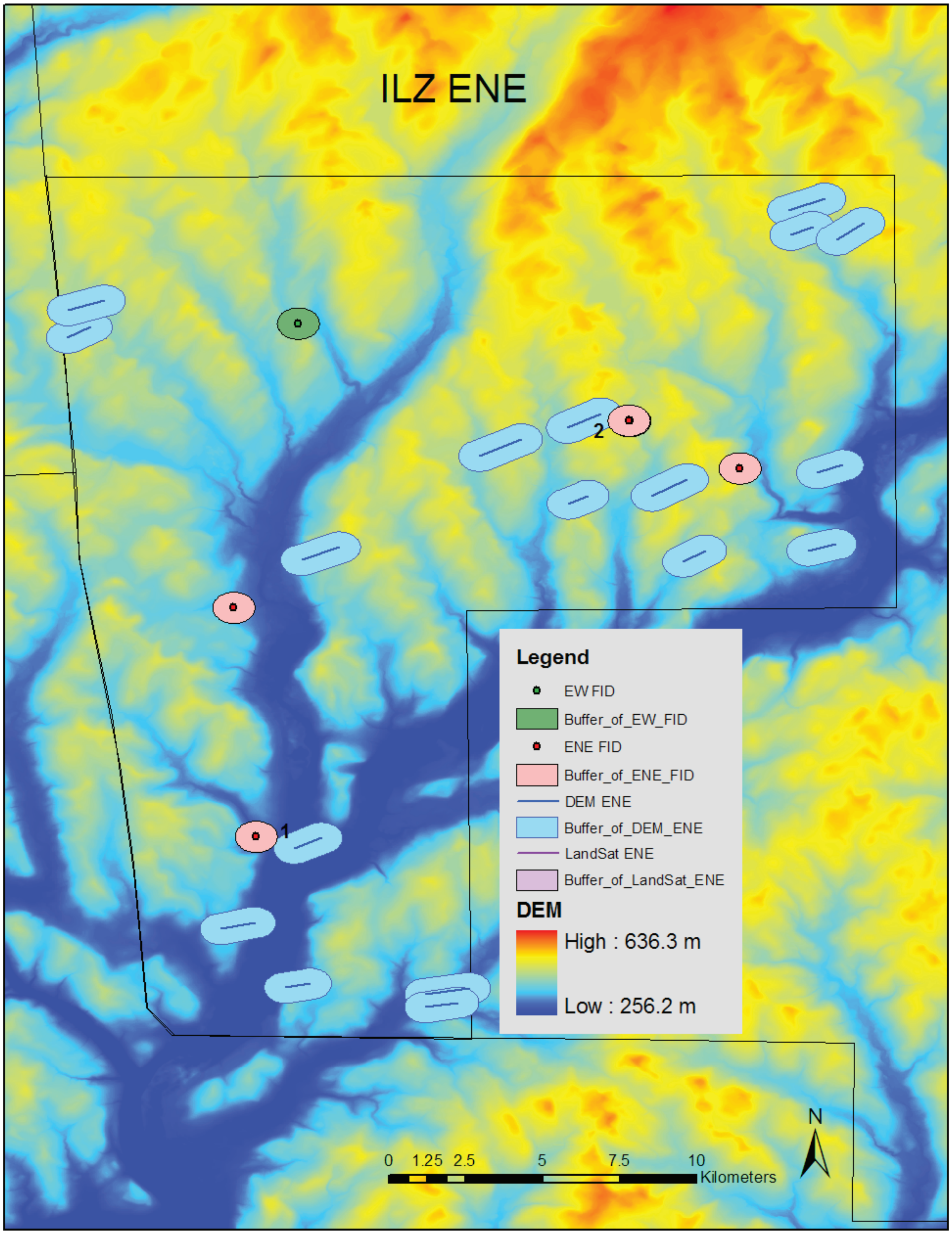
ILZ ENE
1
2
Legend
EW FID
Buffer_of_EW_FID
ENE FID
Buffer_of_ENE_FID
DEM ENE
Buffer_of_DEM_ENE
LandSat ENE
Buffer_of_LandSat_ENE
DEM
High : 636.3 m
Low : 256.2 m
0 1.25 2.5 5 7.5 10
Kilometers
N

Figure 28

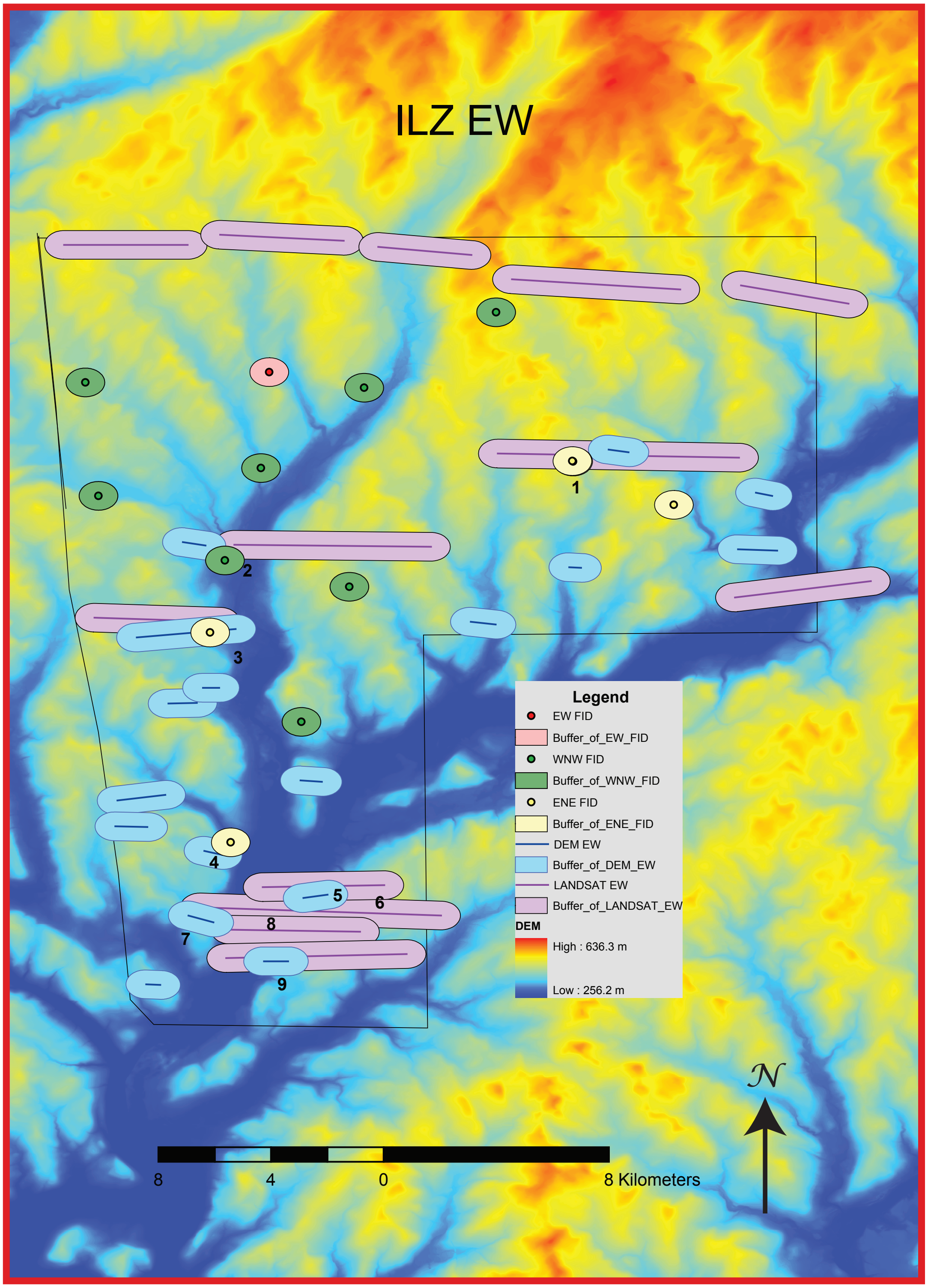
ILZ EW
1
2
3
4
5
6
7
8
9
Legend
EW FID
Buffer_of_EW_FID
WNW FID
Buffer_of_WNW_FID
ENE FID
Buffer_of_ENE_FID
DEM EW
Buffer_of_DEM_EW
LANDSAT EW
Buffer_of_LANDSAT_EW
DEM
High : 636.3 m
Low : 256.2 m
8
4
0
8 Kilometers
N

Figure 29

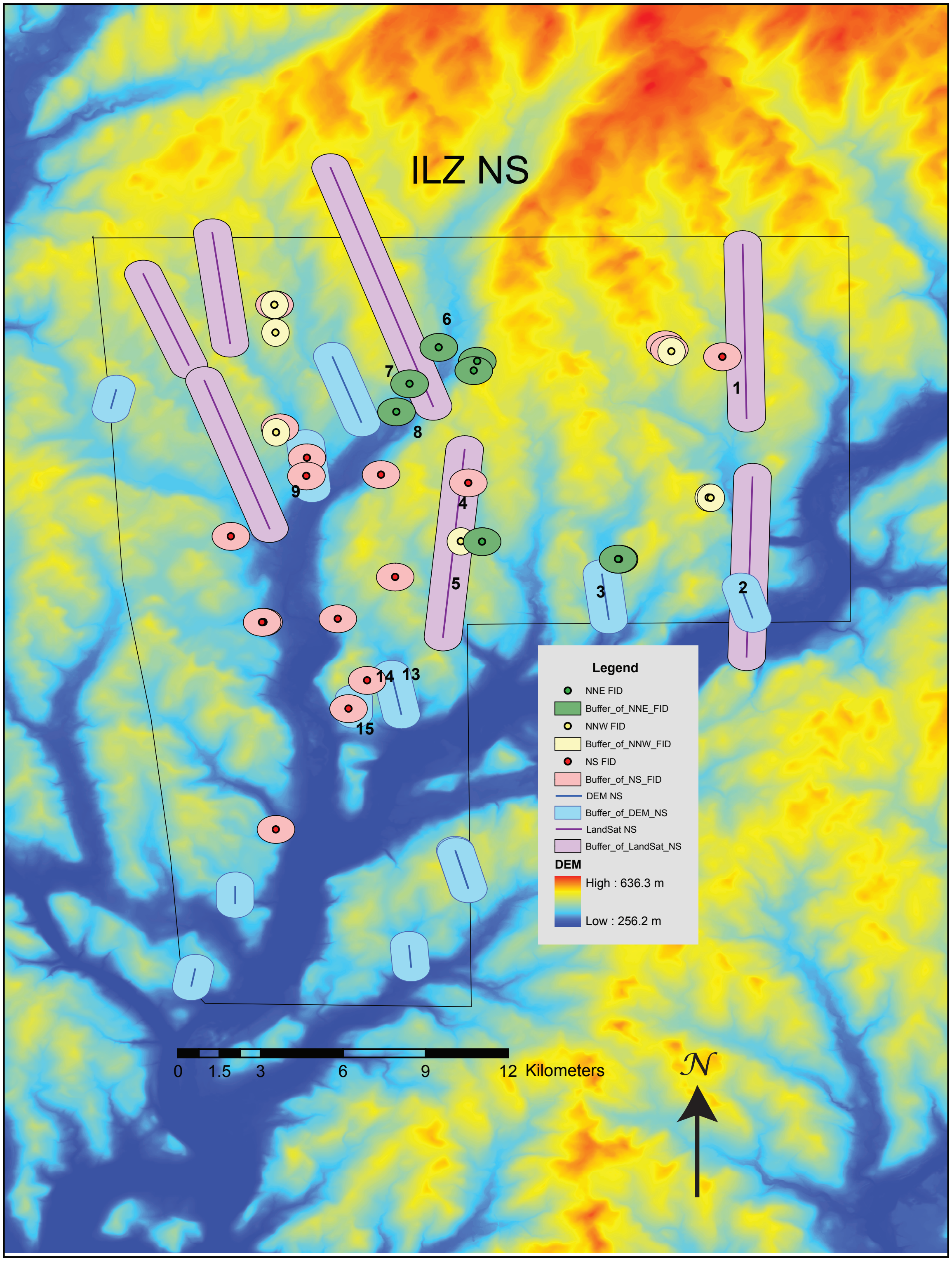
ILZ NS
1
2
3
4
5
6
7
8
9
13
14
15
Legend
NNE FID
Buffer_of_NNE_FID
NNW FID
Buffer_of_NNW_FID
NS FID
Buffer_of_NS_FID
DEM NS
Buffer_of_DEM_NS
LandSat NS
Buffer_of_LandSat_NS
DEM
High : 636.3 m
Low : 256.2 m
0 1.5 3 6 9 12 Kilometers
N

Figure 30

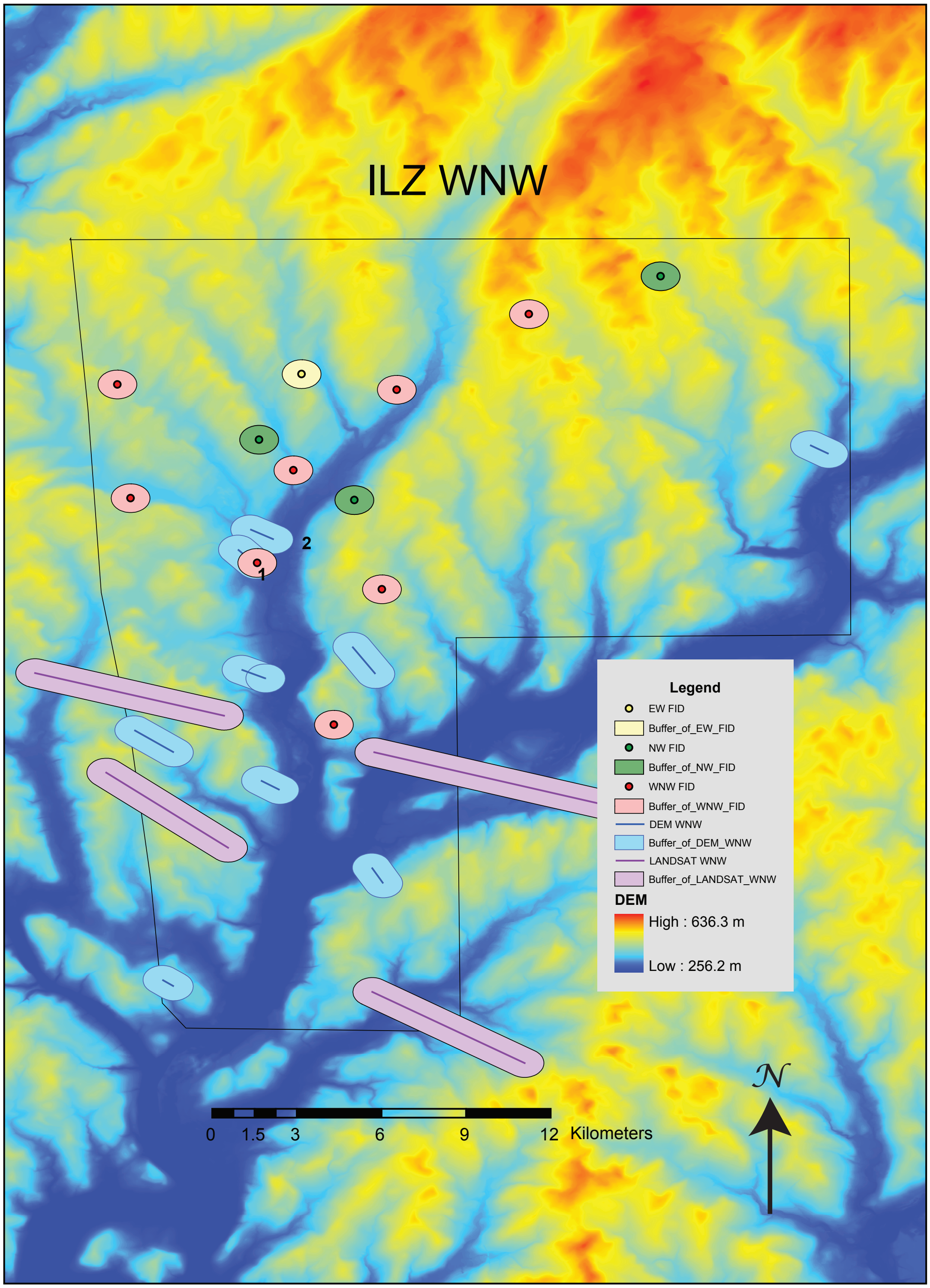

ILZ WNW
2
1
Legend
EW FID
Buffer_of_EW_FID
NW FID
Buffer_of_NW_FID
WNW FID
Buffer_of_WNW_FID
DEM WNW
Buffer_of_DEM_WNW
LANDSAT WNW
Buffer_of_LANDSAT_WNW
DEM
High : 636.3 m
Low : 256.2 m
0 1.5 3 6 9 12 Kilometers
N

Figure 31

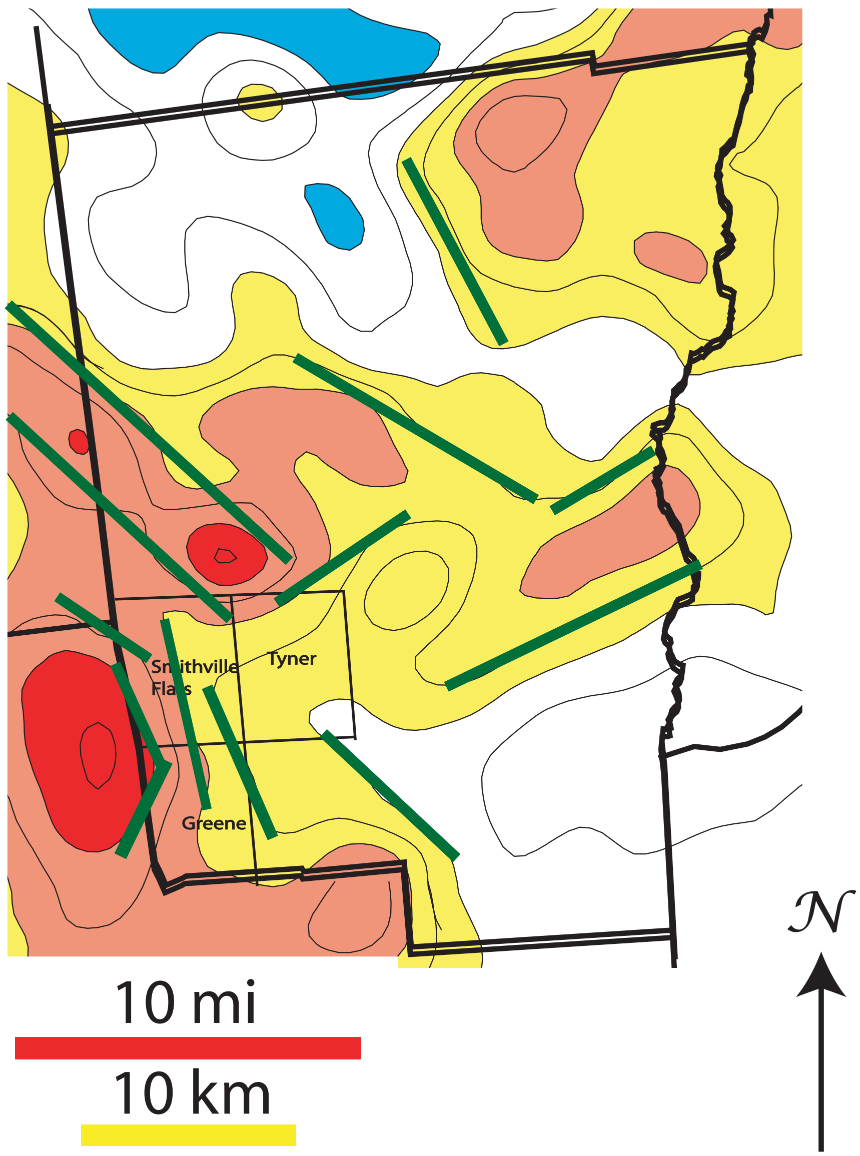

Figure 32

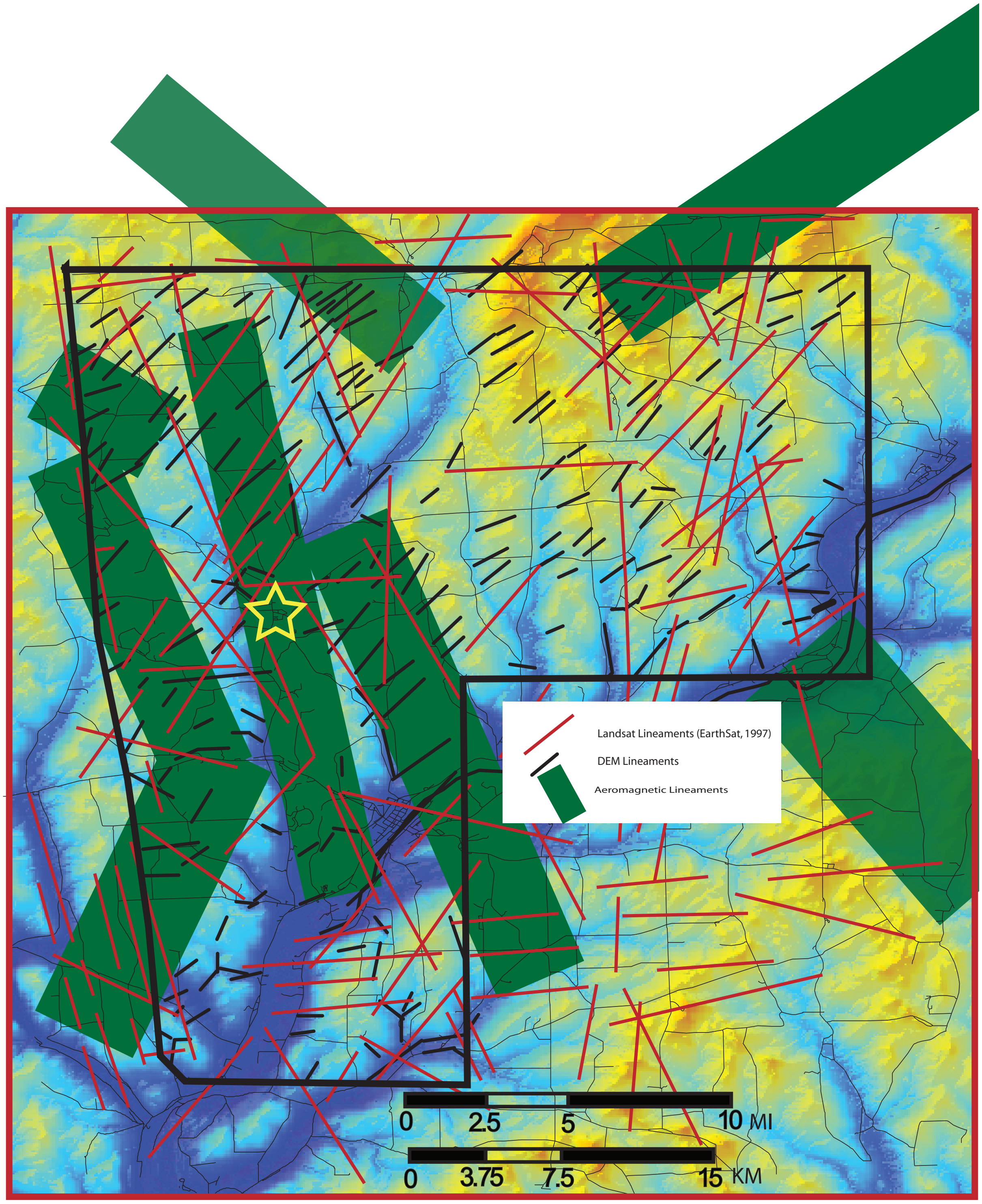
Landsat Lineaments (EarthSat, 1997)
DEM Lineaments
Aeromagnetic Lineaments
0 2.5 5 10 MI
0 3.75 7.5 15 KM

Figure 33

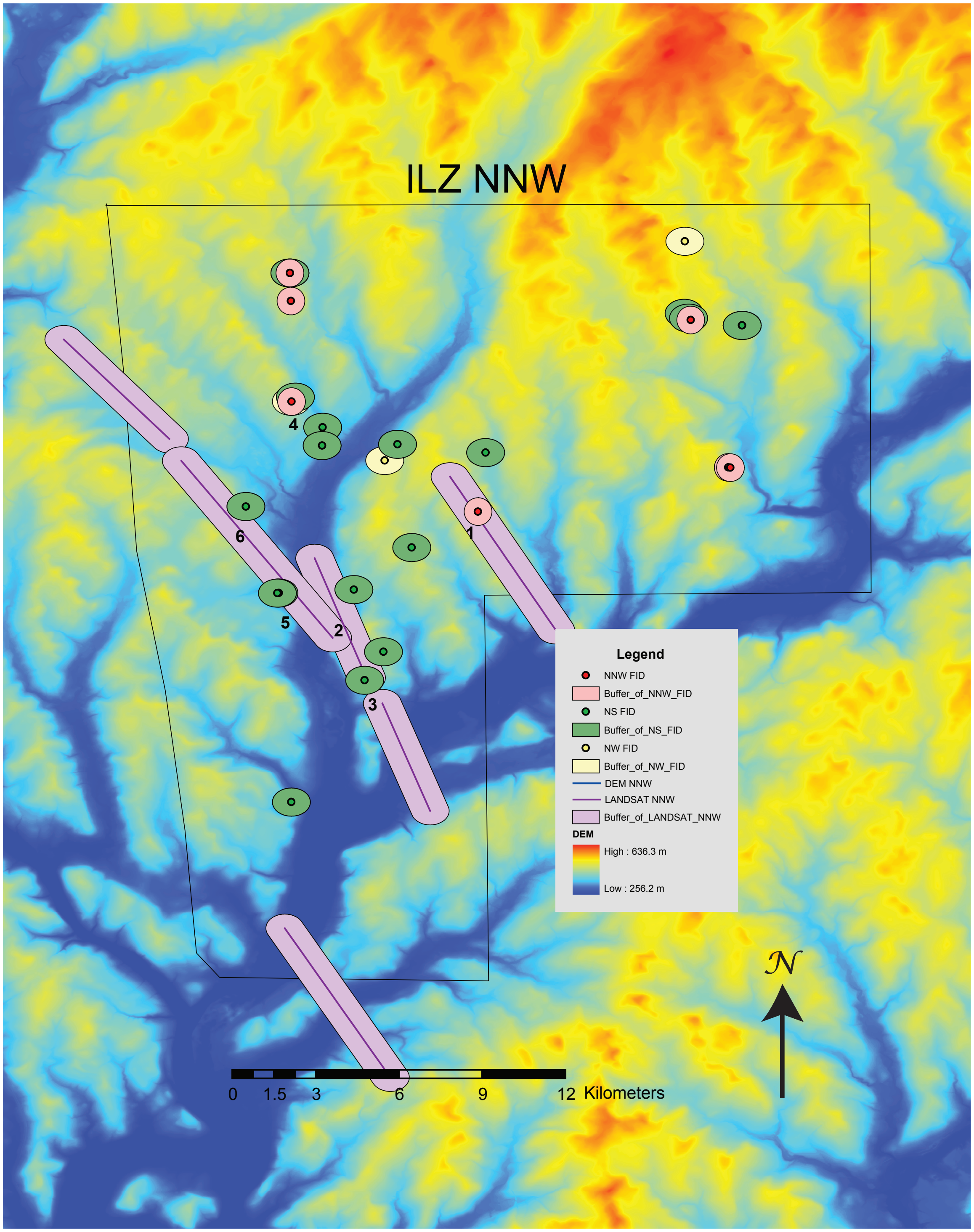
ILZ NNW
Legend
NNW FID
Buffer_of_NNW_FID
NS FID
Buffer_of_NS_FID
NW FID
Buffer_of_NW_FID
DEM NNW
LANDSAT NNW
Buffer_of_LANDSAT_NNW
DEM
High : 636.3 m
Low : 256.2 m
1
2
3
4
5
6
0
1.5
3
6
9
12
Kilometers
N

Figure 34

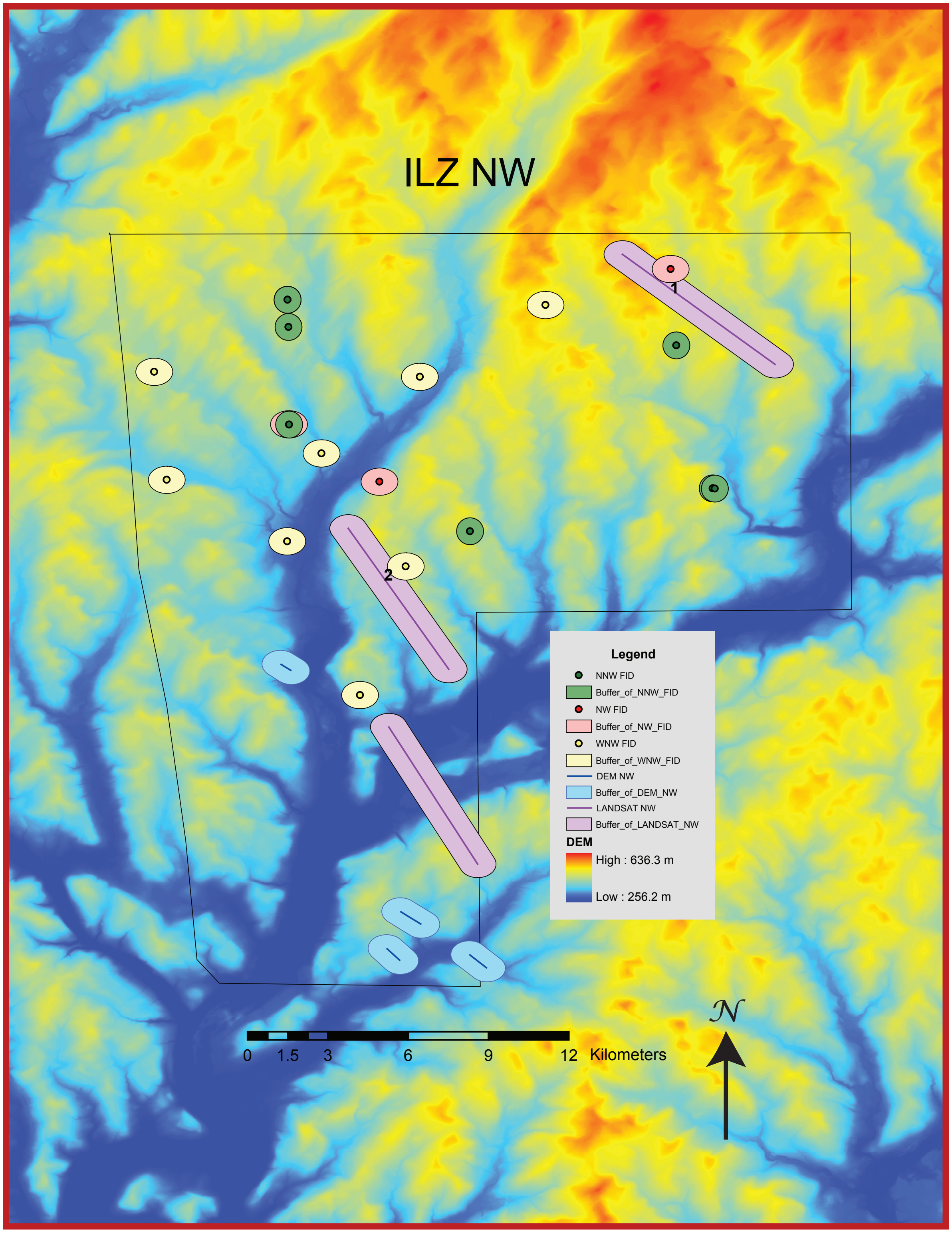
ILZ NW
1
2
Legend
NNW FID
Buffer_of_NNW_FID
NW FID
Buffer_of_NW_FID
WNW FID
Buffer_of_WNW_FID
DEM NW
Buffer_of_DEM_NW
LANDSAT NW
Buffer_of_LANDSAT_NW
DEM
High : 636.3 m
Low : 256.2 m
0 1.5 3 6 9 12 Kilometers
N

Figure 35

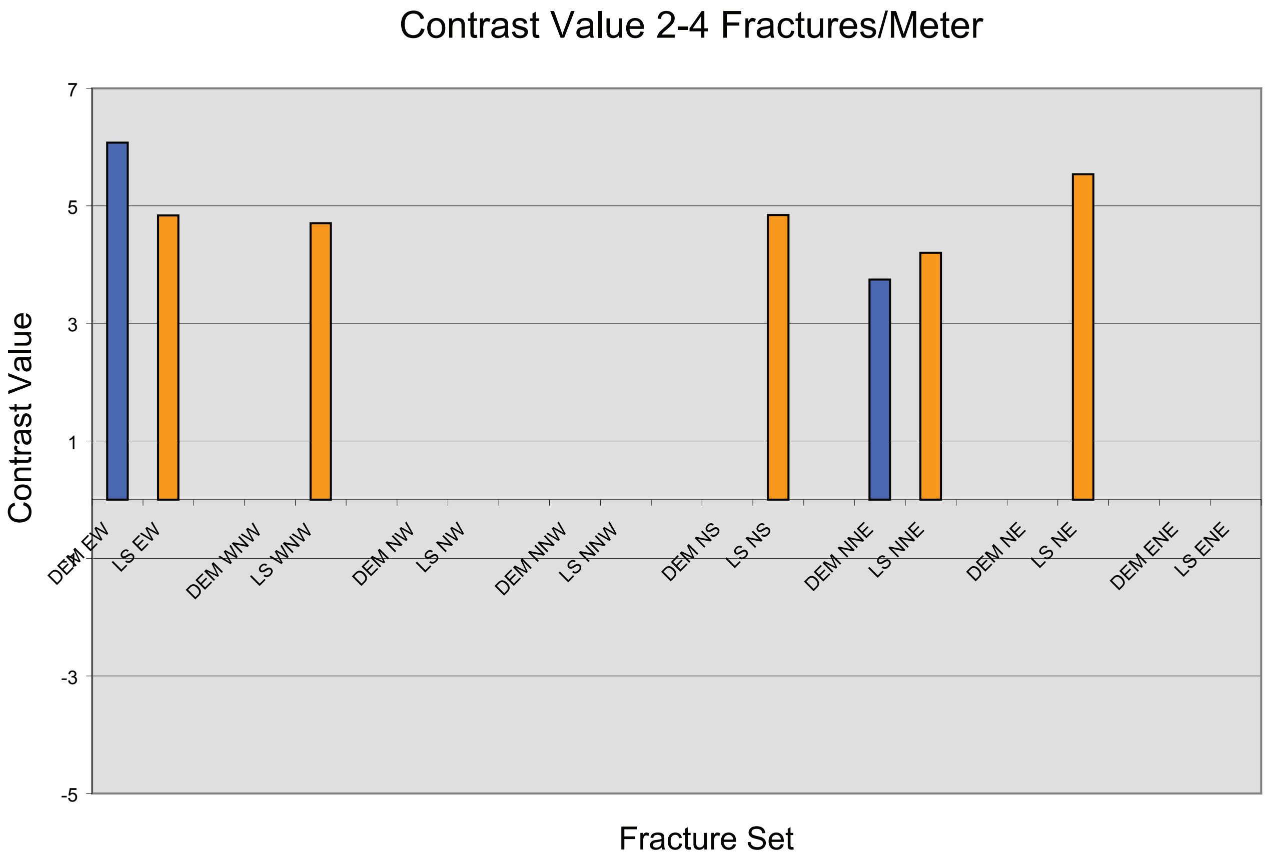

Figure 36a

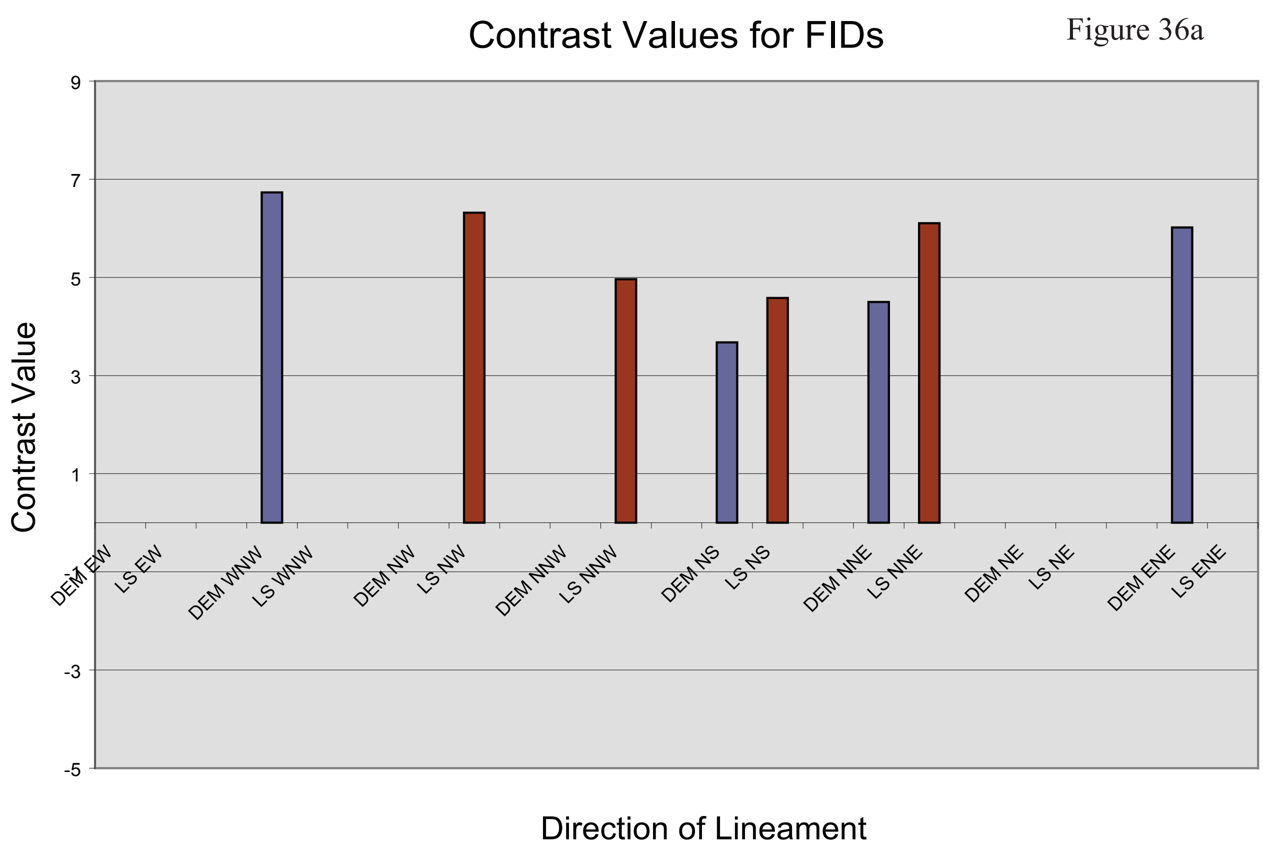

Figure 36b

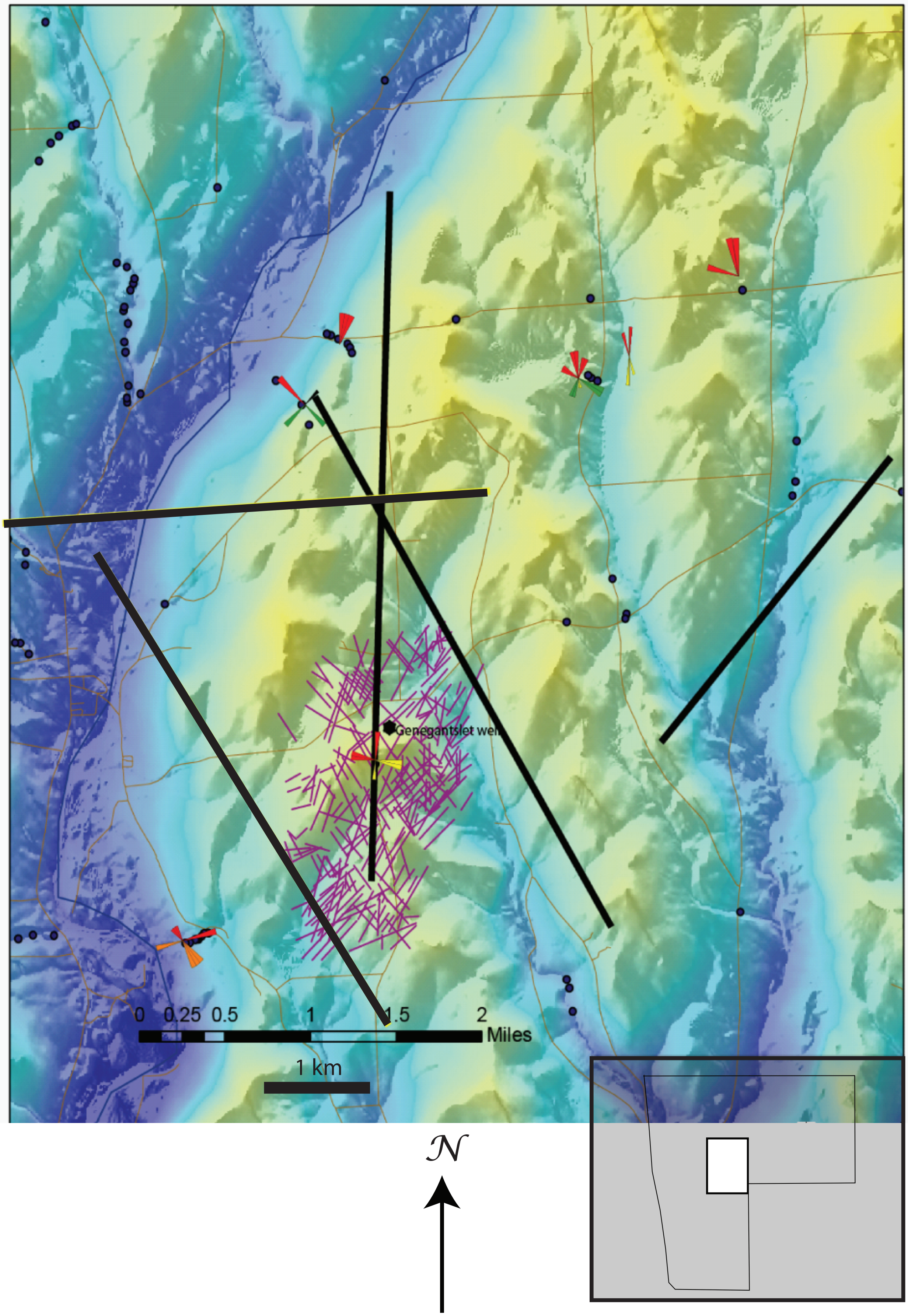

Figure 37

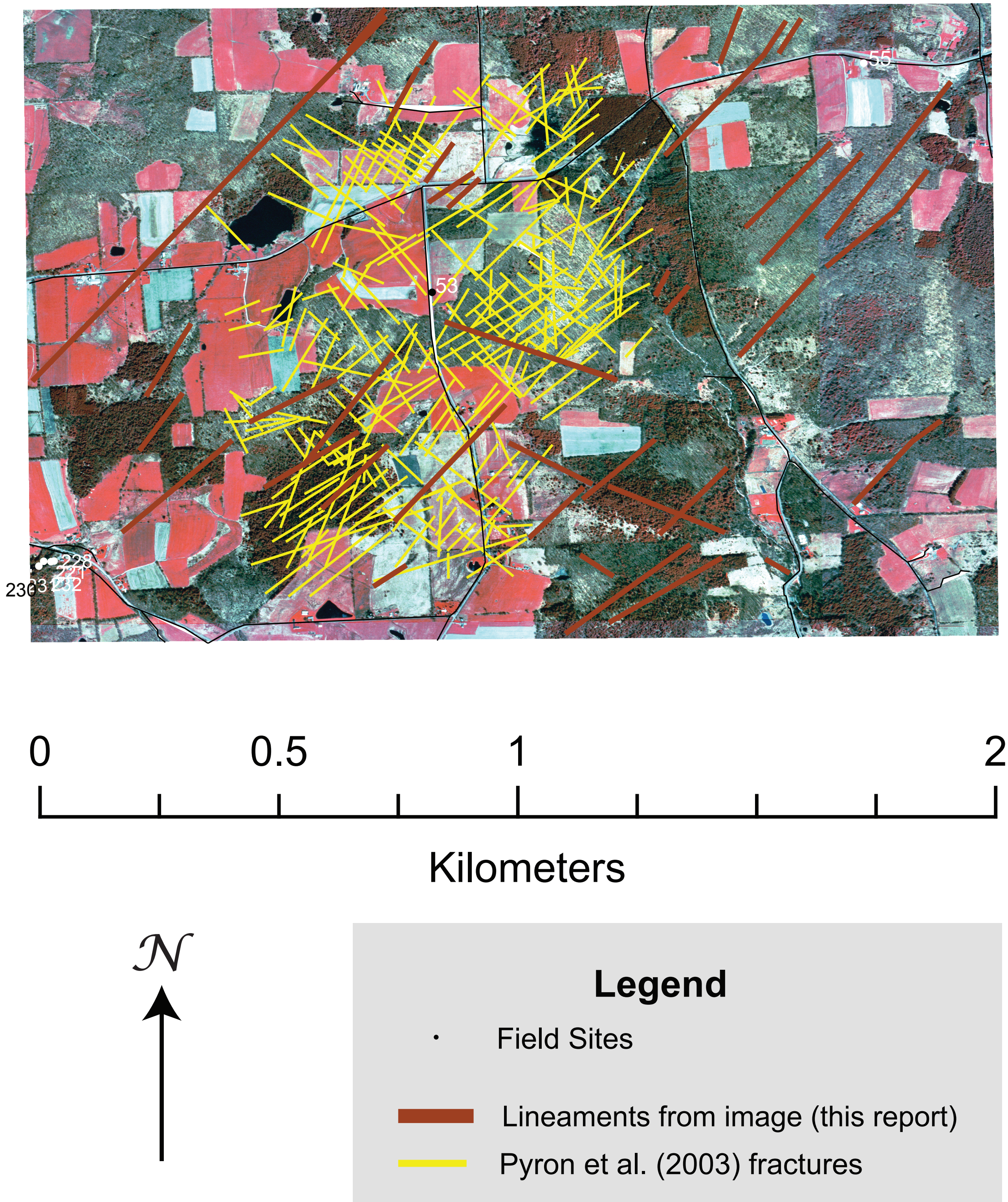
53
55
0
0.5
1
2
Kilometers
N
Legend
Field Sites
Lineaments from image (this report)
Pyron et al. (2003) fractures

Figure 38

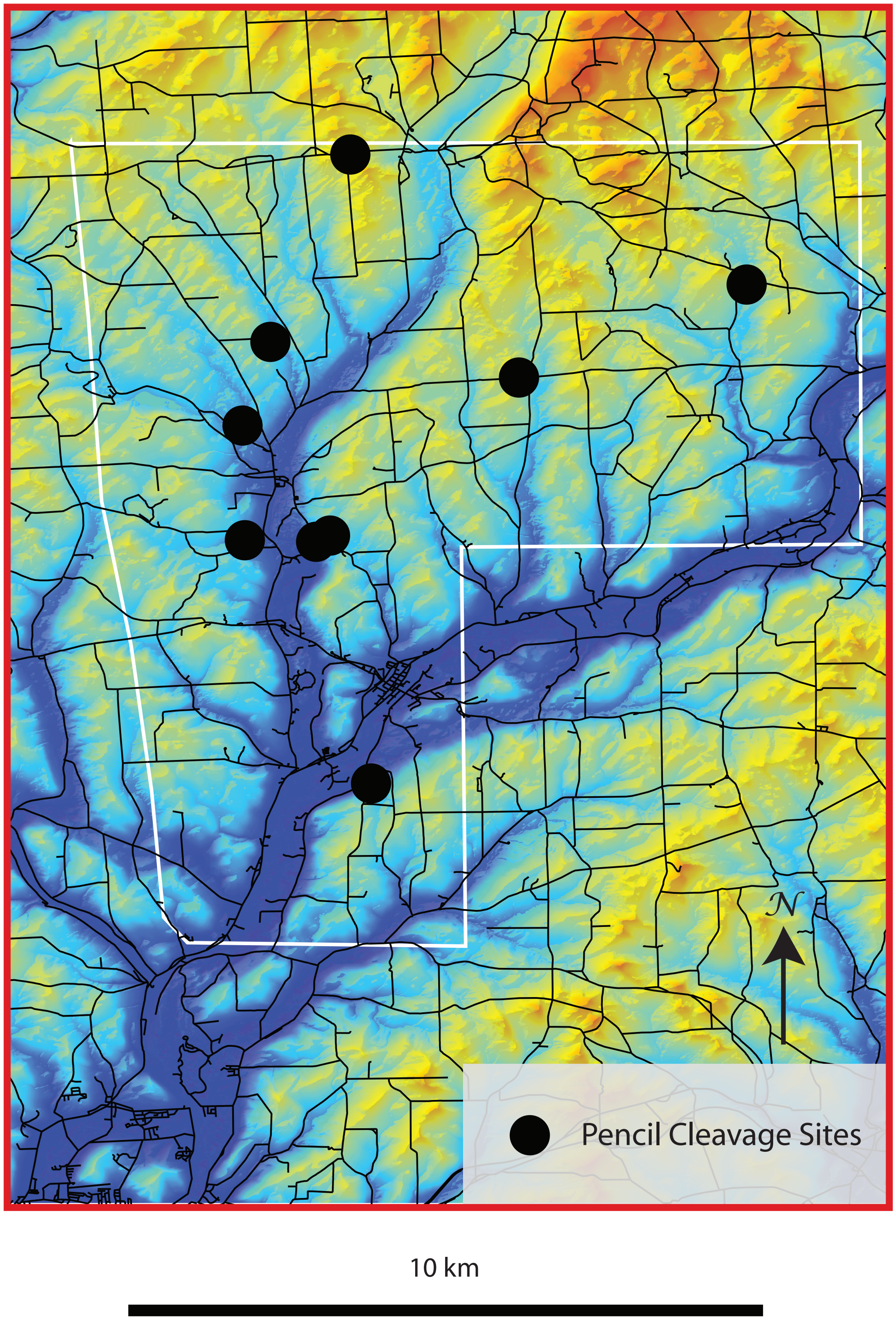

Figure 39

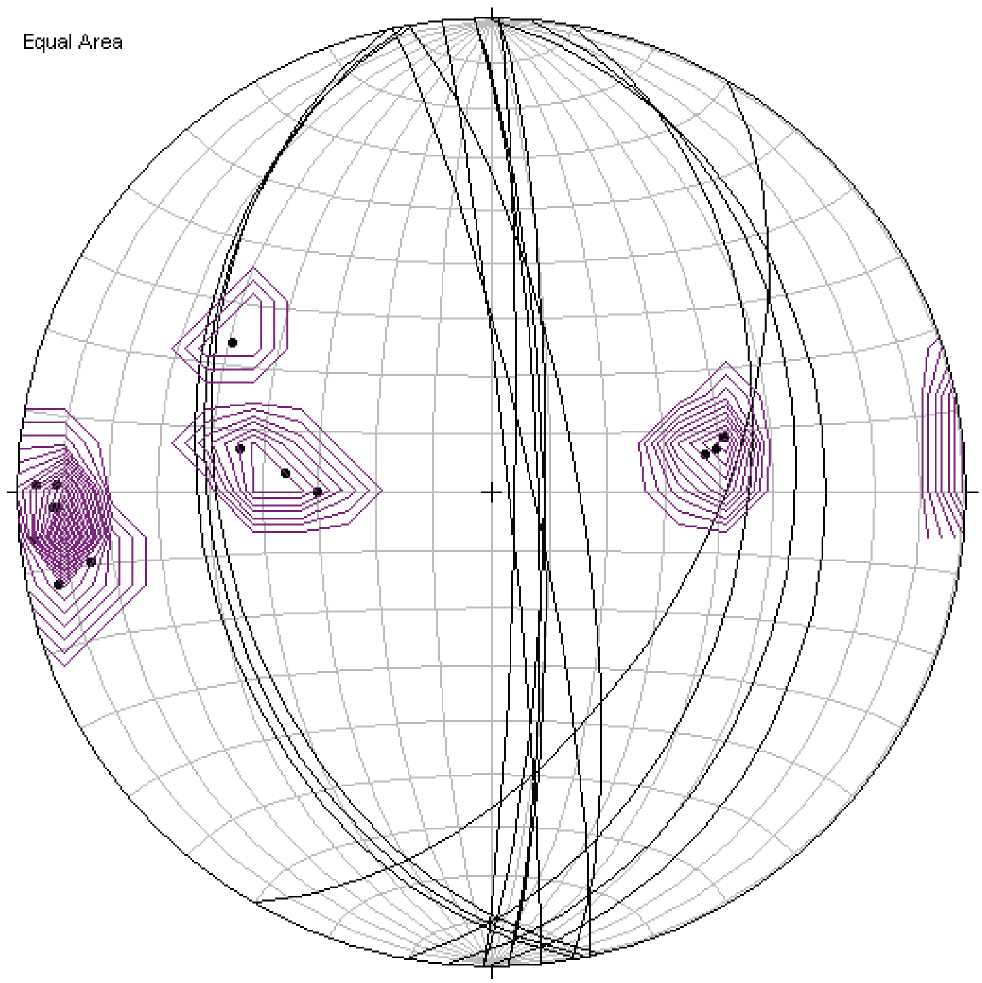

Explanation

Planes (n = 1):

Planes (n = 14):

LINES SCATTER PLOT (n = 14): •

1% AREA CONTOUR OF P-AXES (n = 14):
Contour Int = 2.0% per 1% area

Figure 40

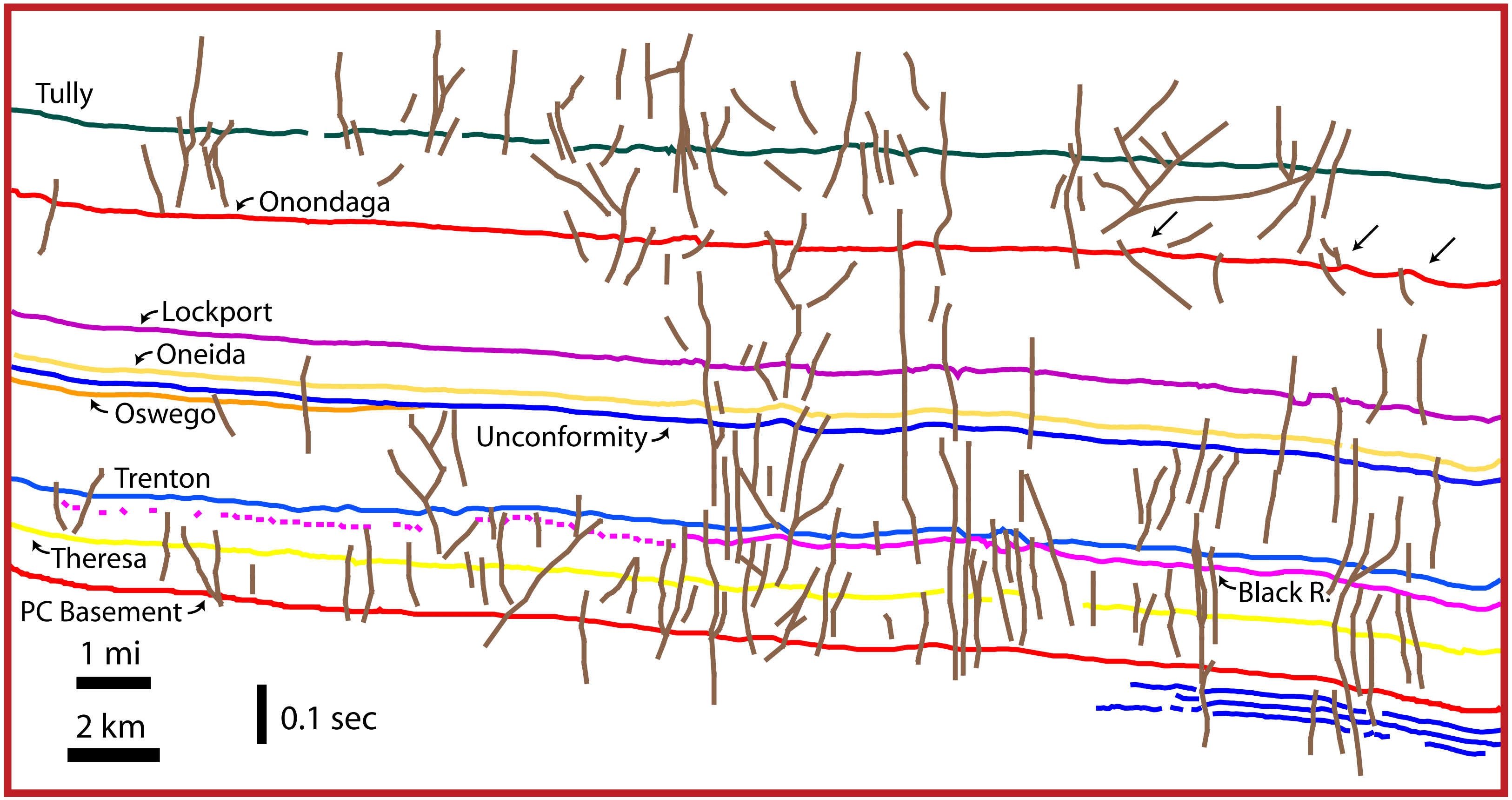

Tully
Onondaga
Lockport
Oneida
Oswego
Unconformity
Trenton
Theresa
PC Basement
Black R.
1 mi
2 km
0.1 sec

Figure 41a

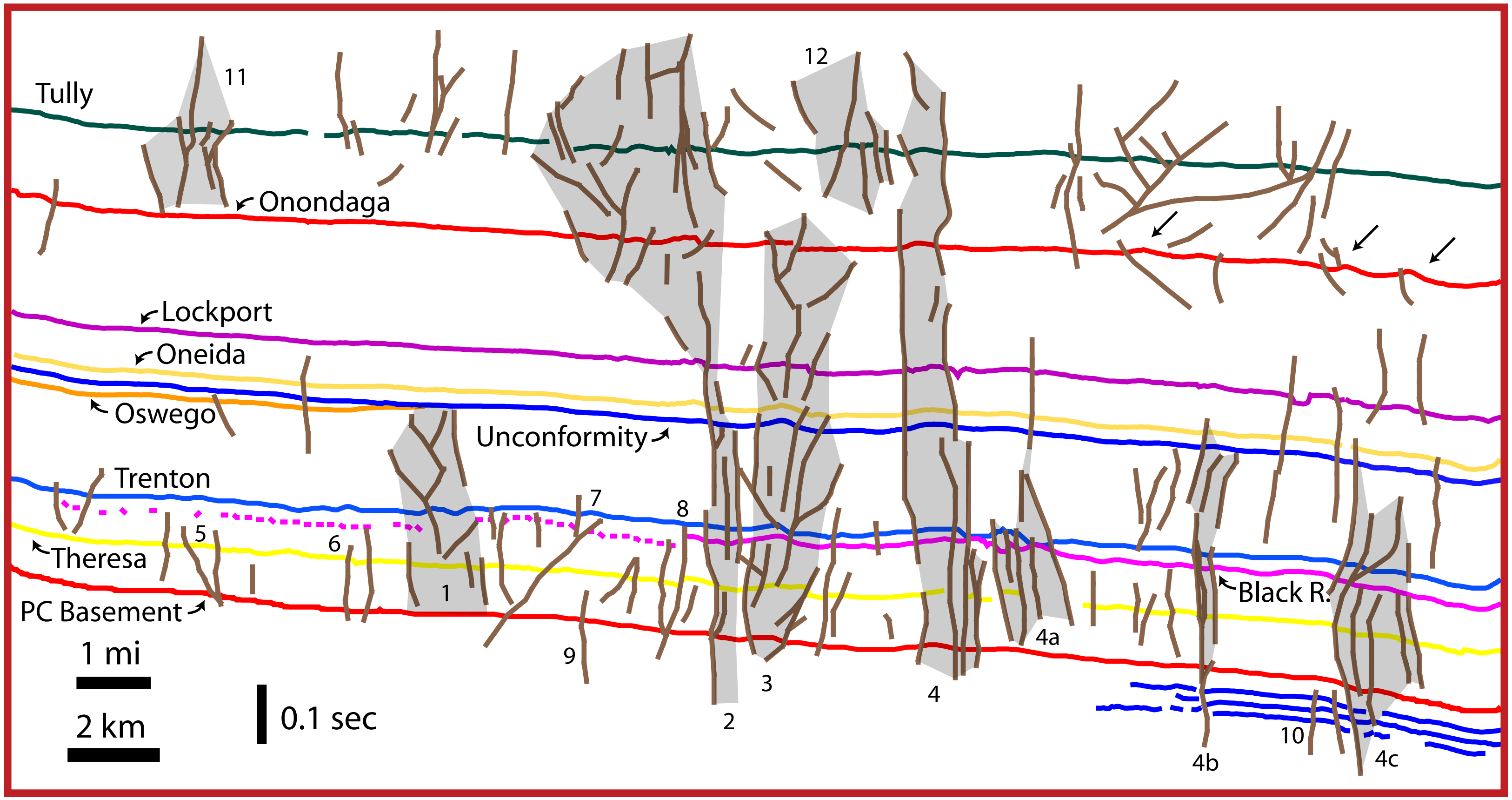
Tully
11
12
Onondaga
Lockport
Oneida
Oswego
Unconformity
Trenton
7
8
5
6
Theresa
1
PC Basement
Black R.
4a
9
3
4
2
1 mi
2 km
0.1 sec
10
4b
4c

Figure 41b

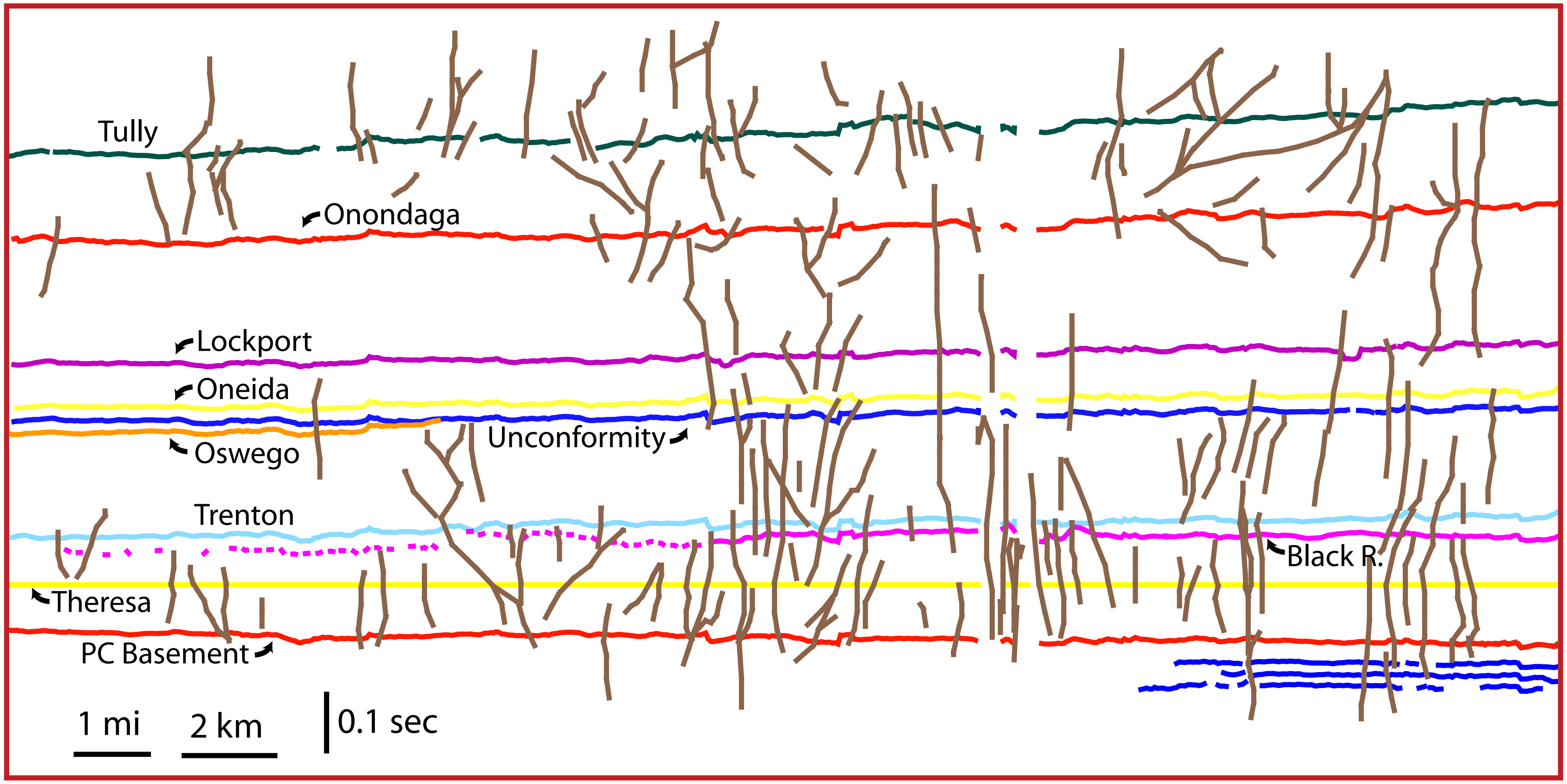
Tully
Onondaga
Lockport
Oneida
Oswego
Unconformity
Trenton
Theresa
PC Basement
Black R.
1 mi
2 km
0.1 sec

Figure 42

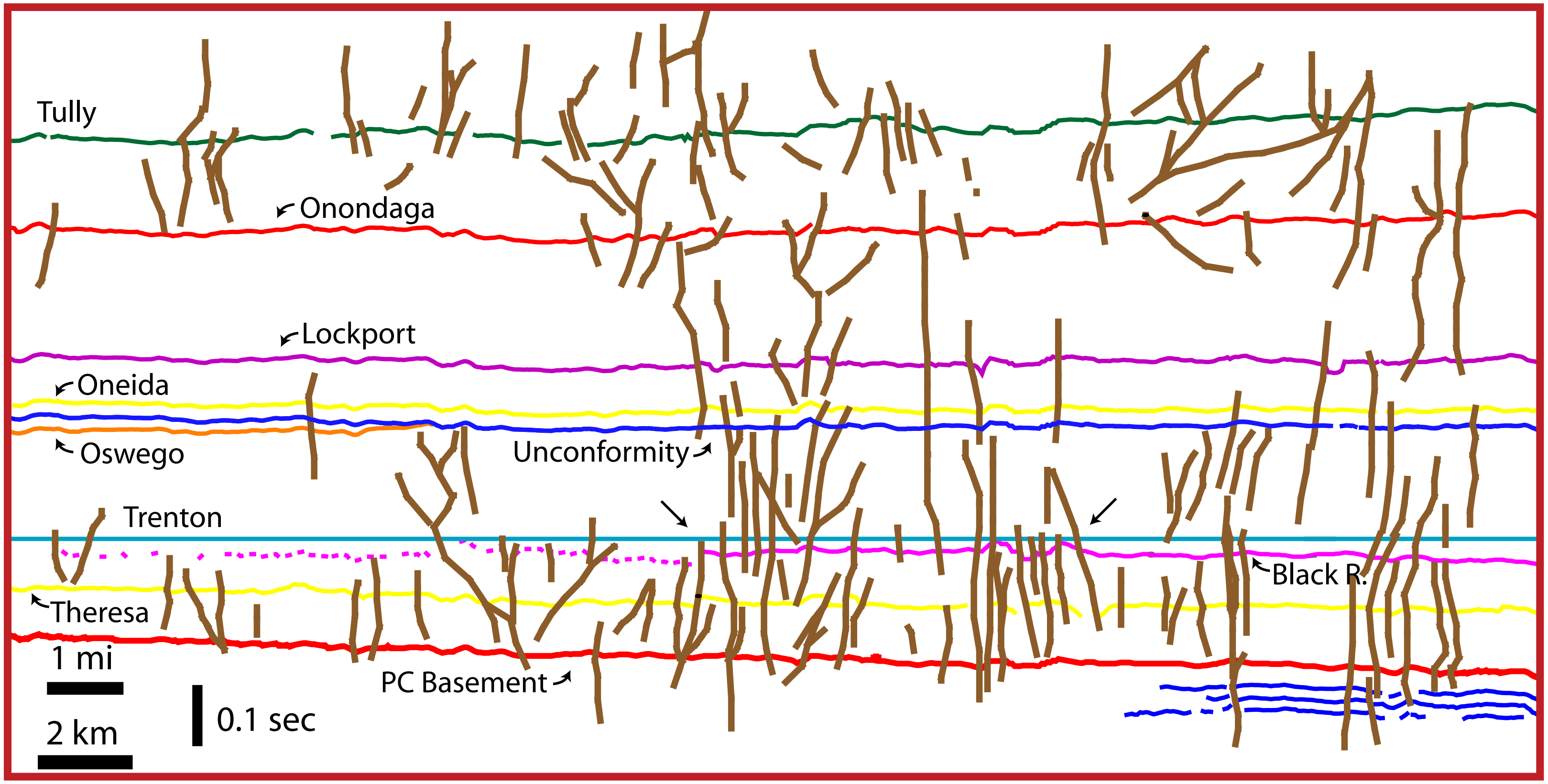
Tully
Onondaga
Lockport
Oneida
Oswego
Unconformity
Trenton
Black R.
Theresa
1 mi
2 km
0.1 sec
PC Basement

Figure 43


Tully
Onondaga
Lockport
Oneida
Oswego
Unconformity
Trenton
Black R.
Theresa
PC Basement
1 mi
2 km
0.1 sec

Figure 44

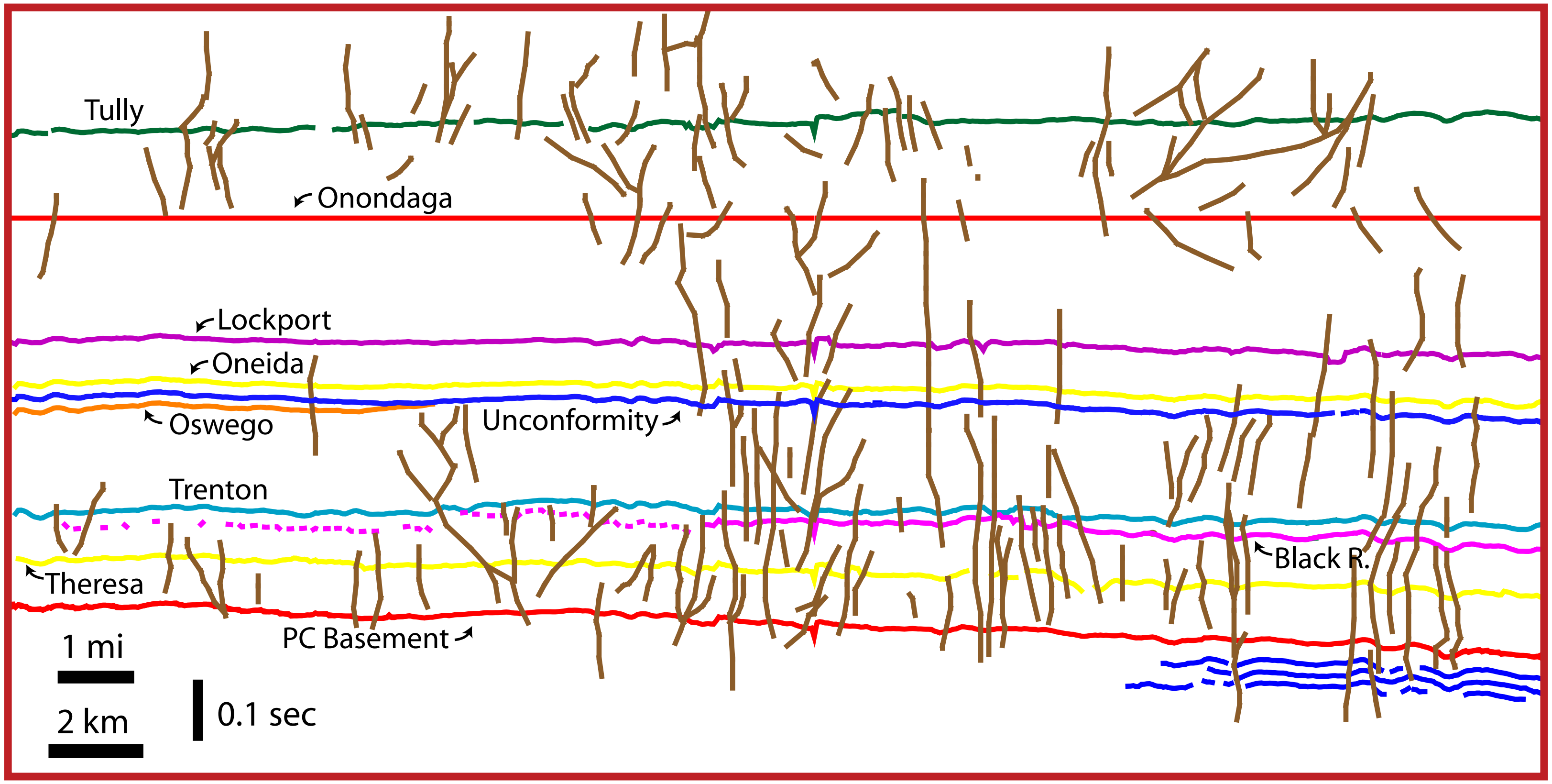
Tully
Onondaga
Lockport
Oneida
Oswego
Unconformity
Trenton
Black R.
Theresa
PC Basement
1 mi
2 km
0.1 sec

Figure 45

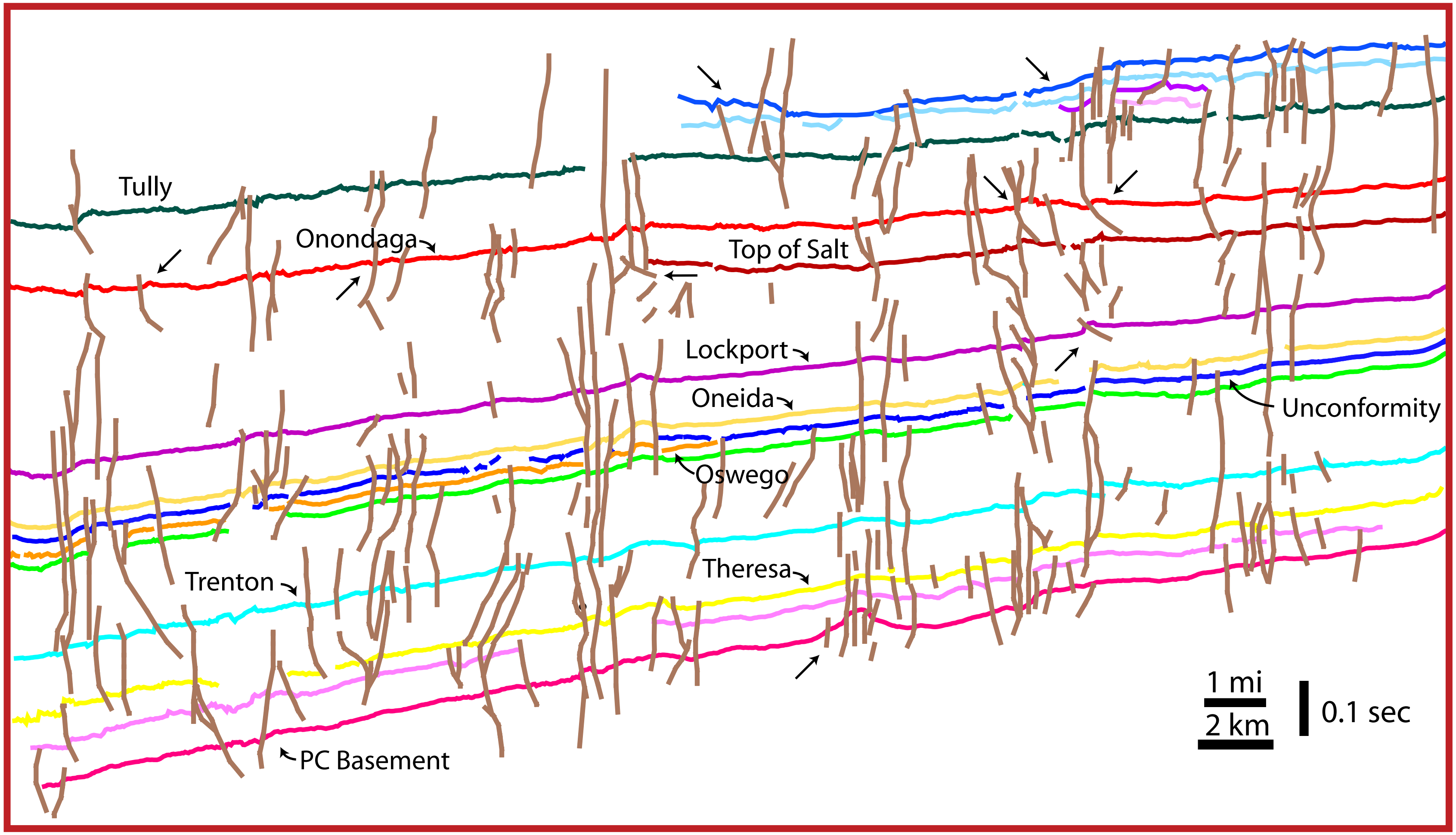
Tully
Onondaga
Top of Salt
Lockport
Oneida
Oswego
Unconformity
Trenton
Theresa
PC Basement
1 mi
2 km
0.1 sec

Figure 46a

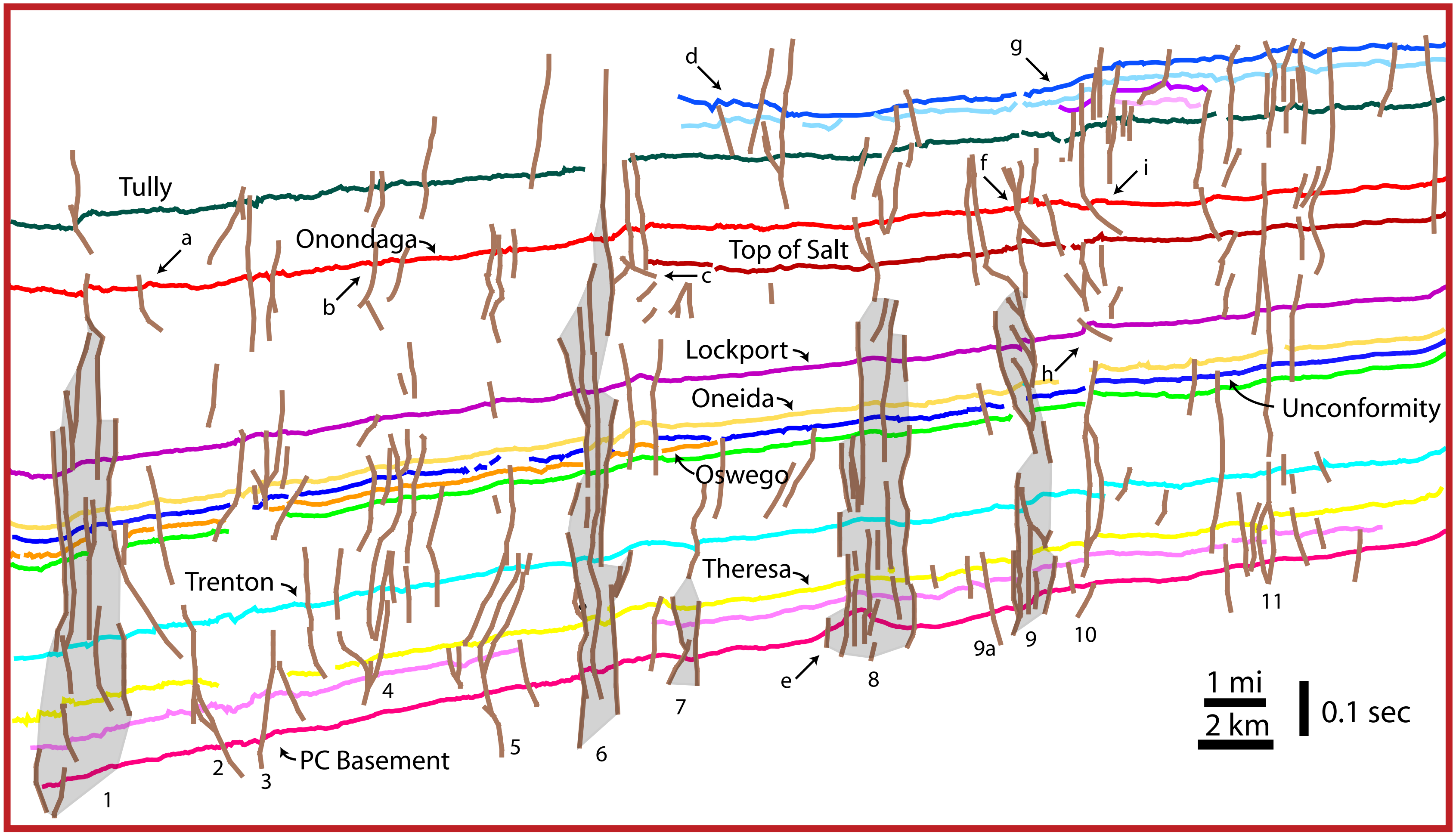
Tully
Onondaga
Top of Salt
Lockport
Oneida
Oswego
Unconformity
Trenton
Theresa
PC Basement
a
b
c
d
e
f
g
h
i
1
2
3
4
5
6
7
8
9a
9
10
11
1 mi
2 km
0.1 sec

Figure 46b

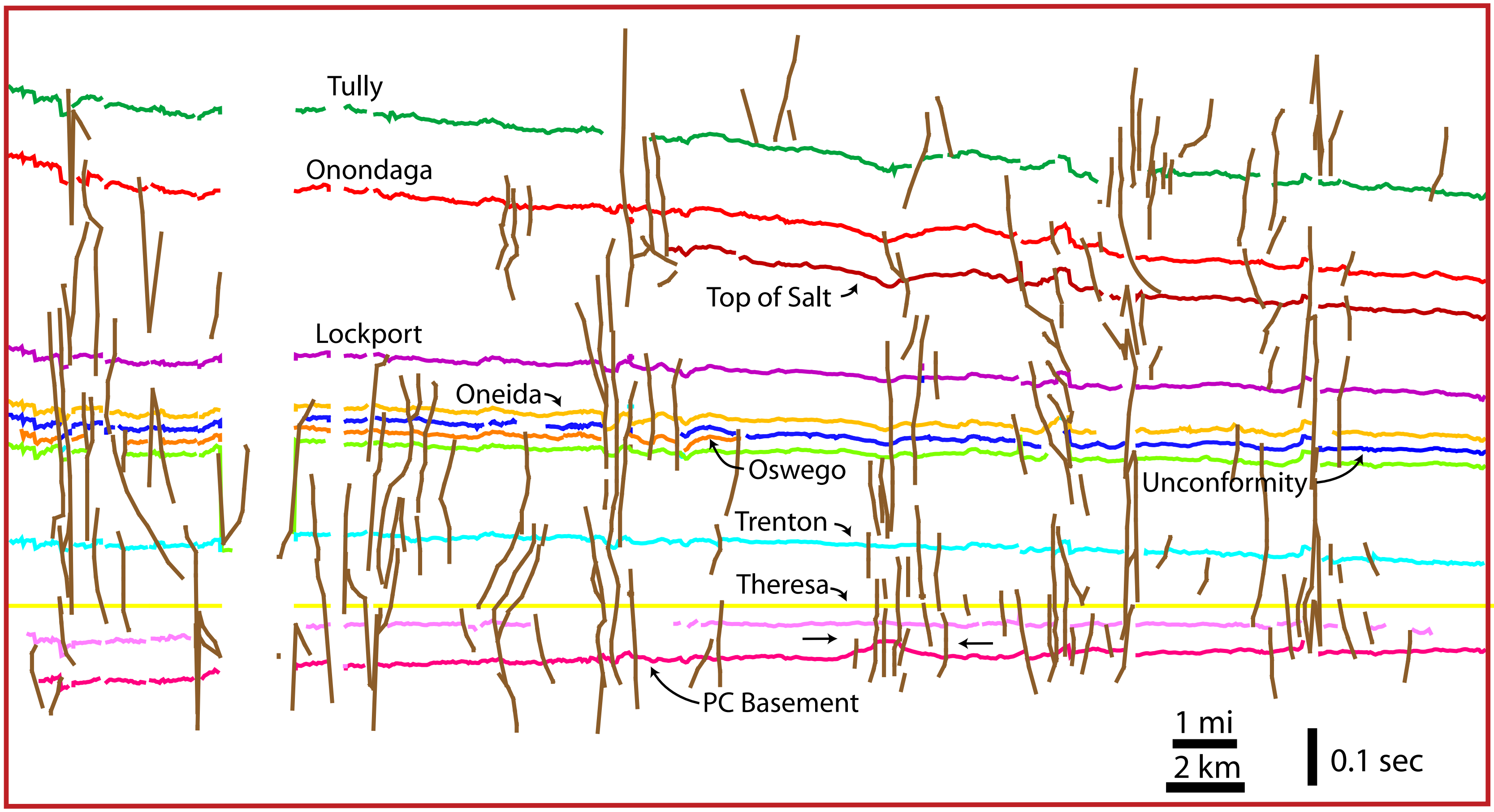
Tully
Onondaga
Top of Salt
Lockport
Oneida
Oswego
Unconformity
Trenton
Theresa
PC Basement
1 mi
2 km
0.1 sec

Figure 47

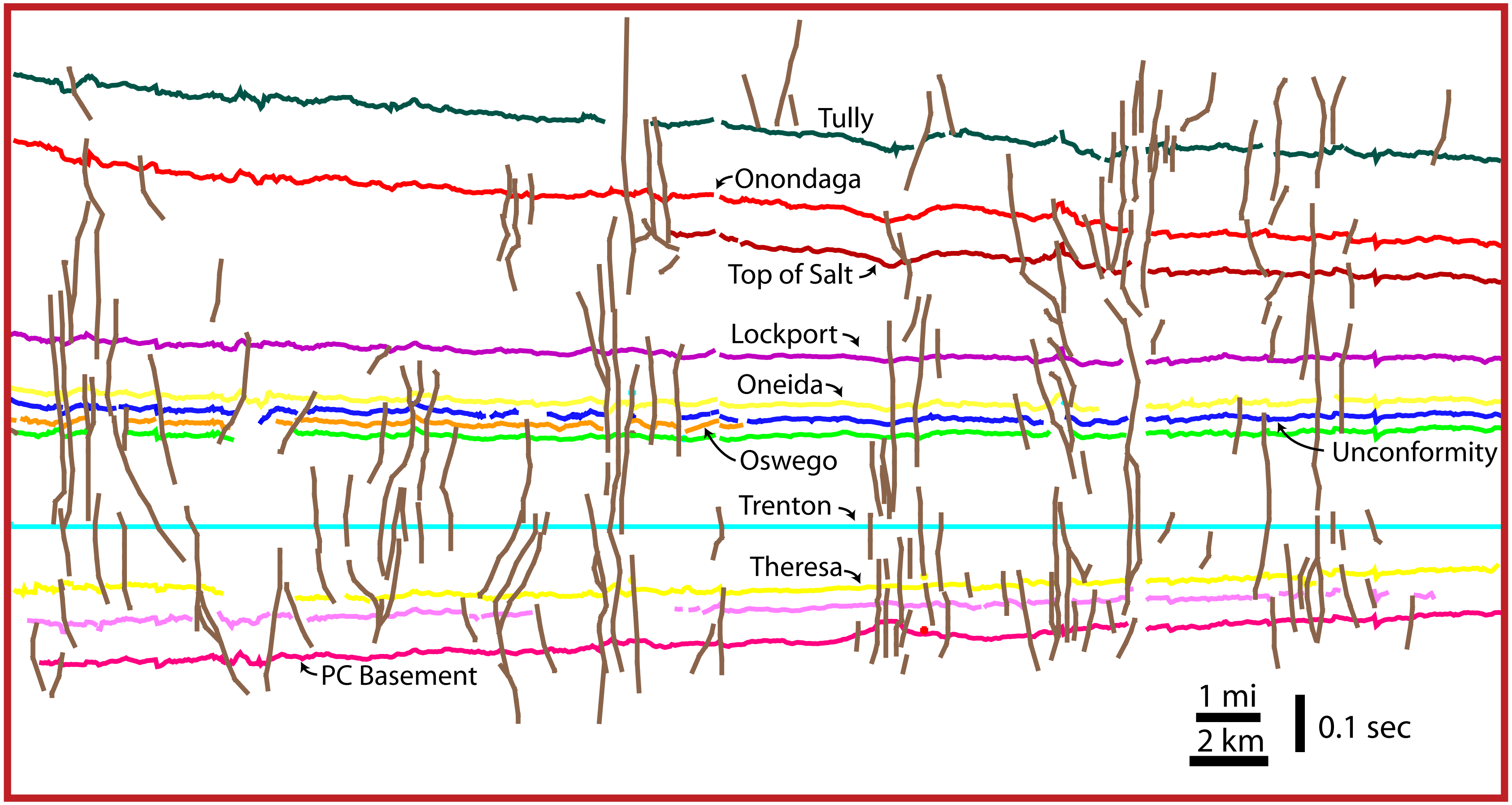
Tully
Onondaga
Top of Salt
Lockport
Oneida
Oswego
Unconformity
Trenton
Theresa
PC Basement
1 mi
2 km
0.1 sec

Figure 48

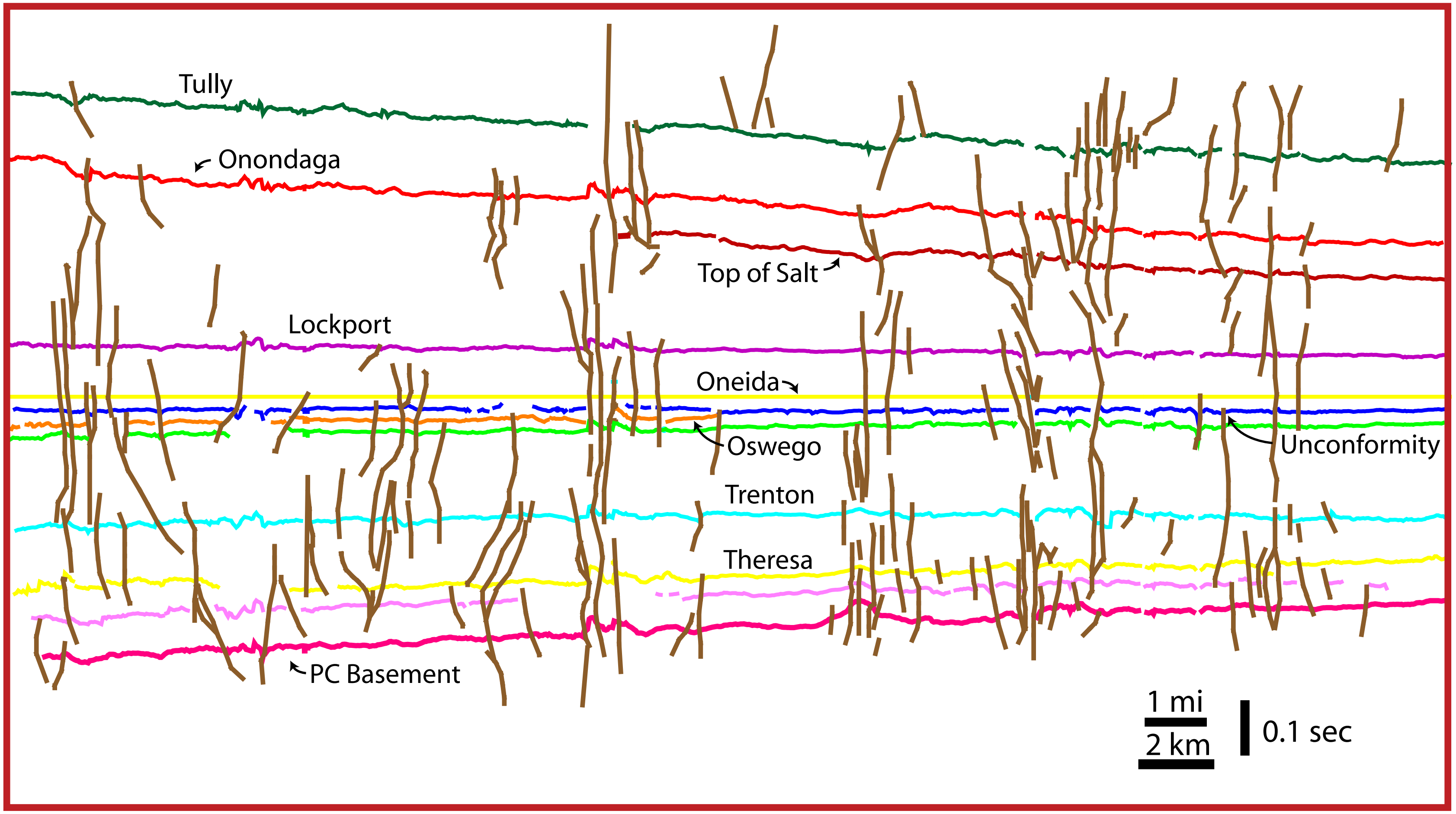
Tully
Onondaga
Top of Salt
Lockport
Oneida
Oswego
Unconformity
Trenton
Theresa
PC Basement
1 mi
2 km
0.1 sec

Figure 49

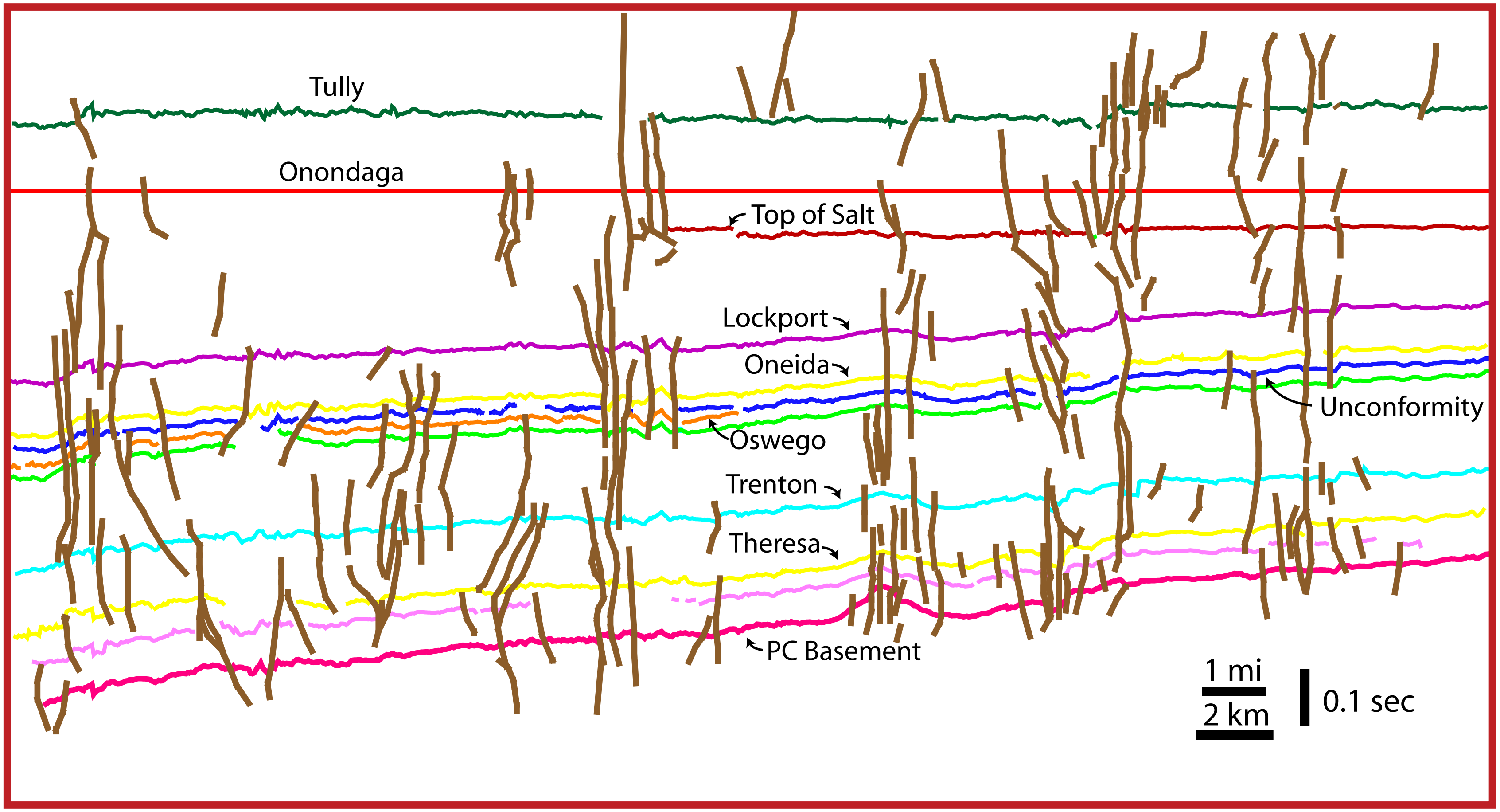

Tully
Onondaga
Top of Salt
Lockport
Oneida
Unconformity
Oswego
Trenton
Theresa
PC Basement
1 mi
2 km
0.1 sec

Figure 50

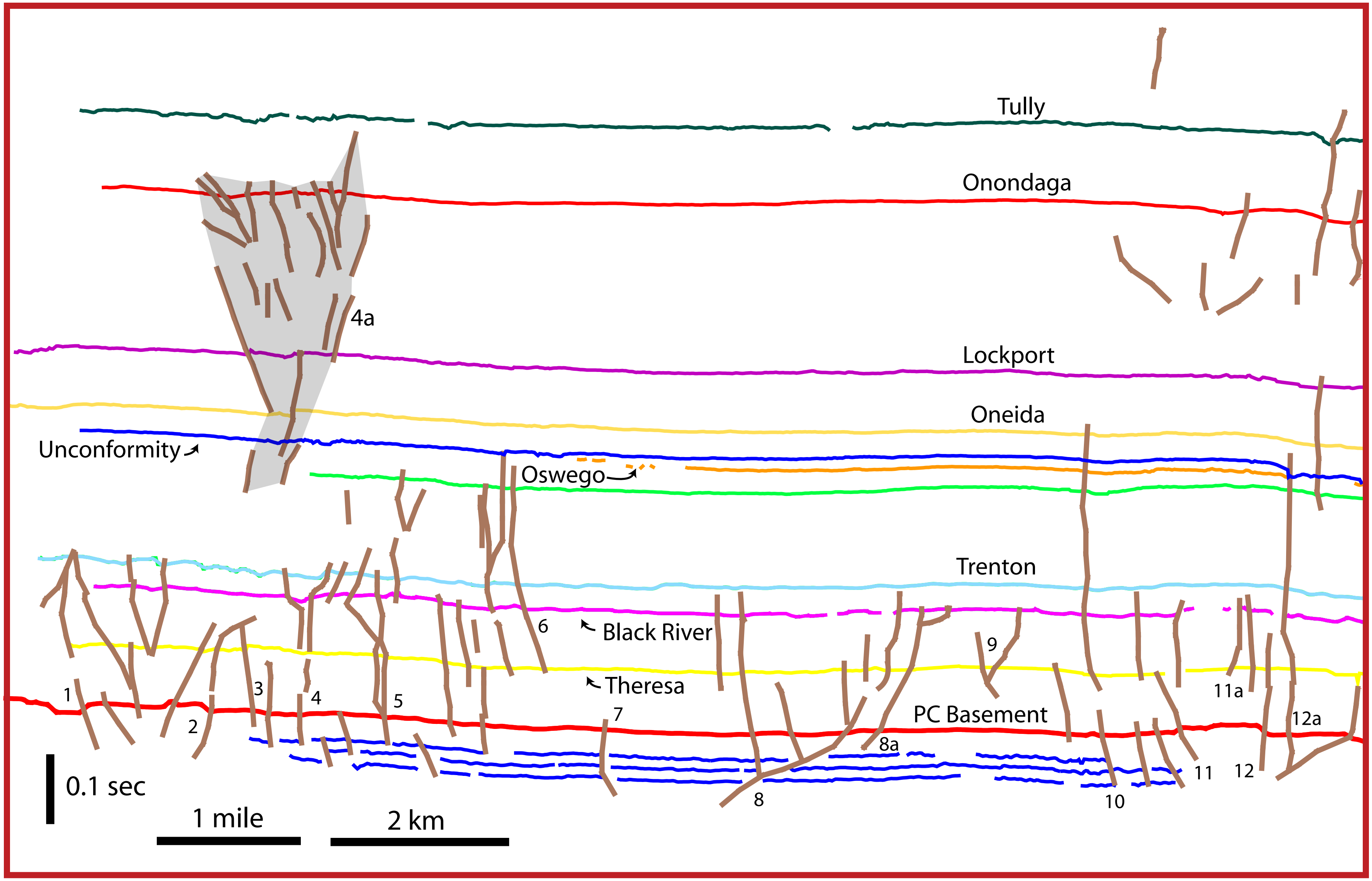

Tully
Onondaga
4a
Lockport
Oneida
Unconformity
Oswego
Trenton
Black River
Theresa
PC Basement
1
2
3
4
5
6
7
8
8a
9
10
11
11a
12
12a
0.1 sec
1 mile
2 km

Figure 51

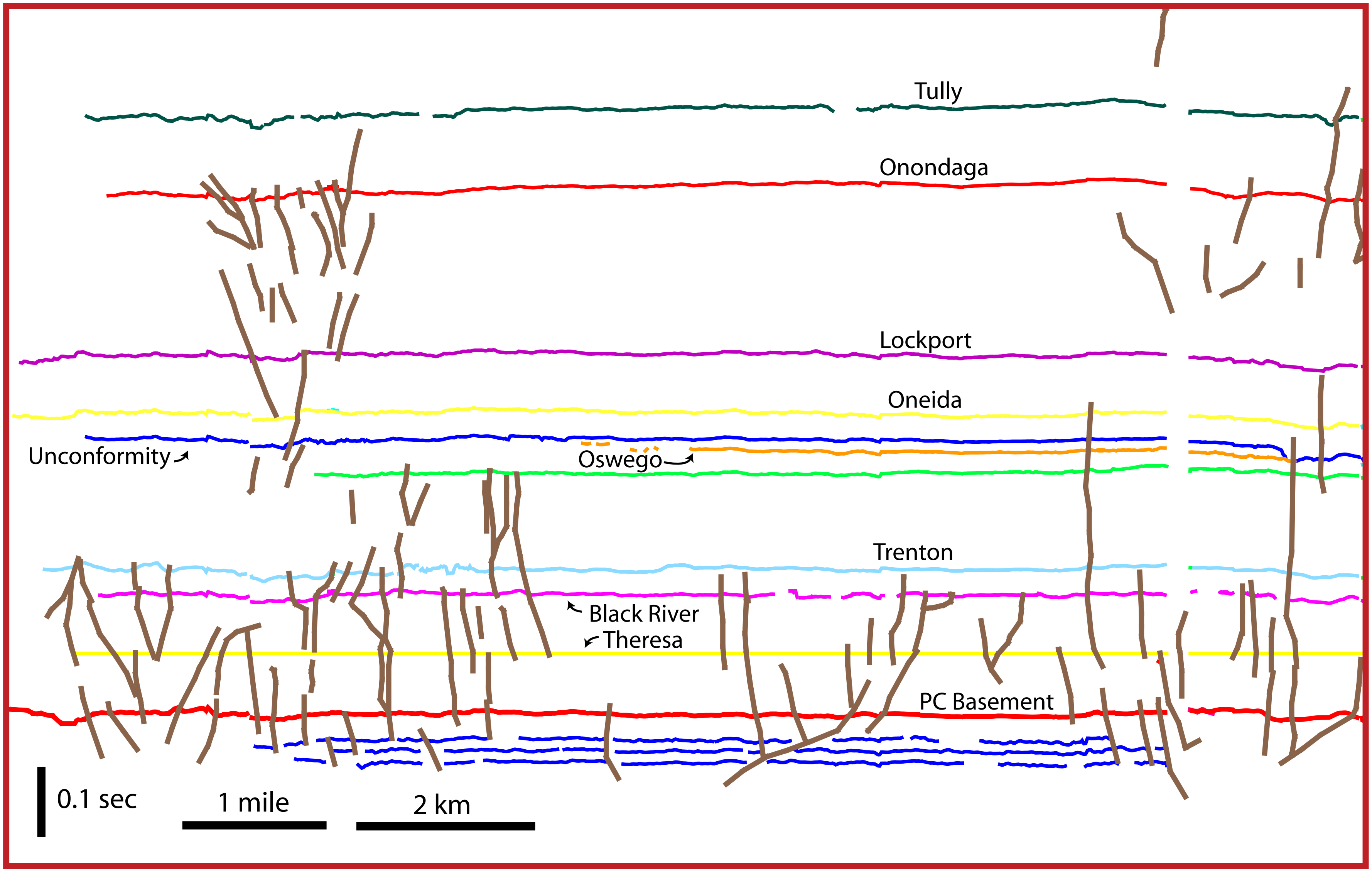
Tully
Onondaga
Lockport
Oneida
Unconformity
Oswego
Trenton
Black River
Theresa
PC Basement
0.1 sec
1 mile
2 km

Figure 52

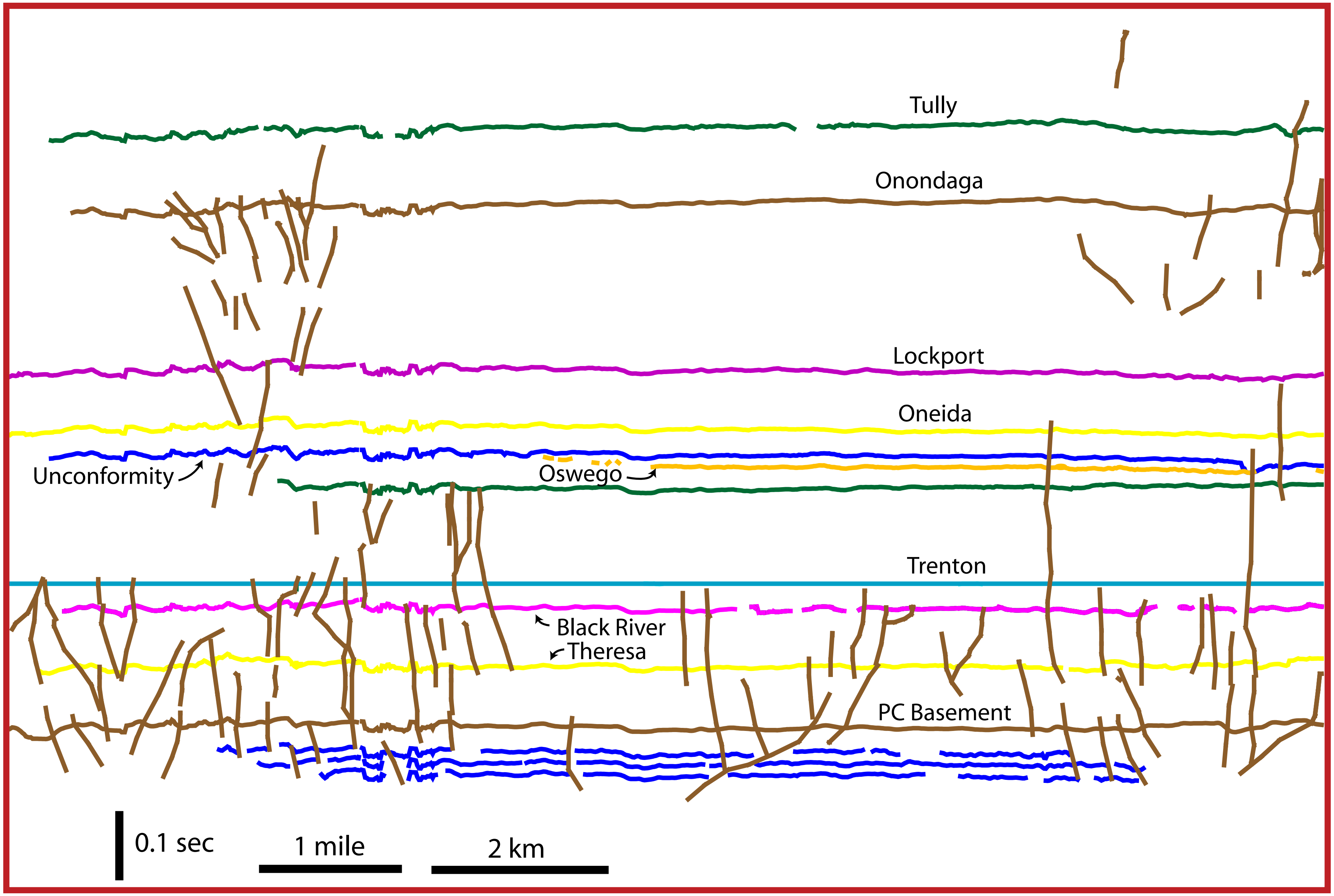
Tully
Onondaga
Lockport
Oneida
Unconformity
Oswego
Trenton
Black River
Theresa
PC Basement
0.1 sec
1 mile
2 km

Figure 53

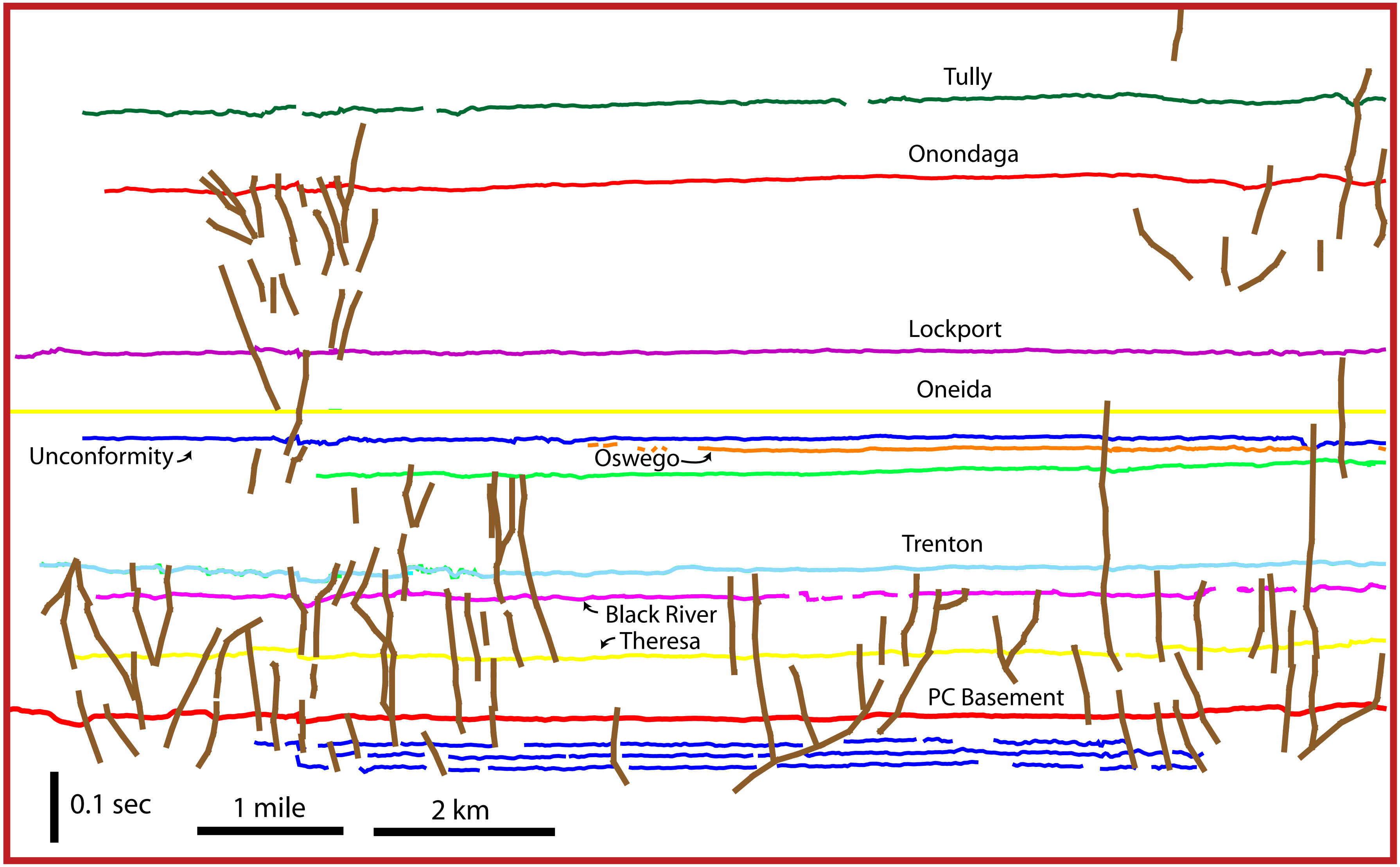
Tully
Onondaga
Lockport
Oneida
Unconformity
Oswego
Trenton
Black River
Theresa
PC Basement
0.1 sec
1 mile
2 km

Figure 54

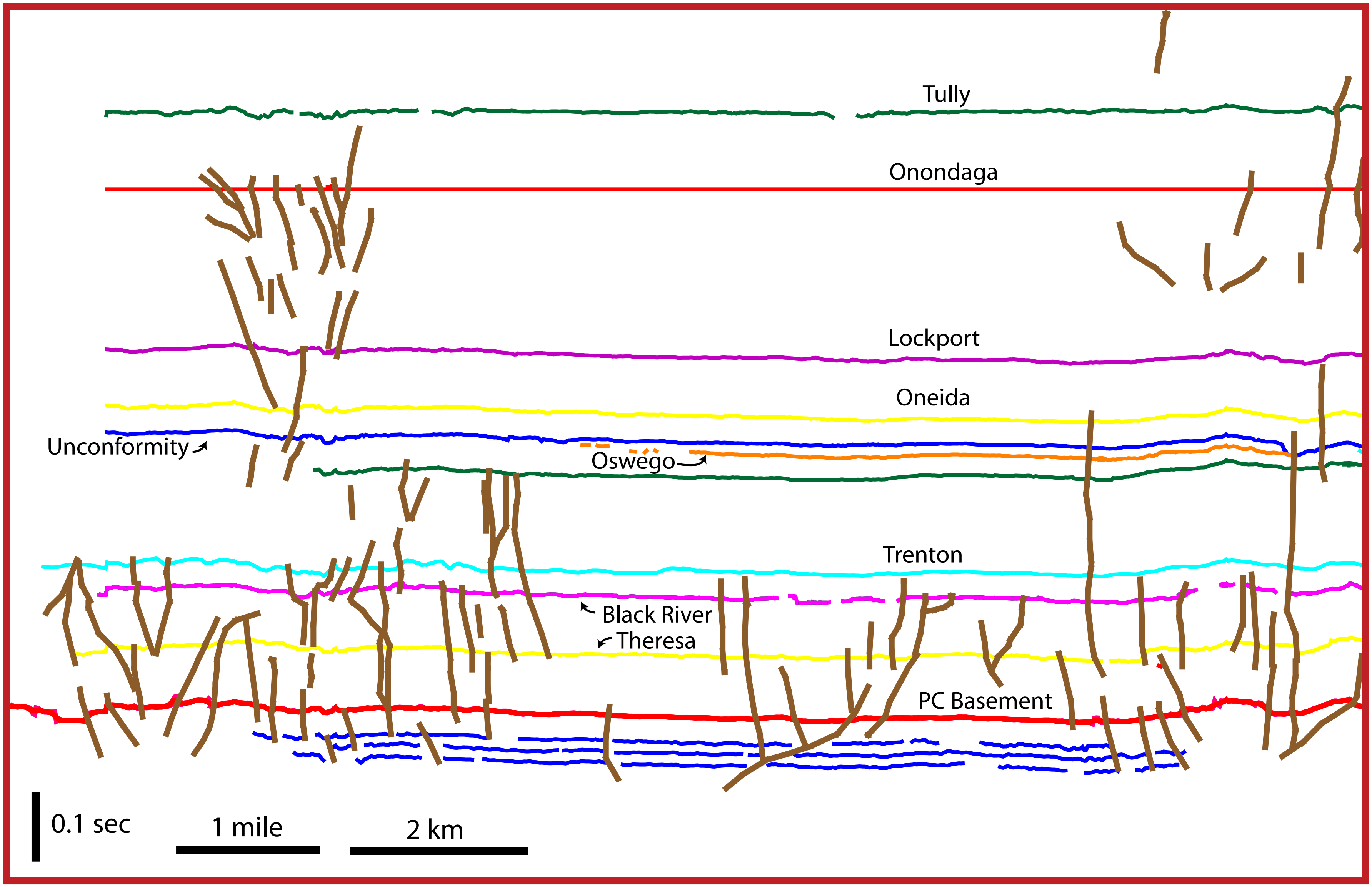
Tully
Onondaga
Lockport
Oneida
Unconformity
Oswego
Trenton
Black River
Theresa
PC Basement
0.1 sec
1 mile
2 km

Figure 55

NS-striking ILZ ID #	NS-striking FIDs	Similar FIDs	1:25,000 DEM LZs	1:250,000 DEM LZs	Slope Aspect	Earthsat LZs	Aeromag LZs	Total:
1			1	1	1			3
2					1	1		2
3			1	1	1			3
4			1		1			2
5						1	1	2
6			1	1	1		1	4
7			1	1				2
8			1	1				2
9			1	1				2
10			1		1			2
11	1	0.5	1	1				3.5
12				1	1	1		3
13		0.5	1	1	1	1		4.5
14		0.5	1		1	1		3.5
15			1		1	1		3
16			1			1		2
17			1	1	1			3
18				1	1			2
19			1	1		1		3
20			1	1				2
21		0.5				1		1.5
22			1	1	1	1		4
23		0.5	1	1	1			3.5
24				1		1		2
25			1	1	1	1		4
26			1	1		1		3
27			1	1		1		3
28			1			1		2
29		0.5	1				1	2.5
30				1		1		2
31			1	1		1		3
32				1		1		2
33				1	1	1	1	4
34			1	1		1	1	4
35						1	1	2
36			1	1	1	1		4
37			1	1				2
38			1			1		2
39			1	1		1		3
40		0.5	1			1		2.5
41		0.5					1	1.5
42		0.5		1				1.5
43		0.5	1					1.5
44		0.5			1			1.5
45	1	0.5		1				2.5
Total:	2	12	31	29	18	25	7	

Table 1

Fracture Set	Number of Fractures	Range of Strike (Deg.)	Average Strike (Deg.)	Standard Deviation (Deg.)
ENE	125	45-85	62.13	8.28
ENE "a"	105	45-72	59.76	6.58
ENE "b"	20	72-85	74.55	4.06
EW	35	85-277	272.83	2.91
NNE	1137	07-45	23.65	5.74
NS	59	342-07	350.32	6.86
NW	39	322-342	329.33	4.98
WNW	1204	277-322	294.37	7.63

Table 2

Fracture Set	Low Orientation	High Orientation	Number of Fractures	Average Strike	Standard Deviation From Average Strike
N	345	9	197	359.23	7.08
NNE	9	40	570	19.95	5.28
NE	41	55	15	48.43	5.612
ENE	56	84	78	68.71	6.54
EW	85	282	68	275.24	4.77
WNW	282	304	346	298.53	14.395
NW	305	323	81	311.7	13.47
NNW	323	344	79	332.05	13.32

Table 3

	EW	WNW	NW	NNW	NS	NNE	NE	ENE	MASTER SCORE
EW		1	1	1	3	2	0	0	8
WNW	0		0	0	7	19	2	1	29
NW	0	0		0	1	3	0	0	4
NNW	1	2	0		1	0	1	3	8
NS	5	0	12	2		2	0	6	27
NNE	5	59	7	4	5		1	1	82
NE	0	0	0	0	0	0		0	0
ENE	0	6	1	5	3	5	0		20
ABUTTING SCORE	11	68	21	12	20	31	4	11	

Table 4

LZ Set	Total Number of LZs	Number of LZs with sites	Number of LZs with sites that have FIDs
NNE	80	18	9
ENE	27	7	2
EW	5	2	0
WNW	33	11	7
NW	36	9	1
NS	48	17	1

Table 5

LZ Set	Total Number of LZs	Number of LZs with sites	Number of LZs with sites that have FIDs
NNE	45	13	7
ENE	33	13	3
EW	4	0	0
WNW	25	13	8
NW	18	5	2
NS	34	6	2

Table 6

LZ Set	Total Number of LZs	Number of LZs with sites	Number of LZs with sites that have FIDs
NNE	7	3	1
ENE	2	0	0
EW	5	4	0
WNW	5	2	2
NW	6	2	1
NS	16	5	0

Table 7

LZ Set	Total Number of LZs	Number of LZs with sites	Number of LZs with sites that have FIDs
NNE	17	7	3
ENE	14	8	2
EW	0	0	0
WNW	14	8	6
NW	4	3	0
NS	21	8	0

Table 8

LZ Set	Total Number of LZs	Number of LZs with sites	Number of LZs with sites that have FIDs
NNE	1	0	0
ENE	1	1	0
EW	1	1	0
WNW	2	1	1
NW	2	2	1
NS	4	1	0

Table 9

NNE-striking ILZ ID #	NNE-striking FIDs	Similar FIDs	1:25,000 DEM LZs	1:250,000 DEM LZs	Slope Aspect LZs	Earthsat LZs	Aeromag LZs	Total:
1				1		1		2
2			1			1		2
3			1	1	1			3
4			1	1	1	1		4
5			1	1		1		3
6			1	1		1		3
7			1			1		2
8			1			1	1	3
9				1		1	1	3
10	1		1	1				3
11			1	1			1	3
12			1	1				2
13			1	1		1		3
14			1	1				2
15		0.5	1	1				2.5
16	1	0.5	1	1				3.5
17			1	1	1			3
18			1	1				2
19			1	1				2
20	1		1	1				3
21			1	1				2
22			1	1				2
23			1	1		1		3
24			1	1	1			3
25			1	1				2
26	1		1	1				3
27			1	1				2
28			1	1				2
29			1	1				2
30			1					1
31	1		1	1		1		4
32			1	1		1		3
33			1	1	1			3
34			1	1	1	1		4
35	1		1	1		1		4
36			1			1		2
37			1	1	1			3
38			1	1	1			3
39	1		1					2
40				1		1		2
41				1		1		2
42				1		1		2
43				1		1		2
44			1	1				2
45	1		1	1		1		4
46	1	0.5			1			2.5
47	1					1		2
48	1		1					2
Total:	11	3	40	39	9	21	3	

Table 10

WNW-striking ILZ ID #	WNW-striking FIDs	Similar FIDs	1:25,000 DEM LZs	1:250,000 DEM LZs	Slope Aspect LZs	Earthsat LZs	Aeromag LZs	Total:
1			1	1	1	1		4
2	1		1					2
3	1		1	1			1	4
4	1							1
5				1	1			2
6			1	1				2
7				1		1		2
8	1	0.5		1				2.5
9			1	1	1			3
10			1	1	1	1		4
11			1	1	1	1		4
12	1		1	1	1	1		5
13			1	1	1	1		4
14			1	1	1	1		4
15			1	1	1	1		4
16			1	1		1		3
17			1	1				2
18			1	1				2
19	1		1	1				3
20	1		1	1				3
21	1		1	1	1	1		5
22			1			1		2
23	1			1				2
24			1	1		1		3
25	1			1		1		3
26	1		1	1		1		4
27			1	1		1		3
28			1	1		1		3
29	1					1		2
30	1			1				2
31	1			1				2
Total:	14	1	22	27	10	17	1	

Table 11

ENE-striking ILZ ID #	ENE-striking FIDs	Similar FIDs	1:25,000 DEM LZs	1:250,000 DEM LZs	Slope Aspect LZs	Earthsat LZs	Aeromag LZs	Total:
1			1	1				2
2			1	1			1	3
3		0.5		1			1	2.5
4			1	1		1		3
5				1		1		2
6			1	1		1		3
7			1	1		1		3
8			1	1		1		3
9			1			1		2
10	1	0.5	1	1				3.5
11	1			1		1		3
12			1	1		1		3
13			1	1				2
14		0.5	1	1				2.5
15		0.5	1	1		1		3.5
16			1			1		2
17	1	0.5	1	1				3.5
18				1	1			2
19				1		1		2
20			1	1				2
21			1	1				2
22			1	1				2
23			1	1				2
24			1		1			2
25			1	1				2
26		0.5	1					1.5
27		0.5		1				1.5
28		0.5		1				1.5
29	1					1		2
30		0.5	1	1				2.5
31			1	1				2
Total:	4	9	23	26	2	12	2	

Table 12

NW-striking ILZ ID #	NW-striking FIDs	Similar FIDs	1:25,000 DEM LZs	1:250,000 DEM LZs	Slope Aspect LZs	Earthsat LZs	Aeromag LZs	Total:
1			1	1	1			3
2				1	1			2
3			1	1				2
4			1	1				2
5	1		1	1				3
6			1	1				2
7	1	0.5	1				1	3.5
8			1	1				2
9				1		1		2
10			1			1	1	3
11			1				1	2
12			1	1				2
13			1	1	1			3
14			1	1	1			3
15		0.5	1	1	1		1	4.5
16		0.5	1	1	1			3.5
17			1		1	1		3
18		0.5	1		1			2.5
19			1		1			2
20			1	1	1	1		4
21			1	1	1			3
22				1	1			2
23	1	0.5	1	1	1			4.5
24			1		1	1		3
25		0.5	1					1.5
Total:	3	6	22	17	14	5	4	

Table 13

EW-striking ILZ ID #	EW-striking FIDs	Similar FIDs	1:25,000 DEM LZs	1:250,000 DEM LZs	Slope Aspect LZs	Earthsat LZs	Aeromag LZs	Total:
1			1	1				2
2		0.5	1				1	2.5
3		0.5	1		1			2.5
4		0.5			1			1.5
5		0.5			1			1.5
Total:	0	4	3	1	3	0	1	

Table 14

Orientation	NNE	ENE	EW	WNW	NW	NS
Actual Contrast Values calculated from Field Data	0.20954	0.630137	#NUM	-0.15885	0.965406	-0.49521
Maximum Possible Contrast Value	10.49573	9.328985	8.111593	11.13741	8.159592	7.846199
Contrast Value where 75% of sites are within the lineament buffer	1.877247	3.115044	3.916901	2.506945	2.574844	2.39516
Contrast Value where 50% of sites are within the lineament buffer	0.778635	2.016432	2.818289	1.408332	1.476237	1.296548

Table 15a

Orientation	NNE	ENE	EW	WNW	NW	NS
Actual Contrast Values calculated from Field Data	0.59629	-0.28616	#NUM	-0.67116	-0.13321	0.197934
Maximum Possible Contrast Value	9.9788	9.018581	8.111593	10.60847	7.871491	7.285507
Contrast Value where 75% of sites are within the lineament buffer	1.918046	2.997255	3.916901	2.547712	2.574842	2.395158
Contrast Value where 50% of sites are within the lineament buffer	0.798814	1.834104	2.818289	1.42848	1.47623	1.296546

Table 15b

Orientation	NNE	ENE	EW	WNW	NW	NS
Actual Contrast Values calculated from Field Data	0.299015	0.40698	#NUM	-0.89434	0.377616	1.296544
Maximum Possible Contrast Value	8.909825	8.41168	7.413405	10.02056	7.465189	6.589849
Contrast Value where 75% of sites are within the lineament buffer	1.877201	3.11503	3.916897	2.506855	2.57484	2.395157
Contrast Value where 50% of sites are within the lineament buffer	0.778588	2.016418	2.818285	1.408243	1.476228	1.296544

Table 15c

ILZ NNE ID #	FID NNE	Counter Clockwise FID	Clockwise FID	1:100000 DEM LZ	EarthSat (1997) LZ	Total
1	0	0	0.5	1	1	2.5
2	0	0	0	1	1	2
3	0	0	0	1	1	2
4	0	0	0	1	1	2
5	0	0	0	0	0	0
6	0	0	0	1	1	2
7	0	0	0	1	1	2
8	0	0	0	1	1	2
9	0	0	0.5	1	1	2.5
10	0	0	0.5	1	0	1.5
11	0	0	0.5	1	0	1.5
12	0	0	0.5	1	1	2.5
13	1	0	0	1	1	3
14	0	0	0	1	1	2
15	0	0	0.5	1	1	2.5
16	0	0	0.5	1	0	1.5
17	0	0	0.5	0	1	1.5
18	0	0	0.5	0	1	1.5
19	0	0	0.5	0	1	1.5
20	0	0	0	1	1	2
21	0	0	0	1	1	2
22	0	0	0.5	1	1	2.5
23	0	0	0	1	1	2
24	1	0	0	1	1	3
25	1	0	0	0	1	2
26	1	0	0	0	1	2
27	0	0	0	1	1	2
28	1	0	0	0	1	2
29	0	0	0	1	1	2
30	0	0	0	1	1	2
31	0	0	0	1	1	2
32	0	0	0	1	1	2
33	0	0	0.5	1	0	1.5
34	0	0	0	1	1	2
35	0	0	0	1	1	2
36	0	0	0.5	1	0	1.5
37	0	0	0.5	1	0	1.5
38	0	0	0.5	1	0	1.5
39	1	0	0	1	0	2
40	1	0	0	1	0	2
41	0	0	0.5	1	0	1.5
42	0	0	0.5	1	0	1.5
43	0	0	0.5	1	0	1.5
44	0	0	0.5	0	1	1.5
45	0	0	0	1	1	2
46	0	0	0.5	0	1	1.5
47	0	0	0	1	1	2
48	0	0	0	1	1	2
49	0	0	0	1	1	2
50	0	0	0	1	1	2
51	0	0	0	1	1	2
52	0	0	0	1	1	2
Total:	**7**	**0**	**10**	**43**	**39**	

Table 16

ILZ NS ID #	FID NS	Counter Clockwise FID	Clockwise FID	1:100000 DEM LZ	EarthSat (1997) LZ	Total
1	1	0	0	0	1	2
2	0	0	0	1	1	2
3	0	0	0.5	1	0	1.5
4	1	0	0	0	1	2
5	0	0.5	0.5	0	1	2
6	0	0	0.5	0	1	1.5
7	0	0	0.5	0	1	1.5
8	0	0	0.5	0	1	1.5
9	0	0	0.5	1	0	1.5
10	1	0	0	1	0	2
11	1	0	0	1	0	2
12	1	0	0	1	0	2
13	1	0	0	1	0	2
14	1	0	0	1	0	2
15	1	0	0	1	0	2
Total	**8**	**0.5**	**3**	**9**	**7**	

Table 17

ILZ EW ID #	FID EW	Counter Clockwise FID	Clockwise FID	1:100000 DEM LZ	EarthSat (1997) LZ	Total
1	0	0	0.5	1	1	2.5
2	0	0.5	0	1	1	2
3	0	0	0.5	1	1	2.5
4	0	0	0.5	1	0	1.5
5	0	0	0	1	1	2
6	0	0	0	1	1	2
7	0	0	0	1	1	2
8	0	0	0	1	1	2
9	0	0	0	1	1	2
Total:	**0**	**0.5**	**1.5**	**9**	**8**	

Table 18

ILZ NE ID #	FID NE	Counter Clockwise FID	Clockwise FID	1:100,000 DEM LZ	EarthSat (1997) LZ	Total
1	0	0	0	1	1	2
2	0	0	0	1	1	2
3	0	0	0	1	1	2
4	0	0	0	1	1	2
5	0	0.5	0	1	0	1.5
6	0	0	0	1	1	2
7	0	0.5	0	1	1	2.5
8	0	0	0.5	1	0	1.5
9	0	0	0	1	1	2
Total:	**0**	**1**	**0.5**	**9**	**7**	

Table 19

ILZ NNW ID #	FID NNW	Counter Clockwise FID	Clockwise FID	1:100000 DEM LZ	EarthSat (1997) LZ	Total
1	1	0	0	0	1	2
2	0	0	0.5	0	1	1.5
3	0	0	0.5	0	1	1.5
4	0	0	0.5	0	1	1.5
5	0	0	0.5	0	1	1.5
6	0	0	0.5	0	1	1.5
Total:	**1**	**0**	**2.5**	**0**	**6**	

Table 20

ILZ WNW ID #	FID WNW	Counter Clockwise FID	Clockwise FID	1:100000 DEM LZ	EarthSat (1997) LZ	Total
1	1	0	0	1	0	2
2	1	0	0	1	0	2
Total:	2	0	0	2	0	

Table 21

ILZ NW ID #	FID NW	Counter Clockwise FID	Clockwise FID	1:100000 DEM LZ	EarthSat (1997) LZ	Total
1	1	0	0	0	1	2
2	0	0	0.5	0	1	1.5
Total:	**1**	**0**	**0.5**	**0**	**2**	

Table 22

ILZ ENE ID #	FID ENE	Counter Clockwise FID	Clockwise FID	1:100000 DEM LZ	EarthSat (1997) LZ	Total
1	1	0	0	1	0	2
2	1	0	0	1	0	2
Total:	**2**	**0**	**0**	**2**	**0**	

Table 23

DEM Lineaments	WNW	NE	NS	NNW	NNE	EW	ENE	NW
Area of F points = 10^2	170	40	70	20	220	50	0	30
Area of L	163100	784600	2700000	0	1523400	301100	319900	62300
Area of ROI	546,750,000	546,750,000	546,750,000	546,750,000	546,750,000	546,750,000	546,750,000	546,750,000
Area of L- Area of F pints	162930	784560	2699930	-20	1523180	301050	319900	62270
# of lineaments	10	41	12	0	94	17	18	4
Area ROI -(area of L + Area of F points)	546,586,730	545,965,360	544,049,930	546,749,980	545,226,380	546,448,850	546,430,100	546,687,670
Area of ROI-Area of F pints	546,749,830	546,749,960	546,749,930	546,749,980	546,749,780	546,749,950	546,750,000	546,749,970
# F points within the L	0	0	0	0	3	3	0	0
# F points outside the L	17	4	7	2	19	2	0	3
# F points	17	4	7	2	22	5	0	3
# of F points within the L/Total # of F points	0	0	0	0	0.136363636	0.6	0	0
(Area of L - Area of F points) / (Area of ROI - Area of F points)	0.000297997	0.001434952	0.004938144	-3.65798E-08	0.002785881	0.00055062	0.000585094	0.000113891
# of F points outside the L / total number of F points	1	0	1	1	0.863636364	0.4	0	1
(Area ROI - (Area of L and F points)/Area of ROI- Area of F points	0.999702	0.998565	0.995062	1.000000	0.997214	0.999449	0.999415	0.999886
Wi+	0	0	0	0	3.890761	6.993645	0	0
Wi-	0.000298	0	0.004951	0.000000	-0.143813	-0.915740	0	0.000114
Contrast	0	0	0	0	3.746948	6.077905	0	0
Maximum Possible Contrast Value	7.504868948	8.117996555	9.0804277	0	5.310784112	5.88366249	6.547094851	7.444300997

Table 24

DEM Lineaments	WNW	NE	NS	NNW	NNE	EW	ENE	NW
Area of F points = 10^2	80	0	190	80	100	10	50	30
Area of L	163100	784600	2700000	0	1523400	301100	319900	62300
Area of ROI	546,750,000	546,750,000	546,750,000	546,750,000	546,750,000	546,750,000	546,750,000	546,750,000
Area of L- Area of F pints	163020	784600	2699810	-80	1523300	301090	319850	62270
# of lineaments	10	41	12	0	94	17	18	4
Area ROI -(area of L + Area of F points)	546,586,820	545,965,400	544,049,810	546,749,920	545,226,500	546,448,890	546,430,050	546,687,670
Area of ROI-Area of F pints	546,749,920	546,750,000	546,749,810	546,749,920	546,749,900	546,749,990	546,749,950	546,749,970
# F points within the L	4	0	5	0	5	0	2	0
# F points outsidethe L	4	0	14	8	5	1	3	3
# F points	8	0	19	8	10	1	5	3
# of F points within the L/Total # of F points	0.5	0	0.26315789	0	0.5	0	0.4	0
(Area of L - Area of F points) / (Area of ROI - Area of F points)	0.00029816	0.00143503	0.00493793	-1.463E-07	0.0027861	0.00055069	0.000585002	0.00011389
# of F points outside the L / total number of F points	0.5	0	0.73684211	1	0.5	1	0.6	1
(Area ROI - (Area of L and F points)/Area of ROI- Area of F points	0.99970169	0.99856497	0.99506173	1	0.99721372	0.99944929	0.999414906	0.99988605
Wi+	7.42472672	0	3.97580885	0	5.18996526	0	6.527603979	0
Wi-	-0.69284883	0	-0.3004311	0	-0.690357	0.00055086	-0.510240359	0.00011395
Contrast	6.73187789	0	3.6753777	0	4.49960825	0.00055086	6.017363621	0.00011395
Maximum Possible Contrast Value	7.50486895	8.11799655	9.0804277	0	5.31078411	5.88366249	0	7.444301

Table 25

LANDSAT	WNW	NE	NS	NNW	NNE	EW	ENE	NW
Area of F points = 10^2	170	40	70	20	22	50	0	30
Area of L	274600	402800	528000	418500	1219700	694100	1660	219700
Area of ROI	546,750,000	546,750,000	546,750,000	546,750,000	546,750,000	546,750,000	546,750,000	546,750,000
Area of L- Area of F pints	274430	402760	527930	418480	1219678	694050	1660	219670
# of lineaments	4	7	7	6	21	13	1	3
Area ROI - (Area of L + Area of F points)	546,475,230	546,347,160	546,221,930	546,331,480	545,530,278	546,055,850	546,748,340	546,530,270
Area of ROI-Area of F pints	546,749,830	546,749,960	546,749,930	546,749,980	546,749,978	546,749,950	546,750,000	546,749,970
# F points within the L	1	1	1	0	4	1	0	0
# F points outside the L	16	3	6	2	18	4	0	3
# F points	17	4	7	2	22	5	0	3
# of F points within the L/Total # of F points	0.058823529	0.25	0.142857143	0	0.181818182	0.2	#DIV/0!	0
(Area of L - Area of F points) / (Area of ROI - Area of F points)	0.00050193	0.000736644	0.000965579	0.000765396	0.002230778	0.00126941	3.03612E-06	0.000401774
# of F points outside the L/ total number of F points	0.941176471	0.75	0.857142857	1	0.818181818	0.8	#DIV/0!	1
(Area ROI - (Area of L + F points)/Area of ROI- Area of F points	0.999497759	0.999263283	0.999034293	0.999234568	0.997769181	0.9987305	0.999996964	0.999598171
Wi+	4.763837064	5.827111653	4.996872962	0	4.400656638	5.05976493	0	0
Wi-	-0.06012225	-0.286945084	-0.153184507	0.000765725	-0.198437385	-0.22187324	0	0.00040191
Contrast	4.703714809	5.540166569	4.843688456	0	4.202219253	4.83789169	0	0
Maximum Possible Contrast Value	6.669317969	7.596577049	7.819620463	7.175213318	6.942783111	6.10555854	7.213480448	12.71097163

Table 26

LANDSAT	WNW	NE	NS	NNW	NNE	EW	ENE	NW
Area of F points = 10^2	80	0	190	80	100	10	50	30
Area of L	274600	402800	528000	418500	1219700	694100	1660	219700
Area of ROI	546,750,000	546,750,000	546,750,000	546,750,000	546,750,000	546,750,000	546,750,000	546,750,000
Area of L- Area of F pints	274520	402800	527810	418420	1219600	694090	1610	219670
# of lineaments	4	7	7	6	21	13	1	3
Area ROI - (Area of L + Area of F points)	546,475,320	546,347,200	546,221,810	546,331,420	545,530,200	546,055,890	546,748,290	546,530,270
Area of ROI-Area of F pints	546,749,920	546,750,000	546,749,810	546,749,920	546,749,900	546,749,990	546,749,950	546,749,970
# F points within the L	0	0	2	1	10	0	0	1
# F points outside the L	8	0	17	7	0	1	5	2
# F points	8	0	19	8	10	1	5	3
# of F points within the L/Total # of F points	0	#DIV/0!	0.10526316	0.125	1	0	0	0.33333333
(Area of L - Area of F points) / (Area of ROI - Area of F points)	0.00050209	0.00073672	0.00096536	0.00076529	0.00223064	0.00126948	2.94467E-06	0.00040177
# of F points outside the L/ total number of F points	1	0	0.89473684	0.875	0	1	1	0.66666667
(Area ROI - (Area of L + F points)/Area of ROI- Area of F points	0.99949776	0.99926328	0.99903429	0.99923457	0.99776918	0.9987305	0.999996964	0.99959817
Wi+	0	0	4.69171842	5.09581954	6.10546854	0	0	6.72100817
Wi-	0.00050237	0	-0.1102595	-0.1327657	0	0.00127031	3.03613E-06	-0.4050632
Contrast	0.00050237	0	4.58145896	4.96305387	6.10546854	0.00127031	3.03613E-06	6.31594498
Maximum Possible Contrast Value	6.66931797	7.59657705	7.81962046	7.17521332	6.9426639	6.10555854	7.213480448	12.7109716

Table 27